Stress analysis of straight and initially curved composite tubular beams using an analytical meshless dimensional reduction method

Saeid Khadem Moshir

A Thesis
In the Department
of
Mechanical, Aerospace and Industrial Engineering

Presented in Partial Fulfillment of the Requirements
for the Degree of
Doctor of Philosophy (Mechanical Engineering) at
Concordia University
Montreal, Quebec, Canada

December 2021

© Saeid Khadem Moshir, 2021

CONCORDIA UNIVERSITY
School of Graduate Studies

This is to certify that the thesis was prepared
By: Saeid Khadem Moshir

Entitled: Stress analysis of straight and initially curved composite tubular beams using an analytical meshless dimensional reduction method

and submitted in partial fulfilment of the requirements for the degree of
DOCTOR OF PHILOSOPHY (Mechanical Engineering)
complies with the regulations of the University and meets the accepted standards with respect to originality and quality.
Signed by the final examining committee:

Dr. Ahmed Soliman	Chair
Dr. Dineshkumar Harursampath	External Examiner
Dr. Khaled E. Galal	External to Program
Dr. Rajamohan Ganesan	Examiner
Dr. Ramin Sedaghati	Examiner
Dr. Suong Van Hoa	Supervisor
Dr. Farjad Shadmehri	Co-supervisor

Approved by

Dr. Ivan Contreras, Graduate Program Director

December 21, 2021

Dr. Mourad Debbabi, Dean
Gina Cody School of Engineering & Computer Science

Abstract

Stress analysis of straight and initially curved composite tubular beams using an analytical meshless dimensional reduction method

Saeid Khadem Moshir, Ph.D.

Concordia University, 2021.

Due to high strength to weight ratio of thermoplastic composite structures, their use attracted industrial interests, especially in the aerospace industry. The application of composite curved tubes for landing gear of helicopters instead of aluminum is the subject of interest for the aerospace industry. The focus of the present work is to study mechanical behavior of composite straight and curved composite tubes subjected to the bending loading which is similar to the loading conditions of cross tubes for landing gear of helicopters during landing. The analysis of these structures with a large number of layers may be computationally expensive. The finite element method is widely used for stress analysis of initially curved composite tubes. This method is computationally expensive for design and optimization process. The main objective of the present thesis is to develop an efficient, simple-input method for stress analysis of initially curved and straight composite tubes under four-point bending loadings. To do so, different methodologies for stress analysis of straight and initially curve tubes are introduced. The advantages and disadvantages of the methods are presented. The first part of this thesis focuses on the stress analysis of straight composite cylinders under pure bending moment. The 3D elasticity of Lekhnitskii is employed to carry out the stress analysis of an anisotropic cylinders with many layers. In the second part, an analytical meshless polynomial based method in conjunction with dimensional reduction method are presented to carry out cross-sectional analysis as well as determining strain distribution in straight and curved composite tubes under bending loading (four-point bending loading) in which the effect of shear strains is taken into consideration. In order to obtain the stiffness constants of the cross-section and strains, the powerful mathematical Variational Asymptotic Method (VAM) is employed to decompose a three-dimensional elasticity problem into a two-dimensional cross-sectional analysis and a one-dimensional analysis along the length. The VAM presents Classical and Timoshenko beam models and cross-sectional stiffness matrices. In the Classical beam model cross-sectional stiffness matrix, the effect of shear is not considered. In order to achieve a more precise beam model for the analysis of initially curved and straight tubular beams, the

Timoshenko-like beam model and the effect of shear strain is taken into consideration. VABS is a commercial finite element-based software for cross-sectional analysis of composite beams having complex cross-section shape. For the case of simple cross-sections such as rectangular, circular and elliptical shape, the modeling process of VABS can be eliminated by employing meshless method. The presented polynomial meshless dimensional reduction method is employed for tubes with circular and elliptical cross-sections which is the main novelty of this work. In the present work, the utilization of the Pascal polynomials for the cross-sectional analysis of the beams takes advantage of the meshless method compared with the three-dimensional finite element method or VABS. Moreover, a one-dimensional finite element solution is provided for straight and initially curved composite tubes. The presented method for the analysis of initially curved and straight tubes is computationally more efficient and simple-input compared to the 3D finite element method. In addition, it eliminates generating two-dimensional cross-sectional mesh and dividing the cross-section into different segments for straight and curved tubes compared to Variational Asymptotic Beam Sectional Analysis (VABS) software. So, the present method can be more efficient and straightforward in terms of modeling procedure compared to VABS. The parametric study such as determining cross-sectional stiffness constants, strains and displacements for design and optimization will be more straightforward.

The experimental tests are carried out to validate the present method of solution. Test setups for four-point bending test of the straight and initially curved tubes are provided by a teamwork at Concordia Center for Composites (CONCOM). The obtained strains at different spots of the tubes as well as the transverse displacement are compared with the theoretical solution. The effect of lay-up sequence, initial curvature on the mechanical behavior of the composite tubes are studied.

Acknowledgment

I would express my gratitude to my father, mother, sister and my brother for without their support and understanding I couldn`t have succeeded in completing this thesis.

My gratitude also extends to my supervisor Dr. Suong Van Hoa and Dr. Farjad Shadmehri whose supports, and directions helped me strive and thrive.

I would like to acknowledge the financial supports provided by NSERC, Bell Helicopter, and Concordia University.

Contributions of Authors

The experimental tests in this thesis have been conducted by a teamwork at Concordia Center for Composites (CONCOM) in which Dr. Ashraf Fathy contributed to fabricate the tests setup, Dr. Daniel Rosca contributed to fabricating the thermoplastic straight and curved composite tubes.

Contents

List of Figures

List of Tables

Nomenclature

Common variables

a_i	Coefficients of the Pascal polynomial	U_0, U_1	Approximations of the strain energy
$[A_1]$, $[A_2]$, $[A_3]$, $[A_4]$	Intermediate matrix expressions	U^e	Element strain energy
$[C]$	Stiffness matrix in material coordinare system	$\overline{u}$, $\overline{v}$, $\overline{w}$	Beam displacement components
$[D]$	Stiffness matrix in the beam coordinate system	w_1, w_2, w_3	Warping variables for cross-section
E	Young modulus	x_1, x_2, x_3	Coordinates of the structure
e_i	Coordinates along principal material directions	α	Fiber angle
$\boldsymbol{F}$	Vector of cross-sectional stress resultant	$[\overline{\alpha}]$	Unknown coefficients matrix
$[Y_1]$, $[Y_2]$, $[Y_3]$	Intermediate matrices	β	Layer angle
h	Beam thickness	γ_{12}, γ_{13}	Shear strains
I	Moment of inertia	γ_{11}	Extensional strain of the reference line in Timoshenko beam
J	Torsional moment of inertia	$\overline{\gamma}_{11}$	Extensional strain of the reference line in Classical beam
$[K^e]$	Element stiffness matrix	$\boldsymbol{\delta}$	Nodal displacement vector
L	Beam length	$\boldsymbol{\varepsilon}$	Generalized Timoshenko strain vector
L_e	Beam element length	$\overline{\boldsymbol{\varepsilon}}$	Generalized classical strain vector
$[M]$	Cross-sectional moment resultant vector	$\varepsilon_{\max}$	Maximum of 1-D strains
m	Order of the Pascal polynomial	θ	Circumferential angle
p	Number of terms in the Pascal polynomial	κ_1 , κ_2 , κ_3	Curvature variables in Timoshnko model
ρ	Radial position of points in cross-section	$\overline{\kappa}_1$, $\overline{\kappa}_2$, $\overline{\kappa}_3$	Curvature variables in classical model

$[S]$	6×6 Timoshenko stiffness cross-sectional matrix	$\bar{\varphi}_{x_1}, \bar{\varphi}_{x_2}, \bar{\varphi}_{x_3}$	Beam element rotations
$[\bar{S}]$	4×4 classical stiffness cross-sectional matrix	$\boldsymbol{\psi}$	1-D strain vector in Timoshenko beam model
$[T]$	element nodal Coordinates matrix	Ω	Cross-section area
$[T_\alpha], [T_\beta]$	transformation matrices	r_o	Outer radius of the cross-section
h	Tubular beam thickness	b_1, b_2, b_3	Triads of x_1, x_2, x_3
$\boldsymbol{R}$	Vector of reference line in deformed shape	$\boldsymbol{r}$	Vector of reference line in un-deformed shape
B_1, B_2, B_3	Triads of deformed beam configuration	$\boldsymbol{g_i}$	Contravariant base vectors
$\boldsymbol{g^i}$	Covariant base vector	λ	Determinant of the metric tensor for the undeformed geometry
k_1, k_2, k_3	Initial curvature	$\boldsymbol{K}$	Final curvature vector
$[D_{\varepsilon\varepsilon}]$, $[D_{h\varepsilon}]$, $[D_{hh}]$, $[D_{hl}]$, $[D_{ll}]$, $[D_{l\varepsilon}]$, $[D_{hR}]$, $[D_{RR}]$, $[D_{R\varepsilon}]$, $[D_{Rl}]$	Matrices carrying information of geometry and material properties of curved tubes	$\boldsymbol{V_k}$	vector of unknown Pascal coefficients
Γ_h, Γ_ε, Γ_R, Γ_l	operators	$[W]$	Matrix of pascal polynomials
$\Lambda_1 - \Lambda_6$	Matrices carrying information of geometry and material properties of straight tubes	$[\hat{\lambda}]$	Transformation matrix
$\boldsymbol{f}$	Element load vector	$\boldsymbol{\zeta}$	Strain vector of reference line

Variables of Chapter 2

x, y, z	Cartesian coordinates	K_i	Arbitrary constants
σ_r , σ_θ, σ_z	Radial, circumferential, longitudinal normal stresses	β_{ij}	Reduced elastic constants
$\tau_{r\theta}, \tau_{rz}, \tau_{\theta z}$	Shear stresses	m_i	Roots of characteristic equations
C_{ij}	Material property constant	κ_x , κ_y	Bending curvatures of center line
A_{ij}	Laminate stiffness constants	M_x, M_y	Bending moment about x and y

1. Chapter1: Introduction

1.1 Introduction

Laminated composite beams play a crucial role due to outstanding mechanical properties in the production of innovative structures which include light-weight, high-stiffness to weight, high damping, excellent corrosion, thermal and high impact resistance. However, the stress analysis of a composite tubular structure under complex loading conditions is often a complex task. This is due to the change of the fiber angle at each layer so that in the three-dimensional finite element analysis (3D FEA) one element is needed to be used for each layer (ply-wise analysis). This issue makes the analysis to be time consuming and expensive procedure. Moreover, the governing equations for composite structures are much more complicated than those of the structures made of isotropic materials. Moreover, the three-dimensional elasticity analysis methods often are not able to consider all the loading effects (*e.g.* shear loading, boundary conditions). Finally, a major source of intricacy is the layer-wise failure of composite materials. In fact, as soon as a layer fails, a sort of delamination occurs or a crack propagates in plies, and material properties and sometimes governing equations could be different. This readily adds a lot of complexity to the analysis of composite structures.

1.2 Motivation

Currently, the helicopter industry uses Aluminum alloys (e.g. 7075 T6) for landing gear structure. Landing gear consists of two parallel curved tubes connecting the two skis of the helicopter as shown in Fig. 1. Although there are many issues in the maintenance, fabrication, and failure weakness due to the corrosion, the aluminum landing gear is the choice of the industry, experimental and theoretical works such as analytical and numerical works have been done for developing the landing gears. Derisi [1] and Moshir el al. [2] tested and analyzed straight thermoplastic orthotropic tubes under three-point and four-point bending loadings. However, an analytical simple-input and fast method which takes into account all the components of the strains, displacements of a composite curved and straight tubes under complex loading such as four-point bending loading is needed. Developing a simple, fast and accurate meshless method for design purpose of an initially curved and straight composite tubes is the main motivation of the present work.

1.3 Literature survey

Due to high strength to weight ratio of the composite with respect to isotropic materials, the attraction of the aerospace industry in applying composite structures is growing in recent years. The conventional Bell helicopter landing gear consists of two parallel curved cross-tubes, each are connected by two longitudinal skid tubes. Fig. (1.1) shows the cross-tube for landing gear of helicopter. The cross-tube of the landing gear of a helicopter consists of initially curved and straight tubes.

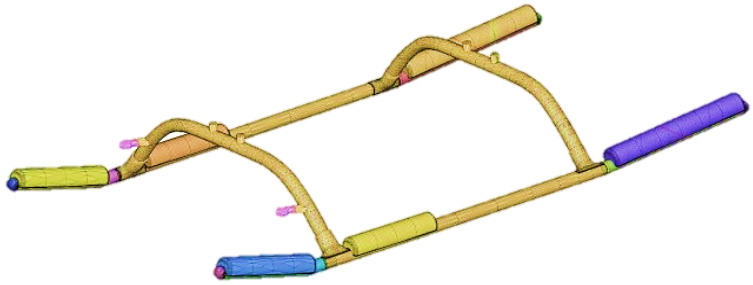

Fig. (1.1) Bell 412 landing gear system [3].

1.3.1 Straight composite tubes

The utilization of aluminum tube for landing gear of helicopter has disadvantages such as the manufacturing problem (acid etching to obtain variation in the thickness), and pit corrosion due to impact by small hard particles from ground during take-off or landing which can reduce the fatigue life of the tube, [4].

Recently, there have been interests in thick composite structures. One type of composite structure is a straight tube that is used for the fabrication of the landing gear of the helicopter or any other engineering structure. Thin composite tubes have many applications and there are a large number of analytical methods for studying the mechanical behavior of these structures. The study of mechanical behavior of composite tubes can be divided into two main categories. The first category treats the composite tubes as multi-layered composite cylinders. These methods usually use three-dimensional (3D) elasticity and use equilibrium equations, displacement field or stress functions to carry out stress analysis of tubes. They are able to analyze composite tubular cylinders (usually straight) under pure bending moment, torsion, internal pressure and extensional loads. In

these methods, the boundary conditions at two ends of a tube, and variation of support and loadings along the length of the tube, are not taken into consideration and so the structural behavior of a composite tube under loading such as transverse displacement cannot be predicted. Also, these methods may not be able to handle initially curved tube. The second category treats the composite tubes as a beam with boundary conditions in which a composite tube mechanical behavior under transverse loading can be evaluated.

1.3.1.1 3D elasticity

To study the elasticity of anisotropic cylindrical body, several solutions have been proposed for the basic equations of the mathematical theory of anisotropic elasticity. Lekhnitskii for the first time, obtained a set of partial differential equations for cylindrical anisotropy problem of single layered cylinder subjected to the axisymmetric loading and bending loading, [5]. Following Lekhnitskii, number of research have been conducted for stress analysis of composite cylinders subjected to axisymmetric loading including internal pressure, hygrothermal loading, torque and tension loading. Davis and Bruce [6] proposed the stress analysis of thick-walled concentric orthotropic cylinders subjected to internal pressure, uniaxial tension or torsion. Hu et al. [7, 8] employed Lekhnitskii's [5] stress functions to study stress distribution of $\pm 55^{\circ}$ filament wound composite tube subjected to internal pressure or tension load. Bouhfas et al. [9] developed an analytical method to study mechanical behavior of thick composite pipes under internal pressure. The model applied the plane strain states of multi-layered cylinders under internal pressure. Akosy et al. [10] conducted stress analysis of laminated homogeneous cylinders subjected to thermal or inertia force due to rotation using 2D equilibrium equations in the cylindrical coordinates. In addition, a number of works have been done regarding the bending of the composite orthotropic cylinders subjected to pure bending moment which also can be considered as the displacement based linear elasticity solution. Yuan [11] provided an exact solution for bending of laminated cylindrical shells using Lekhnitskii's stress functions. He also derived closed form solutions on the basis of classical shell theory and Donnel's theory. In the most notable work, Jolicoeur and Cardou [12] conducted the stress analysis of coaxial orthotropic cylinders in which all the stresses are considered. Two types of interaction at the interfaces between the layers including no slip and no friction are assumed. Under the no slip condition which assumes the perfect bonding between the layers, there is the continuity of the radial stress σ_r, the in-plane plane shear stress $\tau_{r\theta}$ as

well as out-of-plane shear stress τ_{rz} and displacements such as the radial displacement u_r, the circumferential displacement u_θ and the longitudinal displacement *w*. In the no friction case, there is only the continuity of σ_r and u_r. Tarn and Wang [13] applied an exact analytical solution to study extension, torsion, bending, shearing and pressuring of laminated composite tubes based on general expressions for the displacements obtained by Lekhnitskii [5]. For the sake of simplicity, they used the state space approach so that the problem of generalized plane strain, generalized torsion and bending of laminated tubes are formulated for the stress analysis. Xia et al. [14] provided an exact solution based on classical laminate-plate theory for pure bending analysis of multi-layered filament-wound composite pipes based on Lekhnitskii's stress function. It is noted that the out-of-plane shear stress effects were not considered in their analysis. Zhang et al. [15] found that the analytical solution provided by Jolicoeur and Cardou [12] for determining flexural stiffness as well as stress analysis of composite cylindrical tubes under bending loading which was based on stress function of Lekhnitskii [5]. The method presented in [12] was not capable of analyzing cylinders including 0°or 90° helical angle due to some parameters became singular. In order to overcome this issue, they provided a modified limit based solution. In another work, Zhang et al. [16] provided a solution for the composite tubes including 0°or 90° layers and any arbitrary angle. The approximations of singular parameters for special layers (0°or 90°) near other angles are provided. To this end, a Taylor series expansion as a powerful tool for special layers is utilized. Guechy and Hoa [17] obtained flexural stiffness of two-layered thick composite tubes by utilizing the solution based on the three dimensional theory of elasticity proposed by Jolicoeur and Cardou [12]. They examined and compared theoretical results and experimental ones only for tubes with lay-up of [25/-25]. Sun et al. [18] carried out a stress analysis of hollow cylindrical structures including multiple anisotropic layers using stress functions proposed by Lekhnitskii [5]. They also provided solutions for a homogenized composite cylinder with single-layer. Their solution is sufficient for stress analysis of thin-walled or moderately thick-walled hollow composite cylindrical structures. They compared the obtained results which were for composite tube with lay-up excepted for 0 or 90 winding angle degree of the layers by the FEM. Menshykova and Guz [19] investigated stress analysis of multi-layered thick-walled fiber reinforced composite straight pipes manufactured by filament winding process under bending loading. They used the axial stress relation of Lekhnitskii then used stress-strain relation of Xia et

al. [14]. The out-of-plane shear stresses were not taken into account in their solution. Blom et al. [20] tested bending of carbon-fiber reinforced composite cylinders including baseline laminate and circumferentially varying laminate stiffness. They also carried out a FEA of tubes in order to compare between results. Derisi et al. [1] experimentally investigated three and four-point bending of thermoplastic composite tubes in which a strain-controlled design and large deformations are considered. They also carried FEA of tubes using ANSYS software package. They showed that the composite thermoplastic tubes can have the same flexural stiffness, slightly higher strength, load carrying capacity and large strain to failure as an aluminum counterpart. In this research, mostly Lekhnitskii's stress functions are used to obtain a system of partial differential equations. Since the cylinder is under pure bending moment, not only the stresses are independent of the axial coordinate but also the end effects are not taken into account. In addition, it should be noted in the all the studies using Lekhnitskii's stress function, the solutions provided are for straight orthotropic cylinders.

Yazdani et al. [21-23] used a displacement-based method to analyze orthotropic single layered curved tubes under pure bending moment. In his work, a higher-order displacement field of elasticity of thick laminated composite curved tubes is developed employing a displacement approach of Toroidal Elasticity and the layer-wise method. Since the cylinder is under pure bending moment, not only the stresses are independent of the axial coordinate but also the end effects are not taken into account.

1.3.1.2 Classical plate and shell theories

Theories use classical plate and shell assumptions are commonly used for thin-walled beams. The classical shell theory of Donnell's solution for bending of composite cylinders has good agreement for thin-cylinders [24] in which the combination of three-dimensional equilibrium equations of elasticity is applied to obtain the inter-laminar stresses. However, they have substantial difference with 3D elasticity solutions for thick-walled cylinders [25]. Furthermore, the radius to the wall-thickness ratio is limited to 50 (limited to thin) [24]. Tatting et al. [26] provided a nonlinear bending response of finite length of thin composite tubes based on the classical shell theory. The nonlinear strain-displacement relations are implemented where the terms related to the shear strain are kept. Then, they expanded the displacements in terms of a Fourier series in the circumferential direction. The cross-sectional deformations associated with Brazier's flattening influence was

demonstrated using the classical shell theory in which the nonlinear strain-displacement relation of Sander [27] was used. Di and Rothert [28] calculated stress fields of orthotropic cylindrical shells using a higher-order shear deformation theory. Their formulations were derived to present displacement and transverse shear stresses for bending of a thin cross-ply composite straight tube with the simply supported boundary condition at one end. Kollar and Springer [29] provided only some formulations for a stress analysis of thin and thick-walled composite cylinders and cylindrical segments subjected to hygrothermal and mechanical loads (shear, bending and torque). Their analysis is based on the equilibrium equations of Love [30] and applicable to loads which results in small deformation and linearly elastic material. The loads and therefore stresses and strains are independent of the axial direction. Chan et al. [31] presented approaches based on laminate plate and shell theories to calculate the flexural stiffness of thin composite tubes. They also carried out FEA using ANSYS to compare the theories. Saggar [32] experimentally studied four point bending of thin composite tubes and compared their data with classical lamination approach.

1.3.1.3 Brazier effect, [27]

Brazier effect is a nonlinear phenomenon related to the bending of long tubes with deformable cross-section. Because of the curvature of the tube axis subjected to the pure bending, the compressive and tensile stresses act at an angle to the un-rotated cross-section and deform the original circular shape into an oval and flattened pattern, Fig. (1.2). Therefore, the ovalization decreases the moment of inertia and thus the bending rigidity of the cross-section and results in a nonlinear load-displacement relation. Moreover, not only the axial bending stresses increase but also the buckling load is lowered. In order to capture the Brazier effect properly, the nonlinear strain-displacement relation plays an important role. Kim et al. [33] used a modified Brazier approach for bending of composite circular composite spar subjected to bending loading using a linear elastic energy method. The failure mode of the cylinders is determined by flattening the cross-section and the Castigliano's theorem is used for solution.

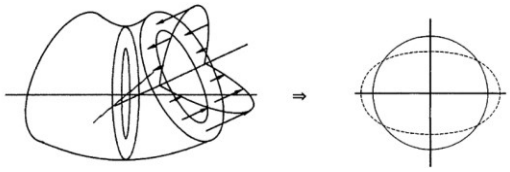

Fig. (1.2) Mechanism of Brazier effect to produce ovalization [26].

1.3.1.4 3D models for analysis of composite tubular straight beams

The other category for analysis of composite tubes treats the composite tubes as beams. Beams are structures in which one dimension is much larger than the other two. A beam theory is often used to model helicopter blades, aircraft wings, wind-turbine blades etc. Depending on the complexity of the beam, beam theories can be divided into *a*) Euler-Bernoulli beam theory, *b*) shear deformable beam theories (*i.e.* Timoshenko theory, third order shear theory, layer wise shear theory, etc.), *c*) 3D beam theories. In 3D beam theories both out-of-plane and in-plane warpings are taken into account. In-plane warpings are due to transverse normal strains and in-plane shear strain. So, effects due to 3D stresses are accounted for 3D beam theories [34]. For laminated composite beams, box beams or tubes, some non-classical effects such as transverse shear deformations, in-plane warpings due to bending and extension, in-plane shear stresses, transverse normal stresses are significant because of anisotropy. These effects are characterized by in-plane and out-of-plane warping displacements. These effects can be accounted for using 3D beam models which include 3D stress effects, geometric nonlinearity and anisotropy and initial curvatures.

The 3D analysis of composite tubular beams can be divided into two groups. The first group applies simplifying assumptions such as displacement or stress field. These analytical models have restrictions for the cross-section geometry. These theories use classical plate and shell assumptions and usually used for thin-walled cross-sections. The non-classical beam theory can be considered as one of the 3D beam models. The other group here called dimensional reduction method does not have any ad-hoc assumption such as displacement field will be discussed hereafter.

1.3.1.5 Non- classical beam theory

The non-classical composite beam theory mainly considers the effect of primary and secondary warpings and transverse shear effects. As the thickness of the beam increases the effect of secondary warping increases. Librescu and Song [35] for the first time presented an approach related to refined theory of thin-walled straight beams with arbitrary cross-section including non-classical effects. Their approach was based on the assumption that a) the original shape of every cross-section of the beam is assumed to remain unchanged after deformation which means that the cross-section does not deform in its own plane, b) the transverse shear effects (τ_{rz} and $\tau_{\theta z}$) were

considered, c) the rate of twist is a function of spanwise coordinate, d) both the primary and secondary warpings are considered, e) the hoop stress resultant is assumed to be negligibly small.

In the work of Rehfield et al. [36], the non-classical effects of the behavior of thin-walled composite beams such as elastic bending-shear coupling and restrained torsional warping were studied. The displacement field is derived in such a way that it has rigid-body translation and rotation of the frame which coincides with the cross-section of the undeformed beam. Further, warping of the cross-section relative to the translated and rotated frame is considered. Kim and White [37] provided an analysis based on non-classical theory for thin and thick-walled composite beams subjected to several loadings in which the primary and secondary warpings, coupled stiffness effects and transverse shear (τ_{rz} and $\tau_{\theta z}$) were taken into account. It is noted stress components such as (normal stress σ_r , hoop stress σ_θ and in-plane shear $\tau_{r\theta}$) are neglected. On the basis of the thin-walled theory proposed by Librescu and Song [35], Shadmehri et al. [38] determined the flexural stiffness of orthotropic composite tubes made of multiple layers. In their work, it was assumed that all deformations are small and the in-plane deformations are not allowed in the cross-section plane. Silvestre [39] presented a formulation of generalized beam theory which is developed to analyze the influence of non-classical effects on the structural behavior of composite circular hollow members. The elastic material couplings, deformation of cross-section, warping deformation and the shear deformations are considered in this theory. The strain-displacement was based on the relations of the Love-Kirchhoff theory where the stress distribution in the section of the tube is not investigated

1.3.1.6 Dimensional reduction method

In another composite beam analysis group, the Variational Asymptotic Method (VAM) has strong appeal. This method can allow the analysis of a 3D problem to be decoupled into a two-dimensional (2D) cross-section analysis and a one-dimensional (1D) analysis. The kinematics of beam deformations can be considered as a linear combination of 1D beam generalized strains and warping deformations of the cross-section. The method has been developed by Hodges and coworkers [40]. The cross-section analysis is carried out which uses 3D elasticity for beam modeling and therefore the simplified kinematic assumptions are not applied. All the components of warping which are the cross-sectional deformations may be coupled together, are calculated. Therefore, 3D stress effects can be evaluated. Hodges and his co-workers were pioneers in the

analysis of cross-section of initially curved and twisted composite box, rectangular, T and I beams using FE method [40-42] and Variational Asymptotic Method (VAM). Prior to their work, Berdichevsky [43] appears to be the first who stated VAM that the geometrically nonlinear problem of the 3D theory of elasticity for a beam can be split into a nonlinear 1D problem and a linear 2D problem (dimensional reduction). In the VAM, the 2D analysis can determine all the stiffness constants of the cross-section of the composite beam including extensional, shear, torsional, bending and their couplings. With the help of FE method, the stiffness matrix of an arbitrary cross-section can be achieved. The VAM perturbs the warping which leads to perturbing the energy functional to different orders, with respect to small parameters and then asymptotically minimize the variational problem. Therefore, this method simplifies the variational problem and eliminates solving differential equations. In addition, Hodges and his co-workers [40, 44] provided a cross-sectional analysis code called VABS (Variational Asymptotic Beam Sectional Analysis) based on the formulation of VAM. The classical model of prismatic beams based on the VAM [45], for initially curved and twisted beams are presented by [46, 47]. It is noted that the classical theory is sufficient in many situations, namely when the beam is slender, is not a thin-walled open section, and undergoes motions with large wavelength (i.e. low-frequency modes of vibration). However, a refined theory is required for high accuracy in other situations. To this regard, Yu et al. [48, 49] formulated a FE based cross-sectional analysis for nonhomogeneous and initially curved and twisted box, rectangular, T and I beams based on 3D elasticity and using VAM. They provided a refined Timoshenko-like model in which the non-classical couplings (extension-shear, bending-shear, and shear torsion) are considered. They reported a 6×6 stiffness matrix of the cross-section for isotropic and anisotropic rectangular and box cross-sections based on Timoshenko-like model of VABS. For the analysis of straight beams with a circular cross-section, Ghafari and Rezaeepazhand [50] used VAM to determine the stiffness matrix of the cross-section of a straight isotropic tube. They obtained 4×4 stiffness matrix of the cross-section based on lower order of the small parameter of the problem that gives the classical beam theory. Rajagopal [51] proposed an analytical closed-form expressions to derive the shear correction factor of isotropic beams with annular cross-section. They extracted the cross-section stiffness matrix of an isotropic tube using VAM. Harursamapth and Hodges [52] used VAM for a thin-walled circular straight tube with Circumferentially Uniform Stiffness (CUS) made of anisotropic material. It is noted that due to the circular symmetry assumption of the tube there is no bending-torsion or extension-

torsion couplings for the CUS tube. The cross-sectional analysis in this solution is non-linear so that this method can incorporate the Brazier effect for analysis of thin-walled tubes. Jian et al. [53] used classical beam model of the VABS for nonlinear sectional analysis of beams with airfoil, and circular cross-section and hyperplastic material. The FE is used in the cross-sectional analysis of the beams. Fang and Yu [54] incorporated the damage modeling constitutive model to the VABS. They compared the elastic-to-damage beam behavior with the finite element analysis (FEA). They studied beams with tubular and rectangular cross-sections. Popescu and Hodges [55] extracted 4×4 Classical and 6×6 Timoshenko stiffness matrices for straight anisotropic tubes using FE based VABS.

1.3.2 Initially curved composite beams and tubes

Composite curved tubes are structures that are used frequently in the aerospace industry. The stress analysis of initially curved thick tubes is more important due to the effect of shear. In addition, for a landing gear structure which is a combination of straight and curved composite tubes, the stress analysis will be more challenging. This is due to change in the location of the neutral axis of the tube at a point where there is a connection in the curved and straight parts. These reasons make the stress analysis of the initially curved composite tubes and beams to be more complicated than straight tubes. In the following section, different methods to study curved beams are presented.

Zupan and Saje [56] presented the equations of the linearized geometrically exact 3D beam theory of curved and twisted beams. They proposed a FE formulation for the linearized theory. Their solution was limited to isotropic material. In addition, the deformations are restricted to be small. Tabarrok et al. [57] presented a set of governing equations and strain-displacement relations in terms of translational and three rotational degrees of freedom for initially curved and twisted isotropic beams. They developed a FE model by using displacement modes of rods. The effects of cross-sectional warping for rods are neglected. In addition, the stress analysis was not performed. Ecsedi and Dluhi [58] utilized 1D mechanical beam model based on the Classical Euler-Bernoulli beam theory for the static and dynamic response analysis and to determine the displacements of non-homogenous symmetrical cross-section of curved beams and closed rings. Hajianmaleki and Qatu [59] applied the First order Shear Deformation Theory (FSDT) with modified ABD matrices to perform static and free vibration of curved rectangular orthotropic beams. Generalized Differential Quadrature (GDQ) method is used to find the exact solutions of simply supported

beams. Yu and Nie [60] derived a formula for the shearing stress as well as radial stress in curved isotropic beams. Moreover, in most FE models of the curved beams the effect of shear deformation has not been considered and the geometries of the curved beams are restricted to be circular and isotropic material. Sheikh [61] and Dasgupta [62] presented a horizontally curved beam element of arbitrary shape which has three nodes and three degrees of freedom at each node for determining displacements of neutral axis of isotropic curved beams. Sarvestani and Hojjati [63] presented a displacement field using Toroidal Elasticity and layerwise method to investigate stresses, strains and deformations of thick laminated composite curved tubes subjected to pure bending moment. In their solution, the curved tube is under pure bending moment so that this solution is not able to calculate the behavior of a curved tube under complex loading (e.g. three-point bending loading).

The above review shows that there is a shortage of developing a fast, simple-input method to analyze composite curved beams and tubes which captures all the effect of strains and deflections under complex loading. In composite beams which there may be elastic coupling among all the forms of deformation, the 3D beam models based on dimensional reduction method [40] are able to take into account all these couplings. In the curved beams the extensional stiffness, the flexural stiffness, and the extension-bending coupling plays a significant role in the mechanical behavior of the curved beams. In addition, the nonlinear 3D beam models take into account lateral large deflection of the beam without ad-hoc assumption. The dimensional reduction method which takes advantage of small parameter of the problem (thickness to length or thickness to radius of curvature ratio) may lead to perform cross-sectional analysis. In the dimensional reduction method of beam structures, a 3D elasticity is split into a two-dimensional (2D) cross-sectional analysis and a 1D beam model. The VAM was introduced to carry out the cross-sectional analysis for modeling of anisotropic beams by Berdichevky [64]. Borri and Merlini [65] presented both linear and nonlinear formulations for initially curved anisotropic beams with large displacement. They obtained geometric stiffness of the cross-section. Giavotto et al. [66] presented a formulation of problem of calculating cross-sectional stiffness matrix and stresses of anisotropic prismatic beams. The cross-section is discretized by FE method. Their work was developed for the case of curved and twisted beams by Borri et al. [67]. For a 3D elasticity formulation of isotropic and anisotropic beams with initial twist and curvature, Cesnik and Hodges [47] applied VAM to perform cross-sectional analysis. The cross-section of the beam is discretized using the FE method. This work turns out a FE based cross-sectional analysis tool called Variational Asymptotic Beam Sectional Analysis

(VABS). Then, a generalized Timoshenko beam model was developed by Yu et al. [48] in the VABS which leads to a fully populated 6×6 stiffness matrix capturing all the elastic couplings of initially curved and twisted beams. Yu et al. [49] developed FE based VABS based on Classical beam model and Timoshenko beam model which considers the transverse shear effect for initially curved and twisted anisotropic beams. To the best of the author's knowledge, a 1D model for analysis of initially curved composite beams has not been done.

1.3.3 Elliptical composite tubes

Composite tubes with elliptical cross-section represent some variation form the circular tubes.

Few studies have been conducted to determine mechanical behavior of elliptical hollow beams. In 1988, Stemple and Lee [68] developed special FEM for the analysis of hollow beams. Each element has three translational and rotational nodes, and 24 warping nodes. Each translational and rotational node has three translational DOF and three rotational DOF. Each warping node has 1 DOF, which is normal to the deformed cross-section. In 1997, Myers and Hyer [69] studied the response of elliptical composite cylinders subjected to internal pressure. They used a semi-analytical approach based on methods of Marguerre, Rayleigh-Ritz and Kantorovich, where the radius of curvature and displacement are approximated by expansions in harmonic series in the circumferential arc-length coordinate, and the coefficients of the displacement series being unknown functions that are solved using the finite-difference method. In 1999, Myers and Hyer extended the method to study the elliptical composite cylinders subjected to compressive loading [70]. Since the radial distance of points on the surface varies along the circumferential directions, in these papers, they used a semi-analytical approach based on the methods of Marguerre, Rayleigh-Ritz, and Kantorovich. In 2001, Lin and Chan [71] developed a method to determine the tension and bending stiffness of elliptical composite tubes using laminate theory, and parallel axis treatment. Akgun and Kurtaran [72] investigated nonlinear analysis of laminated composite elliptical beams using first order shear deformation theory and Von-Karman strain-displacement relation to take into account geometric nonlinearity. They used differential quadrature method for solving the equations. The relative orientation between the fibers and the different coordinate axes are not considered so that only the cross-ply tubes were studied.

The use of finite element method as in reference [68] can obtain results (longitudinal deflection, rotation and transverse deflection). However, for composite tubes with many layers, the

computational time for the beam analysis might be an issue, especially for the parametric study. Myers and Hyer [69, 70] studied only beams with elliptical cross-section that are subjected to internal pressure, and compression load. The work of Lin and Chan [4] only focused on bending stiffness and does not address torsional stiffness. Also, they used laminate theory which does not take shear into consideration.

1.4 Experimental bending tests of composite tubes

The structure of cross-tube for landing gear of helicopters are mainly subjected to four-point bending loadings. Where the two ends of the tubes are connected to the skis so that they can slide during landing. The landing gears have been manufactured from elastic-plastic metal alloys which dissipate energy during plastic bending. The Aluminum 7075-T6 is usually used for the landing gear structure of helicopters. The fracture strain of this aluminum alloy is about 11%, [1].

A large number of studies have been carried out for experimental bending test of composite straight tubes. Derisi and Hoa [1] carried out four-point bending test of [90/0] thermoplastic composite tube for the design of cross-tube for landing gear of helicopters. Then, they performed three-point bending test on thermoplastic (Carbon/PEKK) tubes with lay-up of $[(90^{\circ}_{10} / 0^{\circ}_{10})_3 / \pm 45^{\circ}_{25}]$, in another attempt, they tested a tube with lay-up $[90^{\circ}_{30} / \pm 25^{\circ}_{45} / 90^{\circ}_{5} / \pm 30^{\circ}_{20} / 90^{\circ}_{5} / \pm 45^{\circ}_{20}]$, and the last tube had the lay-up of $[90^{\circ}_{20} / \pm 25^{\circ}_{25} / 90^{\circ}_{5} / \pm 30^{\circ}_{25} / 90^{\circ}_{5} / \pm 45^{\circ}_{10}]$ where they obtained the failure sequence, maximum strain to failure, the equivalent bending stiffness using the laminate theory and load-strain graph. They used glass fiber reinforcements pads to avoid stress concentration and aluminum rings to increase bending stiffness and abrupt failure at the mid-length of the tube. Geuchy and Hoa [17] determined flexural stiffness of thick walled composite tubes using pure bending test. A test setup for pure bending test of thick tubes were fabricated for this purpose. Chen et al. [73] carried out quasi static three-point and crunching test of hat-shaped composite tubes in which different stacking sequence are studied. Characteristics of energy absorption to weight of the hat-shaped tubes were explored. Saggar [32] experimentally investigated four-point bending of composite tubes. They compared the experimental results with the laminated plate and shell theory. The effects of tube radius, stacking sequence, and wall thickness on the bending stiffness and the strength of the tubes were studied. They utilized techniques of x-ray radiography and optical microscopy for the failure process. The lay-up sequences were including the [0/45] tubes. Blom et al. [20] carried out bending test of carbon-fiber-reinforced composite cylinders.

They tested a composite tube including 0°, 90° and $\pm 45^{\circ}$ layers and tubes including variable stiffness layers where the fiber orientations varied in the circumferential direction. They optimized tubes for maximum buckling load carrying capability under bending. The experimental response of the composite tubes were compared with the FEA. Szabó et al. [74] provided an experimental study and ANSYS finite element analysis for bending of filament-wound composite tube including $[\pm 55^{\circ} / \pm 55^{\circ}]$. The tube was subjected to three-point bending loading.

Three and four-point bending tests have been standardized for testing of the metallic and composite beams with rectangular-cross-section. However, there is no standard test for bending test of tubes. On the other hand, similar conditions of the bending of cross-tubes of the landing gear of the helicopters should be considered. To do so, a test setup for three-point and four-point bending test of straight and initially curved (similar to the structure as the cross-tube of helicopter) has been developed at CONCOM (Concordia Center for Composites).

1.5 Objective of the thesis

Regarding the analytical works, a large number of the studies on the stress analysis of composite tubes are limited to the straight tubes and symmetric loading conditions, while the cross-tubes for landing gear of helicopters are subjected to four-point bending loading. Moreover, in most of the methods, only the isotropic tubular beams are studied. In addition, the utilization of 3D finite element analysis for the stress analysis of composite tubes is time consuming. Especially, the 3D finite element analysis may not be efficient for the design and parametric study purposes. Each time one changes some parameters such as the number of layers, lay-up sequences, length and radius of tube cross-section, one has to re-mesh and this is cumbersome.

The objective of the thesis is the development of a simplified, efficient and simple-input method to determine the displacement and strains for straight and curved composite tubular beams. As the outcome of this method, the displacement, and strains can be obtained using less computational time. To analyze the cross-section of tubular straight and curved beams using VAM, one can use the VABS commercial software which needs modeling of cross-section, and it uses finite element for generating mesh over the cross-section. This is time consuming and is not necessary for cross sections of regular shapes such as circular, rectangular, or elliptical. In the present work, the VAM in conjunction with the polynomial based method are used for the first time for composite straight

and curved composite tubes of regular shapes to determine cross-sectional stiffness constants, strain distribution and transverse displacement, without generating mesh over the cross-section.

1.6 Thesis outline

The present work is devoted to development of a simple-input, fast and accurate method for analysis of straight and initially curved composite tubes, of regular shaped section, subjected to complex loading. In the beginning, different methodologies such as 3D elasticity solution provided by Lekhnitskii, non-classical beam theory for composite tubes and 3D FEM are examined and evaluated by comparing with experimental tests. Then, the main novelty of this thesis in the utilization of meshless method in conjunction with VAM is employed to analyze straight and initially curved beams, of regular shaped sections, subjected to complex loading condition. The thesis is divided into the following chapters.

Chapter 1 (Literature review): A literature survey on the different methods for analysis of straight and initially curved composite tubes.

Chapter 2 (Conventional methods for stress analysis of straight composite tubes under pure bending moment): The 3D elasticity solution provided by Lekhnitskii, non-classical beam theory for tubular beams, 3D regular FEM, strength of materials solution, and experiment have been employed to examine the accuracy of each method. The stress analyses of tubes under four-point bending loading, and three-point bending loading were done and compared with experimental tests. The capability of Lekhnitskii's elasticity solution for failure of tubes is examined by 3D regular FEM and experiment.

Chapter 3 (Introduction to Variational Asymptotic Method (VAM)): This chapter introduces the kinematics of anisotropic beam based on decomposition of rotation tensor. The strain field is applied to derive the strain energy of a beam as a 3D body. The powerful method of Variational Asymptotic Method is employed to minimize the strain energy into different orders based on the small parameters of the problem. This work is done by perturbing the warping field into various orders. Then, the cross-sectional discretization is performed using FEM. The first and second approximations of the strain energy lead to Classical and Timoshenko-like beam models. The Classical beam model results in a 4×4 cross-sectional stiffness matrix without the effect of transverse shear. The Timoshenko-like beam model results in a 6×6 cross-sectional stiffness matrix where the effect of transverse shear is considered. In the next step, we introduce the Pascal

polynomials. The Pascal polynomials are transformed into polar coordinates to perform cross-sectional discretization. The cross-sectional discretization is performed using Pascal polynomial.) Then, a 1D FEM solution is developed based on Classical beam model which considers 3D effects of orthotropic material. Finally, the recovery is performed to capture the 3D strains based on Timoshenko-like beam model.

Chapter 4 (Pascal polynomial dimensional reduction method for straight tubes):

In this chapter, the Pascal polynomial method in polar coordinates system in conjunction with VAM has been developed for determining cross-sectional stiffness constants of straight tubes. Then, a 1D FEM solution has been provided for determining the transverse deflections of tube based on Timoshenko beam model. The 1D FEM solution considers all the 3D coupling effects. The validation with 3D regular FEM as well as VABS, and parametric study have been done to examine the method.

Chapter 5 (Dimensional reduction method for structural analysis of Elliptical composite tubes): The Pascal polynomial dimensional reduction method is developed for elliptical orthotropic sections. The cross-sectional analysis of elliptical sections is different from tubes with circular round sections where the orientation of layer through the circumference varies. The validation and parametric studies have been performed to have insight into the mechanical behavior of elliptical composite tubes under complex loadings.

Chapter 6 (Stress analysis of initially curved composite beams):

This chapter provides the use of Pascal polynomial dimensional reduction method in conjunction with VAM for determining the cross-sectional stiffness constants as well as strains of curved tubes under pure bending moment. Then, the provided 1D FEM for the analysis of initially curved beams is presented to obtain the deflections under transverse loadings. The provided meshless Pascal polynomial dimensional reduction method and VAM presented in chapter 3 is evaluated and validated for different cases. First, we compared the obtained cross-sectional stiffness matrices of rectangular sections with the literature. Then, we compared the strain of these beams with 3D regular FEM. Next, the method for initially curved tubes for different levels of complexity of the material and lay-up sequence is examined with regular 3D FEM in terms of strain. The obtained cross-sectional stiffness matrices are also compared with VABS for different values of initial

curvatures. The provided 1D FEM analysis based on Classical beam model for different loading conditions and lay-ups of composite tubes has been compared with regular 3D FEM. The parametric study has been done to observe the effect of initial curvature on the cross-sectional stiffness constants as well as displacements. Finally, the cross-sectional analysis of initially curved tube tested at CONCOM has been carried out using the Pascal polynomial dimensional reduction method and VABS. The obtained strains have been compared with the experimental results.

Chapter 7 (Contributions and conclusions): The main contributions of this thesis and the recommendations for future works are explained.

2 Chapter 2: Conventional methods for stress analysis of straight composite tubes under pure bending moment

This chapter does not deal with dimensional reduction method, but it serves to introduce the complexity of stress analysis of thick composite beams subjected to bending loads, and conventional methods for the solution. This helps to give rationale for the development of the dimensional reduction method.

2.1 Theoretical formulations

In this chapter, the theoretical formulations for the stress analysis of composite straight tubes are provided. First, the analytical 3D elasticity method of Lekhnitskii [5], Jolicoeur and Cardou [12] for determining the stress distribution and flexural stiffness of straight cylindrical anisotropic body under pure bending moment is provided and compared with experimental tests and 3D FEA. Then, other available methods such as non-classical beam theory and strength of materials for determining the flexural stiffness composite tubes will be employed and compared with experiment for a composite tube under four-point bending loading.

2.1.1 Analytical 3D elasticity method of Lekhnitskii [5], Jolicoeur and Cardou [12]

A composite tube consisting of different cylindrical layers (N) is shown in Fig. (2.1). The tube has elastic moduli E_1 and E_2 in fiber and transverse directions of each layer, respectively. The in-plane shear modulus and Poisson's ratios are G_{12}, G_{13}, ν_{12}, ν_{13} and the out-of-plane shear moduli and Poisson's ratio are G_{23} and ν_{23}. The tube with a winding angle of φ which is the angle between z axis and fiber direction is subjected to bending moments M_x and M_y. In the cylindrical coordinate system, r, θ and z are the radial, circumferential and longitudinal directions. The inside radius of each layer is denoted as b_n.

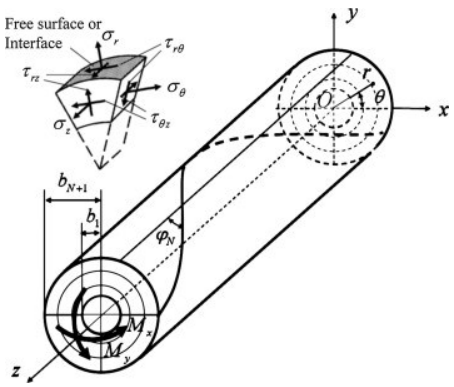

Fig. (2.1) A composite tube subjected to pure bending [16].

The fundamental equations of an analytical mathematical approach were provided by Lekhnitskii [5] for the first time. He derived a set of partial differential equations for anisotropic one cylinder under axisymmetric loading. Following this approach, a coaxial hollow circular orthotropic cylinder subjected to combined bending, tensile and torsion loads was analyzed analytically by Jolicoeur and Cardou [12] in order to obtain stresses, flexural stiffness as well as displacements. Two types of no slip and no friction condition between layers were considered. According to constitutive equations in this approach, the flexural stiffness for a composite tube can be calculated by the following formula

$$(EI)=\sum_{n=1}^{N}\frac{\pi}{C_{33,n}}\left\{\sum_{i=1}^{4}\begin{array}{l}K_{i,n}\left[C_{34,n}g_{i,n}m_{i,n}-C_{13,n}-C_{23,n}\left(m_{i,n}+1\right)\right]\left[\dfrac{b_{n+1}^{m_{i,n}+2}-b_{n}^{m_{i,2}+2}}{m_{i,n}+2}\right]\\ +\left[1-\mu_{1,n}(C_{13,n}+3C_{23,n})+2\mu_{2,n}C_{34}\left(\dfrac{b_{n+1}^{4}-b_{n}^{4}}{4}\right)\right]\end{array}\right\} \tag{2.1}$$

Where C_{ij} (i,j=1..6) are material property constants [75] and β_{ij} are reduced elastic constants as follows

$$\beta_{ij}=C_{ij}-\frac{C_{i3}C_{3j}}{C_{33}} \tag{2.2}$$

K_i are four arbitrary constants which should be obtained, and

$$g_i=\frac{\beta_{24}m_i^2+\left(\beta_{14}+\beta_{24}\right)m_i-\beta_{56}}{\beta_{44}m_i^2-\beta_{55}} \tag{2.3}$$

m_i are roots of the characteristic equation as in the following form, [12]

$$m_{1..4}=\pm\sqrt{\frac{-b\pm\sqrt{b^2-4ac}}{2a}} \tag{2.4}$$

where,

$$
\begin{aligned}
a &= \beta_{22}\beta_{44} - \beta_{24}^2 \\
b &= \beta_{24}\left(2\beta_{14} + \beta_{24} + 2\beta_{56}\right) - \beta_{44}\left(\beta_{11} + 2\beta_{12} + \beta_{22} + \beta_{66}\right) - \beta_{22}\beta_{55} + \beta_{14}^2 \\
c &= \beta_{55}\left(\beta_{11} + 2\beta_{12} + \beta_{22} + \beta_{66}\right) - \beta_{56}^2
\end{aligned} \tag{2.5}
$$

and,

$$
\begin{Bmatrix} \mu_1 \\ \mu_2 \end{Bmatrix} = \begin{bmatrix} -2\beta_{14} - 6\beta_{24} + \beta_{56} & 2\beta_{44} - \beta_{55} \\ -\beta_{11} - 2\beta_{12} + 3\beta_{22} - \beta_{66} & 2\beta_{14} - 2\beta_{24} + \beta_{56} \end{bmatrix}^{-1} \frac{1}{C_{33}} \begin{Bmatrix} 2C_{34} \\ C_{13} - C_{23} \end{Bmatrix} \tag{2.6}
$$

By utilizing continuity conditions at interfaces for either **no slip** or **no friction** cases, the bending stiffness of the composite tube can be obtained. It is noted that in the case of no slip condition between the layers (i.e. there is perfect bonding between layers), there is continuity of stresses σ_r, $\tau_{r\theta}$ and τ_{rz} and of displacements u_r, u_θ and *w*. Whereas, in the case of no friction condition, there is some discontinuity of u_θ and *w*. It means that longitudinal as well as tangential slip between layers are allowed. The in-plane and out-of-plane stresses for either no slip or no friction cases can be expressed as

$$
\sigma_r = \left(\kappa_x \sin(\theta) - \kappa_y \cos(\theta)\right)\left(\sum_{i=1}^{4} K_i r^{m_i - 1} + \mu_1 r\right) \tag{2.7}
$$

$$
\sigma_\theta = \left(\kappa_x \sin(\theta) - \kappa_y \cos(\theta)\right)\left(\sum_{i=1}^{4} K_i \left(m_i + 1\right) r^{m_i - 1} + 3\mu_1 r\right) \tag{2.8}
$$

$$
\sigma_z = \frac{1}{C_{33}}\left(\kappa_x r \sin(\theta) - \kappa_y r \cos(\theta) - C_{13}\sigma_r - C_{23}\sigma_\theta - C_{34}\tau_{\theta z}\right) \tag{2.9}
$$

$$
\tau_{r\theta} = \left(\kappa_x \cos(\theta) + \kappa_y \sin(\theta)\right)\left(-\sum_{i=1}^{4} K_i r^{m_i - 1} - \mu_1 r\right) \tag{2.10}
$$

$$
\tau_{rz} = \left(\kappa_x \cos(\theta) + \kappa_y \sin(\theta)\right)\left(\sum_{i=1}^{4} K_i g_i r^{m_i - 1} + \mu_2 r\right) \tag{2.11}
$$

$$\tau_{\theta z}=\left(\kappa_x \sin(\theta)-\kappa_y \cos(\theta)\right)\left(-\sum_{i=1}^{4} K_i g_i m_i r^{m_i-1}-2\mu_2 r\right) \tag{2.12}$$

In which κ_x and $\kappa_y$are the bending curvatures of the center line.

It was realized by Zhang et al. [16] that in the method provided by Jolicoeur and Cardou [12] some of parameters are singular when the tube includes 0° and 90° layer orientations although the stresses and displacement are nonsingular. Therefore, the continuity condition between 0° layers or 90°layers and other ordinary layers cannot be performed. In order to overcome this issue, Taylor series expansions were applied to obtain parameters for winding angles of the tube including (0° or 90°), [16]. In this method, the flexural stiffness may be calculated as follows

$$\begin{aligned}(EI)=&\sum_{n=1}^{N}\frac{\pi}{C_{33,n}}\left\{\sum_{i=1}^{2}K_{i,n}\left(C_{13,n}+C_{23,n}\left(m_{i,n}+1\right)-C_{34,n}m_{i,n}g_{i,n}\right)\frac{b_n^{m_{i,n}+2}-b_{n+1}^{m_{i,n}+2}}{m_{i,n}+2}\right.\\&+\sum_{j=3}^{4}K_{j,n}^{*}\left(C_{13,n}g_{j,n}^{*}+C_{23,n}\left(m_{j,n}+1\right)g_{j,n}^{*}-C_{34,n}m_{j,n}\right)\frac{b_n^{m_{j,n}+2}-b_{n+1}^{m_{j,n}+2}}{m_{j,n}+2}\\&\left.+\left(\mu_{1,n}\left(C_{13,n}+3C_{23,n}\right)-2\mu_{2,n}C_{34,n}-1\right)\frac{b_n^4-b_{n+1}^4}{4}\right\}\end{aligned} \tag{2.13}$$

The unified coefficients can be introduced as

$$K^{*}=\begin{cases}K_j g_j & \varphi \neq 90\ or\ 0\\ \widetilde{K_j g_j} & \varphi = 90\ or\ 0\end{cases}\quad \text{j=3, 4} \tag{2.14}$$

The calculation of K^{*} is explained below. The corresponding parameters can be introduced as

$$g_j^{*}=\begin{cases}g_j^{-1} & \varphi \neq 0 \ \text{ or } \ 90\\ 0 & \varphi = 0 \ \text{ or } \ 90\end{cases}\quad \text{j=3, 4} \tag{2.15}$$

It should be noted that for the 0° or 90° layers, we have $g_3^{*}=g_4^{*}=0$ by using Eq. (2.14) then the K_3^{*} and K_4^{*} for special layers can be derived by using the continuity condition rather than by using Eq. (2.15).

By applying boundary conditions at inner and outer surfaces of the tube and continuity condition at the interface between the layers, the constants $K_{1,n}^{*}$, $K_{2,n}^{*}$, $K_{3,n}^{*}$ and $K_{4,n}^{*}$ can be determined. The in-plane as well as out-of-plane stresses can be as the following

$$\sigma_r = \left(\kappa_x \sin(\theta) - \kappa_y \cos(\theta)\right)\left(\sum_{i=1}^{2} K_i r^{m_i-1} + \sum_{j=3}^{4} K_j^{*} g_j^{*} r^{m_j-1} + \mu_1 r\right) \tag{2.16}$$

$$\sigma_\theta = \left(\kappa_x \sin(\theta) - \kappa_y \cos(\theta)\right)\left(\sum_{i=1}^{2} K_i (m_i+1) r^{m_i-1} + \sum_{j=3}^{4} K_j^{*} g_j^{*} (m_j+1) r^{m_j-1} + 3\mu_1 r\right) \tag{2.17}$$

$$\tau_{r\theta} = \left(\kappa_x \cos(\theta) + \kappa_y \sin(\theta)\right)\left(-\sum_{i=1}^{2} K_i r^{m_i-1} + \sum_{j=3}^{4} K_j^{*} g_j^{*} r^{m_i-1} - \mu_1 r\right) \tag{2.18}$$

$$\tau_{rz} = \left(\kappa_x \cos(\theta) + \kappa_y \sin(\theta)\right)\left(\sum_{i=1}^{2} K_i g_i r^{m_i-1} + \sum_{j=3}^{4} K_j^{*} r^{m_j-1} + \mu_2 r\right) \tag{2.19}$$

$$\tau_{\theta z} = \left(\kappa_x \sin(\theta) - \kappa_y \cos(\theta)\right)\left(-\sum_{i=1}^{2} K_i g_i m_i r^{m_i-1} - \sum_{j=3}^{4} K_j^{*} m_j r^{m_j-1} - 2\bar{\mu}_2 r\right) \tag{2.20}$$

Using this method, all the stresses are taken into consideration and the distribution of stresses in the thickness of the tube can be achieved.

2.1.2 Strength of materials equation, [17]

The simplest method is the strength of materials approach. The flexural stiffness can be given as:

$$\langle EI \rangle = \sum_{n=1}^{N} \frac{\pi (E_x)_n}{4} (b_{n+1}^4 - b_n^4) \tag{2.21}$$

Where E_n is the modulus along the axial direction for layer n. b_{n+1} and b_n are the outer radius and inner radius of layer n, respectively. E_n can be obtained from the elastic constants of the layer (E_1, E_2, G_{12}) and its fiber orientation θ as [76]:

$$E_x = \frac{E_1}{\cos^4\theta + \frac{E_1}{G_{12}}\sin^2\theta\cos^2\theta + \frac{E_1}{E_2}\sin^4\theta} \tag{2.22}$$

2.1.3 Thin-walled composite tubes

In the thin-walled composite beam theory provided by Librescu and Song [35], in a unified way, a number of necessary effects in the design of composite thin-walled structures such as transverse shear deformation, torsion related nonuniform warping and secondary warping which are assumed to vary across the thickness are taken into consideration [77]. Based on the formulations provided by Shadmehri et al. [38], the flexural stiffness of composite tubes can be determined as follows

$$\langle EI \rangle = \frac{a_{33}a_{44} - a_{34}^2}{a_{44}} \tag{2.23}$$

where,

$$\begin{aligned} a_{33} &= \pi R\left(K_{11}R^2 + 2RK_{14} + K_{44}\right) \\ a_{44} &= \pi R\left(A_{44} + K_{22}\right) \\ a_{34} &= -\pi R\left(K_{12}R + K_{24}\right) \end{aligned} \tag{2.24}$$

R is the average radius of the tube, and we have

$$\begin{aligned} K_{11} &= A_{22} - \frac{A_{12}\left(A_{33}A_{12} - A_{13}A_{23}\right)}{\overline{A}} - \frac{A_{23}\left(A_{23}A_{11} - A_{13}A_{12}\right)}{\overline{A}} \\ K_{14} &= B_{22} - \frac{A_{12}\left(A_{33}B_{12} - A_{13}B_{23}\right)}{\overline{A}} - \frac{A_{23}\left(A_{11}B_{23} - A_{13}B_{12}\right)}{\overline{A}} \\ K_{44} &= D_{22} - \frac{B_{12}\left(A_{33}B_{12} - A_{13}B_{23}\right)}{\overline{A}} - \frac{B_{23}\left(A_{11}B_{23} - A_{13}B_{12}\right)}{\overline{A}} \\ K_{22} &= A_{66} - \frac{A_{16}\left(A_{33}A_{16} - A_{13}A_{36}\right)}{\overline{A}} - \frac{A_{36}\left(A_{11}A_{36} - A_{13}A_{16}\right)}{\overline{A}} \\ K_{12} &= A_{26} - \frac{A_{12}\left(A_{33}A_{16} - A_{13}A_{36}\right)}{\overline{A}} - \frac{A_{23}\left(A_{36}A_{11} - A_{13}A_{16}\right)}{\overline{A}} \\ K_{24} &= B_{24} - \frac{A_{16}\left(A_{33}B_{12} - A_{13}A_{23}\right)}{\overline{A}} - \frac{A_{36}\left(A_{11}B_{23} - A_{13}B_{12}\right)}{\overline{A}} \end{aligned} \tag{2.25}$$

In which, $A_{ij} = \int_{-h/2}^{h/2} \bar{C}_{ij} dz,\ B_{ij} = \int_{-h/2}^{h/2} \bar{C}_{ij} z dz,\ D_{ij} = \int_{-h/2}^{h/2} \bar{C}_{ij} z^2 dz$ are laminate stiffness constants, h is the thickness of each layer, and $\overline{A} = A_{11}A_{33} - A_{13}^2$.

In this approach, it is assumed that all deformations are small, and the in-plane deformations are not allowed in the cross-section plane.

2.2 Evaluation of methods

The theoretical solutions such as 3D elasticity of multi-layered orthotropic cylinder of Lekhnitskii, will be compared with experimental data of three and four-point bending test of Carbon/PEKK composite tubes. First, two composite Carbon/PEKK tubes with 110 and 210 layers under three-point bending loading are analyzed using the 3D elasticity of Lekhnitskii as well as 3D finite element analysis. Next, four-point bending analysis of hybrid composite tube with Carbon/Epoxy and Carbon/PEKK is performed.

2.2.1 Three-point bending analysis of straight composite tubes

In this section, we provided two tubes with 110 and 210 layers. A composite tube (tube number 1) with 110 layers and lay-up $[(90^\circ_{10} / 0^\circ_{10})_3 / \pm 45^\circ_{25}]$ and a thick composite tube (tube number 2) with 210 layers and a complex lay-up $[90^\circ_{30} / \pm 25^\circ_{45} / 90^\circ_5 / \pm 30^\circ_{20} / 90^\circ_5 / \pm 45^\circ_{20}]$ were fabricated by Derisi et al. [1] are studied in which 90° layers are located at inner surface of the tube. The tube number 1 has 56 *mm* and 78 *mm* inner and outer diameters, respectively. The material properties of this composite tube (Carbon/PEKK) are tabulated in Table (2.1).

Table (2.1). Mechanical properties of Carbon/PEKK composite tube.

E_1 (GPa)	140
E_2=E_3 (GPa)	10
G_{12}=G_{13}=G_{23} (GPa)	5.56
$\nu_{12} = \nu_{13}$	0.31
ν_{23}	0.33
X_T (MPa)	1900
X_c (MPa)	1500

Y_T (MPa)	80
Y_c (MPa)	250
S (MPa)	180

where, the X_T and X_c are the strengths in the fiber direction in tension and compression, respectively. Y_T and Y_c are the strengths in the transverse to the fiber direction in tension and compression, respectively. S is the shear strength of the composite material. For the tube which is subjected to three-point bending loading, the bending moment at the mid-length of the tube is

$$M_x = \frac{PL}{4} \tag{2.26}$$

and the load-strain relation at mid-length and bottom surface can be written as

$$\frac{P}{\varepsilon_z} = \frac{8(EI)}{LD_o} \tag{2.27}$$

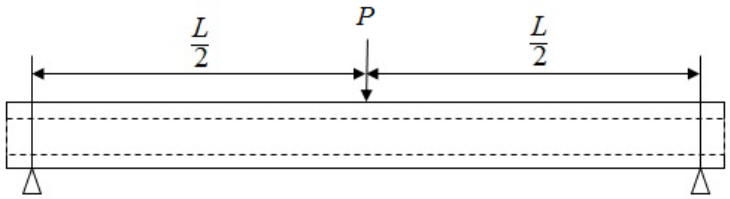

Fig. (2.2). Composite tube subjected to three-point bending loading.

2.2.1.1 Finite element analysis

In order to investigate the stress analysis of composite tubes using FEM, ANSYS 19 3D FEM is employed. The element 3D Solid 185 with 8 nodes and three degrees of freedom at each node has been used for the analysis. The number of elements for a final mesh of each tube in longitudinal, circumferential and thickness directions are shown in Table (2.2). The modeling to find the longitudinal strain has been done in such a way that the tube subjected to bending moment at one side and clamped at other side and the stress/strain distribution are extracted at the mid-length of the tube which are far away from the location of applied moment and the support to eliminate the stress concentrations of the clamped boundary. The magnitude of the moment is equivalent to the values obtained by Eqs. (2.26 and 2.27). In addition, a three-point bending modeling using ANSYS 19 with the same conditions of the test reported by [1] is done for the failure analysis. Fig. (2.3)

shows a schematic drawing of the tube over the boundary support and under loading support. The boundary conditions at the supports are considered as they have $u_x = u_y = 0$ at the nodes which have contact with the supports. The length of supports is 20 *mm*. The loading nose has the length of 45 *mm* and the circumferential angle of 45° of the tube.

Table (2.2). Total number of elements (Longitudinal*Circumferential*thickness) in FEM of each tube.

$[(90^\circ_{10} / 0^\circ_{10})_3 / \pm 45^\circ_{25}]$	$223 \times 61 \times 110$
$[90^\circ_{30} / \pm 25^\circ_{45} / 90^\circ_5 / \pm 30^\circ_{20} / 90^\circ_5 / \pm 45^\circ_{20}]$	$162 \times 62 \times 210$

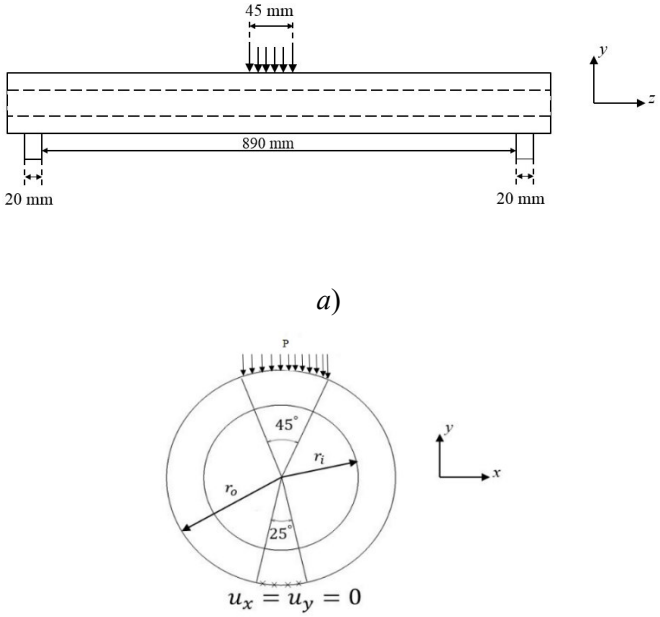

Fig. (2.3). a) A schematic of a tube under three-point bending loading, b) loading and boundary conditions of the tube.

2.2.1.2 Flexural stiffness, failure and stress analysis of tube 1, ($[(90^{\circ}_{10} / 0^{\circ}_{10})_3 / \pm 45^{\circ}_{25}]$)

The tube number 1 with lay-up sequence of $[(90^{\circ}_{10} / 0^{\circ}_{10})_3 / \pm 45^{\circ}_{25}]$ and inner and outer diameters of 56 *mm* and 78 *mm* with the thickness ratio of (0.141) and a span of 890 *mm* is subjected to three-point bending loading. The force-longitudinal strain at the mid-span and bottom of tube is shown in the Fig. (2.4). The slope of the diagram leads to the flexural stiffness of the tube. It can be seen that the Lekhnitskii solution and the FEM predict the flexural stiffness of the tube 22.1% and 20.1% more than the experiment does [1], respectively.

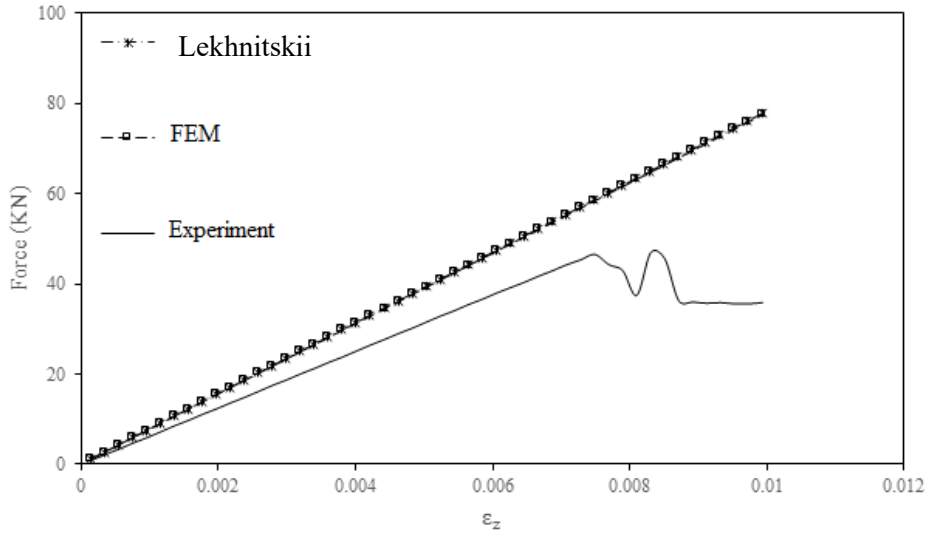

Fig. (2.4) Change of longitudinal strain (mid-length and bottom surface) with applied force for three-point bending of tube 1, $[(90^{\circ}_{10} / 0^{\circ}_{10})_3 / \pm 45^{\circ}_{25}]$.

According to the Tsai-Wu failure criterion, the first ply failure is occurred at the moment of M_x=17.3 KN.m which occurs at the outermost layer of 90° layers. The inter-laminar radial stress distribution at the first ply-failure moment is demonstrated in Fig. (2.5 a). It can be seen that at the 90° and 0° layers the inter-laminar radial stress has stepwise change and it has linear variation at the $\pm 45^{\circ}$ layers. The distribution of circumferential stress through the thickness is shown in the Fig. (2.5 b). The longitudinal stress (Fig. (2.5 a)) is also has fluctuations as the circumferential

stress. The tube does not carry the out-of-plane shear stress $\tau_{\theta z}$ at the 90° and 0° layers, however, it has periodical change at the $\pm 45^{\circ}$ layers as shown in Fig. (2.5 b).

The carried moment of the tube 1 according to the Tsai-Wu, maximum stress criterion and experiment is reported in the Table (2.3). It can be observed there is a large difference between the experimental results and the theoretical ones. The experimental first ply failure value was reported by Derisi [1]. Fig. (2.7) shows the final failure of tube 1 [1].

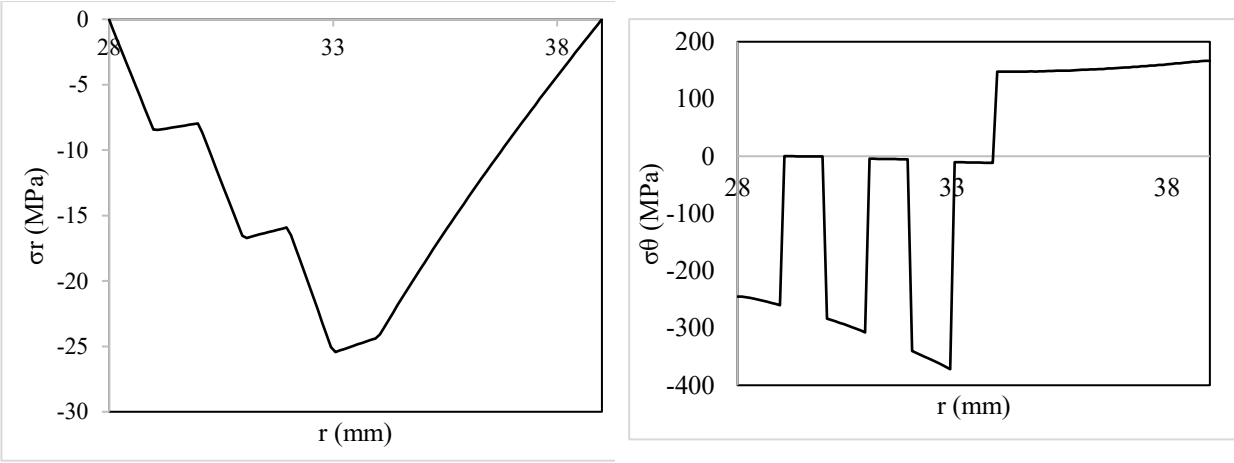

a) *b*)

Fig. (2.5) The distribution of *a*) inter-laminar radial stress b) circumferential stress, through the thickness of the tube 1 ($[(90^{\circ}_{10} / 0^{\circ}_{10})_3 / \pm 45^{\circ}_{25}]$) at $\theta = 90^{\circ}$, at first ply failure based on Tsai-Wu criterion (M_x=17.3 KN.m).

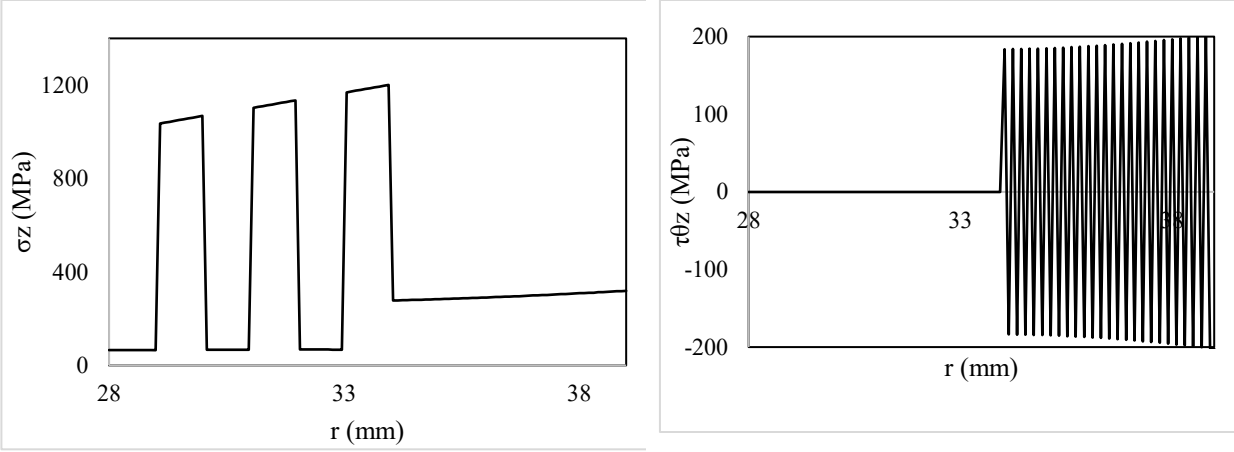

a) *b*)

Fig. (2.6) The distribution of a) the longitudinal stress b) the out-of-plane shear stress through the thickness of the tube 1 ($[(90^{\circ}_{10} / 0^{\circ}_{10})_3 / \pm 45^{\circ}_{25}]$) at $\theta = 90^{\circ}$, at first ply failure based on Tsai-Wu criterion (M_x=17.3 KN.m).

Table (2.3). Bending moment (in KN.m) of the tube 1 at first ply failure.

Method	Maximum stress	Tsai-Wu
Lekhnitskii	20	17.3
FEM	20	17.3
Experiment, [1]	10.0	

Fig. (2.7). Final failure of tube 1 due to stress concentration at the loading nose, [1].

2.2.1.3 Flexural stiffness, stress analysis and failure of tube 2, $[90^{\circ}_{30} / \pm 25^{\circ}_{45} / 90^{\circ}_{5} / \pm 30^{\circ}_{20} / 90^{\circ}_{5} / \pm 45^{\circ}_{20}]$

The stress analysis of the tube 2 with lay-up $[90^{\circ}_{30} / \pm 25^{\circ}_{45} / 90^{\circ}_{5} / \pm 30^{\circ}_{20} / 90^{\circ}_{5} / \pm 45^{\circ}_{20}]$ by considering Lekhnitskii method (no slip) between layers and the FE has been carried out in order to find the distribution of inter-laminar radial, circumferential and shear stresses. The cross-section of the tube is shown in Fig. (2.8). The tube is subjected to pure bending moment M_x=4450 *N.m*. The provided pure bending moments at the ends of the tube are equivalent to three-point loading loads (Eq. (2.26)). Moreover, the stress analysis of this tube has been done by FEM. The inter-laminar radial stress distribution through the thickness of the tube at various circumferential positions $\theta = 30^{\circ}$, 60° and 90° is demonstrated in Fig. (2.9). Although an excellent agreement between the Lekhnitskii and FEM results can be observed, the FEM consumes huge amount of time to find the stress distribution in the tube while the Lekhnitskii's (No slip) takes much less time for this purpose. Therefore, applying FEM can be cumbersome for parametric study. It should be pointed out that σ_r is a function of sine and cosine of angle θ which means that at $\theta = 90^{\circ}$, it has maximum compressive negative value, and it decreases gradually by decreasing the circumferential angle. The radial stress has an effect on the delamination. In addition, it can be realized that at the inside layers of the tube (90° layers, *r*=31.2 *mm*), the radial stress has the maximum magnitude, and it diminishes gradually to zero at the outside layers. The distribution of inter-laminar radial stresses at different angles $\theta = 210^{\circ}, 240^{\circ}$ and 270° are shown in Fig. (2.10). As the angle θ increases, the magnitude of radial stress increases, and it has the maximum distribution at $\theta = 270^{\circ}$ which is a positive value, and it indicates that delamination can be occurred between layers. Moreover, the inter-laminar radial stress has discontinuity at the interface of the layers when the orientation of them varies.

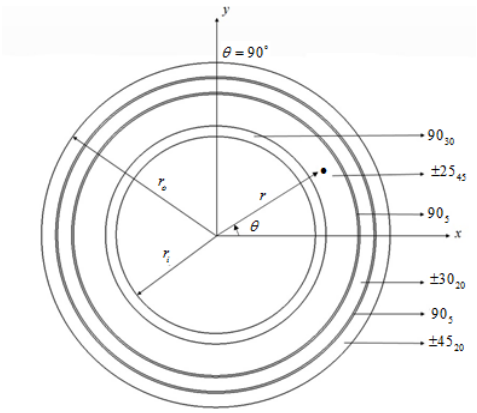

Fig. (2.8) Cross-section of the tube 2 with $[90^{\circ}_{30} / \pm 25^{\circ}_{45} / 90^{\circ}_{5} / \pm 30^{\circ}_{20} / 90^{\circ}_{5} / \pm 45^{\circ}_{20}]$.

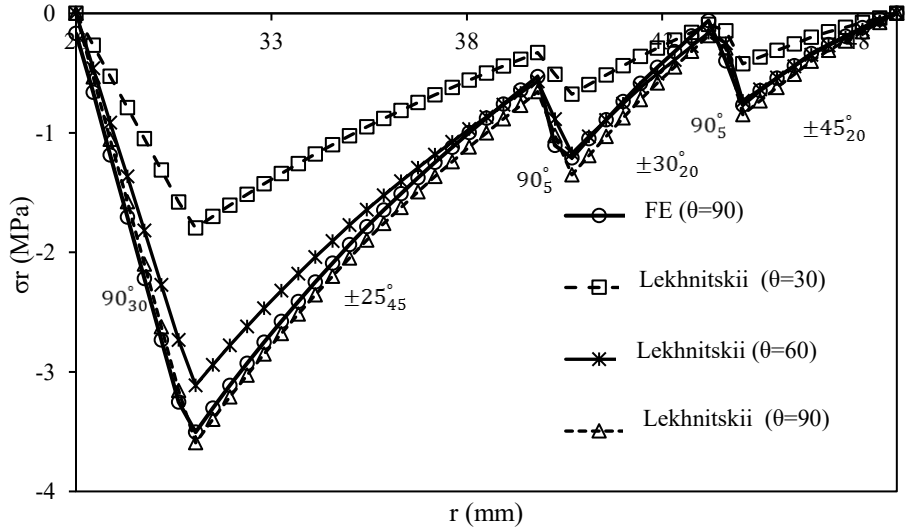

Fig. (2.9). The inter-laminar radial stress through the thickness of the tube 2 at various circumferential positions $\theta = 30^{\circ}$, 60° and 90°, (M_x=4450 N.m.).

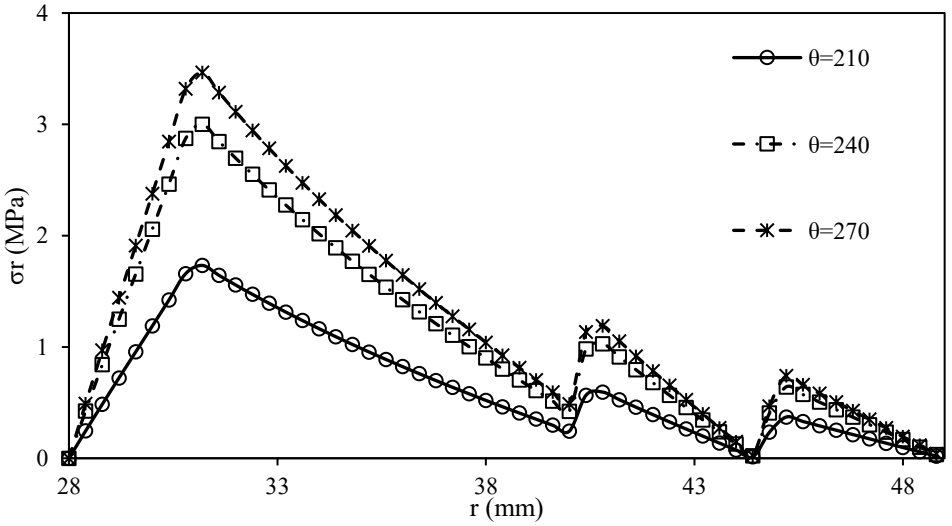

Fig. (2.10). The inter-laminar radial stresses through the thickness of the tube 2 at various circumferential positions $\theta = 210^{\circ}$, 240° and 270°, (M_x=4450 N.m.).

The distribution of circumferential stress at $\theta = 90^{\circ}$ is depicted in Fig. (2.11). This type of stress has substantial effect on the buckling of the tube. A large variation in circumferential stress at 90° layers can be observed. Also, 90° layers can resist circumferential stress. However, low angle layers including $\pm 25^{\circ}$ have less contribution in circumferential stress. The distribution of longitudinal stress through the thickness of the tube is shown in Fig. (2.12). It is seen that although 90° layers have less contribution in longitudinal stress the layers with low winding angle such as $\pm 25^{\circ}$ can have the most longitudinal stress resistance. In other words, low angle layers can provide extensional stiffness and flexural property of the tube. Due to low interlaminar strength of laminated cylinders, the interlaminar stress can cause failure. The in-plane shear stress ($\tau_{r\theta}$) distribution at $\theta = 0^{\circ}$ is shown in Fig. (2.13) where the same behavior as inter-laminar radial stress can be observed. In addition, it is noted that at $\theta = 90^{\circ}$ the in-plane shear stress is close to zero. In Figs. (2.14) and (2.15) the distribution of out-of-plane shear stress ($\tau_{\theta z}$) obtained by Lekhnitskii (No slip) and FE are depicted, respectively. A periodic change of this stress through the thickness of the tube can be observed due to change of the sign of layer angle. Moreover, it is seen that 90°

layers do not have any contribution in out-of-plane shear stress. However, as the layer winding angles decrease, they can resist more this type of stress.

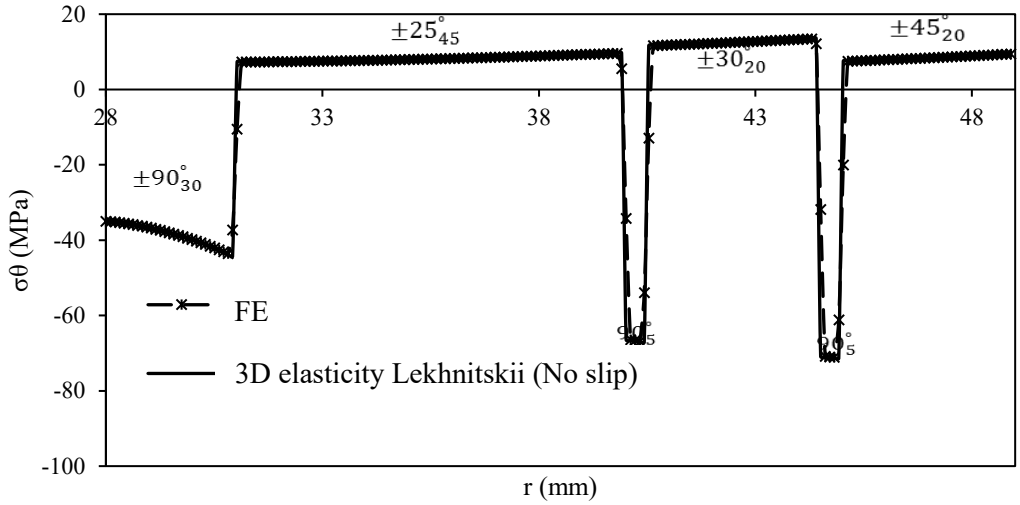

Fig. (2.11). The circumferential stress through the thickness of the tube 2 at circumferential position $\theta = 90^{\circ}$, (M_x=4450 N.m.).

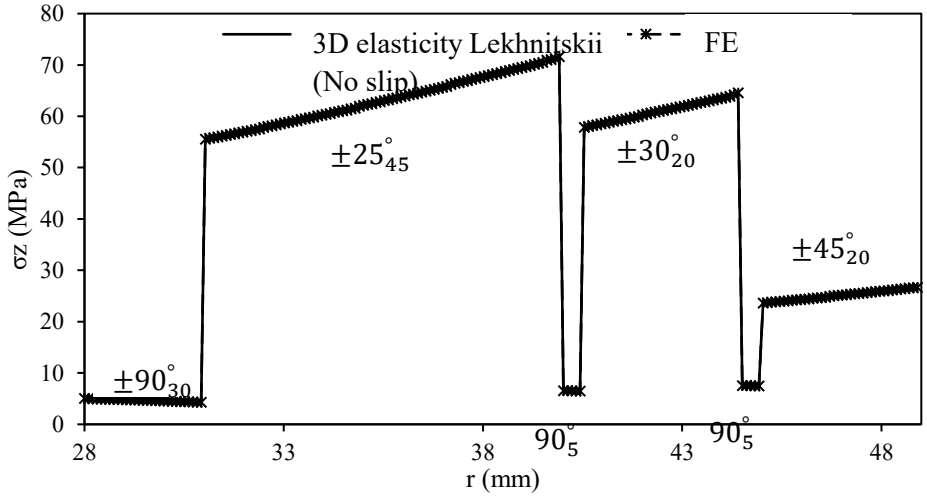

Fig. (2.12). The longitudinal stress distribution through the thickness of the tube 2 at circumferential position $\theta = 90^{\circ}$, (M_x=4450 N.m.).

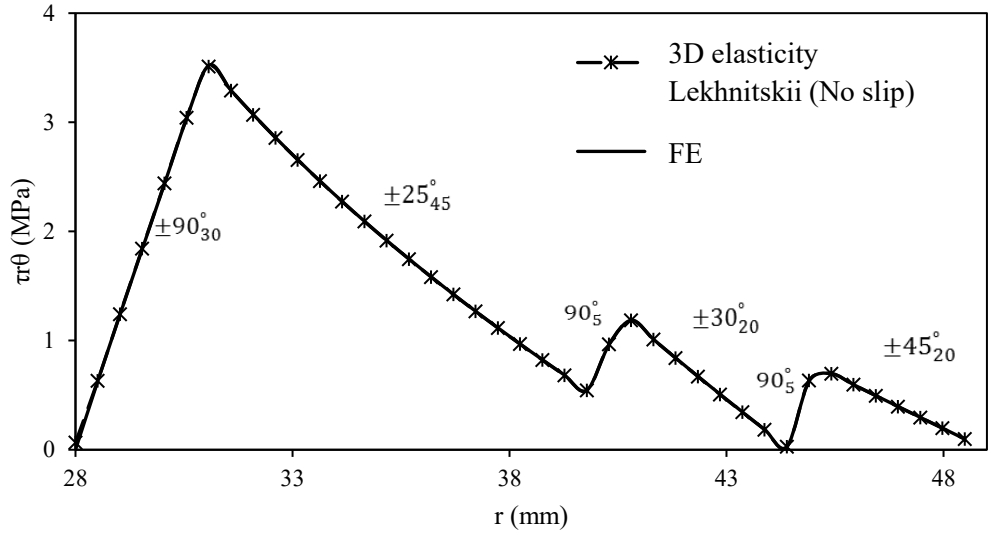

Fig. (2.13). The in-plane shear stress $\tau_{r\theta}$through the thickness of the tube 2 at $\theta = 0^{\circ}$, (M_x=4450 N.m.).

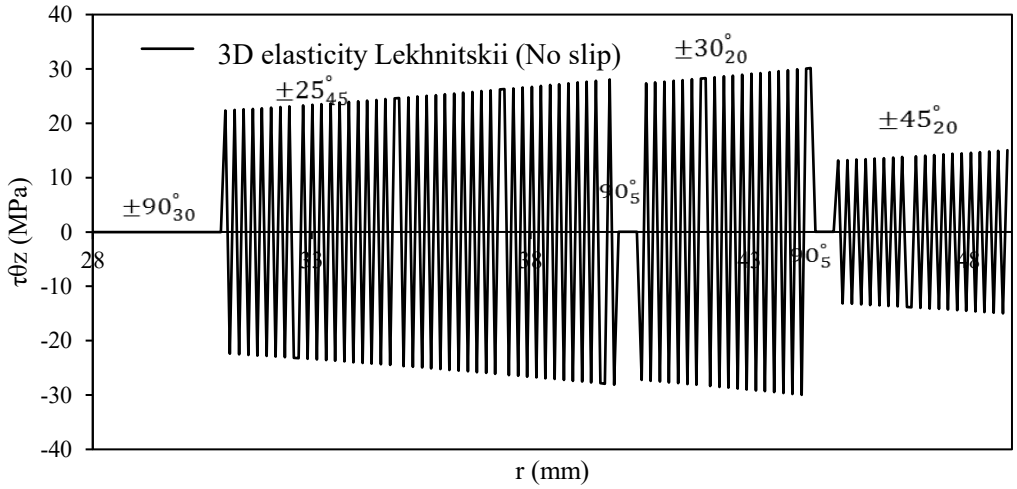

Fig. (2.14). The out-of-plane shear stress $\tau_{\theta z}$through the thickness of the tube 2 at $\theta = 90^{\circ}$, (M_x=4450 N.m.).

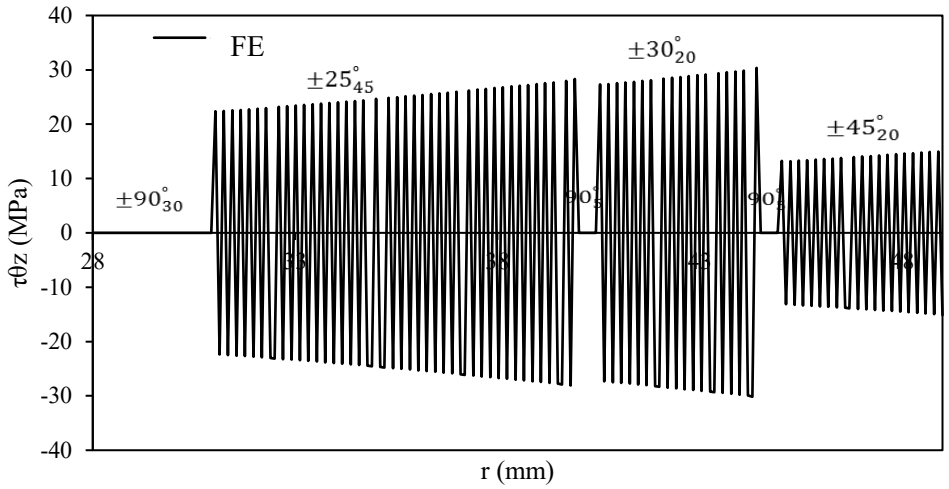

Fig. (2.15). The out-of-plane shear stress $\tau_{\theta z}$through the thickness of the tube 2 at $\theta = 90^{\circ}$, (M_x=4450 N.m.).

In the following section, we study the failure of composite tube 2 and compare the theoretical results with the experimental ones.

The first ply failure analysis of tube 2 ($[90^{\circ}_{30} / \pm 25^{\circ}_{45} / 90^{\circ}_{5} / \pm 30^{\circ}_{20} / 90^{\circ}_{5} / \pm 45^{\circ}_{20}]$) under pure bending load is investigated by using the maximum stress failure criterion, Tsai-Wu failure criterion with Lekhnitskii (No slip) and FE. The maximum bending moment until the first ply failure is shown in Table (2.4). It is seen that first ply failure occurs at outermost 90°_{5} layers at $\theta = 90^{\circ}$ with the transverse matrix cracking in the moment of 47 KN.m.

According to Tsai-Wu criterion, the maximum bending moment carried by the tube until its first ply failure obtained by Lekhnitskii (No slip) method and FE is 35 KN.m. The similar bending moment is also reported through experimental study which is 36.7 KN.m. Fig. (2.16) shows the failure test of the tube. According to Tsai-Wu the first ply failure occurs at the outermost 90°_{5} plies. In addition, the three-point bending analysis using FEM (ANSYS) shows that the first ply failure occurs at the load of 170 KN (37.8 KN.m). In other words, one can apply 3D elasticity analytical Lekhnitskii's (No slip) method without noticeable error for the first ply failure analysis of three-point bending of composite tube where the stress concentration does not have substantial effect on the failure. Moreover, a comparison between the failure moments obtained by two failure criteria shows that the Tsai-Wu has better prediction than maximum stress.

Table (2.4). Maximum bending moment (in KN.m) of the tube 2, $[90^{\circ}_{30} / \pm 25^{\circ}_{45} / 90^{\circ}_{5} / \pm 30^{\circ}_{20} / 90^{\circ}_{5} / \pm 45^{\circ}_{20}]$ until its first ply failure.

Method	Maximum stress	Tsai-Wu
Lekhnitskii	47	35
FEM (pure bending)	47	35
FEM (3-point bending)	52	37.8
Experiment	36.7	

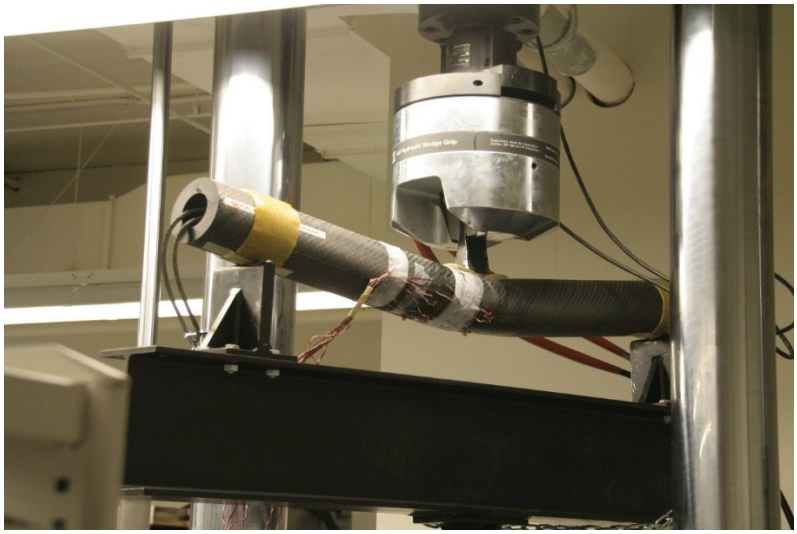

Fig. (2.16). Failure of tube 2, $[90^{\circ}_{30} / \pm 25^{\circ}_{45} / 90^{\circ}_{5} / \pm 30^{\circ}_{20} / 90^{\circ}_{5} / \pm 45^{\circ}_{20}]$ [1].

2.2.2 Stress analysis of composite tube under four-point bending loading using 3D elasticity of Lekhnitskii and FE

The stress analysis of four-point bending of straight composite tube (tube number 3) with lay-up $[(5Harness\ \text{satin})_7 / 90_4 / (\pm 25)_4 / 90_4 / (\pm 35)_4 / 90_4 / (\pm 45)_4]$ is performed using Lekhnitskii solution and compared with experiment in this section. We also provided the solution of strength of material and Thin-walled composite tubes solution [38].

2.2.2.1 Experimental test of tube $[(5Harness\ \text{satin})_7 / 90_4 / (\pm 25)_4 / 90_4 / (\pm 35)_4 / 90_4 / (\pm 45)_4]$

The experimental tests in this thesis have been conducted by a teamwork at Concordia Center for Composites (CONCOM), under the umbrella of the NSERC Industrial Chair on Automated Composites Manufacturing held by Professor Suong V. Hoa, in collaboration with Bell Flight Ltd.

The general configuration of the tubes has been guided by people at Bell Flight (Pierre Beulieu and Simon Bernier). The design and fabrication of the test set up was done by Dr. Ashraf Ahmed Fathy. Dr. Daniel Rosca developed the manufacturing procedure and fabricated the tubes using the Automated Fiber Placement machine at Concordia. Dr. Daniel Rosca and Ashraf Fathy carried out the test of the tubes. The following is reproduced from the joint publication " Moshir SK, Hoa SV, Shadmehri F, Rosca D, Ahmed A. Mechanical behavior of thick composite tubes under four-point bending. Composite structures. 2020; 242:112097.

In order to obtain experimental values to validate the results obtained from the analytical and numerical methods, a straight composite tube was made and tested. The tube was made using an automated fiber placement (AFP) machine available at Concordia Center for Composites. In order to process thermoplastic composites, a hot gas torch was used to melt the thermoplastic resin so that consolidation can be done in-situ. The mandrel needs to be sufficiently stiff to support the compaction load exerted by the placement head of the machine. Another requirement is that the mandrel should be removable to assure the lightness of the final structure. In order to satisfy these requirements, a layer of woven fabric was used on the inner side of the tube. As such the thickness of the tube has the composition as shown in Fig. (2.17).

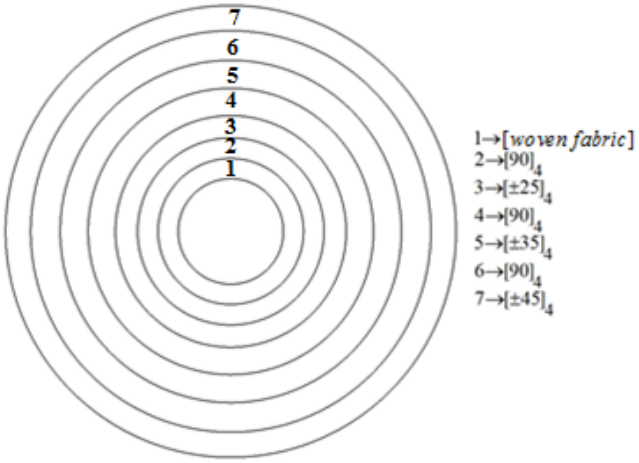

Fig. (2.17). Composition of the thickness of the tube.

The composite tube lay-up has 7 layers of Carbon/Epoxy five-harness satin woven fabric with the thickness of each layer 0.285 *mm*, and 36 layers made of Carbon/PEEK thermoplastic (average layer thickness of 0.115 *mm*), with the following lay sequence:

$$[(5Harness\ \text{satin})_7 / 90_4 / (\pm 25)_4 / 90_4 / (\pm 35)_4 / 90_4 / (\pm 45)_4]$$

The total thickness of the tube is 6.14 *mm*. This lay-up sequence follows the strain-controlled design guidelines developed in [1] where the outer layers should possess larger strain to failure as compared to the inner layers, and the $[90_n]$ layers are used to buffer the effect of transmission of failure from layers with smaller deformation capability to layers of larger deformation capability.

The tube has the length L = 1352.4 *mm*, inner and outer diameters Di = 72.71 *mm* and Do = 85 *mm*, respectively. The material properties of woven fabrics and unidirectional Carbon/PEEK are shown in Tables (2.5) and **(**2.6), respectively.

Table (2.5) Mechanical properties of 5-harness satin, [78]

E_1 *(GPa)*	54
E_2 *(GPa)*	54
E_3 *(GPa)*	9.964
G_{12} *(GPa)*	4
G_{13} *(GPa)*	2.5
G_{23} *(GPa)*	2.5
ν_{12}	0.05
ν_{13}	0.254
ν_{23}	0.289

Table (2.6) Mechanical properties of unidirectional Carbon/PEEK composite [1].

E_1 (GPa)	138
E_2=E_3 (GPa)	10.2
G_{12}=G_{13}=G_{23} (GPa)	5.7
$\nu_{12} = \nu_{13}$	0.31
ν_{23}	0.33

The tube is subjected to four-point bending loading arrangement as shown in the Fig. (2.18). The loading noses and the supports have concave shape which cover 180° of the circumference. The supports and the loading noses are made of steel. The supports can rotate around *x* axis. The 3D schematic and the front view of the test setup are shown in Fig. (2.19a and b). The setup includes the supports with radius the same as the outer radius of the tube. The supports also can rotate. In addition, the loading noses have the cylindrical shape which is the same as the outer radius of the tube. The loading noses are free to rotate. Six rosette strain gauges are installed at the mid-length, on the outer surface of the tube and at circumference positions $\theta = 0^{\circ}, 45^{\circ}, 90^{\circ}, 135^{\circ}, 180^{\circ}, 270^{\circ}$ (coordinate axes shown in Fig. (2.18). Table (2.7) shows the positions of the gauges which are located at the outer surface of the tube, at section A-A. Two T type strain gauges are installed at sections B-B and C-C of the tube, (Table (2.8)).

Table (2.7). Locations of strain gauges on the surface of the tube, Section A-A.

Rosette No.	**Channel No.**	**z (*mm*)**	**θ (degree)**	**Strain gauge angle with z**
1	1	0	88	90
	2	0	90	45
	3	0	92	0
2	4	-1	132	90
	5	-1	134	45
	6	-1	136	0
3	7	-0.5	179	90
	8	-0.5	180	45
	9	-0.5	182	0
4	10	0	272	90
	11	0	270	45
	12	0	268	0
5	13	-1	359	90
	14	-1	360	45
	15	-1	2	0
6	16	-0.5	44	90
	17	-0.5	46	45
	18	-0.5	48	0

Table (2.8). Locations of strain gauges on the surface of the tube, Sections B-B, and C-C.

T type No.	**Channel No. / Type**	**z (*mm*)**	**r (*mm*)**	**θ (degree)**
T1	20 / hoop	431.8	42.5	90
	21 / axial	431.8	42.5	90

T2	22 / hoop	-431.8	42.5	90
	23 / axial	-431.8	42.5	90

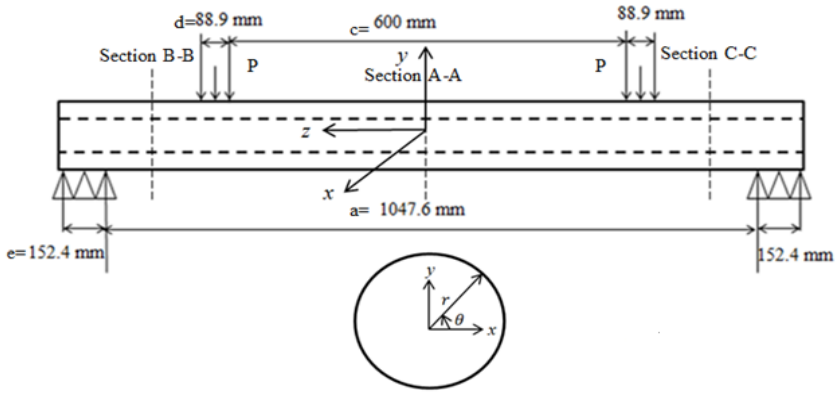

Fig. (2.18). Schematic of composite tube under four-point bending loadings.

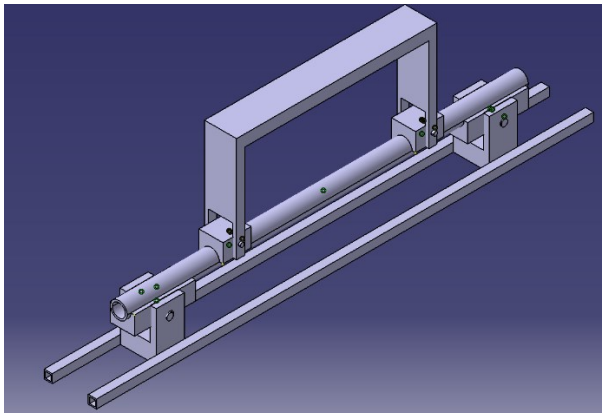

a)

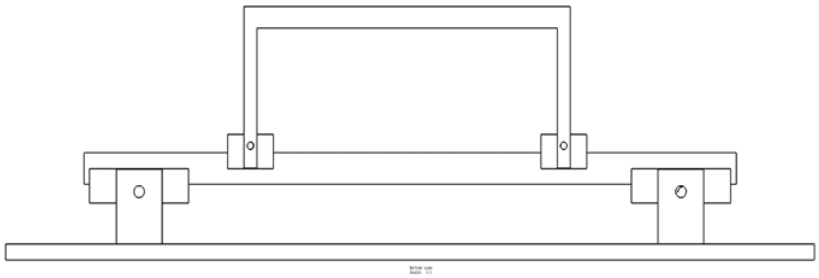

b)

Fig. (2.19) a) 3D schematic of the test setup of a tube under four point bending loading, b) Front view of the test setup of tube under four-point bending loading.

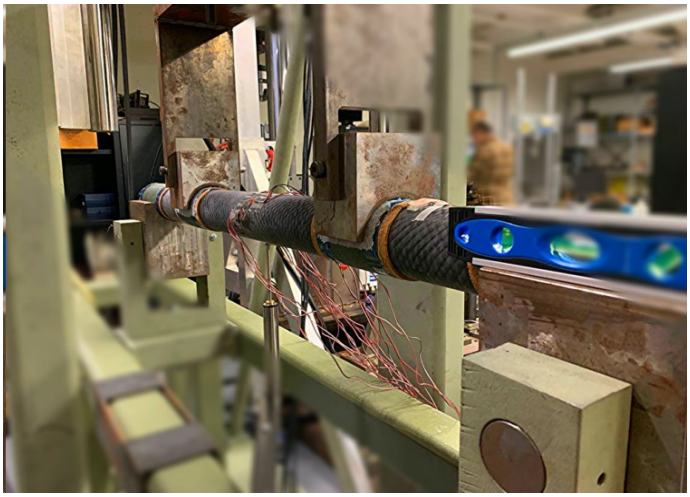

Fig. (2.20) Composite tube in a tube bending test setup.

2.2.2.2 Flexural stiffness of the tube $[(5Harness\ \text{satin})_7 / 90_4 / (\pm 25)_4 / 90_4 / (\pm 35)_4 / 90_4 / (\pm 45)_4]$

Value of the flexural stiffness can be determined using the equivalent product <*EI*>, where *E* stands for modulus of elasticity and *I* for cross section inertia.

- Strength of materials approach: Using Eq. (2.21): $\langle EI \rangle = 33 \times 10^3\ \text{N.m}^2$
- Thin-walled composite tubes: Using Eq. (2.23): $\langle EI \rangle = 62 \times 10^3\ \text{N.m}^2$
- 3D elasticity (Lekhnitskii): Using Eq. (*2.13*): (no-slip condition) $\langle EI \rangle = 57.5 \times 10^3\ \text{N.m}^2$
- 3D elasticity (Lekhnitskii): Using Eq. (*2.13*): (no-friction condition): $\langle EI \rangle = 32.7 \times 10^3\ \text{N.m}^2$

- Experiment: $< EI >= \dfrac{MR}{\varepsilon} = \dfrac{MD_o}{2\varepsilon} = \dfrac{F(a+e-c-d)D_o}{8\varepsilon}$ where

Do is the outer diameter of the tube

a is the length between support point

d is width of the load pad

e is width of the support pad

c is the length between loading point

F is the machine load

ε is the axial strain at mid length of the tube, either at the bottom or top

F/ε is obtained from the slope of the load versus axial strain either at the bottom or top of the tube.

From the above: $\langle EI \rangle = 58.1 \times 10^3\ \text{N.m}^2$

2.2.2.3 Strains of the tube [$(5Harness\ satin)_7 / 90_4 / (\pm 25)_4 / 90_4 / (\pm 35)_4 / 90_4 / (\pm 45)_4$]

Fig. (2.21) shows the experimental strains at θ = 0° (rosette # 5) and θ = 180° (rosette # 3). The calculated values show that these strains are 0. Reasons for this are presented in the Discussion section below.

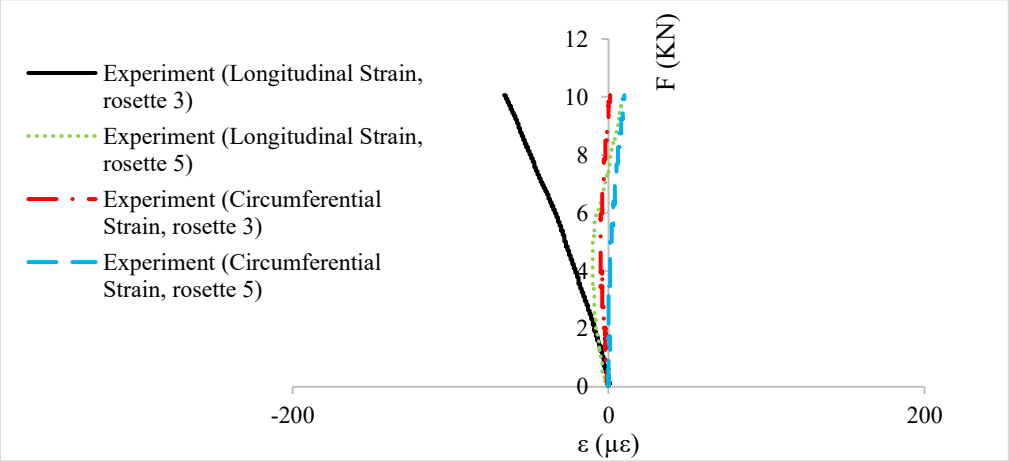

Fig. (2.21). Longitudinal and circumferential strains versus load F at $\theta = 0^{\circ}$ and $\theta = 180^{\circ}$ (F=2P). (Strains from rosettes 3 and 5)

Fig. (2.22) shows the strain variations at $\theta = 45^{\circ}$. (Strain rosette # 6), and Fig. (*2.23*) shows the strains at θ = 135° (rosette # 2). These two positions are nominally symmetrical with respect to the vertical axis of the cross section. It can be observed from these two figures that the calculated values are the same. However, the longitudinal strains in Fig. (2.22) are larger than the calculated strains while those in Fig. (2.23) are smaller than the calculated strains. Reasons for this are given in the Discussion section below.

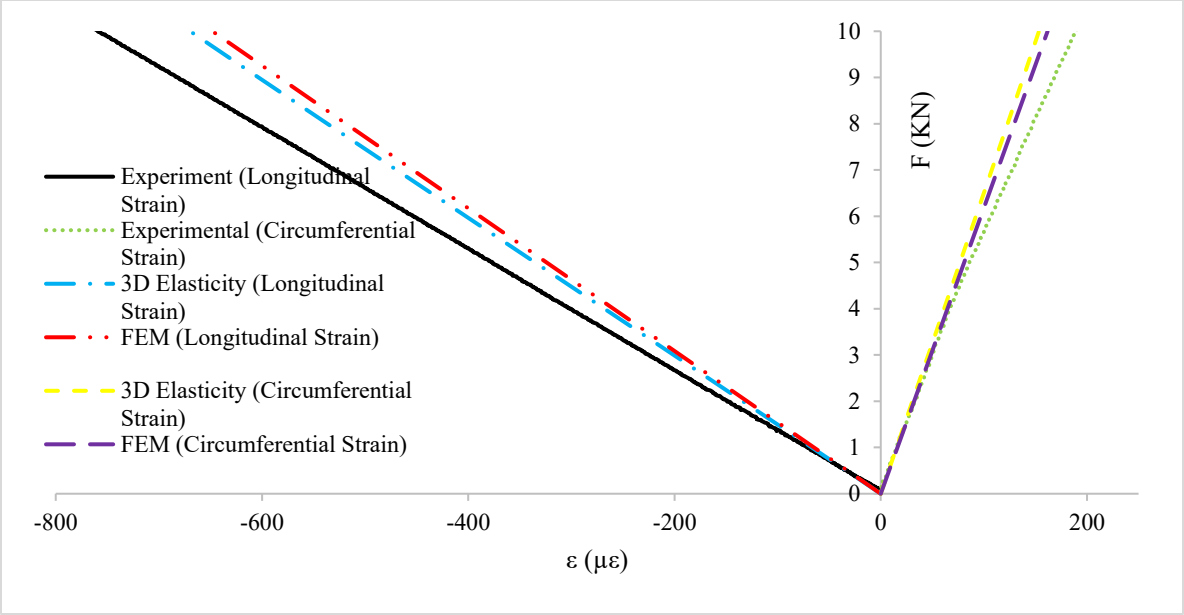

Fig. (2.22). Longitudinal and circumferential strains versus machine loading at $\theta = 45^{\circ}$, (rosette # 6) (F=2P).

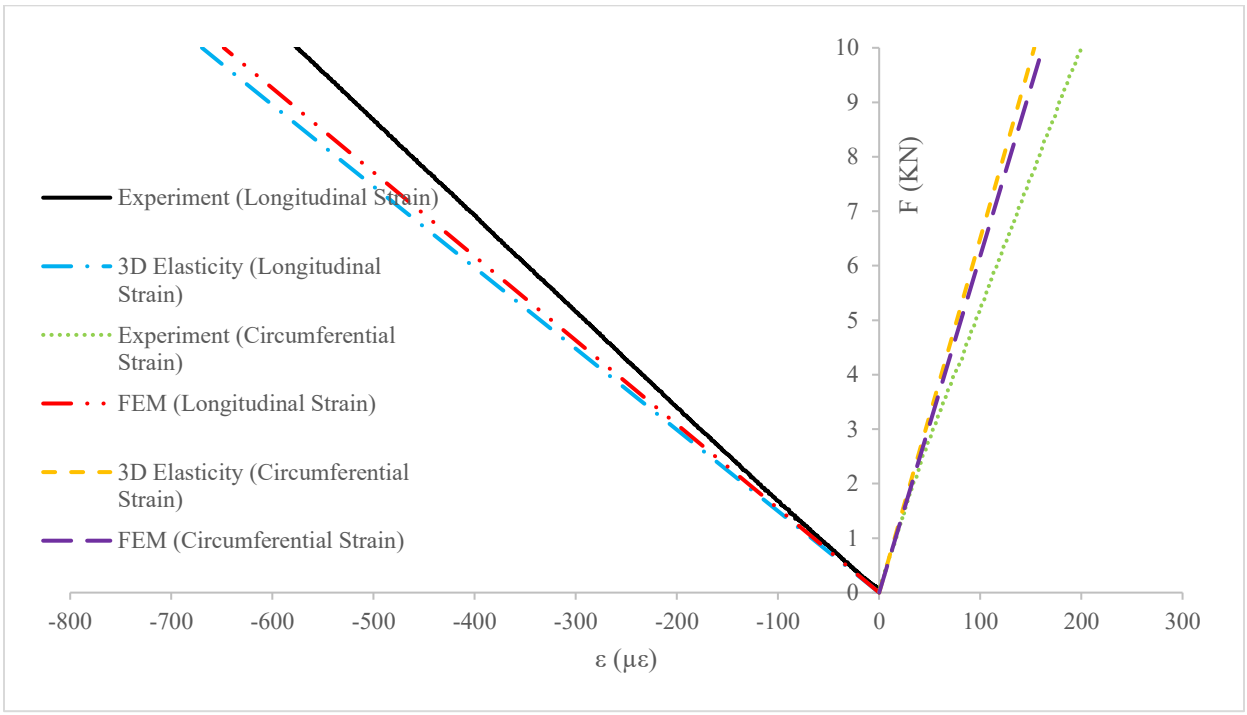

Fig. (2.23). Longitudinal and circumferential strains versus load F at $\theta = 135^{\circ}$, (F=2P). (rosette # 2)

Fig. (2.24) shows the variation of the strains at θ = 90º (strain rosette # 1, top of the section), and Fig. (2.25) shows the strains at θ = 270º (rosette # 4, bottom of the section). Results obtained from 3D elasticity solution (no-slip condition), FEM, and experiments are shown. It can be seen that the results agree very well.

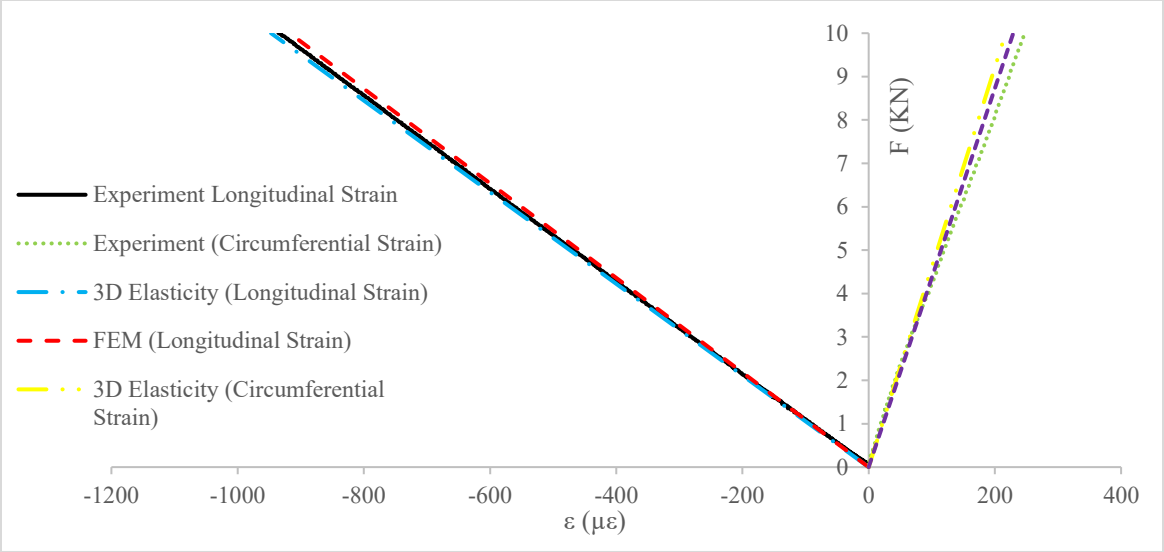

Fig. (2.24). Longitudinal and circumferential strains versus load F at $\theta = 90^{\circ}$, (F=2P).

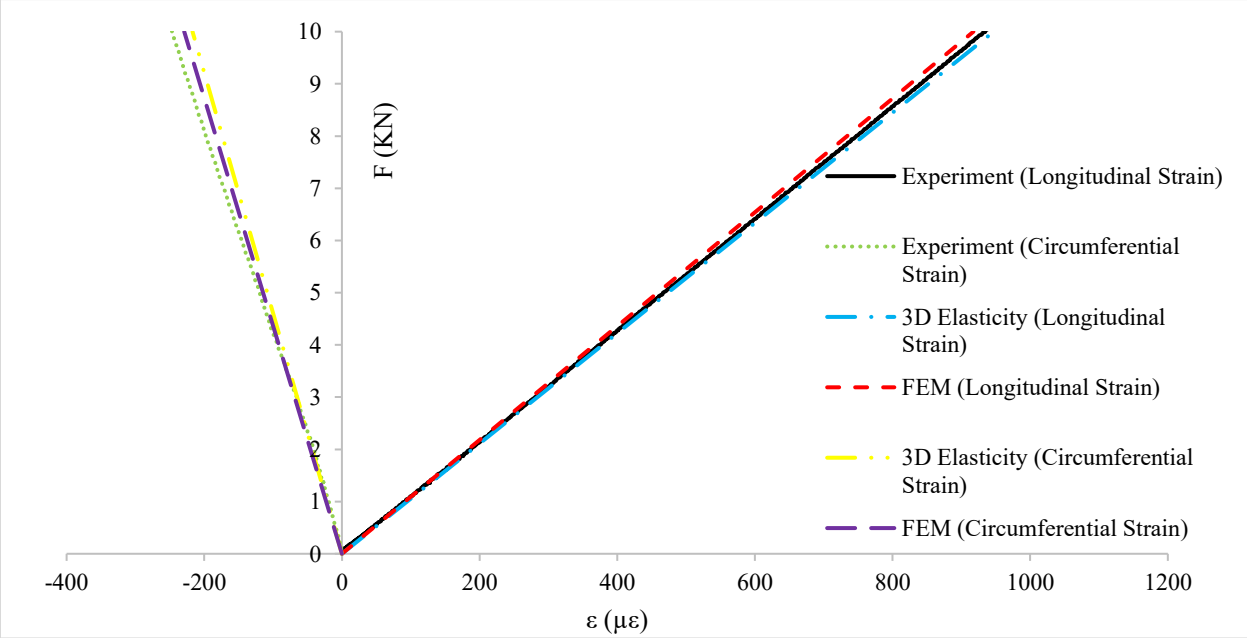

Fig. (2.25). Longitudinal and circumferential strains versus machine loading at $\theta = 270^{\circ}$, (rosette # 4) (F=2P).

Fig. (2.26) shows the strains variation at $\theta = 90^{\circ}$, section B-B, (T#1)

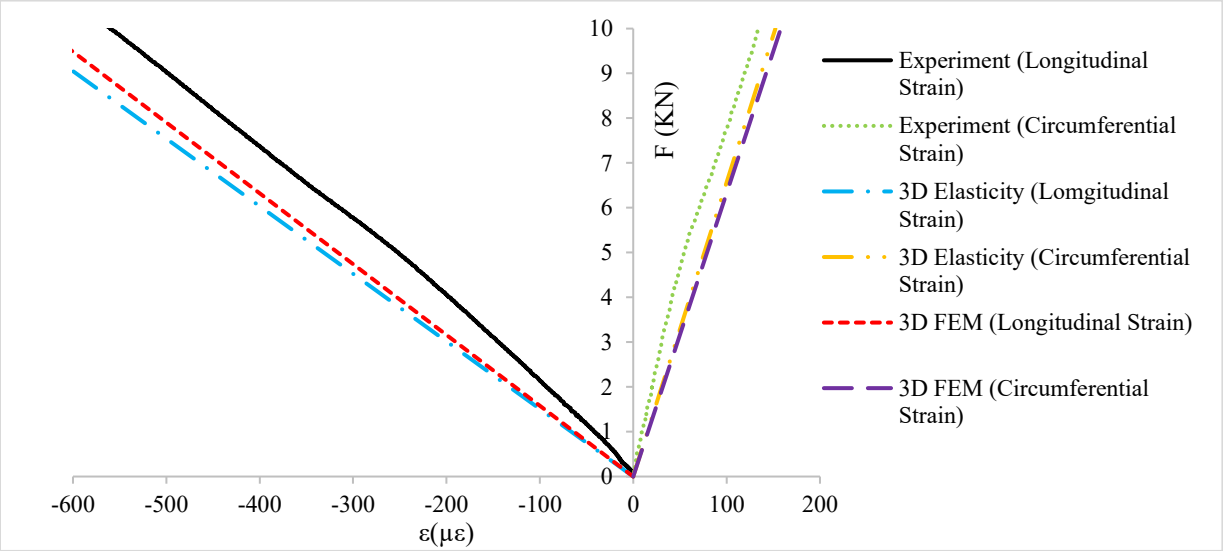

Fig. (2.26). Longitudinal and circumferential strains versus machine loading at $\theta = 90^{\circ}$, (Section B-B, rosette # T1), (F=2P).

2.2.3 Discussion

Flexural stiffness:

- There is general agreement between values obtained using thin-walled theory (Eq. (2.23)), 3D elasticity (Eq. (2.1) using no-slip condition), and experimental measurement. Values of <EI> obtained from these methods vary from 57,500 N.m^2 to 62,000 N.m^2, giving an average of 59,200 N.m^2 with deviation of 4.7%.
- The strength of materials solution (Eq. (2.21)) seems to agree with the 3D elasticity solution (Eq. ((2.1)) using no friction condition). The *EI* values are 33,000 N.m^2 and 32,700 N.m^2 which are very close. However, these values are much smaller than the experimental value. No friction condition means that the layers are not bonded together, which is far from reality.

Strains

- Fig. (2.21) shows the strains at θ = 0º and 180º, which are the horizontal positions of the section. It is expected that the strains be close to 0. Rosette # 3 show small values because it is located at θ = 182º which is slightly away from 180º.
- Fig. (2.22) and (2.23) show the strains at θ = 45º (rosette # 6) and 135º (rosette # 2). These are supposed to be symmetric positions on the tube. However, the longitudinal strains at θ

= 45° are larger than the calculated strains while those at θ = 135° are smaller than the calculated strains. Examination of Table (2.7) shows that the axial gage in rosette # 6 is located at θ = 48° while that of rosette # 2 is located at θ = 136°. The distance from the neutral axis of the axial strain in rosette # 6 is more than that of the axial strain in rosette # 2. This may explain the larger amplitude in the gage at the nominal θ = 45°.

- Fig. (2.24) and (2.25) show the strains at θ = 90° (rosette # 1, top of section) and at θ = 270° (rosette # 4, bottom of the section). There is a good agreement between the 3D elasticity solution, FEM solution and experimental measurement.
- The above analysis shows that the analytical methods (3D analytical with no-slip condition, and FEM) can predict the strains well. The small differences can be explained due to the slight deviation of the position of the gages as compared to the theoretical positions. Between 3D analytical and FEM, 3D analytical is simpler and less time consuming.
- It is of interest to compare the experimental longitudinal strains from Figs. (2.24) and (2.26). Fig. (2.24) shows the strain from rosette # 1 which is at the top and mid-length of the tube. This is the region of pure bending. Fig. (2.26) shows the strain from T1 gage at section B-B, which is at the top of the cylinder but located within the region where there is a bending moment and a shear load. From Table (2.8) and Fig. (2.18), it can be shown that the bending moment at section B-B is $M_{B\text{-}B}$ = (168.2 *mm*) P, and the pure bending moment at section A-A is $M_{A\text{-}A}$ = (255.6 *mm*)P. At a load F = 10 kN, Fig. (2.24) shows a longitudinal experimental strain of about -940 με while Fig. (2.26) shows a longitudinal experimental strain of about -565 με. The ratio between the bending moments is (255.6/168.2 = 1.52) while the ratio between the two strains is (940/565 = 1.66). If one were to use the section A-A under pure bending moment as the reference, the strain due to bending at section B-B would be (-940)(168.2)/(255.6) = -618.6 με. The difference between -618.6 με and -565με (53.6 με) is due to the presence of the shear load at section B-B. The ratio (53.6/618.6 = 8.7%) represents the relative importance of shear with respect to bending moment.
- It is of interest to see the variation of the circumferential strain along the circumferential direction. This can be done by plotting the calculated circumferential strains at different θ values. Fig. (2.27) shows the variation. It can be seen that at the top of the section A-A, the longitudinal strain is compressive while the circumferential strain is tensile. The opposite occurs at the bottom of the section.

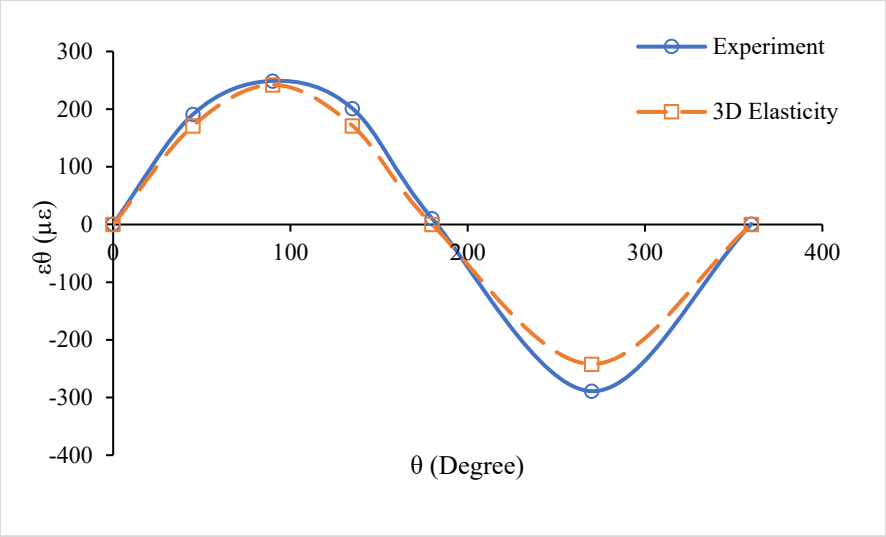

Fig. (2.27). Variation of the circumferetial strain versus circumference at the outer surface of the tube, mid-length. (F=10 KN).

2.3 Conclusion

In this chapter, the 3D elasticity solution of Lekhnitskii for pure bending of straight composite cylindrical tubes is employed to predict flexural stiffness as well as failure of composite tubes. The predicted failure load is compared with experimental test.

- The stress and failure analyses of composite tubes with different lay-up are investigated to find the correlation between the analytical method proposed by [16], FEM and experimental results.
- The failure load based on the Tsai-Wu obtained by the analytical method does not agree well with the experiment for tube with $[(90^{\circ}_{10} / 0^{\circ}_{10})_3 / \pm 45^{\circ}_{25}]$ which stress concentration effect (due to loading nose) is dominant in the failure of this tube. However, there is a good agreement between the experimental results and the analytical method for tube $[90^{\circ}_{30} / \pm 25^{\circ}_{45} / 90^{\circ}_{5} / \pm 30^{\circ}_{20} / 90^{\circ}_{5} / \pm 45^{\circ}_{20}]$. It means that the effect of stress concentration does not have substantial effect on the failure of the tube $[90^{\circ}_{30} / \pm 25^{\circ}_{45} / 90^{\circ}_{5} / \pm 30^{\circ}_{20} / 90^{\circ}_{5} / \pm 45^{\circ}_{20}]$ and the analytical method (using Tsai-Wu) which capable of analyzing tubes under pure bending moment may have a good agreement with the experiment.

- It was shown that for flexural stiffness, the thin-walled theory, 3D elasticity (with no slip condition), FEM show results that agree well with experimental values, while the strength of materials approach, and 3D elasticity (with no friction condition) agree with each other but both give flexural stiffness values much lower than the experimental values.
- For strains, it is also shown that the analytical method (3D elasticity solution with no slip condition), and FEM can obtain results that agree with experimental measurement. Among the calculated method, 3D elasticity solution is less time consuming, and simpler.
- The strains at sections where there is a combination of bending moment, and a shear load shows that there is significant influence of the shear load on the strains.

In this chapter, the stress analysis of straight composite tubes using conventional methods including 3D FEM, 3D elasticity of Lekhnitskii, non-classical beam theory has been presented. The 3D FEM is able to take into account the effect of boundary conditions and loading effect as stress concentration. However, the computational time is considerable. The 3D elasticity solution of Lekhnitskii is a fast method while it treats a composite tube as a multi-layered cylinder under pure bending moment in which the effect of boundary conditions is not taken into account. As such the longitudinal and transverse deflections of the tube subjected to transverse loadings cannot be calculated. The VABS and the meshless dimensional reduction methods which are based on VAM will be presented in the next chapter treat a composite tube as a beam. Therefore, one can model a straight and curved tubes with the desired boundary conditions. The methods consider a composite beam as a 3D body so that all the effects of shear and normal strains will be considered without any ad-hoc assumption.

3 Chapter 3: Introduction to Variational Asymptotic Method (VAM)

The kinematics of the initially curved beam deformation formulations based on the concept of the rotational decomposition will be demonstrated, [40]. The motion and deformation of the set of particles that make up the cross-sectional plane of the undeformed beam can be considered as rigid body translation and rotation of the undeformed beam plus a relatively small elastic deformation. The concept of rotational decomposition is that the large rotation of the beam cross-section is separated into two parts as local rotation and global rotation. The rigid translation and rotation of the cross-sectional frame are grouped with the beam global deformation, whereas the deformation of the cross-section is classified as local deformation or, simply, warping. Then, the 3D strains and the energy formulation for an orthotropic beam and the Variational Asymptotic Method (VAM) for the cross-sectional analysis of the beams will be presented [49]. Based on the VAM, different orders of the strain energy which are obtained by perturbations of warping field through orders of small parameters of the problem are obtained. The VAM is used to minimize the strain energy to obtain unknown of the problem which is the warping. This method splits the 3D strain energy into a 2D cross-sectional analysis and a 1D through the length. The VABS uses 2D FEM for cross-sectional discretization. Next, the analytical meshless dimensional reduction method for the cross-sectional analysis of anisotropic tubular curved beams will be introduced, [79]. The Pascal polynomials which are defined in Cartesian coordinates system are transformed to polar coordinates system to carry out cross-sectional discretization. The complete procedure of kinematics of the beam theory and VABS is reported by Hodges [40].

3.1 Dimensional reduction method using variational asymptotic method

Theoretical derivations begin with 3D formulations of the kinematic of the beam along with strain energy that governs the behavior of structure in terms of intrinsic 1D variables and 3D warping functions. The VAM is then applied to split the 3D problem into a 1D beam analysis and 2D cross-sectional analysis. The 2D analysis provides constitutive models such as classical beam model and Timoshenko model, for the 1D global analysis. Recovery analysis for 3D displacement, strain field and stress are found expressions that are consistent with the procedure to attain the strain energy. The flow chart of VABS is shown in Fig. (3.1). The gray box in the flow chart indicates that the FE shape functions will be used for cross-sectional discretization in the VABS.

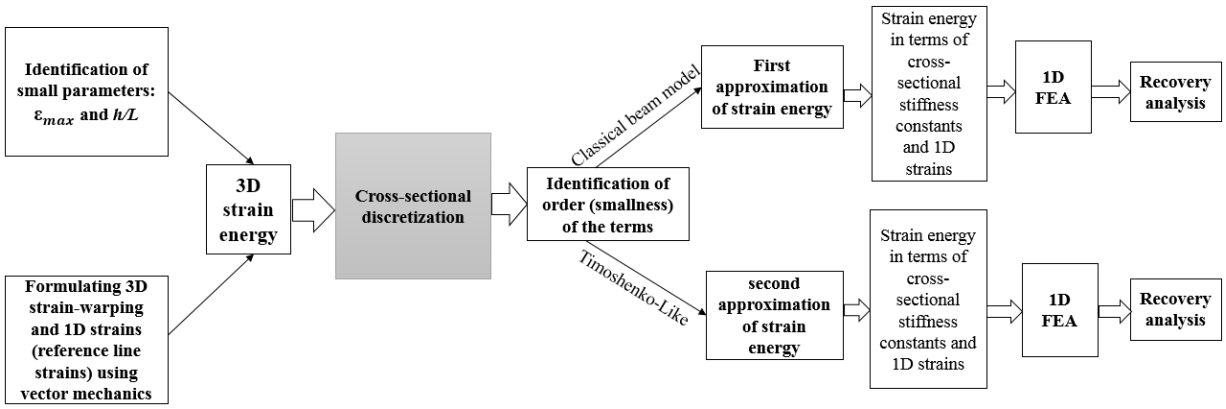

Fig. (3.1) Flow chart summarizing the VABS method.

The VAM consists of many steps. Details of the steps are presented below.

3.1.1 Step 1: Identification of small parameters and formulation for 3-D strains

In step 1, three aspects are considered. One is the identification of the small parameters essential for the application of VAM. The small parameters are the maximum of the axial strain ε_{max}, the thickness-to-radius ratio of the tube (h / r_o) and the radius-to-length ratio of the tube(r_o / L), or thickness-to-radius of curvature of the tubular beam (h/R) [52]. It is assumed that the $h / r_o \ll 1$ and $r_o / L \ll 1$ or $r_o / R \ll 1$. So that one can conclude that $h / L \ll 1$. The other aspect is the formulation to obtain relations between the 3D strains in terms of warping functions and the 1D strains, using vector mechanics.

3.1.2 Step 2: Kinematical relations

Consider an anisotropic beam with a circular hollow cross-section. The orthonormal coordinates x_1, x_2 and x_3 with triad b_1, b_2 and b_3 are considered for the undeformed beam cross-section, (Fig. (3.2)). The location of the reference line of the undeformed cross-section is denoted by the position vector $\boldsymbol{r}$. The location of reference line of the deformed cross-section is denoted by $\boldsymbol{R}$. The triad T_1, T_2 and T_3 are attached to the cross-section in the deformed configuration. It is noted that T_1 is tangent to the reference line of the deformed configuration. This means that the transverse shear is a part of warping field. A triad B_1, B_2 and B_3 is also defined in the deformed beam configuration where B_1 is not necessarily tangent to the beam reference line. A polar coordinate system is defined where ρ is the radius of each point on the cross-section and θ is the circumferential angle. The

position vector of any particle in the undeformed beam $\hat{\boldsymbol{r}}$ and the deformed beam $\hat{\boldsymbol{R}}$ are as follows.

$$\hat{\boldsymbol{r}} = \boldsymbol{r}(x_1) + x_\alpha b_\alpha,\ \alpha = 2,\ 3 \tag{3.1}$$

$$\hat{\boldsymbol{R}}(x_1, x_2, x_3) = \boldsymbol{R}(x_1) + x_\alpha T_\alpha(x_1) + w_i(x_1, x_2, x_3) T_i(x_1) \tag{3.2}$$

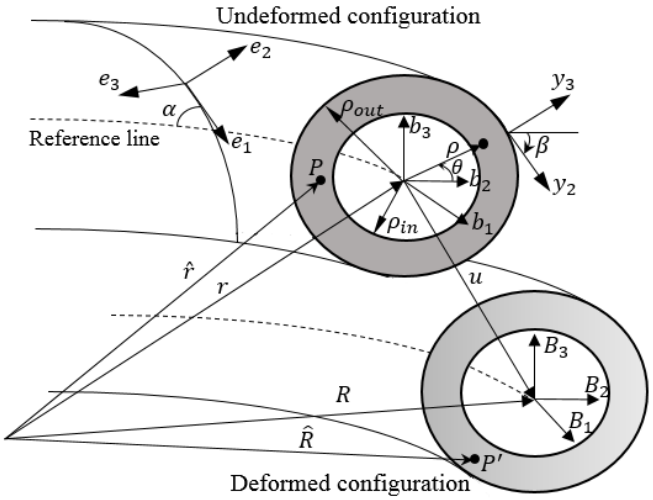

Fig. (3.2). Deformed and undeformed configurations of a tubular curved beam cross-section.

where, w_i (i=1, 2, 3) representing the components of unknown warping functions which should be determined. w_1, w_2 and w_3 is the warping displacement of each point of the cross-section along x_1, x_2 and x_3, respectively. The warping functions are the difference between the position of deformed body and those which are described by deformation of the reference curve x_1 in terms of $\boldsymbol{R} + x_2 T_2 + x_3 T_3$ where $\boldsymbol{R} = \boldsymbol{r} + \boldsymbol{u}$. Where $\boldsymbol{u}$ describes the beam displacement. The 1D moment-strain measures $\bar{\boldsymbol{\kappa}}_i$ are defined based on the rate of change along x_1 of the triad T_i. $\bar{\boldsymbol{\kappa}}_1$ is the twist, $\bar{\boldsymbol{\kappa}}_2$ and $\bar{\boldsymbol{\kappa}}_3$ are the curvatures of the reference line about x_2, x_3, respectively. we have,

$$T_i' = \left(k_j + \bar{\kappa}_j\right) T_j \times T_i \quad i, j = 1, 2, 3 \tag{3.3}$$

where, k_1 is the initial twist, k_2 and k_3 are initial curvatures of the reference line about x_2 and x_3, respectively. k_i are defined in b_i basis. The following 1D generalized strains are defined.

$$\boldsymbol{R}' = (1 + \gamma_{11}) T_1 + 2\gamma_{1\alpha} T_\alpha \quad \alpha = 2,\ 3 \tag{3.4}$$

$$T_i' = \boldsymbol{K} \times T_i \tag{3.5}$$

In which the prime denotes derivative to x_1, γ_{11} is the longitudinal strain of the reference line, $\gamma_{1\alpha}$ are the transverse shears. $\boldsymbol{K}$ is the final curvature of the reference line of the beam and $\bar{\kappa}_j = K_i - k_i$ The contravariant base vectors for the undeformed configuration is defined as follows.

$$g_i(x_1, x_2, x_3) = \frac{\partial \hat{\boldsymbol{r}}}{\partial x_i} \tag{3.6}$$

For a beam with initial curvature, we have:

$$\begin{aligned} \boldsymbol{g_1} &= \frac{\partial \hat{\boldsymbol{r}}}{\partial x_1} = \frac{\partial \boldsymbol{r}(x_1)}{\partial x_1} + \frac{\partial}{\partial x_1}(x_2 \boldsymbol{b_2}) + \frac{\partial}{\partial x_1}(x_3 \boldsymbol{b}_3) = \boldsymbol{b_1}(1 - x_2 k_3 + x_3 k_2) \\ \boldsymbol{g}_2 &= \frac{\partial \hat{\boldsymbol{r}}}{\partial x_2} = \boldsymbol{b}_2,\ \boldsymbol{g_3} = \frac{\partial \hat{\boldsymbol{r}}}{\partial x_3} = \boldsymbol{b}_3 \end{aligned} \tag{3.7}$$

The covariant base vectors of the deformed configuration of a beam with initial curvatures are expressed as

$$\boldsymbol{g}^i(x_1, x_2, x_3) = \frac{1}{2\sqrt{\lambda}} e_{ijk} \boldsymbol{g_j} \times \boldsymbol{g_k};\ \boldsymbol{g^1} = \frac{\boldsymbol{b_1}}{\sqrt{\lambda}}, \boldsymbol{g}^2 = \boldsymbol{b_2}, \boldsymbol{g^3} = \boldsymbol{b_3} \tag{3.8}$$

Where λ is the determinant of the metric tensor for the undeformed geometry $\lambda_{ij} = (\lambda_i . \lambda_j)$ and e_{ijk} is the permutation symbol. we have:

$$\sqrt{\lambda} = g_1 . (g_2 \times g_3) = g_1 . b_1 = 1 - x_2 k_3 + x_3 k_2 \tag{3.9}$$

The covariant components of the deformed state of a beam with initial curvature can be obtained as

$$\begin{aligned} \boldsymbol{G_1} &= \frac{\partial \hat{R}}{\partial x_1} = \boldsymbol{R'} + x_2 \boldsymbol{T_2'} + x_3 \boldsymbol{T_3'} + w_1' \boldsymbol{T_1} + w_1 \boldsymbol{T_1'} + w_2' \boldsymbol{T_2} + w_2 \boldsymbol{T_2'} + w_3' \boldsymbol{T_3} + w_3 \boldsymbol{T_3'} \\ &= ((1 + \gamma_{11}) - x_2(k_3 + \bar{\kappa}_3) + x_3(k_2 + \bar{\kappa}_2) + w_1' - w_2(k_3 + \bar{\kappa}_3) + w_3(k_2 + \bar{\kappa}_2)) \boldsymbol{T_1} \\ &+ (-x_3 \bar{\kappa}_1 + w_1(k_3 + \bar{\kappa}_3) + w_2' - w_3 \bar{\kappa}_1) \boldsymbol{T}_2 \\ &+ (x_2(k_1 + \bar{\kappa}_1) - w_1(k_2 + \bar{\kappa}_2) + w_2 \bar{\kappa}_1 + w_3') \boldsymbol{T}_3 \end{aligned} \tag{3.10}$$

$$\boldsymbol{G_2} = \frac{\partial \hat{\boldsymbol{R}}}{\partial x_2} = \boldsymbol{T}_2 + \frac{\partial w_1}{\partial x_2}\boldsymbol{T_1} + \frac{\partial w_2}{\partial x_2}\boldsymbol{T}_2 + \frac{\partial w_3}{\partial x_2}\boldsymbol{T}_3;\ \boldsymbol{G_3} = \frac{\partial \hat{\boldsymbol{R}}}{\partial x_3} = \boldsymbol{T}_3 + \frac{\partial w_1}{\partial x_3}\boldsymbol{T_1} + \frac{\partial w_2}{\partial x_3}\boldsymbol{T}_2 + \frac{\partial w_3}{\partial x_3}\boldsymbol{T}_3$$

The deformation gradient tensor can be formulated as

$$F_{ij} = T_i.\boldsymbol{G}_k\boldsymbol{g}^k.b_j \tag{3.11}$$

The Jauman-Cauchy strain components for small local rotation are given by

$$\Gamma_{ij} = \frac{1}{2}\left(F_{ij} + F_{ji}\right) - \delta_{ij} \tag{3.12}$$

where, δ_{ij} is the Kronecker delta. The strain components for a beam with initial curvature is written as follows.

$$\begin{aligned}
&\Gamma_{11} = \frac{1}{2}(F_{11} + F_{11}) - \delta_{11} = \frac{1}{2}(\boldsymbol{T_1G_1g^1b_1} + \boldsymbol{T_1G_2g^2b_1} + \boldsymbol{T_1G_3g^3b_1}) - \frac{1}{\sqrt{\lambda}} \\
&= \frac{1}{\sqrt{\lambda}}(\bar{\gamma}_{11} - x_2(k_3 + \bar{\kappa}_3) + x_3(k_2 + \bar{\kappa}_2) + w_1' - w_2(k_3 + \bar{\kappa}_3) + w_3(k_2 + \bar{\kappa}_2)) \\
&\Gamma_{12} = \frac{1}{2}(F_{12} + F_{21}) - \delta_{12} = \frac{1}{2}(\boldsymbol{T_1G_1g^1b_2} + \boldsymbol{T_1G_2g^2b_2} + \boldsymbol{T_1G_3g^3b_2} + \boldsymbol{T_2G_1g^1b_1} \\
&+\boldsymbol{T_2G_2g^2b_1} + \boldsymbol{T_2G_3g^3b_1}) = \frac{1}{2}(\frac{\partial w_1}{\partial x_2} + \frac{1}{\sqrt{\lambda}}(-x_3(\bar{\kappa}_1) + w_1(k_3 + \bar{\kappa}_3) + w_2' - w_3\bar{\kappa}_1)) \\
&\Gamma_{13} = \frac{1}{2}(F_{13} + F_{31}) - \delta_{13} = \frac{1}{2}(\boldsymbol{T_1G_1g^1b_3} + \boldsymbol{T_1G_2g^2b_3} + \boldsymbol{T_1G_3g^3b_3} + \boldsymbol{T_3G_1g^1b_1} \\
&+\boldsymbol{T_3G_2g^2b_1} + \boldsymbol{T_3G_3g^3b_1}) = \frac{1}{2}(\frac{\partial w_1}{\partial x_3} + \frac{1}{\sqrt{\lambda}}(x_2(\bar{\kappa}_1) - w_1(k_2 + \bar{\kappa}_2) + w_2\bar{\kappa}_1 + w_3')) \\
&\Gamma_{23} = \frac{1}{2}(F_{23} + F_{32}) - \delta_{23} = \frac{1}{2}(\boldsymbol{T_2G_1g^1b_3} + \boldsymbol{T_2G_2g^2b_3} + \boldsymbol{T_2G_3g^3b_3} + \boldsymbol{T_3G_1g^1b_2} \\
&+\boldsymbol{T_3G_2g^2b_2} + \boldsymbol{T_3G_3g^3b_2}) = \frac{1}{2}(\frac{\partial w_2}{\partial x_3} + \frac{\partial w_3}{\partial x_2}) \\
&\Gamma_{22} = \frac{1}{2}(F_{22} + F_{22}) - \delta_{22} = \frac{1}{2}(\boldsymbol{T_2G_1g^1b_2} + \boldsymbol{T_2G_2g^2b_2} + \boldsymbol{T_2G_3g^3b_2}) - \frac{1}{\sqrt{\lambda}} = \frac{\partial w_2}{\partial x_2} \\
&\Gamma_{33} = \frac{1}{2}(F_{33} + F_{33}) - \delta_{33} = \frac{1}{2}(\boldsymbol{T_3G_1g^1b_3} + \boldsymbol{T_3G_2g^2b_3} + \boldsymbol{T_3G_3g^3b_3}) - \frac{1}{\sqrt{\lambda}} = \frac{\partial w_3}{\partial x_3}
\end{aligned} \tag{3.13}$$

One can express Γ as

$$\boldsymbol{\Gamma} = [\Gamma_h]\boldsymbol{w} + [\Gamma_\varepsilon]\bar{\boldsymbol{\varepsilon}} + [\Gamma_R]\boldsymbol{w} + [\Gamma_l]\boldsymbol{w}' \tag{3.14}$$

$$\boldsymbol{\Gamma} = [\Gamma_{11}\ 2\Gamma_{12}\ 2\Gamma_{13}\ \Gamma_{22}\ 2\Gamma_{23}\ \Gamma_{33}]^T \tag{3.15}$$

where, $\bar{\varepsilon}$ is the 1D strain of the reference line of the beam as

$$\bar{\boldsymbol{\varepsilon}} = \begin{bmatrix} \bar{\gamma}_{11} & \bar{\kappa}_1 & \bar{\kappa}_2 & \bar{\kappa}_3 \end{bmatrix}^T \tag{3.16}$$

The warping displacements of the cross-section of the beam are defined as the following vector.

$$\boldsymbol{w} = [w_1\ w_2\ w_3]^T \tag{3.17}$$

The operators in Eq. (3.14) can be defined as

$$[\Gamma_h] = \begin{bmatrix} 0 & 0 & 0 \\ \dfrac{\partial}{\partial x_2} & 0 & 0 \\ \dfrac{\partial}{\partial x_3} & 0 & 0 \\ 0 & \dfrac{\partial}{\partial x_2} & 0 \\ 0 & \dfrac{\partial}{\partial x_3} & \dfrac{\partial}{\partial x_2} \\ 0 & 0 & \dfrac{\partial}{\partial x_3} \end{bmatrix}, \quad [\Gamma_\varepsilon] = \frac{1}{\sqrt{\lambda}} \begin{bmatrix} 1 & 0 & x_3 & -x_2 \\ 0 & -x_3 & 0 & 0 \\ 0 & x_2 & 0 & 0 \\ 0 & 0 & 0 & 0 \\ 0 & 0 & 0 & 0 \\ 0 & 0 & 0 & 0 \end{bmatrix} \tag{3.18}$$

$$[\Gamma_R] = \frac{1}{\sqrt{\lambda}} \begin{bmatrix} 0 & -k_3 & -k_2 \\ k_3 & 0 & 0 \\ k_2 & 0 & 0 \\ 0 & 0 & 0 \\ 0 & 0 & 0 \\ 0 & 0 & 0 \end{bmatrix}, \quad [\Gamma_l] = \frac{1}{\sqrt{\lambda}} \begin{bmatrix} 1 & 0 & 0 \\ 0 & 1 & 0 \\ 0 & 0 & 1 \\ 0 & 0 & 0 \\ 0 & 0 & 0 \\ 0 & 0 & 0 \end{bmatrix}$$

3.1.3 Strain energy

The strain energy of the curved beam with the cross-section area of Ω and the length *L* can be described as follows.

$$2U = \int_L \iint_\Omega \boldsymbol{\Gamma}^T D \boldsymbol{\Gamma} dx_2 dx_3 dx_1 = \int_L \iint_\Omega ([\Gamma_h]\boldsymbol{w} + [\Gamma_\varepsilon]\bar{\boldsymbol{\varepsilon}} + [\Gamma_R]\boldsymbol{w} + [\Gamma_l]\boldsymbol{w}')^T [D]([\Gamma_h]\boldsymbol{w} + [\Gamma_\varepsilon]\bar{\boldsymbol{\varepsilon}} + [\Gamma_R]\boldsymbol{w} + [\Gamma_l]\boldsymbol{w}') dx_2 dx_3 dx_1 \tag{3.19}$$

[D] is a matrix of material stiffness which carries the information of material property and fiber orientation and layer orientation as follows.

$$[D] = [T_\beta]^{-1}[T_\alpha]^{-1}[C][T_\alpha]^{-1}[T_\beta]^{-T} \tag{3.20}$$

where [C] is the 6 × 6 anisotropic material stiffness matrix Eq. (*3.21*) which relates the stresses and strains in the material coordinates e_1, e_2, e_3, [80], $[T_\alpha]$ is the transformation matrix Eq. (*3.22*) that transforms fiber orientation in its own plane by angle α and $[T_\beta]$ is the transformation matrix Eq. (3.23) which transforms layer orientation by angle β with the coordinates y_1, y_2 and y_3 to the beam coordinates (x_1, x_2, x_3) as shown in Fig. (3.3).

$$[C] = \begin{bmatrix} \frac{1}{E_1} & 0 & 0 & -\frac{\nu_{21}}{E_2} & 0 & -\frac{\nu_{31}}{E_3} \\ 0 & \frac{1}{G_{12}} & 0 & 0 & 0 & 0 \\ 0 & 0 & \frac{1}{G_{13}} & 0 & 0 & 0 \\ -\frac{\nu_{12}}{E_1} & 0 & 0 & \frac{1}{E_2} & 0 & -\frac{\nu_{32}}{E_3} \\ 0 & 0 & 0 & 0 & \frac{1}{G_{23}} & 0 \\ -\frac{\nu_{13}}{E_1} & 0 & 0 & -\frac{\nu_{23}}{E_2} & 0 & \frac{1}{E_3} \end{bmatrix}^{-1} \tag{3.21}$$

$$[T_\alpha]=\begin{bmatrix} \cos^2(\alpha) & 2\cos(\alpha)\sin(\alpha) & 0 & \sin^2(\alpha) & 0 & 0 \\ -\cos(\alpha)\sin(\alpha) & \cos^2(\alpha)-\sin^2(\alpha) & 0 & \cos(\alpha)\sin(\alpha) & 0 & 0 \\ 0 & 0 & \cos(\alpha) & 0 & \sin(\alpha) & 0 \\ \sin^2(\alpha) & -2\sin(\alpha)\cos(\alpha) & 0 & \cos^2(\alpha) & 0 & 0 \\ 0 & 0 & -\sin(\alpha) & 0 & \cos(\alpha) & 0 \\ 0 & 0 & 0 & 0 & 0 & 1 \end{bmatrix} \tag{3.22}$$

$$[T_\beta]=\begin{bmatrix} 1 & 0 & 0 & 0 & 0 & 0 \\ 0 & \cos(\beta) & \sin(\beta) & 0 & 0 & 0 \\ 0 & -\sin(\beta) & \cos(\beta) & 0 & 0 & 0 \\ 0 & 0 & 0 & \cos^2(\beta) & 2\sin(\beta)\cos(\beta) & \sin^2(\beta) \\ 0 & 0 & 0 & -\sin(\beta)\cos(\beta) & \cos^2(\beta)-\sin^2(\beta) & \cos(\beta)\sin(\beta) \\ 0 & 0 & 0 & \sin^2(\beta) & -2\cos(\beta)\sin(\beta) & \cos^2(\beta) \end{bmatrix} \tag{3.23}$$

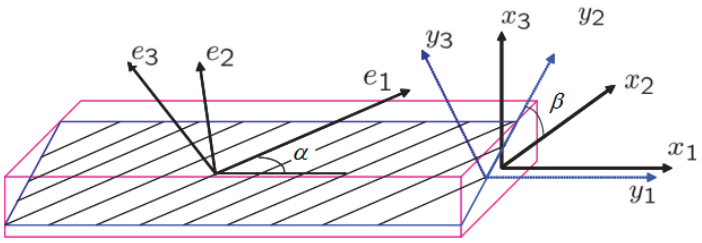

Fig. (3.3) The fiber and layer coordinates in the VABS.

3.1.4 Step 3: cross-sectional discretization using finite element method in VABS

In Eq. (3.19), the unknowns are the warping functions $w(x_1, x_2, x_3)$, and the strains of the reference line $\overline{\boldsymbol{\varepsilon}}$. The VABS approach to provide solution is to assume that the warping function is a product of two entities, one is some function of x_2 and x_3, and the other is function of only on x_1.

The warping field is discretized as

$$\boldsymbol{w}(x_1, x_2, x_3) = [W(x_2, x_3)]\boldsymbol{V}(x_1) \tag{3.24}$$

where, $[W(x_2, x_3)]$ is the matrix of finite-element shape functions, and $\boldsymbol{V}(x_1)$ as a column vector of the nodal values of the warping displacement over the cross-section in VABS method.

In VABS, in order to eliminate the warping (w) from the strain energy of Eq. (3.19), one has to turn to a numerical solution. The FE is the choice of the VABS, in which arbitrary geometry and material distribution are present in the domain of the problem. Since the domain must be homogenous at the element level, elements are not allowed to cross a lamina boundary. In addition, due to the manufacturing process used in laminated composite structures, the planar quadrilateral element is the recommended choice. There are three types of elements generated to deal with the cross-section discretization. *a*) 4-node rectangular element, *b*) 6-node isoparametric element, *c*) 8-node isoparametric element, they are presented in Fig. (3.4).

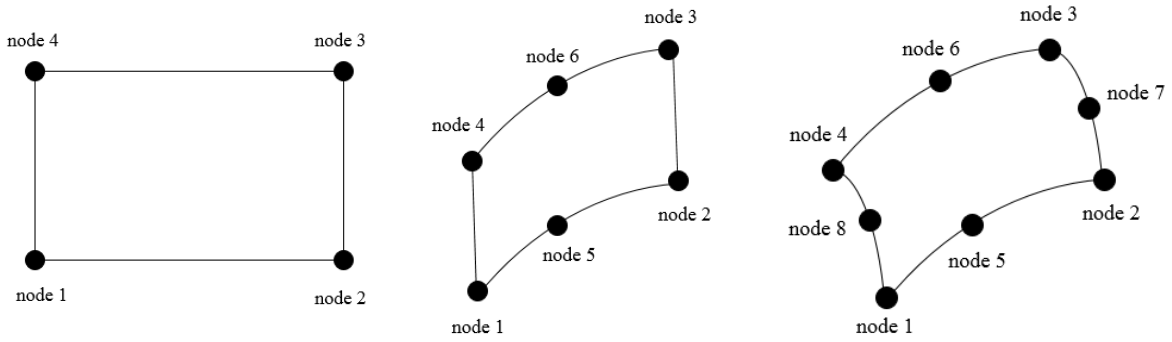

a) *b*) *c*)

Fig. (3.4). *a*) four-node rectangular element; *b*) six-node isoparametic element; c) eight-node isoparametic element [47].

The 4-node rectangular element has the main advantage of being simple. However, for most of the practical applications, the cross-section has one or more curved boundaries and a higher-order interpolation is necessary. So, quadratic interpolation was used on each side of the element along with isoparametric formulation, providing a way to model curved boundaries. That leads to the 8-node isoparametric element, [47].

3.1.5 Step 4: Asymptotically-Correct Refined Theory

According to the VAM, the warping field is perturbed using the small parameter of the beam as Eq. (3.25).

$$\boldsymbol{w} = \underset{\varepsilon_{\max}}{\boldsymbol{w}_0} + \underset{\varepsilon_{\max} h/L}{\boldsymbol{w}_1} \quad or \quad W = \underset{\varepsilon_{\max}}{w_0} + \underset{\varepsilon_{\max} h/R}{w_1} \tag{3.25}$$

where, $\boldsymbol{w}_0$ has the order of $\varepsilon_{\max}$ and $\boldsymbol{w}_1$ has the order of $\varepsilon_{\max} h / L$ or $\varepsilon_{\max} h / R$. We can write:

$$\boldsymbol{w}_0 = \underset{\varepsilon_{\max}}{W\boldsymbol{V}_0}\ ,\ \boldsymbol{w}_1 = \underset{\varepsilon_{\max}h/L}{W\boldsymbol{V}_1}\ \text{ or }\ \boldsymbol{w}_1 = \underset{\varepsilon_{\max}h/R}{W\boldsymbol{V}_1} \tag{3.26}$$

and,

$$\boldsymbol{V} = \boldsymbol{V}_0 + \boldsymbol{V}_1 \tag{3.27}$$

Therefore, the strain field can be expressed as

$$\boldsymbol{\Gamma} = \underset{\varepsilon_{\max}}{\Gamma_\varepsilon \bar{\boldsymbol{\varepsilon}}} + \underbrace{\Gamma_h W\boldsymbol{V}_0}_{\varepsilon_{\max}} + \underbrace{\Gamma_h W\boldsymbol{V}_1}_{\varepsilon_{\max}h/L} + \underbrace{\Gamma_R W\boldsymbol{V}_0}_{\varepsilon_{\max}} + \underbrace{\Gamma_R W\boldsymbol{V}_1}_{\varepsilon_{\max}h/R} + \underbrace{\Gamma_l W\boldsymbol{V}_0'}_{\varepsilon_{\max}h/L} + \underbrace{\Gamma_l W\boldsymbol{V}_1'}_{\varepsilon_{\max}(h/L)^2} \tag{3.28}$$

In the strain field of Eq. (3.28), the first and second terms have the order of $\varepsilon_{\max}$, the third term has the order of $\varepsilon_{\max}h/L$ and the fifth term has the order of $\varepsilon_{\max}h/R$, and the last term has the order of the $\varepsilon_{\max}(h/L)^2$. By considering Eqs. (3.27), (3.28) and Eq. (3.19), the strain energy of an initially curved anisotropic can be expressed as follows.

$$\begin{aligned}
2U = \int_L \iint_{\boldsymbol{\Omega}} \Bigg(& \underbrace{\boldsymbol{V}_0^T[D_{hh}]\boldsymbol{V}_0}_{\varepsilon_{\max}^2} + 2\underbrace{\boldsymbol{V}_0^T[D_{hh}]\boldsymbol{V}_1}_{\varepsilon_{\max}^2(h/L)} + \underbrace{\boldsymbol{V}_1^T[D_{hh}]\boldsymbol{V}_1}_{\varepsilon_{\max}^2(h/L)^2} + 2\underbrace{\boldsymbol{V}_0^T[D_{h\varepsilon}]\bar{\boldsymbol{\varepsilon}}}_{\varepsilon_{\max}^2} + 2\underbrace{\boldsymbol{V}_1^T[D_{h\varepsilon}]\bar{\boldsymbol{\varepsilon}}}_{\varepsilon_{\max}^2(h/L)} + 2\underbrace{\boldsymbol{V}_0^T[D_{hR}]\boldsymbol{V}_0}_{\varepsilon_{\max}^2(h/L)} \\
& + 2\underbrace{\boldsymbol{V}_0^T[D_{hR}]\boldsymbol{V}_1}_{\varepsilon_{\max}^2(h/L)^2} + 2\underbrace{\boldsymbol{V}_1^T[D_{hR}]\boldsymbol{V}_1}_{\varepsilon_{\max}^2(h/L)^3} + 2\underbrace{\boldsymbol{V}_0^T[D_{hl}]\boldsymbol{V}_0'}_{\varepsilon_{\max}^2(h/L)} + 2\underbrace{\boldsymbol{V}_0^T[D_{hl}]\boldsymbol{V}_1'}_{\varepsilon_{\max}^2(h/L)^2} + 2\underbrace{\bar{\boldsymbol{\varepsilon}}^T[D_{\varepsilon R}]\boldsymbol{V}_1}_{\varepsilon_{\max}^2(h/L)^2} + 2\underbrace{\bar{\boldsymbol{\varepsilon}}^T[D_{\varepsilon l}]\boldsymbol{V}_0'}_{\varepsilon_{\max}^2(h/L)} \\
& + 2\underbrace{\bar{\boldsymbol{\varepsilon}}^T[D_{\varepsilon l}]\boldsymbol{V}_1'}_{\varepsilon_{\max}^2(h/L)^2} + 2\underbrace{\boldsymbol{V}_1^T[D_{hl}]\boldsymbol{V}_0'}_{\varepsilon_{\max}^2(h/L)^2} + 2\underbrace{\boldsymbol{V}_1^T[D_{hl}]\boldsymbol{V}_1'}_{\varepsilon_{\max}^2(h/L)^3} + \underbrace{\bar{\boldsymbol{\varepsilon}}^T[D_{\varepsilon\varepsilon}]\bar{\boldsymbol{\varepsilon}}}_{\varepsilon_{\max}^2} + 2\underbrace{\bar{\boldsymbol{\varepsilon}}^T[D_{\varepsilon R}]\boldsymbol{V}_0}_{\varepsilon_{\max}^2(h/L)} + 2\underbrace{\boldsymbol{V}_0^T[D_{Rh}]\boldsymbol{V}_1}_{\varepsilon_{\max}^2(h/L)} \\
& + \underbrace{\boldsymbol{V}_0^T[D_{RR}]\boldsymbol{V}_0}_{\varepsilon_{\max}^2(h/L)^2} + 2\underbrace{\boldsymbol{V}_0^T[D_{RR}]\boldsymbol{V}_1}_{\varepsilon_{\max}^2(h/L)^3} + \underbrace{\boldsymbol{V}_1^T[D_{RR}]\boldsymbol{V}_1}_{\varepsilon_{\max}^2(h/L)^4} + 2\underbrace{\boldsymbol{V}_0^T[D_{Rl}]\boldsymbol{V}_0'}_{\varepsilon_{\max}^2(h/L)^2} + 2\underbrace{\boldsymbol{V}_0^T[D_{Rl}]\boldsymbol{V}_1'}_{\varepsilon_{\max}^2(h/L)^3} + 2\underbrace{\boldsymbol{V}_1^T[D_{Rl}]\boldsymbol{V}_0'}_{\varepsilon_{\max}^2(h/L)^3} \\
& + 2\underbrace{\boldsymbol{V}_1^T[D_{Rl}]\boldsymbol{V}_1'}_{\varepsilon_{\max}^2(h/L)^4}) + \underbrace{\boldsymbol{V}_0'^T[D_{ll}]\boldsymbol{V}_0'}_{\varepsilon_{\max}^2(h/L)^2} + 2\underbrace{\boldsymbol{V}_0'^T[D_{ll}]\boldsymbol{V}_1'}_{\varepsilon_{\max}^2(h/L)^3} + \underbrace{\boldsymbol{V}_1'^T[D_{ll}]\boldsymbol{V}_1'}_{\varepsilon_{\max}^2(h/L)^4} \Bigg) dx_3 dx_2 dx_1
\end{aligned} \tag{3.29}$$

where, the matrices $[D_{\varepsilon\varepsilon}]$, $[D_{h\varepsilon}]$, $[D_{hh}]$, $[D_{hl}]$, $[D_{ll}]$, $[D_{l\varepsilon}]$, $[D_{hR}]$, $[D_{RR}]$, $[D_{R\varepsilon}]$, and $[D_{Rl}]$ carry the information on the material properties and geometry of the cross-section as

$$[D_{hh}]=\int_{\Omega}\int[\Gamma_h W]^T[D][\Gamma_h W]dx_2dx_3,\ [D_{h\varepsilon}]=\int_{\Omega}\int[\Gamma_h W]^T[D][\Gamma_\varepsilon]dx_2dx_3$$
$$[D_{hl}]=\int_{\Omega}\int[\Gamma_h W]^T[D][\Gamma_l W]dx_2dx_3,\ [D_{\varepsilon\varepsilon}]=\int_{\Omega}\int[\Gamma_\varepsilon]^T[D][\Gamma_\varepsilon]dx_2dx_3$$
$$[D_{ll}]=\int_{\Omega}\int[\Gamma_l W]^T[D][\Gamma_l W]dx_2dx_3,\ [D_{l\varepsilon}]=\int_{\Omega}\int[\Gamma_l W]^T[D][\Gamma_\varepsilon]dx_2dx_3 \tag{3.30}$$
$$[D_{hR}]=\int_{\Omega}\int[\Gamma_h W]^T[D][\Gamma_R W]dx_2dx_3,\ [D_{RR}]=\int_{\Omega}\int[\Gamma_R W]^T[D][\Gamma_R W]dx_2dx_3$$
$$[D_{R\varepsilon}]=\int_{\Omega}\int[\Gamma_R W]^T[D][\Gamma_\varepsilon]dx_2dx_3\ ,\ [D_{Rl}]=\int_{\Omega}\int[\Gamma_R W]^T[D][\Gamma_l W]dx_2dx_3$$

3.1.6 Step 5: First and second approximation of the strain energy

The expression of the energy in Eq. (3.29) has terms of different orders. By dropping terms of smaller magnitudes, different levels of solution can be obtained.

3.1.6.1 First Approximation

The first approximation in the warping field in the VAM comes from keeping the terms up to order $\varepsilon_{\max}^2$ in the strain energy of Eq. (3.29). Therefore, the order-zero of the linear strain density is as follows.

$$2U_0=\int_L(\boldsymbol{V}_0^T[D_{hh}]\boldsymbol{V}_0+2\boldsymbol{V}_0^T[D_{h\varepsilon}]\bar{\boldsymbol{\varepsilon}}+\bar{\boldsymbol{\varepsilon}}^T[D_{\varepsilon\varepsilon}]\bar{\boldsymbol{\varepsilon}})dx_1 \tag{3.31}$$

The strain energy in Eq. (3.31) is minimized with respect to the unknown warping V_0 using the following relation.

$$\frac{\partial U_0}{\partial \boldsymbol{V}_0}=0 \tag{3.32}$$

This yields the classical beam model in which the effects of transverse shear are neglected. Substituting Eq. (3.31) into Eq. (3.32) leads to

$$[D_{h\varepsilon}]\bar{\boldsymbol{\varepsilon}}+[D_{hh}]\boldsymbol{V}_0=0 \tag{3.33}$$

Therefore, the unknown warping coefficients according to the order-zero of the strain energy is obtained as

$$\boldsymbol{V}_0 = -[D_{hh}]^{-1}[D_{h\varepsilon}]\bar{\boldsymbol{\varepsilon}} \equiv [\hat{V}_0]\bar{\boldsymbol{\varepsilon}} \tag{3.34}$$

It is difficult to invert the matrix $[D_{hh}]$ in Eq. (3.34). To find the inverse of this matrix, a mathematical Pseudo method [81] is used. Using the obtained column matrix of Eq. (3.34) and the order-zero of the strain energy Eq. (3.31), the first approximation of strain energy and stiffness constants of the classical beam model can be achieved as follows.

$$2U_0 = \int_L (\bar{\boldsymbol{\varepsilon}}^T([\hat{V}_0]^T[D_{h\varepsilon}] + [D_{\varepsilon\varepsilon}])\bar{\boldsymbol{\varepsilon}})dx_1 = \int_L \begin{Bmatrix} \bar{\gamma}_{11} \\ \bar{\kappa}_1 \\ \bar{\kappa}_2 \\ \bar{\kappa}_3 \end{Bmatrix}^T \begin{bmatrix} \bar{S}_{11} & \bar{S}_{12} & \bar{S}_{13} & \bar{S}_{14} \\ \bar{S}_{21} & \bar{S}_{22} & \bar{S}_{23} & \bar{S}_{24} \\ \bar{S}_{31} & \bar{S}_{32} & \bar{S}_{33} & \bar{S}_{34} \\ \bar{S}_{41} & \bar{S}_{42} & \bar{S}_{43} & \bar{S}_{44} \end{bmatrix} \begin{Bmatrix} \bar{\gamma}_{11} \\ \bar{\kappa}_1 \\ \bar{\kappa}_2 \\ \bar{\kappa}_3 \end{Bmatrix} dx_1 \tag{3.35}$$

Once can write,

$$2U_0 = \int_L \bar{\boldsymbol{\varepsilon}}^T[\bar{S}]\bar{\boldsymbol{\varepsilon}}\, dx_1 \tag{3.36}$$

where $\bar{S}$ is a 4×4 stiffness matrix that expresses the beam cross-sectional stiffness coefficients. For a cross-section with area Ω, second moment of inertia *I,* polar moment of inertia *J,* elastic modulus *E* and shear modulus *G*, the stiffness constant $\bar{S}_{11}$ or $(E\Omega)$ is extensional stiffness, $\bar{S}_{22}$ or (GJ) is torsional stiffness, $\bar{S}_{33}$ or $(EI)_{x_2}$ and $\bar{S}_{44}$ or $(EI)_{x_3}$ are cross-sectional bending stiffness about x_2 and x_3 coordinates, respectively. Moreover, $\bar{S}_{12}$ is the extension-twist coupling, $\bar{S}_{13}$ and $\bar{S}_{14}$ are the extension-bending coupling stiffnesses.

3.1.6.2 Second approximation

The first approximation which leads to the classical beam model may not be accurate sufficiently for analysis of composite tubular beams with various lay-ups through the section. The second approximation of the strain energy with considering the transverse shear effect (Timoshenko refinement) may be accurate to predict the behavior of composite tubes. The strain energy up to order $O(\varepsilon_{\max}^2 h^2 / L^2)$ can be written as

$$
\begin{aligned}
2U_1 = \int_L & (2\boldsymbol{V}_0^T([D_{hR}]\boldsymbol{V}_1 + [D_{hl}]\boldsymbol{V}_1') + 2\boldsymbol{V}_1^T([D_{hR}]\boldsymbol{V}_0 + [D_{hl}]\boldsymbol{V}_0') + \boldsymbol{V}_1^T[D_{hh}]\boldsymbol{V}_1 \\
& + 2\boldsymbol{V}_1'^T[D_{l\varepsilon}]\bar{\boldsymbol{\varepsilon}} + 2\boldsymbol{V}_0^T[D_{Rl}]\boldsymbol{V}_0' + \boldsymbol{V}_0'^T[D_{ll}]\boldsymbol{V}_0' + \boldsymbol{V}_0^T[D_{RR}]\boldsymbol{V}_0 + 2\boldsymbol{V}_1^T[D_{R\varepsilon}]\bar{\boldsymbol{\varepsilon}} \\
& + 2\boldsymbol{V}_0^T([D_{hR}]\boldsymbol{V}_0 + [D_{hl}]\boldsymbol{V}_0') + 2\boldsymbol{V}_0^T[D_{R\varepsilon}]\bar{\boldsymbol{\varepsilon}} + 2\boldsymbol{V}_0'^T[D_{l\varepsilon}]\bar{\boldsymbol{\varepsilon}} + \boldsymbol{V}_0^T[D_{hh}]\boldsymbol{V}_0 + 2\boldsymbol{V}_0^T[D_{h\varepsilon}]\bar{\boldsymbol{\varepsilon}} \\
& + \bar{\boldsymbol{\varepsilon}}^T[D_{\varepsilon\varepsilon}]\bar{\boldsymbol{\varepsilon}})dx_1
\end{aligned}
\tag{3.37}
$$

It is noted that in the equation above the terms $2\boldsymbol{V}_0^T[D_{hh}]\boldsymbol{V}_1$ and $2\boldsymbol{V}_1^T[D_{h\varepsilon}]\bar{\boldsymbol{\varepsilon}}$ cancel out each other, [46]. Also, in Eq. (3.37), the term $\boldsymbol{V}_0^T[D_{hh}]\boldsymbol{V}_0$ is not mentioned in the strain energy obtained by Hodges [40]. However, this term is of low order. In order to eliminate the derivatives of the warping ($\boldsymbol{V}_1'$), the Eq. (3.37) is integrated by parts. We have:

$$
\begin{aligned}
2U_1 = \int_L & (2\boldsymbol{V}_0^T[D_{hR}]\boldsymbol{V}_1 - 2\boldsymbol{V}_0'^T[D_{hl}]\boldsymbol{V}_1' + 2\boldsymbol{V}_1^T[D_{hR}]\boldsymbol{V}_0 + 2\boldsymbol{V}_1^T[D_{hl}]\boldsymbol{V}_0' + \boldsymbol{V}_1^T[D_{hh}]\boldsymbol{V}_1 \\
& - 2\boldsymbol{V}_1^T[D_{l\varepsilon}]\bar{\boldsymbol{\varepsilon}}' + 2\boldsymbol{V}_0^T[D_{Rl}]\boldsymbol{V}_0' + \boldsymbol{V}_0'^T[D_{ll}]\boldsymbol{V}_0' + \boldsymbol{V}_0^T[D_{RR}]\boldsymbol{V}_0 + 2\boldsymbol{V}_1^T[D_{R\varepsilon}]\bar{\boldsymbol{\varepsilon}} \\
& + 2\boldsymbol{V}_0^T([D_{hR}]\boldsymbol{V}_0 + [D_{hl}]\boldsymbol{V}_0') + 2\boldsymbol{V}_0^T[D_{R\varepsilon}]\bar{\boldsymbol{\varepsilon}} + 2\boldsymbol{V}_0'^T[D_{l\varepsilon}]\bar{\boldsymbol{\varepsilon}} + \boldsymbol{V}_0^T[D_{hh}]\boldsymbol{V}_0 \\
& + 2\boldsymbol{V}_0^T[D_{h\varepsilon}]\bar{\boldsymbol{\varepsilon}} + \bar{\boldsymbol{\varepsilon}}^T[D_{\varepsilon\varepsilon}]\bar{\boldsymbol{\varepsilon}})dx_1
\end{aligned}
\tag{3.38}
$$

Substituting Eq. (3.34) back into Eq. (3.38), and using Euler-Lagrange equation ($\frac{\partial U_1}{\partial V_1} = 0$), we have:

$$
\begin{aligned}
V_1 = & -[D_{hh}]^{-1}\Big((-[D_{l\varepsilon}] + [D_{hl}][\hat{V}_0] - [\hat{V}_0]^T[D_{hl}])\bar{\boldsymbol{\varepsilon}}' + ([\hat{V}_0]^T[D_{Rh}] + [D_{Rh}][\hat{V}_0] \\
& + [D_{R\varepsilon}])\bar{\boldsymbol{\varepsilon}}\Big) \equiv [V_{1S}]\bar{\boldsymbol{\varepsilon}}' + [V_{1R}]\bar{\boldsymbol{\varepsilon}}
\end{aligned}
\tag{3.39}
$$

Substituting Eq. (3.39) to Eq. (3.38), we have

$$
\begin{aligned}
2U_1 = \int_L \Big(& \bar{\boldsymbol{\varepsilon}}^T ([\hat{V}_0]^T[D_{h\varepsilon}] + [D_{\varepsilon\varepsilon}] + 2[\hat{V}_0]^T[D_{hR}][\hat{V}_0] + 2[\hat{V}_0]^T[D_{R\varepsilon}] \\
& + [V_{1R}]^T[D_{hh}][V_{1R}] + 2[V_{1R}]^T[D_{hR}][\hat{V}_0] + 2[V_{1R}]^T[D_{hR}]^T[\hat{V}_0] + 2[V_{1R}]^T[D_{hR}][\hat{V}_0] \\
& + 2[V_{1R}]^T[D_{hR}]^T[\hat{V}_0] + 2[V_{1R}]^T[D_{R\varepsilon}] + [\hat{V}_0][D_{RR}][\hat{V}_0])\bar{\boldsymbol{\varepsilon}} + \bar{\boldsymbol{\varepsilon}}^T(2[\hat{V}_0]^T[D_{hl}]\boldsymbol{V}_0 \\
& + 2[\hat{V}_0][D_{l\varepsilon}]^T + [V_{1R}]^T[D_{hh}][V_{1S}] + [V_{1S}][D_{hh}]^T[V_{1R}]^T + 2[V_{1S}][D_{hR}]^T[\hat{V}_0]^T \\
& + 2[V_{1S}][D_{hR}][\hat{V}_0]^T + 2[V_{1S}][D_{R\varepsilon}]^T + 2[V_{1R}][D_{hl}][\hat{V}_0] + 2[\hat{V}_0]^T[D_{hl}][V_{1R}] \\
& + 2[V_{1R}][D_{l\varepsilon}]^T + 2[\hat{V}_0]^T[D_{Rl}])\bar{\boldsymbol{\varepsilon}}' + \bar{\boldsymbol{\varepsilon}}'^T([V_{1S}][D_{hh}][V_{1S}] + 2[V_{1S}]^T[D_{hl}][\hat{V}_0] \\
& + [\hat{V}_0]^T[D_{ll}][\hat{V}_0])\bar{\boldsymbol{\varepsilon}}' + \bar{\boldsymbol{\varepsilon}}^T(2[V_0]^T[D_{hl}][V_{1S}] + 2[D_{l\varepsilon}]^T[V_{1S}])\bar{\boldsymbol{\varepsilon}}'')dx_1
\end{aligned}
\tag{3.40}
$$

The above strain energy can be rewritten in the following form

$$
2U_1 = \int_L \left(\bar{\boldsymbol{\varepsilon}}^T[Y_1]\bar{\boldsymbol{\varepsilon}} + 2\bar{\boldsymbol{\varepsilon}}^T[Y_2]\bar{\boldsymbol{\varepsilon}}' + \bar{\boldsymbol{\varepsilon}}'^T[Y_3]\bar{\boldsymbol{\varepsilon}}' + 2\bar{\boldsymbol{\varepsilon}}^T[Y_4]\bar{\boldsymbol{\varepsilon}}'' \right) dx_1 \tag{3.41}
$$

where,

$$
\begin{aligned}
[Y_1] = & [\hat{V}_0]^T[D_{h\varepsilon}] + [D_{\varepsilon\varepsilon}] + 2[\hat{V}_0]^T[D_{hR}][\hat{V}_0] + 2[\hat{V}_0]^T[D_{R\varepsilon}] + [V_{1R}]^T[D_{hh}][V_{1R}] \\
& + 2[V_{1R}]^T[D_{hR}][\hat{V}_0] + 2V_{1R}^T[D_{hR}]^T[\hat{V}_0] + 2V_{1R}^T[D_{hR}]\hat{V}_0 + 2[V_{1R}]^T[D_{hR}]^T[\hat{V}_0] + \\
& 2[V_{1R}]^T[D_{R\varepsilon}] + [\hat{V}_0][D_{RR}][\hat{V}_0]
\end{aligned}
\tag{3.42}
$$

$$
\begin{aligned}
[Y_2] = & 2[\hat{V}_0]^T[D_{hl}][V_0] + 2[\hat{V}_0][D_{l\varepsilon}]^T + [V_{1R}]^T[D_{hh}][V_{1S}] + [V_{1S}][D_{hh}]^T[V_{1R}]^T \\
& + 2[V_{1S}][D_{hR}]^T[\hat{V}_0]^T + 2[V_{1S}][D_{hR}][\hat{V}_0]^T + 2[V_{1S}][D_{R\varepsilon}]^T + 2[V_{1R}][D_{hl}][\hat{V}_0] \\
& + 2[\hat{V}_0]^T[D_{hl}][V_{1R}] + 2[V_{1R}][D_{l\varepsilon}]^T + 2[\hat{V}_0]^T[D_{Rl}]
\end{aligned}
\tag{3.43}
$$

$$
[Y_3] = [V_{1S}][D_{hh}][V_{1S}] + 2[V_{1S}]^T[D_{hl}][\hat{V}_0] + [\hat{V}_0]^T[D_{ll}][\hat{V}_0] \tag{3.44}
$$

$$
[Y_4] = 2[V_0]^T[D_{hl}][V_{1S}] + 2[D_{l\varepsilon}]^T[V_{1S}] \tag{3.45}
$$

The matrix $[Y_1]$ is the classical cross-sectional stiffness matrix corresponding to the second order strain energy which takes into account the initial curvature of the beam. This matrix will be used for 1D analysis of the beam.

The Eq. (3.41) involves derivatives of $\bar{\boldsymbol{\varepsilon}}$. In order to eliminate the derivatives of the classical strain measures, Popescu and Hodges [55] used 1D equilibrium equations to build a relationship between the strains and derivatives of strains. One has to change the asymptotically-correct formulation to

be expressed by the strain measures of Timoshenko theory. Because of shear deformation, B_1 is not tangent to the x_1. Based on the relation between T_i and B_i and assuming small strains, one can derive a kinematic identity between classical strains in the T_i system and the Timoshenko strains in the B_i system. So, we have

$$\bar{\boldsymbol{\varepsilon}} = \boldsymbol{\varepsilon} + [Q]\boldsymbol{\gamma}_s' + [P]\boldsymbol{\gamma}_s \tag{3.46}$$

$$[P] = \begin{bmatrix} 0 & 0 \\ k_2 & k_3 \\ 0 & 0 \\ 0 & 0 \end{bmatrix},\ [Q] = \begin{bmatrix} 0 & 0 \\ 0 & 0 \\ 0 & -1 \\ 1 & 0 \end{bmatrix} \tag{3.47}$$

Where, $\boldsymbol{\varepsilon} = \begin{bmatrix} \gamma_{11} & \kappa_1 & \kappa_2 & \kappa_3 \end{bmatrix}^T$ represents the 1D generalized strains associated with B_i system due to extension, torsion and bending, and $\boldsymbol{\gamma}_s = \begin{bmatrix} 2\gamma_{12} & 2\gamma_{13} \end{bmatrix}^T$ is the column matrix of transverse shear strain measures associated with the B_i basis. By substituting Eq. (3.47) into the strain energy Eq. (3.41), one has

$$\begin{aligned} 2U_1 = \int_L \Big(& \left(\boldsymbol{\varepsilon} + [Q]\gamma_s' + [P]\boldsymbol{\gamma}\right)^T [Y_1]\left(\boldsymbol{\varepsilon} + [Q]\boldsymbol{\gamma}_s' + [P]\boldsymbol{\gamma}_s\right) + 2\left(\boldsymbol{\varepsilon} + [Q]\boldsymbol{\gamma}_s' + [P]\boldsymbol{\gamma}_s\right) \\ & [Y_2]\left(\boldsymbol{\varepsilon} + [Q]\boldsymbol{\gamma}_s' + [P]\boldsymbol{\gamma}_s\right)' + \left(\boldsymbol{\varepsilon} + [Q]\boldsymbol{\gamma}_s' + [P]\boldsymbol{\gamma}_s\right)'^T [Y_3]\left(\boldsymbol{\varepsilon} + [Q]\boldsymbol{\gamma}_s' + [P]\boldsymbol{\gamma}_s\right)' \\ & +2\left(\boldsymbol{\varepsilon} + [Q]\boldsymbol{\gamma}_s' + [P]\boldsymbol{\gamma}_s\right)^T [Y_4]\left(\boldsymbol{\varepsilon} + [Q]\boldsymbol{\gamma}_s' + [P]\boldsymbol{\gamma}_s\right)'' \Big) dx_1 \end{aligned} \tag{3.48}$$

By neglecting the higher order terms, the strain energy in the form of Timoshenko-like beam strain measures can be expressed as

$$\begin{aligned} 2U_1 = \int_L \Big(& \boldsymbol{\varepsilon}^T [Y_1]\boldsymbol{\varepsilon} + 2\boldsymbol{\varepsilon}^T [Y_1][Q]\boldsymbol{\gamma}_s' + 2\boldsymbol{\varepsilon}^T [Y_1][P]\boldsymbol{\gamma}_s + 2\boldsymbol{\varepsilon}^T [Y_2]\boldsymbol{\varepsilon}' + \boldsymbol{\varepsilon}'^T [Y_3]\boldsymbol{\varepsilon}' \\ & +2\boldsymbol{\varepsilon}^T [Y_4]\boldsymbol{\varepsilon}'' \Big) dx_1 \end{aligned} \tag{3.49}$$

The generalized Timoshenko strain energy should be written as

$$2U = \int_L \left(\boldsymbol{\varepsilon}^T [X_1]\boldsymbol{\varepsilon} + 2\boldsymbol{\varepsilon}^T [X_2]\boldsymbol{\gamma}_s + \boldsymbol{\gamma}_s{}^T [X_3]\boldsymbol{\gamma}_s \right) dx_1 \tag{3.50}$$

The $[X_1]$ is a 4×4, $[X_2]$ is a 4×2, and $[X_3]$ is a 2×2 unknown matrices. If the generalized Timoshenko theory is asymptotically-correct, Eqs. (3.49) and Eq. (3.50) should be equivalent. To

make Eq. (3.50) fit into the generalized Timoshenko form as in Eq. (3.41), one has to express the derivatives of the strain measures in terms of strain measures themselves. So, one has to eliminate the derivatives in Eq. (3.41). Using the equilibrium equations is a feasible way to achieve this. The nonlinear 1D equilibrium equations for initially curved and twisted beams without distributed forces can be written as, [48].

$$\begin{aligned} &\boldsymbol{F}' + [\tilde{K}]\boldsymbol{F} = 0 \\ &\boldsymbol{M}' + [\tilde{K}]\boldsymbol{M} + (\tilde{\boldsymbol{e}}_1 + \tilde{\boldsymbol{\rho}})\boldsymbol{F} = 0 \end{aligned} \tag{3.51}$$

and,

$$\begin{aligned} &\tilde{\boldsymbol{e}}_1 = [1 \quad 0 \quad 0]^T; \tilde{\boldsymbol{\rho}} = [\gamma_{11} \quad 2\gamma_{12} \quad 2\gamma_{12}]^T; \boldsymbol{K} = \boldsymbol{k} + \bar{\boldsymbol{\kappa}} \\ &[\tilde{K}] = \begin{bmatrix} 0 & -k_3 & -k_2 \\ k_3 & 0 & 0 \\ k_2 & 0 & 0 \end{bmatrix} \end{aligned} \tag{3.52}$$

Where, $\boldsymbol{F}$ is the column matrix of the cross-sectional stress resultant measures as $\boldsymbol{F} = \begin{bmatrix} F_1 & F_2 & F_3 \end{bmatrix}^T$ in the B_i basis, and $\boldsymbol{M}$ is the column matrix of the cross-sectional moment resultant measures as $\boldsymbol{M} = \begin{bmatrix} M_1 & M_2 & M_3 \end{bmatrix}^T$ in the B_i basis. The terms of order O(h^3) are considered. Because the strain energy is only asymptotically-correct up to the second order of the h, nonlinear terms in the equilibrium equations do not affect the strain energy. As such, for the purpose of creating the cross-sectional model, Eq. (3.51) can be simplified to

$$\begin{Bmatrix} F_2' \\ F_3' \end{Bmatrix} + [D_1] \begin{Bmatrix} F_1 \\ M_1 \\ M_2 \\ M_3 \end{Bmatrix} = 0 \tag{3.53}$$

$$\begin{Bmatrix} F_1' \\ M_1' \\ M_2' \\ M_3' \end{Bmatrix} + [D_2] \begin{Bmatrix} F_1 \\ M_1 \\ M_2 \\ M_3 \end{Bmatrix} + [D_3] \begin{Bmatrix} F_2 \\ F_3 \end{Bmatrix} = 0 \tag{3.54}$$

In which,

$$[D_1]=\begin{bmatrix} k_3 & 0 & 0 & 0 \\ -k_2 & 0 & 0 & 0 \end{bmatrix}$$

$$[D_2]=\begin{bmatrix} 0 & 0 & 0 & 0 \\ 0 & 0 & -k_3 & k_2 \\ 0 & k_3 & 0 & 0 \\ 0 & -k_2 & 0 & 0 \end{bmatrix} \tag{3.55}$$

$$[D_3]=[Q]-[D_1]^T$$

The $\boldsymbol{\varepsilon}'$ and $\boldsymbol{\gamma}'$ can be expressed in terms of $\boldsymbol{\varepsilon}$ and $\boldsymbol{\gamma}$ from Eqs. (3.54) and (3.55) as

$$\boldsymbol{\varepsilon}'=[N]^{-1}([B_1]\boldsymbol{\gamma}_s+[B_2]\boldsymbol{\varepsilon}) \tag{3.56}$$

$$\boldsymbol{\gamma}_s'=-[X_3]^{-1}[([X_2]^T[N]^{-1}[B_1]+[D_1][X_2])\boldsymbol{\gamma}_s+([X_2]^T[N]^{-1}[B_2]+[D_1][X_1])\boldsymbol{\varepsilon}] \tag{3.57}$$

where,

$$[B_1]=-[D_3][X_3]+([X_2][X_3]^{-1}[D_1]-[D_2])[X_2] \tag{3.58}$$

$$[B_2]=[B_1][X_3]^{-1}[X_2]^T+([X_2][X_3]^{-1}[D_1]-[D_2])[Y_1] \tag{3.59}$$

$$N=[X_1]-[X_2][X_3]^{-1}[X_2]^T \tag{3.60}$$

Differentiating the both sides of Eq. (3.58), we can express $\bar{\boldsymbol{\varepsilon}}''$ in terms of $\bar{\boldsymbol{\varepsilon}}$ and $\boldsymbol{\gamma}$ as

$$\begin{aligned}\boldsymbol{\varepsilon}''=&[N]^{-1}\left(([X_2][X_3]^{-1}[D_1]-[D_2])[B_1]-[B_1][X_3]^{-1}[D_1][X_2]\right)\boldsymbol{\gamma}_s \\ &+[N]^{-1}\left(([X_2][X_3]^{-1}[D_1]-[D_2])[B_2]-[B_1][X_3]^{-1}([D_1][X_1])\right)\boldsymbol{\varepsilon}\end{aligned} \tag{3.61}$$

Substitution of Eqs. (3.56), (3.57) and (3.61) back into Eq. (3.49), the Timoshenko-like strain energy expression can be obtained. By setting Eqs. (3.49) and (3.50) equal to each other, the following expressions for the $[X_1]$, $[X_2]$ and $[X_3]$ can be extracted, [40].

$$[X_3]=[B_1]^T[N]^{-1}[Y_3][N]^{-1}[B_1] \tag{3.62}$$

$$[X_2] = -[Y_1][Q][X_3]^{-1}([Y_2][N]^{-1}[B_1] + [D_1][Y_2]) + [X_2][X_1]^{-1}[B_1]$$
$$+[B_2]^T[N]^{-1}[Y_3][Y_1]^{-1}[B_1] + [Y_1][P] + [Y_4][N]^{-1}[([X_2][X_3]^{-1}[D_1]$$
$$-[D_2])[B_1] - [B_1][X_3]^{-1}[D_1][X_2]]$$

$$[X_1] = [Y_1] - 2[Y_1][Q][X_3]^{-1}([X_2][N]^{-1}[B_2] + [D_1][X_1]) + 2[Y_2][N]^{-1}[B_2]$$
$$+[B_2]^T[N]^{-1}[Y_3][N]^{-1}[B_2] + 2[Y_3][N]^{-1}[([X_2][X_3]^{-1}[D_1] - [D_2])[B_2]$$
$$-[B_1][X_3]^{-1}[D_1][X_1]]$$

The Eq. (3.62) is a system of matrix equations. The perturbation method is used to solve this, [49]. The details of the solution procedure are reported in Yu et al. [49]. The one-dimensional strain energy in the form of Timoshenko theory can be expressed as

$$2U_1 = \int_L \begin{Bmatrix} \boldsymbol{\varepsilon} \\ \boldsymbol{\gamma}_s \end{Bmatrix}^T \begin{bmatrix} [X_1]_{4\times4} & [X_2]_{4\times2} \\ [X_2]^T_{4\times2} & [X_3]_{2\times2} \end{bmatrix} \begin{Bmatrix} \boldsymbol{\varepsilon} \\ \boldsymbol{\gamma}_s \end{Bmatrix} dx_1 \tag{3.63}$$

From the above strain energy relation, the strain energy in the form of Timoshenko can be rearranged as the following.

$$2U_1 = \int_L \boldsymbol{\psi}^T[S]\boldsymbol{\psi}^T dx_1 = \int_L \begin{Bmatrix} \gamma_{11} \\ 2\gamma_{12} \\ 2\gamma_{13} \\ \kappa_1 \\ \kappa_2 \\ \kappa_3 \end{Bmatrix}^T \begin{bmatrix} S_{11} & S_{12} & S_{13} & S_{14} & S_{15} & S_{16} \\ S_{12} & S_{22} & S_{23} & S_{24} & S_{25} & S_{26} \\ S_{13} & S_{23} & S_{33} & S_{34} & S_{35} & S_{36} \\ S_{14} & S_{24} & S_{34} & S_{44} & S_{45} & S_{46} \\ S_{15} & S_{25} & S_{35} & S_{45} & S_{55} & S_{56} \\ S_{16} & S_{26} & S_{36} & S_{46} & S_{56} & S_{66} \end{bmatrix} \begin{Bmatrix} \gamma_{11} \\ 2\gamma_{12} \\ 2\gamma_{13} \\ \kappa_1 \\ \kappa_2 \\ \kappa_3 \end{Bmatrix} dx_1 \tag{3.64}$$

In Eq. (3.64), $\boldsymbol{\psi} = \begin{bmatrix} \gamma_{11} & 2\gamma_{12} & 2\gamma_{13} & \kappa_1 & \kappa_2 & \kappa_3 \end{bmatrix}^T$ and [*S*] is a 6 × 6 cross-sectional Timoshenko stiffness matrix.

In the Timoshenko model of Eq. (3.64), S_{11} is the extensional, S_{22} and S_{33} are shear cross-section stiffness constants in the x_2 and x_3 directions, respectively, S_{44} is the twisting stiffness, and S_{55} and S_{66} are bending stiffnesses in the x_2 and x_3 directions, respectively. The other stiffnesses are the coupling stiffness (*i.e.* S_{14} is the extension-twisting coupling stiffness constant). The one-dimensional strain energy relation Eq. (3.64) stands for the one-dimensional beam model which

includes the 3D deformation effects of the cross-section. Using this 1D beam strain energy with the contribution of beam cross-sectional stiffness matrix, the 1D static analysis can be conducted.

3.1.7 Recovery analysis

The 3D strain distribution through the thickness of the tube can be obtained using Eqs. (3.14), (3.46), (3.56), (3.57) , and the following recovery relation.

$$\Gamma = \left[(\Gamma_a + \Gamma_R)(V_0 + V_{1R}) + \Gamma_\varepsilon\right]\bar{\varepsilon} + \left[(\Gamma_a + \Gamma_R)V_{1S} + \Gamma_l(V_0 + V_{1R})\right]\bar{\varepsilon}' + \Gamma_l V_{1S}\bar{\varepsilon}'' \tag{3.65}$$

Use of $\boldsymbol{\varepsilon}$ obtained from Eq. (3.66) [40].

$$\begin{Bmatrix} \gamma_{11} \\ 2\gamma_{12} \\ 2\gamma_{13} \\ \kappa_1 \\ \kappa_2 \\ \kappa_3 \end{Bmatrix} = \begin{bmatrix} S_{11} & S_{12} & S_{13} & S_{14} & S_{15} & S_{16} \\ S_{12} & S_{22} & S_{23} & S_{24} & S_{25} & S_{26} \\ S_{13} & S_{23} & S_{33} & S_{34} & S_{35} & S_{36} \\ S_{14} & S_{24} & S_{34} & S_{44} & S_{45} & S_{46} \\ S_{15} & S_{25} & S_{35} & S_{45} & S_{55} & S_{56} \\ S_{16} & S_{26} & S_{36} & S_{46} & S_{56} & S_{66} \end{bmatrix}^{-1} \begin{Bmatrix} F_1 \\ F_2 \\ F_3 \\ M_1 \\ M_2 \\ M_3 \end{Bmatrix} \tag{3.66}$$

3.2 Dimensional reduction using Pascal polynomial method

In Eq. (3.24), the warping functions are assumed to be a product of functions $W(x_2, x_3)$ and $V(x_1)$. The VABS software performs FEA for cross-sectional discretization of Eq. (3.24). It provides the equivalent stiffness for the section to be used in the subsequent 1D analysis (step 7) and recovery of the strains (step 8). The procedure solution of Pascal polynomial method is demonstrated in Fig. (3.5).

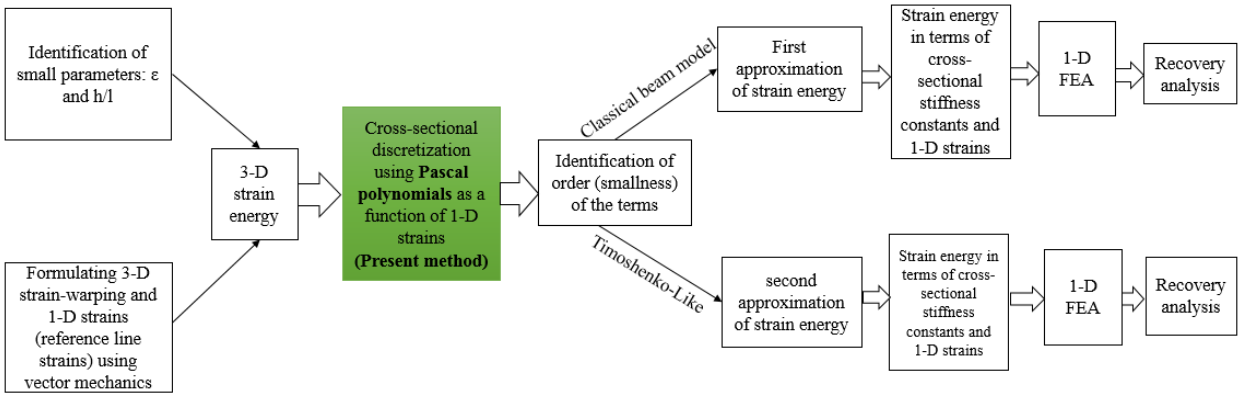

Fig. (3.5). Pascal polynomial method solution procedure.

For composite beams of circular sections consisting of many layers such as that shown in Fig. (3.5), the procedure to discretize the section using VABS is complex. The cross-section modeling procedure includes: *a*) Defining two laminate sections as upper and lower laminate sections (the upside of the horizontal solid line is the upper laminate section and downside is the lower laminate section) as shown in Fig. (3.6a), *b*) Decomposing each laminated section into segments and defining the lamination direction based on the defined mold lines (Fig. (3.6b)), *c*) Generating areas of each layer (Fig. (3.6c)), *d*) Meshing the areas over the cross-section using triangular or quadrilateral elements (Fig. **(**3.6d)).

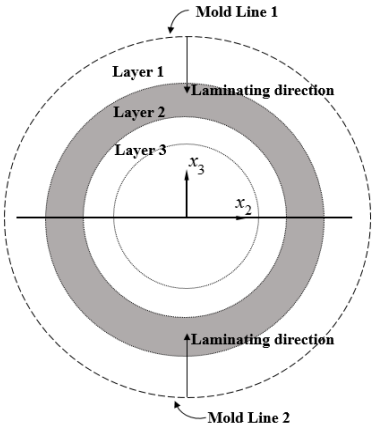

a) Cross-sectional modeling of a tube.

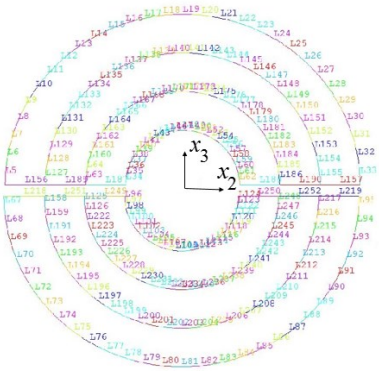

b) Segments of the laminated section.

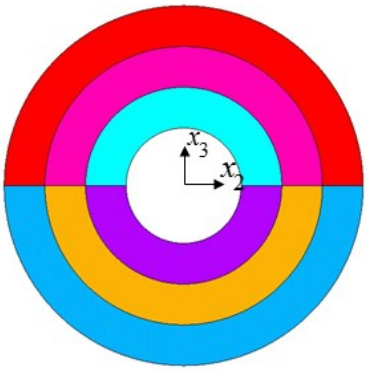

c) Area of each layer.

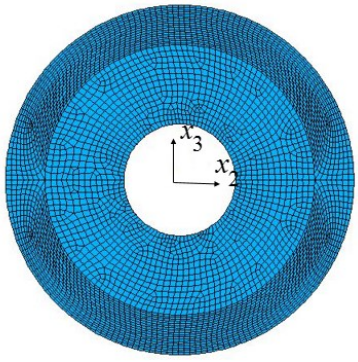

d) The generated mesh of the cross-section.

Fig. (3.6) Discretization procedure in VABS.

The modeling process of the circular cross-section in the VABS is time-consuming, particularly for parametric study. The analysis of composite circular cross-section can be more straightforward and faster using polynomial based method.

Note that in Eq. (3.19), the first equality expresses the strain energy in terms of the 3D strains, and the second equality expresses the strain energy in terms of the warping functions *w*, its derivative with respect to the axis x_1 ($\boldsymbol{w}'$), and the 1D strains of the reference line. For the analysis of composite tube, a cylindrical coordinate system is introduced. Fig. (3.2) shows the beam Cartesian coordinates (x_1, x_2, and x_3) located on the centroid of the cross-section, material coordinates (e_1, e_2, and e_3) where e_1 is along the fiber direction, and the beam reference line. The position of an arbitrary point in the cross-section is shown by a radial position ρ and a circumferential angle θ in the polar coordinate system. α represents the fiber orientation angle in its plane (winding angle). The cross-section of a single-layered tube with the inner and outer radius of ρ_{in} and ρ_{out}, respectively. The angle β denotes the layer orientation to axis x_2. A relation between [*C*] and [*D*] is required. This is done through two coordinate transformations. In the first transformation, the axis e_1 is rotated by an angle α to coincide with x_1. The transformation matrix $[T_\alpha]$ is given as Eq. (3.22) at the end of this rotation, the axes e_2, e_3 become e_2', e_3' and these may not coincide with the axes x_2, x_3. The angle β between the axis e_2' and x_2 which takes into account the orientation of the layer is used. A rotation of the axis e_2' by angle β to coincide with axis x_2 is done through a rotation matrix $[T_\beta]$ as shown in Eq. (3.23). As such one has

$$[D] = [T_\beta]^{-1}[T_\alpha]^{-1}[C][T_\alpha]^{-T}[T_\beta]^{-T} \tag{3.67}$$

The relation between the circumferential angle and layer orientation can be introduced by a change of variable as $\beta = \theta - \frac{\pi}{2}$. In the discretization of warping field of Eq. (3.24) used by VABS, the function $[W(x_2, x_3)]$ consists of FE shape functions, and the vector $\boldsymbol{V}$ is a column matrix of the nodal values of the warping displacement over the cross-section, [40]. In the proposed Pascal polynomial approach, $w_k(x_1, x_2, x_3)$ is proposed to be a simple polynomial as

$$\begin{aligned} w_k(x_1, x_2, x_3) = {} & a_1 + a_2 x_2 + a_3 x_3 + a_4 x_2^2 + a_5 x_2 x_3 + a_6 x_3^2 + a_7 x_2^3 + a_8 x_2^2 x_3 \\ & + a_9 x_2 x_3^2 + a_{10} x_3^3 + a_{11} x_2^4 + a_{12} x_2^3 x_3 + a_{13} x_2^2 x_3^2 + a_{14} x_2 x_3^3 + a_{15} x_3^4 \end{aligned} \tag{3.68}$$

where, k =1, 2, 3. w_k can be expressed in the vector form as

$$w_k = \lfloor 1 \; x_2 \; \ldots \; x_2 x_3^3 \; x_3^4 \rfloor . [a_1 \; a_2 \ldots a_{14} \; a_{15}]^{\mathrm{T}} \tag{3.69}$$

The cross-sectional discretization in the polynomial method would be as follows.

$$w_k(x_1, x_2, x_3) = \boldsymbol{W_k}(x_2, x_3)\boldsymbol{V_k}(x_1) \tag{3.70}$$

where the vector $\boldsymbol{V_k}$ consists of unknown Pascal coefficients a_i which is a function of axial coordinate and should be determined. The Pascal polynomials as the warping functions are used for the whole section and the strain energy will be minimized with respect to a vector of coefficients $\boldsymbol{V_k}(x_1)$. It should be pointed out that in VABS which applies FE, the warping at the common nodes at the interface between layers must set be to the same value, while in the Pascal polynomial method, the warping functions will be considered for the whole domain so that the problem of continuity of warping at the interfaces will be ensured. Using the polar coordinates, the transformation can be as $x_2 = \rho\cos(\theta)$ and $x_3 = \rho\sin(\theta)$. For polynomial with order *m* (*i.e. m* = 4), we have

$$\begin{aligned}\boldsymbol{W} = [1 \quad & \rho\cos(\theta) \quad \rho\sin(\theta) \quad \rho^2\cos^2(\theta) \quad \rho^2\cos(\theta)\sin(\theta) \quad \rho^2\sin^2(\theta) \\ & \rho^3\cos^3(\theta) \quad \rho^3\cos(\theta)\sin^2(\theta) \quad \rho^3\cos^2(\theta)\sin(\theta) \quad \rho^3\sin^3(\theta) \quad \rho^4\cos^4(\theta) \\ & \rho^4\cos(\theta)\sin^3(\theta) \quad \rho^4\cos^3(\theta)\sin(\theta) \quad \rho^4\cos^2(\theta)\sin^2(\theta) \quad \rho^4\sin^4(\theta)]\end{aligned} \tag{3.71}$$

and,

$$\boldsymbol{V_k}(x_1) = a(x_1) \tag{3.72}$$

The order of the polynomial can determine the accuracy of solution. A large number of layers will require higher polynomial order to assure accuracy. From Eq. (4), $w = [w_1 \; w_2 \; w_3]^T$, the matrix form for the warping function is

$$\begin{Bmatrix} w_1 \\ w_2 \\ w_3 \end{Bmatrix} = \begin{bmatrix} [W_1]_{1\times p} & [O]_{1\times p} & [O]_{1\times p} \\ [O]_{1\times p} & [W_2]_{1\times p} & [O]_{1\times p} \\ [O]_{1\times p} & [O]_{1\times p} & [W_3]_{1\times p} \end{bmatrix}_{3\times q} \cdot \begin{Bmatrix} V_1(x_1) \\ V_2(x_1) \\ V_3(x_1) \end{Bmatrix} \equiv [W].\boldsymbol{V}, \; where \; q = 3p \tag{3.73}$$

where, *p* is the number of terms in the polynomial and $O_{1\times p}$ is a null matrix. The relation between the polynomial order *m* and the number of terms in the polynomial is $p = (m^2 + 3m + 2)/2$.

The matrices $[D_{\varepsilon\varepsilon}]$, $[D_{h\varepsilon}]$, $[D_{hh}]$, $[D_{hl}]$, $[D_{ll}]$, $[D_{l\varepsilon}]$, $[D_{hR}]$, $[D_{RR}]$, $[D_{R\varepsilon}]$, and $[D_{Rl}]$ for *n* number of layers in the polynomial method for composite tube with *n* number of layers can be expressed as follows.

$$[D_{\varepsilon\varepsilon}]=\int_0^{2\pi}\int_{\rho_{in}}^{\rho_{out}}[\Gamma_\varepsilon]^T[D][\Gamma_\varepsilon]\rho d\rho d\theta=\sum_{i=1}^{n}(\iint_{\Omega_i}[\Gamma_\varepsilon]^T[D^i][\Gamma_\varepsilon]\rho d\rho d\theta)$$

$$[D_{h\varepsilon}]=\int_0^{2\pi}\int_{\rho_{in}}^{\rho_{out}}[\Gamma_h W]^T[D][\Gamma_\varepsilon]\rho d\rho d\theta=\sum_{i=1}^{n}(\iint_{\Omega_i}[\Gamma_h W]^T[D^i][\Gamma_\varepsilon]\rho d\rho d\theta)$$

$$[D_{hh}]=\int_0^{2\pi}\int_{\rho_{in}}^{\rho_{out}}[\Gamma_h W]^T[D][\Gamma_h W]\rho d\rho d\theta=\sum_{i=1}^{n}(\iint_{\Omega_i}[\Gamma_h W]^T[D^i][\Gamma_h W]\rho d\rho d\theta)$$

$$[D_{hl}]=\int_0^{2\pi}\int_{\rho_{in}}^{\rho_{out}}[\Gamma_h W]^T[D][\Gamma_l W]\rho d\rho d\theta=\sum_{i=1}^{n}(\iint_{\Omega_i}[\Gamma_h W]^T[D^i][\Gamma_l W]\rho d\rho d\theta)$$

$$[D_{ll}]=\int_0^{2\pi}\int_{\rho_{in}}^{\rho_{out}}[\Gamma_l W]^T[D][\Gamma_l W]\rho d\rho d\theta=\sum_{i=1}^{n}(\iint_{\Omega_i}[\Gamma_l W]^T[D^i][\Gamma_l W]\rho d\rho d\theta)$$

$$[D_{l\varepsilon}]=\int_0^{2\pi}\int_{\rho_{in}}^{\rho_{out}}[\Gamma_l W]^T[D][\Gamma_\varepsilon]\rho d\rho d\theta=\sum_{i=1}^{n}(\iint_{\Omega_i}[\Gamma_l W]^T[D^i][\Gamma_\varepsilon]\rho d\rho d\theta)$$

$$[D_{hR}]=\int_0^{2\pi}\int_{\rho_{in}}^{\rho_{out}}[\Gamma_h W]^T[D][\Gamma_R W]\rho d\rho d\theta=\sum_{i=1}^{n}(\iint_{\Omega_i}[\Gamma_h W]^T[D^i][\Gamma_R W]\rho d\rho d\theta)$$

$$[D_{RR}]=\int_0^{2\pi}\int_{\rho_{in}}^{\rho_{out}}[\Gamma_R W]^T[D][\Gamma_R W]\rho d\rho d\theta=\sum_{i=1}^{n}(\iint_{\Omega_i}[\Gamma_R W]^T[D^i][\Gamma_R W]\rho d\rho d\theta)$$

$$[D_{R\varepsilon}]=\int_0^{2\pi}\int_{\rho_{in}}^{\rho_{out}}[\Gamma_R W]^T[D][\Gamma_\varepsilon]\rho d\rho d\theta=\sum_{i=1}^{n}(\iint_{\Omega_i}[\Gamma_R W]^T[D^i][\Gamma_\varepsilon]\rho d\rho d\theta)$$

$$[D_{Rl}]=\int_0^{2\pi}\int_{\rho_{in}}^{\rho_{out}}[\Gamma_R W]^T[D][\Gamma_l W]\rho d\rho d\theta=\sum_{i=1}^{n}(\iint_{\Omega_i}[\Gamma_R W]^T[D^i][\Gamma_l W]\rho d\rho d\theta) \quad (3.74)$$

The integrations above over the cross-section are done using Gauss quadrature method. To do so, at first the warping functions which were transferred to polar coordinates are transformed to the Cartesian coordinate using $\rho=\sqrt{x_2^2+x_3^2}$, and $\theta=\tan^{-1}(x_3/x_2)$. Then, the Gauss quadrature method is applied as Eqs. (3.75a) and (3.76).

$$\int_a^b \int_c^d f(x_2) f(x_3) dx_2 dx_3 = \tag{3.75}$$
$$\frac{b-a}{2} \int_{-1}^{1} \int_{-1}^{1} f(\frac{b-a}{2}\xi + \frac{b+a}{2}) f(\frac{d-c}{2}\eta + \frac{d+c}{2}) d\xi d\eta$$

$$\int_a^b \int_c^d f(x_2) f(x_3) dx_2 dx_3 = \tag{3.76}$$
$$\frac{b-a}{2}\frac{d-c}{2} \sum_{i=1}^{n} \sum_{j=1}^{n} \chi_i \chi_j f(\frac{b-a}{2}\xi_i + \frac{b+a}{2}) f(\frac{d-c}{2}\eta_j + \frac{d+c}{2})$$

where, $a = -\rho_i, b = \rho_i, c = -\sqrt{\rho_i^2 - x_2^2}, d = \sqrt{\rho_i^2 - x_2^2}$. This integration calculation is done for inner and outer radiuses of each layer and then they are subtracted to calculate the final values of integration over cross-section of each layer. ρ_i can be inner and outer radius of *i*th layer. The weight and abscissae for *n*=10 are shown in the Table (3.1).

Table (3.1). Weight and Abscissae for *n*=10

i	Weight (χ_i)	Abscissa (ξ_i, η_i)
1	0.2955242247147529	-0.1488743389816312
2	0.2955242247147529	0.1488743389816312
3	0.2692667193099963	-0.4333953941292472
4	0.2692667193099963	0.4333953941292472
5	0.2190863625159820	-0.6794095682990244
6	0.2190863625159820	0.6794095682990244
7	0.1494513491505806	-0.8650633666889845
8	0.1494513491505806	0.8650633666889845
9	0.0666713443086881	-0.9739065285171717
10	0.0666713443086881	0.9739065285171717

The use of VAM and VABS can greatly reduce the computational time and efforts for beams or tubes with complex cross-section, [49]. For tubular composites with a large number of layers, the use of Pascal polynomial simplifies the input data and provides better insight into the problem.

3.3 Conclusion

In this chapter, the cross-sectional analysis for initially curved anisotropic beams based on VAM is brought in. A finite element discretization is introduced for solving 2D minimization problem. The minimization problem is generated by application of VAM, which enables the solution of

problems related to functionals when there are small parameters. The use of VAM produces a model that has derivatives of classical 1D generalized strain measures (extension, twist and bending).

Then the Pascal polynomial dimensional reduction method is introduced. The Pascal polynomials are applied to the warping field and the cross-sectional discretization is performed. For beams with tubular cross-section, the polynomials are transformed to the polar coordinate system. The present method does not need to generate mesh where in the VABS one needs to generate mesh and model the tubular cross-section of the tube. It is noted that the order of polynomial has effect on the accuracy of the solution.

4 Chapter 4: Pascal polynomial dimensional reduction method for straight tubes

In this chapter, the polynomial based dimensional reduction method for analysis of straight composite tubes with circular cross-section is developed. The dimensional reduction procedure of chapter 3 is reduced for the case of straight tubes. A simple example of the meshless Pascal polynomial based dimensional reduction method is introduced for unidirectional tubes. Then, the polynomial based solution is provided for tubes in the general case of tubes with arbitrary lay-up. Finally, a 1D FE solution is developed for determining transverse deflection of composite tubes under four-point bending loading. Next, the numerical results and discussion are represented for validation of the present method for composite tubes and compared with ANSYS 3D, VABS, literature and experiment.

4.1 Strain energy of a straight tube

Consider a composite beam with a circular cross-section. The orthonormal coordinates x_1, x_2 and x_3 are considered for the undeformed beam cross-section, Fig. (4.1). A polar coordinate is defined where ρ is the radius and θ is the circumferential angle over the cross-section. The origin of the coordinate is located at the centroid of the cross-section. At a point on the circle, the tangent at the point makes an angle β with respect to the horizontal axis x_2. The strain energy of a straight beam with the cross-section area Ω is expressed as follows [40].

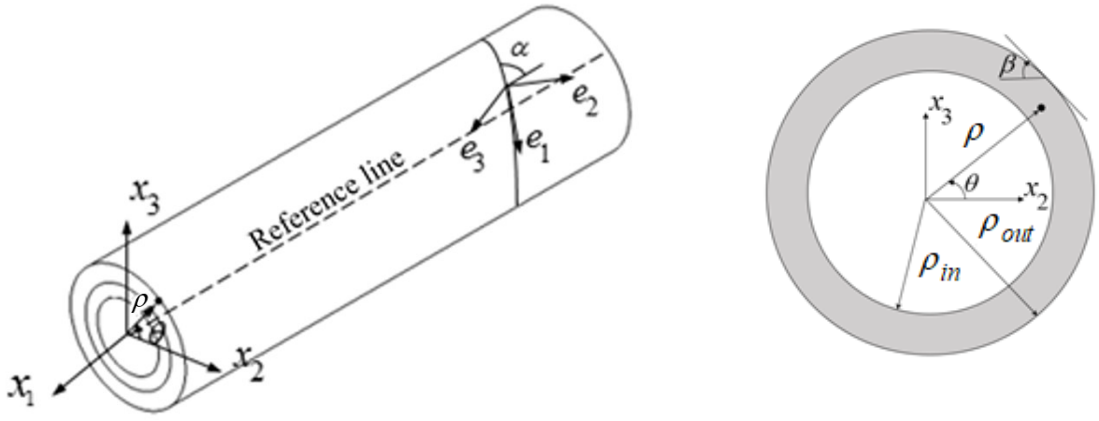

a) *b*)

Fig. (4.1). *a*) Coordinate systems of a composite tubular beam, *b*) The layer orientation of (β) in the circumference of a one-layer tube with inner and outer radius ρ_{in} and $\rho_{out.}$

$$
\begin{aligned}
2U &= \int_L \iint_\Omega [\boldsymbol{\Gamma}]^T [D][\boldsymbol{\Gamma}] dx_2 dx_3 dx_1 \\
&= \int_L \iint_\Omega ([\Gamma_h]\boldsymbol{w} + [\Gamma_\varepsilon]\bar{\boldsymbol{\varepsilon}} + [\Gamma_l]\boldsymbol{w}')^T [D]([\Gamma_h]\boldsymbol{w} + [\Gamma_\varepsilon]\bar{\boldsymbol{\varepsilon}} + [\Gamma_l]\boldsymbol{w}') dx_2 dx_3 dx_1
\end{aligned} \tag{4.1}
$$

The strain field $\boldsymbol{\Gamma} = [\Gamma_{11}\ \ 2\Gamma_{12}\ \ 2\Gamma_{13}\ \ \Gamma_{22}\ \ 2\Gamma_{23}\ \ \Gamma_{33}]^T$ for a straight beam can be expressed as follows, [49].

$$
\boldsymbol{\Gamma} = [\Gamma_h]\boldsymbol{w} + [\Gamma_\varepsilon]\bar{\boldsymbol{\varepsilon}} + [\Gamma_l]\boldsymbol{w}' \tag{4.2}
$$

where, the 1D strains of the reference line $\bar{\varepsilon}$ can be expressed in terms of $\bar{\gamma}_{11}$ (the extensional strain), $\bar{\kappa}_1$ (twist per unit length), $\bar{\kappa}_2$ and $\bar{\kappa}_3$ (bending curvatures of the reference axis of the beam about x_2 and x_3, respectively), as the following

$$
\bar{\boldsymbol{\varepsilon}} = \begin{bmatrix} \bar{\gamma}_{11} & \bar{\kappa}_1 & \bar{\kappa}_2 & \bar{\kappa}_3 \end{bmatrix}^T \tag{4.3}
$$

Moreover, $(\bullet)'$ stands for derivative with respect to x_1. The operators $[\Gamma_h]$, $[\Gamma_\varepsilon]$ and $[\Gamma_l]$ are expressed in Eq. (3.18) with $k_2 = k_3 = 0$. The warping displacements of the cross-section of the beam are defined as the following vector.

$$
\boldsymbol{w} = [w_1\ \ w_2\ \ w_3]^T \tag{4.4}
$$

where w_1 represents the warping displacement of the cross-section in direction x_1 (out-of-plane) and w_2 and w_3 are in-plane warping displacements of an arbitrary point in directions x_2 and x_3 (in-plane), respectively. The calculated warping functions in terms of 1D strains of reference line of the beam results in transformation of 3D model into a 1D beam model which maintains the 3D effects. Using the 3D strain field above, the dimensional reduction process can be performed. The material stiffness matrix [D] which carries the information of material property and fiber orientation and layer orientation as follows. The matrices $[T_\beta]$, $[T_\alpha]$, and $[C]$ are introduced in Eq. (3.20).

$$
[D] = [T_\beta]^{-1}[T_\alpha]^{-1}[C][T_\alpha]^{-T}[T_\beta]^{-T} \tag{4.5}
$$

4.2 Example of pascal polynomial dimensional reduction method for a straight unidirectional circular tube

In this section, we use the Pascal polynomial based dimensional reduction method and we will arrive at the strain energy of the Classical beam model. The cross-sectional stiffness constants of the unidirectional straight tubular section based on Classical beam model will be determined. Then, the polynomial based dimensional reduction method for straight tubes will be demonstrated. The strain energy of the Eq. (5.18) for an orthotropic beam can be written in the following form.

$$
\begin{aligned}
2U = \int_L \iint_\Omega \Bigg(& \left(A_1 D_{11} + A_2 D_{21} + A_3 D_{31} + \frac{\partial w_2}{\partial x_2} D_{41} + \left(\frac{\partial w_2}{\partial x_3} + \frac{\partial w_3}{\partial x_2} \right) D_{51} + \frac{\partial w_3}{\partial x3} D_{61} \right) A_1 \\
& + \left(A_1 D_{12} + A_2 D_{22} + A_3 D_{32} + \frac{\partial w_2}{\partial x_2} D_{42} + \left(\frac{\partial w_2}{\partial x_3} + \frac{\partial w_3}{\partial x_2} \right) D_{52} + \frac{\partial w_3}{\partial x_3} D_{62} \right) A_2 \\
& + \left(A_1 D_{13} + A_2 D_{23} + A_3 D_{33} + \frac{\partial w_2}{\partial x_2} D_{43} + \left(\frac{\partial w_2}{\partial x_3} + \frac{\partial w_3}{\partial x_2} \right) D_{53} + \frac{\partial w_3}{\partial x_3} D_{63} \right) A_3 \\
& + \left(A_1 D_{14} + A_2 D_{24} + A_3 D_{34} + \frac{\partial w_2}{\partial x_2} D_{44} + \left(\frac{\partial w_2}{\partial x_3} + \frac{\partial w_3}{\partial x_2} \right) D_{54} + \frac{\partial w_3}{\partial x_3} D_{64} \right) \frac{\partial w_2}{\partial x_2} \\
& + \left(A_1 D_{15} + A_2 D_{25} + A_3 D_{35} + \frac{\partial w_2}{\partial x_2} D_{45} + \left(\frac{\partial w_2}{\partial x_3} + \frac{\partial w_3}{\partial x_2} \right) D_{55} + \frac{\partial w_3}{\partial x_3} D_{65} \right) \left(\frac{\partial w_2}{\partial x_3} + \frac{\partial w_3}{\partial x_2} \right) \\
& + \left(A_1 D_{16} + A_2 D_{26} + A_3 D_{36} + \frac{\partial w_2}{\partial x_2} D_{46} + \left(\frac{\partial w_2}{\partial x_3} + \frac{\partial w_3}{\partial x_2} \right) D_{56} + \frac{\partial w_3}{\partial x_3} D_{66} \right) \frac{\partial w_3}{\partial x_3} \Bigg) dx_3 dx_2 dx_1
\end{aligned}
\tag{4.6a}
$$

where,

$$
\begin{aligned}
A_1 &= \bar{\gamma}_{11} + x_3 \bar{\kappa}_2 - x_2 \bar{\kappa}_3 + \frac{\partial w_1}{\partial x_1} + x_3 \frac{\partial w_1}{\partial x_2} - x_2 \frac{\partial w_1}{\partial x_3} \\
A_2 &= \frac{\partial w_1}{\partial x_2} - (x_3 \bar{\kappa}_1 + \frac{\partial w_2}{\partial x_1} + x_3 \frac{\partial w_2}{\partial x_2} - x_2 \frac{\partial w_2}{\partial x_3}) \\
A_3 &= \frac{\partial w_1}{\partial x_3} + (x_2 \bar{\kappa}_1 + \frac{\partial w_3}{\partial x_1} + x_3 \frac{\partial w_3}{\partial x_2} - x_2 \frac{\partial w_3}{\partial x_2})
\end{aligned}
\tag{4.6b}
$$

In the dimensional reduction method, three characteristic parameters are introduced. The characteristic size of domain Ω is denoted by h. $\varepsilon_{\max}$ is the maximum of the 1D strain vector and L is the characteristic length of the beam, [46]. According to the VAM, we now consider the perturbation in the warping field using the small parameter of the problem as follows.

$$w_1 = w_{10} + w_{11};\ w_2 = w_{20} + w_{21};\ w_3 = w_{30} + w_{31}$$
$$\varepsilon_{\max} \quad \varepsilon_{\max}\frac{h}{L} \qquad \varepsilon_{\max} \quad \varepsilon_{\max}\frac{h}{L} \qquad \varepsilon_{\max} \quad \varepsilon_{\max}\frac{h}{L}$$

$$\frac{\partial w_1}{\partial x_i} = \frac{\partial w_{10}}{\partial x_i} + \frac{\partial w_{11}}{\partial x_i};\ \frac{\partial w_2}{\partial x_i} = \frac{\partial w_{20}}{\partial x_i} + \frac{\partial w_{21}}{\partial x_i};\ \frac{\partial w_3}{\partial x_i} = \frac{\partial w_{30}}{\partial x_i} + \frac{\partial w_{31}}{\partial x_i} \qquad i=2,3 \tag{4.7}$$
$$\varepsilon_{\max} \quad \varepsilon_{\max}\frac{h}{L} \qquad \varepsilon_{\max} \quad \varepsilon_{\max}\frac{h}{L} \qquad \varepsilon_{\max} \quad \varepsilon_{\max}\frac{h}{L}$$

$$\frac{\partial w_1}{\partial x_1} = \frac{\partial w_{10}}{\partial x_1} + \frac{\partial w_{11}}{\partial x_1};\ \frac{\partial w_2}{\partial x_1} = \frac{\partial w_{20}}{\partial x_1} + \frac{\partial w_{21}}{\partial x_1};\ \frac{\partial w_3}{\partial x_1} = \frac{\partial w_{30}}{\partial x_1} + \frac{\partial w_{31}}{\partial x_1}$$
$$\varepsilon_{\max}\frac{h}{L} \quad \varepsilon_{\max}(\frac{h}{L})^2 \qquad \varepsilon_{\max}\frac{h}{L} \quad \varepsilon_{\max}(\frac{h}{L})^2 \qquad \varepsilon_{\max}\frac{h}{L} \quad \varepsilon_{\max}(\frac{h}{L})^2$$

Substituting the Eq. (4.7) into Eq. (4.6) and selecting the order $O(\varepsilon_{\max}^2)$, one can obtain first approximation of the strain energy of an orthotropic beam as follows.

$$\begin{aligned}
2U_0 = \int_L\int_\Omega\int\Bigg(&\left(\frac{\partial w_{10}}{\partial x_2}D_{22} + \frac{\partial w_{10}}{\partial x_3}D_{32} + \frac{\partial w_{20}}{\partial x_2}D_{42} + \left(\frac{\partial w_{20}}{\partial x_3} + \frac{\partial w_{30}}{\partial x_2}\right)D_{52} + \frac{\partial w_{30}}{\partial x_3}D_{62}\right)\frac{\partial w_{10}}{\partial x_2} + \left(\frac{\partial w_{10}}{\partial x_2}D_{23} + \frac{\partial w_{10}}{\partial x_3}D_{33} + \frac{\partial w_{20}}{\partial x_2}D_{43}\right.\\
&\left. + \left(\frac{\partial w_{20}}{\partial x_3} + \frac{\partial w_{30}}{\partial x_2}\right)D_{53} + \frac{\partial w_{30}}{\partial x_3}D_{63}\right)\frac{\partial w_{10}}{\partial x_3} + \left(\frac{\partial w_{10}}{\partial x_2}D_{24} + \frac{\partial w_{10}}{\partial x_3}D_{34} + \frac{\partial w_{20}}{\partial x_2}D_{44} + \left(\frac{\partial w_{20}}{\partial x_3} + \frac{\partial w_{30}}{\partial x_2}\right)D_{54} + \frac{\partial w_{30}}{\partial x_3}D_{64}\right)\frac{\partial w_{20}}{\partial x_2}\\
&+ \left(\frac{\partial w_{10}}{\partial x_2}D_{25} + \frac{\partial w_{10}}{\partial x_3}D_{35} + \frac{\partial w_{20}}{\partial x_2}D_{45} + \left(\frac{\partial w_{20}}{\partial x_3} + \frac{\partial w_{30}}{\partial x_2}\right)D_{55} + \frac{\partial w_{30}}{\partial x_3}D_{65}\right)\left(\frac{\partial w_{20}}{\partial x_3} + \frac{\partial w_{30}}{\partial x_2}\right) + \left(\frac{\partial w_{10}}{\partial x2}D_{26} + \frac{\partial w_{10}}{\partial x_3}D_{36} + \frac{\partial w_{20}}{\partial x_2}D_{46}\right.\\
&\left. + \left(\frac{\partial w_{20}}{\partial x_3} + \frac{\partial w_{30}}{\partial x_2}\right)D_{56} + \frac{\partial w_{30}}{\partial x3}D_{66}\right)\frac{\partial w_{30}}{\partial x_3} + \left(2\frac{\partial w_{10}}{\partial x_2}D_{21} + 2\frac{\partial w_{10}}{\partial x_3}D_{31} + 2\frac{\partial w_{20}}{\partial x_2}D_{41} + \left(2\frac{\partial w_{20}}{\partial x_3} + 2\frac{\partial w_{30}}{\partial x_2}\right)D_{51} + 2\frac{\partial w_{30}}{\partial x_3}D_{61}\right)\\
&\left(\gamma_{11} + x_3\bar{\kappa}_2 - x_2\bar{\kappa}_3\right) - \left(2\frac{\partial w_{10}}{\partial x_2}D_{22} + 2\frac{\partial w_{10}}{\partial x_3}D_{32} + 2\frac{\partial w_{20}}{\partial x_2}D_{42} + \left(2\frac{\partial w_{20}}{\partial x_3} + 2\frac{\partial w_{30}}{\partial x_2}\right)D_{52} + 2\frac{\partial w_{30}}{\partial x_3}D_{62}\right) + \left(2\frac{\partial w_{10}}{\partial x_2}D_{23}\right.\\
&\left. + 2\frac{\partial w_{10}}{\partial x_3}D_{33} + 2\frac{\partial w_{20}}{\partial x_2}D_{43} + \left(2\frac{\partial w_{20}}{\partial x_3} + 2\frac{\partial w_{30}}{\partial x_2}\right)D_{53} + 2\frac{\partial w_{30}}{\partial x_3}D_{63}\right)x_2\bar{\kappa}_1 + \left(\gamma_{11} + x_3\bar{\kappa}_2 - x_2\bar{\kappa}_3\right)D_{11} - \frac{1}{\sqrt{\lambda}}x_3\bar{\kappa}_1D_{21}\\
&+ x_2\bar{\kappa}_1D_{31} + \left(\gamma_{11} + x_3\bar{\kappa}_2 - x_2\bar{\kappa}_3\right)D_{11} - x_3\bar{\kappa}_1D_{21} + x_2\bar{\kappa}_1D_{31}\Bigg)dx_3dx_2dx_1
\end{aligned} \tag{4.8}$$

The Pascal polynomials are introduced to each component of the warping functions.

$$\begin{aligned}
w_{10}(x_1,x_2,x_3) &= a_1(x_1) + a_2(x_1)x_2 + a_3(x_1)x_3 + a_4(x_1)x_2^2 + a_5(x_1)x_3x_2 + a_6(x_1)x_3^2\\
w_{20}(x_1,x_2,x_3) &= a_7(x_1) + a_8(x_1)x_2 + a_9(x_1)x_3 + a_{10}(x_1)x_2^2 + a_{11}(x_1)x_3x_2 + a_{12}(x_1)x_3^2\\
w_{30}(x_1,x_2,x_3) &= a_{13}(x_1) + a_{14}(x_1)x_2 + a_{15}(x_1)x_3 + a_{16}(x_1)x_2^2 + a_{17}(x_1)x_3x_2 + a_{18}(x_1)x_3^2
\end{aligned} \tag{4.9}$$

We consider the material properties for a unidirectional tube as, [82]

$$\begin{aligned}
&E_1 = E_t; E_2 = E_3 = E_p; \nu_{12} = \nu_{13} = \nu_{tp}; \nu_{21} = \nu_{12}E_2 / E_1; \nu_{23} = \nu_p;\\
&\nu_{32} = \nu_{23}E_3 / E_2; \nu_{31} = \nu_{13}E_3 / E_1; G_{12} = G_{13} = G_t; G_{23} = G_p
\end{aligned} \tag{4.10}$$

where, $G_p = \dfrac{E_p}{2(1+\nu_p)}$ and p stands for "in-plane" and t strands for "transverse". It can be shown that for the case of tubes made by unidirectional composites (fibers oriented along the axis of the tube), [D] = [C]. Substituting Eq. (4.8) into Eq. (4.9), we have:

$$
\begin{aligned}
2U_0 = \int_L \iint_\Omega \Bigg(& \left(\frac{(\bar{\kappa}_2 x_3 - \bar{\kappa}_3 x_2 + \bar{\gamma}_{11}) E_t^2 (\nu_p - 1)}{A_4} - \frac{(2a_{10}x_2 + a_{11}x_3 + a_8) E_p E_t \nu_{tp}}{A_5} - \frac{(a17 x_2 + 2a_{18}x_3 + a_{15}) E_p E_t \nu_{tp}}{A_5} \right) \\
& (\bar{\kappa}_2 x_3 - \bar{\kappa}_3 x_2 + \bar{\gamma}_{11}) + (-\bar{\kappa}_1 x_3 + 2a_4 x_2 + a_5 x_3 + a_2)^2 G_t + (\bar{\kappa}_1 x_2 + a_5 x_2 + 2a_6 x_3 + a_3)^2 G_t \\
& + \left(-\frac{(\bar{\kappa}_2 x_3 - \bar{\kappa}_3 x_2 + \bar{\gamma}_{11}) E_p E_t \nu_{tp}}{A_5} + \frac{(2a_{10}x_2 + a_{11}x_3 + a_8) E_p (\nu_{tp}^2 E_p - E_t)}{A_6} - \frac{(a_{17}x_2 + 2a_{18}x_3 + a_{15}) E_p (\nu_{tp}^2 E_p + \nu_p E_t)}{A_6} \right) \\
& (2a_{10}x_2 + a_{11}x_3 + a_8) + \frac{(a_{11}x_2 + 2a_{12}x_3 + 2a_{16}x_2 + a_{17}x_3 + a_{14} + a_9)^2 E_p}{2(\nu_p + 1)} \\
& + \left(-\frac{(\bar{\kappa}_2 x_3 - \bar{\kappa}_3 x_2 + \bar{\gamma}_{11}) E_p E_t \nu_{tp}}{A_5} - \frac{(2a_{10}x_2 + a_{11}x_3 + a_8) E_p (\nu_{tp}^2 E_p + \nu_p E_t)}{A_6} + \frac{(a_{17}x_2 + 2a_{18}x_3 + a_{15}) E_p (\nu_{tp}^2 E_p - E_t)}{A_6} \right) \\
& (a_{17}x_2 + 2a_{18}x_3 + a_{15}) \Bigg) dx_3 dx_2 dx_1
\end{aligned}
\tag{4.11a}
$$

where,

$$
\begin{aligned}
A_4 &= (\nu_p - 1) E_t + 2\nu_{tp}^2 E_p \\
A_5 &= 2\nu_{tp}^2 E_p + \nu_p E_t - E_t \\
A_6 &= 2(E_p \nu_p + E_p)\nu_{tp}^2 + E_t \nu_p^2 - E_t
\end{aligned}
\tag{4.11b}
$$

We perform the change of variables to polar coordinates as ($x_2 = \rho cos\theta, x_3 = \rho sin\theta$) for Eq. (4.11). The integration of Eq. (4.11) in polar coordinates leads to an equation in terms of the Pascal coefficients a_i and (i=1..18). The procedure of VAM is to minimize the obtained strain energy with respect to unknown warping. So, the strain energy is minimized with respect to each Pascal coefficient as

$$
\frac{\partial U_0}{\partial a_i} = 0, \; i=1..18 \tag{4.12}
$$

The Eq. (4.12), leads to a system of algebraic equations with nine equations and nine variables. Substituting the obtained coefficients into the strain energy, one can obtain the final strain energy with the polynomial order of (m=2) as follows.

$$
\begin{aligned}
2U_0 = {} & \frac{\pi}{2\nu_{tp}^2 E_p \nu_p + 2\nu_{tp}^2 E_p + E_t \nu_p^2 - E_t} (2\bar{\gamma}_{11}^2 \nu_{tp}^2 \rho_{in}{}^2 E_p E_t \nu_p - 2\bar{\gamma}_{11}^2 \nu_{tp}^2 \rho_{out}{}^2 E_p E_t \nu_p \\
& + \frac{1}{2}\bar{\kappa}_2{}^2 \nu_{tp}^2 \rho_{in}{}^4 E_p E_t \nu_p - \frac{1}{2}\bar{\kappa}_2{}^2 \nu_{tp}^2 \rho_{out}{}^4 E_p E_t \nu_p + \frac{1}{2}\bar{\kappa}_3{}^2 \nu_{tp}^2 \rho_{in}{}^4 E_p E_t \nu_p - \frac{1}{2} K3^2 \nu_{tp}^2 \rho_{out}{}^4 E_p E_t \nu_p \\
& + \bar{\kappa}_1{}^2 \rho_{in}{}^4 E_p G_t \nu_p \nu_{tp}^2 - \bar{\kappa}_1{}^2 \rho_{out}{}^4 E_p G_t \nu_p \nu_{tp}^2 - \frac{1}{2}\bar{\kappa}_1{}^2 \rho_{in}{}^4 E_t G_t + \frac{1}{2}\bar{\kappa}_1{}^2 \rho_{out}{}^4 E_t G_t + \frac{1}{4}\bar{\kappa}_2{}^2 \rho_{in}{}^4 E_t^2 \nu_p^2 \\
& - \frac{1}{4}\bar{\kappa}_2{}^2 \rho_{out}{}^4 E_t^2 \nu_p^2 + \frac{1}{4}\bar{\kappa}_3{}^2 \rho_{in}{}^4 E_t^2 \nu_p^2 - \frac{1}{4}\bar{\kappa}_3{}^2 \rho_{out}{}^4 E_t^2 \nu_p^2 + \bar{\gamma}_{11}{}^2 \rho_{in}{}^2 E_t^2 \nu_p^2 - \bar{\gamma}_{11}{}^2 \rho_{out}{}^2 E_t^2 \nu_p^2 \\
& + \frac{1}{4}\bar{\kappa}_2{}^2 \rho_{out}{}^4 E_t^2 + \bar{\gamma}_{11}{}^2 \rho_{out}{}^2 E_t^2 - \bar{\gamma}_{11}{}^2 \rho_{in}{}^2 E_t^2 - \frac{1}{4}\bar{\kappa}_2{}^2 \rho_{in}{}^4 E_t^2 + 2\bar{\gamma}_{11}{}^2 \nu_{tp}^2 \rho_{in}{}^2 E_p E_t - 2\bar{\gamma}_{11}{}^2 \nu_{tp}^2 \rho_{out}{}^2 E_p E_t \\
& + \frac{1}{4}\bar{\kappa}_3{}^2 \rho_{out}{}^4 E_t^2 - \frac{1}{4}\bar{\kappa}_3{}^2 \rho_{in}{}^4 E_t^2 + \bar{\kappa}_1{}^2 \rho_{in}{}^4 E_p G_t \nu_{tp}^2 + \frac{1}{2}\bar{\kappa}_1{}^2 \rho_{in}{}^4 E_t G_t \nu_p^2 - \bar{\kappa}_1{}^2 \rho_{out}{}^4 E_p G_t \nu_{tp}^2 \\
& - \frac{1}{2}\bar{\kappa}_1{}^2 \rho_{out}{}^4 E_t G_t \nu_p^2 + \frac{1}{2}\bar{\kappa}_2{}^2 \nu_{tp}^2 \rho_{in}{}^4 E_p E_t - \frac{1}{2}\bar{\kappa}_2{}^2 \nu_{tp}^2 \rho_{out}{}^4 E_p E_t + \frac{1}{2}\bar{\kappa}_3{}^2 \nu_{tp}^2 \rho_{in}{}^4 E_p E_t \\
& - \frac{1}{2}\bar{\kappa}_3{}^2 \nu_{tp}^2 \rho_{out}{}^4 E_p E_t)
\end{aligned}
\tag{4.13}
$$

Selecting the coefficients of $\bar{\gamma}_{11}{}^2$ results in $\bar{S}_{11}$ (extensional stiffness) , coefficients of $\bar{\kappa}_1{}^2, \bar{\kappa}_2{}^2,$ and $\bar{\kappa}_3{}^2$ lead to $\bar{S}_{22}$ (torsional stiffness), $\bar{S}_{33}$ (bending stiffness about x_2) and $\bar{S}_{44}$ (bending stiffness about x_3), respectively as Eq. (4.14).

$$
\bar{S}_{11} = \pi E_1(\rho_{out}^2 - \rho_{in}^2);\ \bar{S}_{22} = \frac{\pi}{2}(\rho_{out}^4 - \rho_{in}^4);\ \bar{S}_{33} = \frac{\pi}{4} E_1(\rho_{out}^4 - \rho_{in}^4);\ \bar{S}_{44} = \frac{\pi}{4} E_1(\rho_{out}^4 - \rho_{in}^4) \tag{4.14}
$$

4.3 General case: circular tubular cross-section with arbitrary lamination [79]

For a composite circular tube with arbitrary fiber angle and arbitrary number of layers, we use matrix notation. In the dimensional reduction method, the strain energy is minimized with respect to the unknown warping functions to find the warping field in terms of 1D strains of the reference line of the beam. The warping field $\boldsymbol{w}$ is approximated by the Pascal polynomials as follows.

$$
w_k(x_1, x_2, x_3) = [W(x_2, x_3)]\boldsymbol{V}_k(x_1) \tag{4.15}
$$

where,

$$
W(x_2, x_3) = [W_1 \quad \ldots \quad W_n],\ \boldsymbol{V}_k = [V_0^k \quad V_1^k \quad \ldots \quad V_n^k]^T,\ k = 1, 2, 3 \tag{4.16}
$$

$W(x_2, x_3)$ includes Pascal polynomials and $\boldsymbol{V}_k(x_1)$ consists of unknown coefficients which is a function of axial coordinate and should be determined. It should be pointed out that the warping functions are used for the whole section so that the strain energy will be minimized with respect

to a vector of coefficients $\boldsymbol{V}(x_1)$. For the case of cross-section, the Pascal polynomials will be transformed to polar coordinates by changing variables as ($x_2 = \rho cos\theta, x_3 = \rho sin\theta$). For the polynomial order four ($m = 4$), the warping functions can be described as

$$[W(r,\theta)] = \begin{bmatrix} W_{1\times p} & O_{1\times p} & O_{1\times p} \\ O_{1\times p} & W_{1\times p} & O_{1\times p} \\ O_{1\times p} & O_{1\times p} & W_{1\times p} \end{bmatrix}_{3\times q}, \text{ where } q = 3p$$

$$\begin{aligned} W = [1 \quad & \rho\cos(\theta) \quad \rho\sin(\theta) \quad \rho^2\cos^2(\theta) \quad \rho^2\cos(\theta)sin(\theta) \\ & \rho^2\sin^2(\theta) \quad \rho^3\cos^3(\theta) \quad \rho^3\cos(\theta)\sin^2(\theta) \quad \rho^3\cos^2(\theta)\sin(\theta) \\ & \rho^3\sin^3(\theta) \quad \rho^4\cos^4(\theta) \quad \rho^4\cos(\theta)\sin^3(\theta) \quad \rho^4\cos^3(\theta)\sin(\theta) \\ & \rho^4\cos^2(\theta)\sin^2(\theta) \quad \rho^4\sin^4(\theta)] \end{aligned} \tag{4.17}$$

where, p is the number of terms in the polynomial and $O_{1\times p}$ is a null matrix. The number of terms p for a polynomial with an order m is $p = (m^2 + 3m + 2)/2$. The total warping field can be written as Eq. (4.18).

$$\boldsymbol{w}(x_1, r, \theta) = \begin{bmatrix} W_{1\times p} & O_{1\times p} & O_{1\times p} \\ O_{1\times p} & W_{1\times p} & O_{1\times p} \\ O_{1\times p} & O_{1\times p} & W_{1\times p} \end{bmatrix} \begin{Bmatrix} \boldsymbol{V}_1 \\ \boldsymbol{V}_2 \\ \boldsymbol{V}_3 \end{Bmatrix} \tag{4.18}$$

$\boldsymbol{V_1}$, $\boldsymbol{V_2}$ and $\boldsymbol{V_3}$ are the vectors which consist of pascal coefficients. It is noted that the Pascal polynomials are used for the whole section and therefore there is no need to generate mesh for the cross-section of the elliptical beam consisting many layers. The strain energy can be written by substituting the warping function of Eq. (4.18) into Eq. (4.1) as

$$2U = \int_L \left(\bar{\boldsymbol{\varepsilon}}^T [\Lambda_1] \bar{\boldsymbol{\varepsilon}} + \boldsymbol{V}^T [\Lambda_2] \boldsymbol{V} + 2\boldsymbol{V}^T [\Lambda_3] \bar{\boldsymbol{\varepsilon}} + 2\boldsymbol{V}^T [\Lambda_4] \boldsymbol{V}' + 2\boldsymbol{V}'^T [\Lambda_5] \bar{\boldsymbol{\varepsilon}} + \boldsymbol{V}'^T [\Lambda_6] \boldsymbol{V}' \right) dx_1 \tag{4.19}$$

where the matrices (Λ_1 - Λ_6) for n number of layers can be expressed in the following form

$$
\begin{aligned}
[\Lambda_1] &= \int_0^{2\pi}\int_{\rho_{in}}^{\rho_{out}} [\Gamma_\varepsilon]^T[D][\Gamma_\varepsilon]\rho d\rho d\theta = \sum_{i=1}^{n}\left(\iint_{\Omega_i}[\Gamma_\varepsilon]^T[D^i][\Gamma_\varepsilon]\rho d\rho d\theta\right)\\
[\Lambda_2] &= \int_0^{2\pi}\int_{\rho_{in}}^{\rho_{out}} [\Gamma_h W]^T[D][\Gamma_h W]\rho d\rho d\theta = \sum_{i=1}^{n}\left(\iint_{\Omega_i}[\Gamma_h W]^T[D^i][\Gamma_h W]\rho d\rho d\theta\right)\\
[\Lambda_3] &= \int_0^{2\pi}\int_{\rho_{in}}^{\rho_{out}} [\Gamma_h W]^T[D][\Gamma_\varepsilon]\rho d\rho d\theta = \sum_{i=1}^{n}\left(\iint_{\Omega_i}[\Gamma_h W]^T[D^i][\Gamma_\varepsilon]\rho d\rho d\theta\right)\\
[\Lambda_5] &= \int_0^{2\pi}\int_{\rho_{in}}^{\rho_{out}} [\Gamma_l W]^T[D][\Gamma_\varepsilon]\rho d\rho d\theta = \sum_{i=1}^{n}\left(\iint_{\Omega_i}[\Gamma_l W]^T[D^i][\Gamma_\varepsilon]\rho d\rho d\theta\right)\\
[\Lambda_4] &= \int_0^{2\pi}\int_{\rho_{in}}^{\rho_{out}} [\Gamma_h W]^T[D][\Gamma_l W]\rho d\rho d\theta = \sum_{i=1}^{n}\left(\iint_{\Omega_i}[\Gamma_h W]^T[D^i][\Gamma_l W]\rho d\rho d\theta\right)\\
[\Lambda_6] &= \int_0^{2\pi}\int_{\rho_{in}}^{\rho_{out}} [\Gamma_l W]^T[D][\Gamma_l W]\rho d\rho d\theta = \sum_{i=1}^{n}\left(\iint_{\Omega_i}[\Gamma_l W]^T[D^i][\Gamma_l W]\rho d\rho d\theta\right)
\end{aligned}
\tag{4.20}
$$

The Eq. (4.20) is the counterpart of Eq. (3.20) which was used for initially curved tubes. The strain energy of Eq. (4.19) should be minimized with respect to unknown warping coefficients $\boldsymbol{V}$. The VAM is applied to minimize the strain energy in which it perturbs the strain energy into different orders according to the small parameters of the problem and then the strain energy is minimized using the Euler-Lagrange equation, [49]. Based on the VAM, the unknown warping coefficients will be perturbed as follows where $\boldsymbol{V_1}$ is one order higher than $\boldsymbol{V_0}$. We have

$$\boldsymbol{V}=\boldsymbol{V_0}+\boldsymbol{V_1} \tag{4.21}$$

4.3.1 First approximation (Classical beam model)

The first approximation of the strain energy is obtained as follows.

$$2U_0 = \int_L (\boldsymbol{V}_0^T[\Lambda_2]\boldsymbol{V}_0 + 2\boldsymbol{V}_0^T[\Lambda_3]\bar{\boldsymbol{\varepsilon}} + \bar{\boldsymbol{\varepsilon}}^T[\Lambda_1]\bar{\boldsymbol{\varepsilon}})dx_1 \tag{4.22}$$

The Euler-Lagrange equation as Eq. (4.23) is used to minimize the strain energy with respect to the unknown warping $\boldsymbol{V}_0$.

$$\frac{\partial U_0}{\partial \boldsymbol{V}_0} = 0 \tag{4.23}$$

Substituting Eq. (4.22) into Eq. (4.23) leads to

$$[\Lambda_3]\bar{\boldsymbol{\varepsilon}}+[\Lambda_2]\boldsymbol{V}_0=0 \tag{4.24}$$

The unknown warping coefficients obtained using the first approximation of the strain energy is

$$\boldsymbol{V}_0=-[\Lambda_2]^{-1}[\Lambda_3]\bar{\boldsymbol{\varepsilon}}\equiv[\hat{V}_0]\bar{\boldsymbol{\varepsilon}} \tag{4.25}$$

The matrix Λ_2 is singular and non-invertible. Pseudo method [81] is used to evaluate its inverse. Substituting Eq. (4.25) into Eq. (4.22), one can achieve the first approximation of strain energy and obtain stiffness constants of a tube with a circular cross-section based on the classical beam model.

$$2U_0=\int_L \bar{\boldsymbol{\varepsilon}}^T([\hat{V}_0]^T[\Lambda_3]+[\Lambda_1])\bar{\boldsymbol{\varepsilon}}dx_1=\int_L \bar{\boldsymbol{\varepsilon}}^T\begin{bmatrix}\bar{S}_{11} & \bar{S}_{12} & \bar{S}_{13} & \bar{S}_{14}\\ \bar{S}_{21} & \bar{S}_{22} & \bar{S}_{23} & \bar{S}_{24}\\ \bar{S}_{31} & \bar{S}_{32} & \bar{S}_{33} & \bar{S}_{34}\\ \bar{S}_{41} & \bar{S}_{42} & \bar{S}_{43} & \bar{S}_{44}\end{bmatrix}\bar{\boldsymbol{\varepsilon}}dx_1=\int_L \bar{\boldsymbol{\varepsilon}}^T[\bar{S}]\bar{\boldsymbol{\varepsilon}}dx_1 \tag{4.26}$$

where $\bar{S}$ is a 4×4 classical stiffness matrix that expresses the beam cross-sectional stiffness coefficients. $\bar{S}_{11}$ is extensional stiffness, $\bar{S}_{22}$ is torsional stiffness, $\bar{S}_{33}$ and $\bar{S}_{44}$ are cross-sectional bending stiffness about x_2 and x_3 coordinates, respectively. In addition, $\bar{S}_{12}$ is the extension-twist coupling, $\bar{S}_{13}$ and $\bar{S}_{14}$ are the extension-bending coupling stiffness, $\bar{S}_{23}$ and $\bar{S}_{24}$ are the torsion-bending coupling stiffness.

4.3.2 Second approximation (Timoshenko-like beam)

Utilizing the Eqs. (4.19) and (4.21), the second approximation of the strain energy will be achieved by collecting the order $O(\varepsilon_{\max}^2(\frac{h}{L})^2)$ as follows.

$$\begin{aligned}2U_1=\int_L(&\boldsymbol{V}_1^T[\Lambda_2]\boldsymbol{V}_1+\bar{\boldsymbol{\varepsilon}}^T[\Lambda_1]\bar{\boldsymbol{\varepsilon}}+\boldsymbol{V}_0^T[\Lambda_2]\boldsymbol{V}_0+\boldsymbol{V}_0'^T[\Lambda_6]\boldsymbol{V}_0'+2\boldsymbol{V}_0^T[\Lambda_3]\bar{\boldsymbol{\varepsilon}}+2\boldsymbol{V}_0'^T[\Lambda_5]\bar{\boldsymbol{\varepsilon}}\\&+2\boldsymbol{V}_1'^T[\Lambda_5]\bar{\boldsymbol{\varepsilon}}+2\boldsymbol{V}_0'^T[\Lambda_4]\boldsymbol{V}_0+2\boldsymbol{V}_0^T[\Lambda_4]\boldsymbol{V}_1'+2\boldsymbol{V}_0'^T[\Lambda_4]\boldsymbol{V}_1)dx_1\end{aligned} \tag{4.27}$$

The energy functional Eq. (4.27) is minimized with respect to unknown warping $\boldsymbol{V}_1$. The following relation is obtained.

$$-[\Lambda_4]^T\boldsymbol{V}_0'+[\Lambda_{hl}]\boldsymbol{V}_0'+[\Lambda_{hh}]\boldsymbol{V}_1-[\Lambda_{l\varepsilon}]^T\bar{\boldsymbol{\varepsilon}}'=0 \tag{4.28}$$

Therefore, $\boldsymbol{V}_1$ can be obtained as

$$\boldsymbol{V_1} = [\Lambda_2]^{-1}\left[([\Lambda_4]^T - [\Lambda_4])\hat{V}_0 + [\Lambda_5]^T\right]\overline{\boldsymbol{\varepsilon}}' \equiv \hat{V}_1\overline{\boldsymbol{\varepsilon}}' \tag{4.29}$$

Substitution of Eqs. (4.25, and 4.29) into Eq. (4.27) leads to the following 1D strain energy.

$$2U_1 = \int_L \left(\overline{\boldsymbol{\varepsilon}}^T[A_1]\overline{\varepsilon} + \overline{\boldsymbol{\varepsilon}}'^T[A_2]\overline{\boldsymbol{\varepsilon}} + \overline{\boldsymbol{\varepsilon}}'^T[A_3]\overline{\boldsymbol{\varepsilon}}' + \overline{\boldsymbol{\varepsilon}}^T[A_4]\overline{\boldsymbol{\varepsilon}}''\right)dx_1 \tag{4.30}$$

In which the relations A_1, A_2, A_3 and A_4 are as follows, [55].

$$\begin{aligned}
[A_1] &= [\Lambda_1] + 2\hat{V}_0^T[\Lambda_3] + \hat{V}_0[\Lambda_2]\hat{V}_0 \\
[A_2] &= 2[\Lambda_5]\hat{V}_0 + 2\hat{V}_0^T[\Lambda_4]\hat{V}_0 \\
[A_3] &= 2\hat{V}_1^T[\Lambda_4]\hat{V}_0 + \hat{V}_1^T[\Lambda_2]\hat{V}_1 + \hat{V}_0^T[\Lambda_6]\hat{V}_0 \\
[A_4] &= 2\hat{V}_0^T[\Lambda_4]\hat{V}_1 + 2[\Lambda_5]\hat{V}_1
\end{aligned} \tag{4.31}$$

Since the 1D strain energy of Eq. (4.30) includes derivatives of generalized strains, it will be complicated to perform 1D analysis and it is preferred to transform it to Timoshenko-like beam model [40] is used by deriving the equilibrium equations of the cross-section, and the generalized strain energy of the Timoshenko beam model. So, the effect of shear will be taken into account and the cross-sectional reference plane is not normal to the reference line in contrast to Classical beam model. The generalized Timoshenko beam model can be presented as

$$2U_1 = \int_L \left(\boldsymbol{\varepsilon}^T[Y_1]\boldsymbol{\varepsilon} + 2\boldsymbol{\varepsilon}^T[Y_2]\boldsymbol{\gamma}_s + \boldsymbol{\gamma}_{\mathbf{s}}{}^T[Y_3]\boldsymbol{\gamma}_{\mathbf{s}}\right)dx_1 \tag{4.32}$$

In which $[Y_1]$, $[Y_2]$ and $[Y_3]$ are unknown stiffness matrices and $\boldsymbol{\gamma}_{\mathbf{s}} = \begin{bmatrix} 2\gamma_{12} & 2\gamma_{13} \end{bmatrix}^T$ includes generalized shear strains caused by the transverse shear deformation. $\boldsymbol{\varepsilon} = \begin{bmatrix} \gamma_{11} & \kappa_1 & \kappa_2 & \kappa_3 \end{bmatrix}^T$ contains Timoshenko model generalized strains. In the transformation to the generalized Timoshenko beam model, we need to find the matrices $[Y_1]$, $[Y_2]$ and $[Y_3]$. The details of the transformation to the generalized Timoshenko beam model are provided in Yu et al. [49]. The unknown stiffness matrices $[Y_1]$, $[Y_2]$ and $[Y_3]$ are obtained as follows.

$$\begin{aligned}
[Y_3] &= \left([P]^T[A_1]^{-1}([A_3] - [A_2]^T[A_1]^{-1}[A_2])[A_1]^{-1}[P]\right)^{-1} \\
[Y_2] &= [A_2]^T[A_1]^{-1}[P][Y_3] \\
[Y_1] &= [Y_2][G]^{-1}[Y]^T + [A_1]
\end{aligned} \tag{4.33}$$

The strain energy Eq. (4.32) is rearranged to the form of strain energy of Eq. (4.34) which takes into account the effect of shear.

$$2U_1 = \int_L \boldsymbol{\psi}^T \begin{bmatrix} S_{11} & S_{12} & S_{13} & S_{14} & S_{15} & S_{16} \\ S_{12} & S_{22} & S_{23} & S_{24} & S_{25} & S_{26} \\ S_{13} & S_{23} & S_{33} & S_{34} & S_{35} & S_{36} \\ S_{14} & S_{24} & S_{34} & S_{44} & S_{45} & S_{46} \\ S_{15} & S_{25} & S_{35} & S_{45} & S_{55} & S_{56} \\ S_{16} & S_{26} & S_{36} & S_{46} & S_{56} & S_{66} \end{bmatrix} \boldsymbol{\psi} dx_1 = \int_L \boldsymbol{\psi}^T [S] \boldsymbol{\psi} dx_1 \tag{4.34}$$

where, $\boldsymbol{\psi} = \begin{bmatrix} \gamma_{11} & 2\gamma_{12} & 2\gamma_{13} & \kappa_1 & \kappa_2 & \kappa_3 \end{bmatrix}^T$. Moreover, the 6×6 matrix S contains the Timoshenko-Like cross-sectional stiffness constants. S_{11} is the extensional stiffness, S_{22} and S_{33} are shear stiffness along x_2 and x_3, respectively and S_{44} is the torsional stiffness, S_{55} $(EI)_{x_2}$ and S_{66} $(EI)_{x_3}$ are bending stiffness about x_2 and x_3, respectively. The off-diagonal elements are coupling stiffness constants *i.e.*, S_{14} is the extension-twist coupling and so on.

4.4 1D analysis of straight beams

The strain energy Eq. (4.34) which is applied for 1D beam analysis, includes 3D deformation effects of the cross-section. Therefore, the 1D static analysis of the tubular beam can be performed using this strain energy equation. The 1D strain energy of beam element is as follows.

$$2U^e = \int_{L_e} \left\{ \boldsymbol{\psi}^T [S] \boldsymbol{\psi} \right\} dx_1 \tag{4.35}$$

where $\boldsymbol{\psi} = \begin{bmatrix} \gamma_{11} & 2\gamma_{12} & 2\gamma_{13} & \kappa_1 & \kappa_2 & \kappa_3 \end{bmatrix}^T$ and L_e is the element length. We can calculate the stiffness of an element if we express the strains in Eq. (4.35) in terms of degrees of freedom of beam element. For a Timoshenko beam model, we can use an element with three nodes which can prevent shear locking [83]. The element and its coordinate are shown in Fig. (4.2). The element has 6 degrees of freedom at each node including three displacements ($\overline{u}$, $\overline{v}$ and $\overline{w}$) and three cross-sectional rotations ($\overline{\varphi}_{x_1}, \overline{\varphi}_{x_2}, \overline{\varphi}_{x_3}$) in the x_1, x_2 and x_3, respectively. Hence, eighteen degrees of freedom for the element is considered. In this model, the following polynomials for the approximation of the degree of freedom in the length is used, [84].

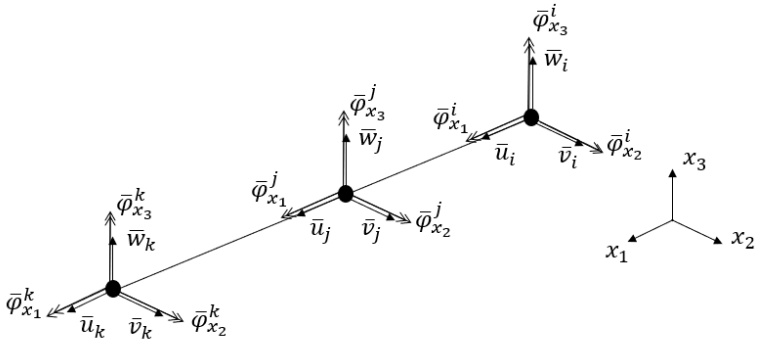

Fig. (4.2). A beam element with three nodes, [83].

$$\bar{u} = \bar{\alpha}_1 + \bar{\alpha}_2 x_1 + \bar{\alpha}_3 x_1^2 \tag{4.36a}$$

$$\bar{v} = \bar{\alpha}_4 + \bar{\alpha}_5 x_1 + \bar{\alpha}_6 x_1^2 + \bar{\alpha}_7 x_1^3 \tag{4.36b}$$

$$\bar{w} = \bar{\alpha}_8 + \bar{\alpha}_9 x_1 + \bar{\alpha}_{10} x_1^2 + \bar{\alpha}_{11} x_1^3 \tag{4.36c}$$

$$\bar{\varphi}_{x_1} = \bar{\alpha}_{12} + \bar{\alpha}_{13} x_1 + \bar{\alpha}_{14} x_1^2 \tag{4.36d}$$

$$2\gamma_{12} = \bar{\alpha}_{15} + \bar{\alpha}_{16} x_1 \tag{4.36e}$$

$$2\gamma_{13} = \bar{\alpha}_{17} + \bar{\alpha}_{18} x_1 \tag{4.36f}$$

For a Timoshenko beam model, the 1D strains can be written as

$$\gamma_{11} = \bar{u}' \tag{4.37a}$$

$$\kappa_1 = \bar{\varphi}'_{x_1} \tag{4.37b}$$

$$\kappa_2 = \bar{\varphi}'_{x_2} \tag{4.37c}$$

$$\kappa_3 = \bar{\varphi}'_{x_3} \tag{4.37d}$$

$$2\gamma_{12} = \bar{v}' - \bar{\varphi}_{x_3} \tag{4.37e}$$

$$2\gamma_{13} = \bar{w}' + \bar{\varphi}_{x_2} \tag{4.37f}$$

It is noted that the $\bar{\varphi}_{x_2}$ and $\bar{\varphi}_{x_3}$ are the bending rotations of the beam section with respect to x_2 and x_3, respectively, while $2\gamma_{12}$ and $2\gamma_{13}$ are rotation of beam section about x_3 and x_2 for transverse shear deformation, respectively. Using strain-displacement Eq. (4.37) and Eq. (4.36), the rotations can be expressed as

$$\bar{\varphi}_{x_2} = \bar{\alpha}_{17} + \bar{\alpha}_{18} x_1 - \bar{\alpha}_9 - 2\bar{\alpha}_{10} x_1 - 3\bar{\alpha}_{11} x_1^2 \tag{4.38a}$$

$$\bar{\varphi}_{x_3} = -\bar{\alpha}_{15} - \bar{\alpha}_{16}x_1 + \bar{\alpha}_5 + 2\bar{\alpha}_6 x_1 + 3\bar{\alpha}_7 x_1^2 \tag{4.38b}$$

The column matrix of degrees of freedom of the beam element will be as follows.

$$\begin{aligned}\boldsymbol{\delta} = [&\bar{u}^i \quad \bar{v}^i \quad \bar{w}^i \quad \bar{\varphi}^i_{x_1} \quad \bar{\varphi}^i_{x_2} \quad \bar{\varphi}^i_{x_3} \\ &\bar{u}^j \quad \bar{v}^j \quad \bar{w}^j \quad \bar{\varphi}^j_{x_1} \quad \bar{\varphi}^j_{x_2} \quad \bar{\varphi}^j_{x_3} \\ &\bar{u}^k \quad \bar{v}^k \quad \bar{w}^k \quad \bar{\varphi}^k_{x_1} \quad \bar{\varphi}^k_{x_2} \quad \bar{\varphi}^k_{x_3}]^T\end{aligned} \tag{4.39}$$

The unknown coefficients matrix is as the following.

$$\bar{\boldsymbol{\alpha}} = [\bar{\alpha}_1 \quad \bar{\alpha}_2 \ldots \bar{\alpha}_{18}] \tag{4.40}$$

The unknowns ($\bar{\alpha}_1 - \bar{\alpha}_{18}$) in the Eq. (4.36) are expressed in terms of the nodal displacement vector $\boldsymbol{\delta}$ by substituting $\bar{u}$, $\bar{v}$, $\bar{w}$, $\bar{\varphi}_{x_1}$, $\bar{\varphi}_{x_2}$ and $\bar{\varphi}_{x_3}$ at all three nodes of the beam element. we have

$$\boldsymbol{\delta} = [T]\bar{\boldsymbol{\alpha}} \text{ or } \bar{\boldsymbol{\alpha}} = [T]^{-1}\boldsymbol{\delta} \tag{4.41}$$

The matrix [T] has an order of 18×18 includes the element nodal coordinates. The 1-D strain vector $\boldsymbol{\psi}$ can be expressed in terms of $\bar{\boldsymbol{\alpha}}$ using Eq. (4.37) as

$$\boldsymbol{\psi} = [N]\bar{\boldsymbol{\alpha}} \tag{4.42}$$

where matrix [N] has order of 6×18 which is a function of x_1. Finally, the strain vector $\boldsymbol{\psi}$ can be expressed in terms of nodal displacement vector $\boldsymbol{\delta}$ using Eq. (4.42) as

$$\boldsymbol{\psi} = [N][T]^{-1}\boldsymbol{\delta} = [R]\boldsymbol{\delta} \tag{4.43}$$

The strain energy relation of the element can be written as

$$U^e = \frac{1}{2}\boldsymbol{\delta}^T \left\{ \int_{L_e} [R]^T [S][R] dx_1 \right\} \boldsymbol{\delta} \tag{4.44}$$

The stiffness matrix of the beam element is

$$[K^e] = \int_{L_e} [R^T][S][R] dx_1 \tag{4.45}$$

The nodal force vector caused by external loads and moments can be expressed as

$$\boldsymbol{f} = [f_1^i \quad f_2^i \quad f_3^i \quad m_1^i \quad m_2^i \quad m_3^i \quad f_1^j \quad f_2^j \quad f_3^j \quad m_1^j \quad m_2^j \quad m_3^j \quad f_1^k \quad f_2^k \quad f_3^k \quad m_1^k \quad m_2^k \quad m_3^k]^T \tag{4.46}$$

where f is the vector of nodal force and f_1^i, f_1^j, f_1^k are extensional forces, f_2^i, f_2^j, f_2^k and f_3^i, f_3^j, f_3^k are transverse forces at nodes i, j and k, and m_1^i, m_1^j, m_1^k are the torsional moments, m_2^i, m_2^j, m_2^k and m_3^i, m_3^j, m_3^k are bending moments at nodes i, j and k. The nodal displacement vector is achieved as follows.

$$\boldsymbol{\delta} = [K^e]^{-1} \boldsymbol{f} \tag{4.47}$$

4.5 Stress analysis of straight circular tube under four-point loading using Pascal polynomial dimensional reduction method and VABS

In this section, the pascal polynomial based dimensional reduction method presented in this chapter is used for cross-sectional analysis (determining cross-sectional stiffness constants), determination of strain distribution in the cross-section and finding transverse displacement under four-point bending loading. The presented polynomial based dimensional reduction method is examined with several examples of isotropic and orthotropic tubes with various range of thicknesses. Then, the four-point bending analysis of the straight composite tube tested in chapter (2) will be performed.

A program in Maple 15 has been developed named AMTSM (Analytical Meshless Tubular Sectional Method). To do so, various tubular sections with different lay-ups are utilized as case studies. The parametric study to investigate the effect of polynomial order and lay-up sequence on the accuracy of the method is presented.

4.5.1 Aluminum tube

An aluminum 6061 T6 [85] isotropic tubular section with the elastic modulus E=69.7 GPa, Poisson ratio $\nu = 0.33$, an outer diameter D_{out} =88.9 *mm* and the thickness h=3.175 *mm* is studied. The obtained stiffness constants reported in Table (4.1) are compared with those extracted through the latest version of VABS as VABS 3.8 with the Classical beam model, and the Timoshenko beam model. The comparison between the proposed method and VABS 3.8 results of Timoshenko and Classical are in terms of the stiffness constants which are obtained from 6×6 stiffness matrix

(Timoshenko beam model) and 4×4 matrix (Classical beam model), respectively. As mentioned before, in the Timoshenko beam model, the effect of shear is considered while in the Classical beam model the effect of shear is not considered. It is noted that the present solution (Aluminum tube) has been done with (m=4) of Pascal polynomials. On the other hand, the VABS 3.8 analysis is carried out with 6000 elements. It is observed that there is no difference in the obtained Timoshenko and Classical beam models in both methods of solutions.

Table (4.1). The non-zero cross-sectional stiffness constants of an aluminum tube.

(non-zero stiffness constants)	Present (Classical beam model)	Present (Timoshenko beam model)	VABS 3.8 (Classical beam model)	VABS 3.8 (Timoshenko beam model)	Strength of materials
S_{11} (N)	5.891×10^7	5.891×10^7	5.959×10^7	5.959×10^7	5.959×10^7
S_{22} (N)	-	1.140×10^7	-	1.122×10^7	-
S_{33} (N)	-	1.140×10^7	-	1.122×10^7	-
S_{44} (N.m^2)	4.168×10^4	4.168×10^4	4.121×10^4	4.168×10^4	4.217×10^4
S_{55} (N.m^2)	5.419×10^4	5.419×10^4	5.482×10^4	5.482×10^4	5.482×10^4
S_{66} (N.m^2)	5.419×10^4	5.419×10^4	5.482×10^4	5.482×10^4	5.482×10^4

4.5.2 Composite tube with lay-up , [20 / -70 / 20 / (-70)$_2$ / 20] , [55]

As a second case study for the validation of the presented Pascal polynomial dimensional reduction method, a **thin** Circumferentially Uniform Stiffness (CUS) composite tubular section is studied and the stiffness constants are compared with those in Ref. [55] which used an earlier version of VABS, Ref. [36], and VABS 3.8. The obtained results are tabulated in Table (4.2). The tube has lay-up sequence $[20/-70/20/(-70)_2/20]$ as shown in Fig. (4.3). It has inner diameter D_{in} = 1.934 *in* (49.12 *mm*) and outer diameter D_{out} = 2 *in* (50.8 *mm*) with the thickness of each layer of 0.0055 *in* (0.1397 *mm*). It is made of IM6/R6376 with the material properties as $E_{11}=23.1\times10^6$ *psi* (159.268 *GPa*), $E_{22}=1.4\times10^6$ *psi* (9.652 *GPa*), $\nu_{12}=\nu_{13}=\nu_{23}=0.338$ and $G_{12}=0.73\times10^6$ *psi* (5.033 *GPa*). The stiffness constants based on the Timoshenko beam model (proposed method) agree well with Rehfield et al. [36]. There are errors in the VABS (Timoshenko) results obtained by Popescu and Hodges [55] with respect to both present (Timoshenko) and Rehfield et al. [36]. This error was modified in the higher versions of VABS proposed by Yu et al. [49]. To this end,

we analyzed this tube using VABS 3.8 with 7588 elements and the obtained results are reported. It can be seen that there is a large difference in the obtained stiffness constants between Timoshenko solution and Classical Solution, which can be due to the higher-order approximation of energy in Timoshenko and considering the shear effect. There is a sign difference in the calculated S_{14} and S_{36} of Rehfield et al. [36] and the results of Ref. [55] which can be a result of sign convention in each of the works. Moreover, the stiffness constants of the tube are computed with different orders of the polynomial (m=3 and 4). The obtained stiffness constants are converged by m=4.

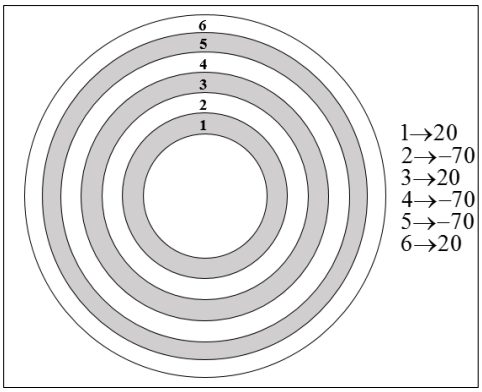

Fig. (4.3) Cross-section with lay-up of $[20/-70/20/-70_2/20]$.

Table (4.2). Stiffness constants of CUS tube, $[20/-70/20/-70_2/20]$.

(non-zero stiffness constants)	Beam theory	S_{11} ($\times 10^6$) (lb)	S_{22} ($\times 10^5$) (lb)	S_{33} ($\times 10^5$) (lb)	S_{14} ($\times 10^5$) (lb.in)	S_{25} ($\times 10^6$) (lb.in)	S_{36} ($\times 10^6$) (lb.in)	S_{44} ($\times 10^5$) ($lb.in^2$)	S_{55} ($\times 10^5$) ($lb.in^2$)	S_{66} ($\times 10^5$) ($lb.in^2$)
m=3	(Cl.)	1.938	-	-	-6.452	-	-	4.408	4.902	4.902
	(Tim.)	1.938	2.333	2.333	-6.452	3.226	3.226	4.408	9.364	9.364
m = 4	(Cl.)	1.938	-	-	-6.452	-	-	4.408	4.799	4.799
	(Tim.)	1.938	2.333	2.333	-6.452	3.226	3.226	4.408	9.364	9.364
m = 5	(Cl.)	1.938	-	-	-6.452	-	-	4.407	4.799	4.799
	(Tim.)	1.938	2.280	2.280	-6.452	3.226	3.226	4.407	9.364	9.364
m = 7	(Cl.)	1.938	-	-	-6.452	-	-	4.407	4.798	4.798
	(Tim.)	1.938	2.279	2.279	-6.452	3.226	3.226	4.407	9.363	9.363
VABS 3.8	(Cl.)	1.896	-	-	-6.249	-	-	4.386	4.798	4.901

	(Tim.)	1.896	2.276	2.259	-6.161	3.220	3.028	4.386	9.354	8.959
Rehfield et al. [36]	**Non-Cl.**	1.972	2.317	2.317	6.680	-3.340	4.634	4.159	9.862	9.862
Popescu and Hodges [55]	**(Cl.)**	1.886	-	-	6.086	-	-	4.159	4.831	4.831
Popescu and Hodges [55]	**(Tim.)**	1.886	1.137	1.137	6.086	-1.609	-1.609	4.159	7.109	7.109

4.5.3 A thick composite tube with lay-up $[90_{30}/\pm 25_{45}/90_5/\pm 30_{20}/90_5/\pm 45_{20}]$

The third case study is related to a **thick** composite tube with complicated lay-up sequence $[90_{30}/\pm 25_{45}/90_5/\pm 30_{20}/90_5/\pm 45_{20}]$. The tube is fabricated using Automated Fiber Placement (AFP) technique with material of Carbon/PEKK with $E_1 = 138.3\ GPa$, $E_2 = E_3 = 10.1\ GPa$, $\nu_{12} = \nu_{13} = 0.31$, $\nu_{23} = 0.33$ and $G_{12} = G_{13} = G_{23} = 5.56\ GPa$. The tube has inner and outer diameters $D_{in} = 56\ mm$ and $D_{out} = 98\ mm$, respectively. The tube cross-section is meshed using VABS 3.8 with 9098 elements as shown in Fig. (4.4). The obtained stiffness constants are reported in Table (4.3). There is a large difference in the obtained flexural stiffness (S_{55} and S_{66}) between Cl. and Timoshenko models. In addition, the obtained stiffness constants are compared with those of the 3D elasticity solution of Lekhnitskii for multi-layered composite tubes proposed by Jolicoeur and Cardou [12] and Moshir et al. [2] with no-slip assumption at the interfaces of the layers as well as Shadmehri et al. [38] who used non-classical beam theory to calculate flexural stiffness of composite tube. A good agreement between the obtained stiffness constants and the literature is observed.

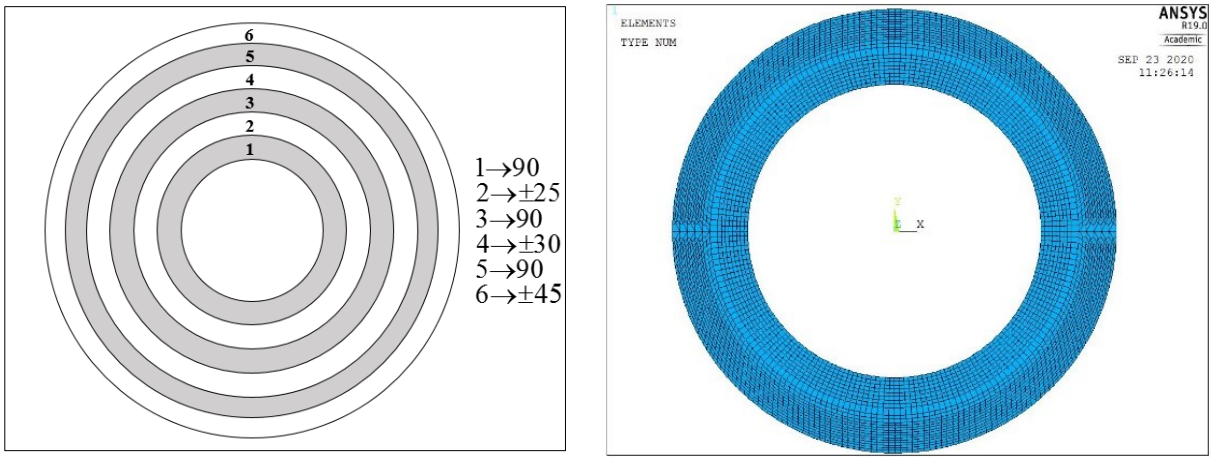

Fig. (4.4). *a*) The lay-up sequence, *b*) generated mesh of the composite tube with 9098 number of elements.

Table (4.3). Non-zero stiffness constants for tube $[90_{30}/\pm25_{45}/90_5/\pm30_{20}/90_5/\pm45_{20}]$.

(non-zero stiffness constants)	**Beam theory**	S_{11} $(\times10^8)$ ***(N)***	S_{22} $(\times10^7)$ ***(N)***	S_{33} $(\times10^7)$ ***(N)***	S_{14} $(\times10^6)$ ***(N.m)***	S_{25} $(\times10^6)$ ***(N.m)***	S_{36} $(\times10^6)$ ***(N.m)***	S_{44} $(\times10^5)$ ***($N.m^2$)***	S_{55} $(\times10^5)$ ***($N.m^2$)***	S_{66} $(\times10^5)$ ***($N.m^2$)***
***m*=4**	**(Cl.)**	2.955	-	-	-5.088	-	-	1.795	1.035	1.035
	(Tim.)	2.955	5.073	5.073	-5.088	2.408	5.073	1.795	2.178	2.178
***m*=5**	**(Cl.)**	2.953	-	-	-5.087	-	-	1.795	1.017	1.031
	(Tim.)	2.953	5.008	5.010	-5.087	2.407	2.378	1.795	2.175	2.160
***m*=7**	**(Cl.)**	2.953	-	-	-5.087	-	-	1.795	1.017	1.017
	(Tim.)	2.953	5.008	5.010	-5.087	2.407	2.378	1.795	2.175	2.160
VABS 3.8	**(Cl.)**	2.945	-	-	-5.071	-	-	1.787	0.993	0.994
	(Tim.)	2.945	4.786	4.786	-5.071	2.328	2.326	1.787	2.126	2.125
Shadmehri et al. [38]	**Non-Cl.**	-	-	-	-	-	-	-	2.228	2.228
Jolicoeur and Cardou [12]	**3D elasticity**	-	-	-	-	-	-	-	2.162	2.162

4.5.4 Effect of polynomial order (m), and lay-up sequence, on the accuracy of the stiffness constants of the cross-section

The selected order of Pascal polynomial in the warping field, and lay-up sequence may affect the accuracy of not only the stiffness constants of the tube but also on the 3D strains of the tube. To this end, we examined composite tubes with material properties $E_1 = 140\ GPa$, $E_2 = E_3 = 10\ GPa$, $v_{12} = v_{13} = 0.31$, $v_{23} = 0.33$ and $G_{12} = G_{13} = G_{23} = 5.53\ GPa$. The outer and inner radiuses of the tubes are r_{out}=59 *mm* and r_{out}=39 *mm,* respectively. The thickness of each layer is assumed to be 2 *mm*. Note that all the following reported stiffness constants are in *SI*.

4.5.4.1 Unidirectional composite tube [0_{10}]

The effect of polynomial order on the accuracy of stiffness constants of a unidirectional tube is investigated in Table (4.4). Values are compared with those obtained from VABS 3.8. Except for S_{22} and S_{33} of (m=2), the other stiffness constants are close to which obtained by VABS 3.8. The obtained S_{22} and S_{33} of orders (m=5 and 7) are more accurate compared to other orders. It is noted that both the obtained Timoshenko and Classical are the same.

Table (4.4). Stiffness constants for tube [0_{10}], r_{out}=0.059 *m*, ply thickness t=2 *mm,* for both (Cl. and Tim.).

(non-zero stiffness constants)	S_{11} $(\times 10^8)$	S_{22} $(\times 10^7)$	S_{33} $(\times 10^7)$	S_{44} $(\times 10^4)$	S_{55} $(\times 10^6)$	S_{66} $(\times 10^6)$
***m*=2**	8.620	3.404	3.404	8.516	1.077	1.077
Diff.%	0	87.130	87.130	0	0	0
***m*=3**	8.620	1.983	1.983	8.516	1.077	1.077
Diff.%	0	9.015	9.015	0	0	0
***m*=4**	8.620	1.983	1.983	8.516	1.077	1.077
Diff.%	0	9.015	9.015	0	0	0
***m*=5**	8.620	1.890	1.890	8.516	1.077	1.077
Diff.%	0	3.903	3.903	0	0	0
***m*=7**	8.620	1.890	1.890	8.516	1.077	1.077
Diff.%	0	3.903	3.903	0	0	0
VABS 3.8	8.620	1.819	1.819	8.516	1.077	1.077
Strength of mat.	8.620	-	-	8.516	1.077	1.077

4.5.4.2 Composite tubes with lay-up [$90_5/0_5$]

The effect of polynomial order (m) on the accuracy of the obtained flexural stiffness of cross-ply tube [$90_5/0_5$], is demonstrated in Table (4.5). It is observed that the obtained Classical and Timoshenko flexural stiffness of the tube are similar when polynomial order increases. Increasing the polynomial order from 4 to 7 does not have a significant effect on the accuracy of the predicted flexural stiffness for tubes. Also, both the Timoshenko and Classical common stiffness constants are the same. The obtained results converge for [$90_5/0_5$] with order (m=7) of the polynomial.

Table (4.5). Stiffness constants for tube [$90_5/0_5$], r_{out}=0.059 m, ply thickness t=2 mm, for both (Cl. and Tim.) theories.

(non-zero stiffness constants)	S_{11} $(\times 10^8)$	S_{22} $(\times 10^7)$	S_{33} $(\times 10^7)$	S_{44} $(\times 10^4)$	S_{55} $(\times 10^5)$	S_{66} $(\times 10^5)$
***m*=2**	5.104	3.405	3.405	8.516	7.315	7.315
Diff.%	1.189	65.935	65.935	0	0.480	0.480
***m*=3**	5.047	2.207	2.207	8.516	7.315	7.315
Diff.%	0.059	7.553	7.553	0	0.480	0.480
***m*=4**	5.047	2.207	2.207	8.516	7.281	7.281
Diff.%	0.059	7.553	7.553	0	0.480	0.013
***m*=5**	5.047	2.131	2.189	8.516	7.281	7.281
Diff.%	0.059	6.676	6.676	0	0.480	0.013
***m*=7**	5.045	2.131	2.189	8.516	7.281	7.281
Diff.%	0.029	6.676	6.676	0	0.480	0.013
VABS 3.8	5.044	2.052	2.052	8.516	7.280	7.280
Strength of mat.	5.026	-	-	8.516	7.256	7.256

4.5.4.3 Composite tubes with lay-up [$\pm 60_5$]

The influence of polynomial order on the non-zero stiffness constants of the tube $[\pm 60_5]$ is investigated, as shown in Table (4.6). It is observed that for order (m=2) of the polynomial, except for S_{14}, there is no significant difference between the obtained (Cl.) results and those obtained by VABS 3.8. By increasing the order of the polynomial, the values of S_{14} become close to VABS 3.8. The two stiffness constants S_{22} and S_{33} of the order (m=2) have a large difference compared

with VABS 3.8. As the polynomial order increases, the difference decreases noticeably. A very good agreement between the results of the present approach with (m=7) compared to VABS 3.8 is observed. In addition, it can be observed that the Classical and Timoshenko stiffness constants for this type of lay-up sequence $[\pm\alpha_5]$ are the same.

Table (4.6). Stiffness constants for tube $[\pm 60_5]$, r_{out}=59 *mm*, ply thickness t=2 *mm,* for both (Cl. and Tim.).

(non-zero stiffness constants)	Beam theory	S_{11} $(\times 10^7)$	S_{22} $(\times 10^7)$	S_{33} $(\times 10^7)$	S_{14} $(\times 10^4)$	S_{25} $(\times 10^4)$	S_{36} $(\times 10^5)$	S_{44} $(\times 10^5)$	S_{55} $(\times 10^4)$	S_{66} $(\times 10^4)$
	(Cl.)	7.281	-	-	-3.340	-	-	4.395	9.085	9.085
	Diff%	0.289	-	-	25.346	-	-	0.365	0.0771	0.0771
***m*=2**	**(Tim.)**	7.281	9.410	9.410	-3.340	2.226	2.226	4.395	9.085	9.085
	Diff%	0.289	4.416	4.416	25.346	14.318	14.351	0.365	0.066	0.066
	(Cl.)	7.261	-	-	-4.351	-	-	4.390	9.084	9.084
	Diff%	0.013	-	-	2.749	-	-	0.251	f0.055	0.055
***m*=3**	**(Tim.)**	7.261	9.118	9.118	-4.351	2.094	2.094	4.390	9.085	9.085
	Diff%	0.013	1.176	1.176	2.749	19.399	19.399	0.251	0.066	0.066
	(Cl.)	7.261	-	-	-4.351	-	-	4.390	9.075	9.075
	Diff%	0.013	-	-	2.749	-	-	0.251	0.033	0.033
***m*=4**	**(Tim.)**	7.261	9.128	9.128	-4.351	2.565	2.565	4.390	9.076	9.076
	Diff%	0.013	1.287	1.287	2.749	1.270	1.270	0.251	0.044	0.033
	(Cl.)	7.260	-	-	-4.383	-	-	4.389	9.075	9.075
	Diff%	0.000	-	-	2.033	-	-	0.228	0.033	0.033
***m*=5**	**(Tim.)**	7.260	9.106	9.124	-4.383	2.552	2.567	4.389	9.076	9.076
	Diff%	0.000	1.043	1.242	2.033	1.770	1.231	0.228	0.033	0.033
	(Cl.)	7.263	-	-	-4.844	-	-	4.390	9.077	9.077
	Diff%	0.0413	-	-	8.270	-	-	0.251	0.011	0.011
m=7	**(Tim.)**	7.263	9.108	9.125	-4.844	2.749	2.762	4.390	9.078	9.078
	Diff%	0.0413	1.065	1.253	8.270	5.812	6.271	0.251	0.011	0.011
VABS 3.8	**(Cl.)**	7.260	-	-	-4.474	-	-	4.379	9.078	9.078
	(Tim.)	7.260	9.012	9.012	-4.474	2.598	2.599	4.379	9.079	9.079

4.5.4.4 Composite tubes with lay-up [$45_5/15_5$]

To further investigate the effect of lay-up sequence on the accuracy of the present approach, we evaluate flexural stiffness of angle-ply [$45_5/15_5$] tube. Table (4.7) shows the effect of polynomial order on the stiffness of tubes [$45_5/15_5$]. Also, it is seen that increasing Pascal polynomial order, increases the accuracy of stiffness prediction.

There is a large difference between the obtained flexural stiffness (S_{55} and S_{66}) of the Classical and Timoshenko for both methods. This means that combination of angle-ply layers causes difference between the Classical and Timoshenko results. This difference between Classical and Timoshenko is due to the effect of shear strains which are considered in Timoshenko beam model. It is observed that the other common stiffness constants of the Classical and Timoshenko are the same. The percentage difference of the m=2 values compared to VABS 3.8 is large. By increasing the polynomial order to (m=5 or 7), the percentage difference decreases. The maximum of the percentage difference between the present results and VABS 3.8 is 7.690 for $S_{22,}$ whereas the minimum of the percentage difference is 0.485 for flexural stiffness (S_{66}).

Table (4.7). Stiffness constants for tube [$45_5/15_5$], r_{out}=59 *mm*, ply thickness t=2 *mm,* (Cl. and Tim.)

(non-zero stiffness constants)	**Beam theory**	S_{11} $(\times 10^8)$	S_{22} $(\times 10^7)$	S_{33} $(\times 10^7)$	S_{14} $(\times 10^6)$	S_{25} $(\times 10^6)$	S_{36} $(\times 10^6)$	S_{44} $(\times 10^5)$	S_{55} $(\times 10^5)$	S_{66} $(\times 10^5)$
***m*=2**	**(Cl.)**	4.615	-	-	-6.805	-	-	2.533	4.884	4.884
	Diff%	3.847	-	-	17.024	-	-	29.300	7.152	7.152
	(Tim.)	4.615	7.482	7.482	-6.805	3.603	3.603	2.533	6.619	6.619
	Diff%	3.847	42.081	42.081	17.024	16.038	16.038	29.300	3.599	3.599
***m*=3**	**(Cl.)**	4.479	-	-	-6.004	-	-	2.060	4.692	4.692
	Diff%	0.078	-	-	3.250	-	-	5.155	2.939	2.939
	(Tim.)	4.479	6.833	6.833	-6.004	3.532	3.532	2.060	6.518	6.518
	Diff%	0.078	29.756	29.756	3.250	13.752	13.752	5.155	2.019	2.019
***m*=4**	**(Cl.)**	4.479	-	-	-6.004	-	-	2.060	4.620	4.620
	Diff%	0.078	-	-	3.250	-	-	5.155	1.360	1.360
	(Tim.)	4.479	5.690	5.690	-6.004	3.203	3.203	2.060	6.424	6.424
	Diff%	0.078	8.051	8.051	3.250	3.156	3.156	5.155	0.547	0.547
***m*=5**	**(Cl.)**	4.468	-	-	-5.939	-	-	2.023	4.613	4.619

	Diff%	0.540	-	-	2.132	-	-	3.266	1.206	1.338
	(Tim.)	4.468	5.678	5.675	-5.939	3.205	3.197	2.023	6.423	6.420
	Diff%	0.540	7.823	7.766	2.132	3.220	2.962	3.266	0.532	0.485
	(Cl.)	4.468	-	-	-5.939	-	-	2.023	4.613	4.617
m=7	***Diff%***	0.540	-	-	2.132	-	-	3.266	1.206	1.338
	(Tim.)	4.468	5.671	5.662	-5.939	3.203	3.194	2.023	6.422	6.420
	Diff%	0.540	7.690	7.519	2.132	3.156	2.866	3.266	0.532	0.485
	(Cl.)	4.444	-	-	-5.815	-	-	1.959	4.558	4.558
VABS 3.8	**(Tim.)**	4.444	5.266	5.266	-5.815	3.105	3.105	1.959	6.389	6.389

4.5.5 Validation of 3D strains

4.5.5.1 Distribution of strain in tube $[90_{40}/25_{40}/90_{20}/30_{40}/90_{20}/45_{40}]$

To study the capability of the present method to predict strain distribution in the cross-section, the distribution of the 3-D strain components in a composite cross-section with a complex lay-up $[90_{40}/25_{40}/90_{20}/30_{40}/90_{20}/45_{40}]$, the material properties of the section (4.5.4), the length of 1 m, outer radius r_{out} = 59 *mm*, inner radius r_{in} = 39 *mm* and thickness of each layer 0.1 *mm* subjected to a pure bending moment M_2 =1 K*N.m* are illustrated in Figs. (4.5) to (4.8), respectively. The distribution variation and magnitude of Γ_{11}, $2\Gamma_{12}$, Γ_{22} and Γ_{33} of the present method with (*m*=7) have a good correlation with respect to ANSYS 3D. The distribution of the normal strains through the thickness at $\theta = 90^{\circ}$ of the circumference are demonstrated in Fig. (4.9). The obtained results of the present method are compared with ANSYS 3D FE solution. In the ANSYS 3D solution, the element SOLID 185 has been used. The tube body is meshed with 3,192 k elements. The total computational time of ANSYS 3D solution is 55 minutes while the present polynomial method computational time is only 15 seconds.

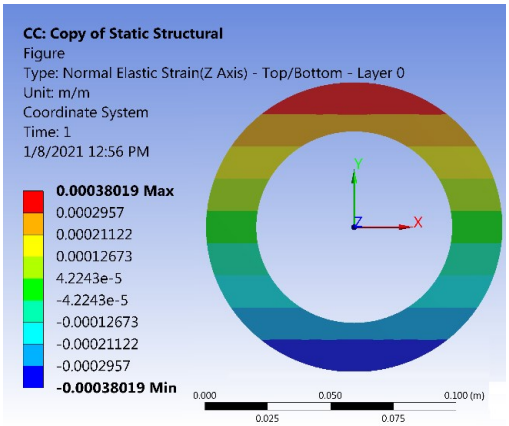

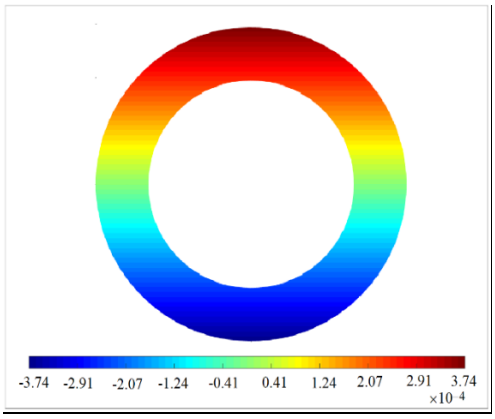

a) ANSYS 3-D *b*) Present

Fig. (4.5). Distribution of Γ_{11} in the tubular section $[90_{40}/25_{40}/90_{20}/30_{40}/90_{20}/45_{40}]$ under ($M_2 = 1$ KN.m), *a*) ANSYS 3D, *b*) present.

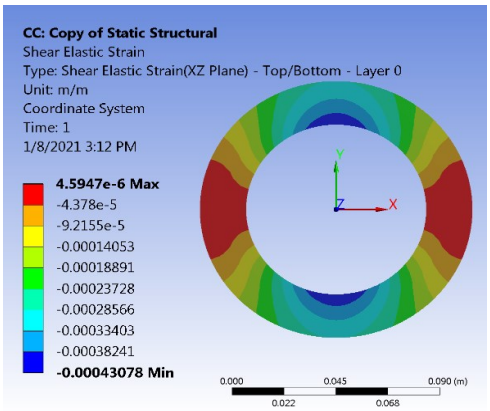

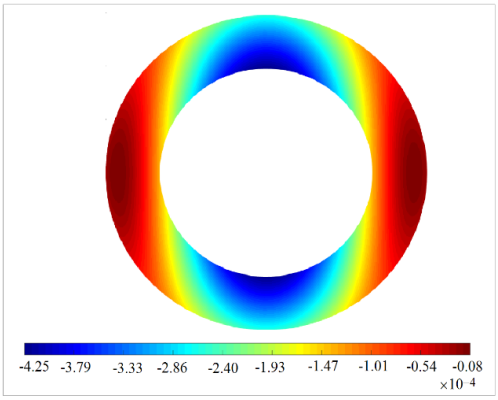

a) ANSYS 3-D *b*) Present

Fig. (4.6). Distribution of Γ_{12} in the section $[90_{40}/25_{40}/90_{20}/30_{40}/90_{20}/45_{40}]$ under ($M_2 = 1$ KN.m), *a*) ANSYS 3D, *b*) present.

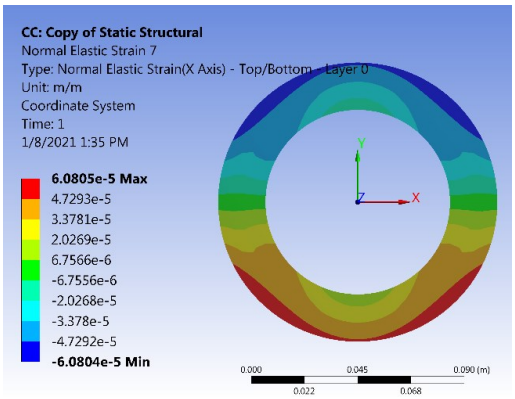

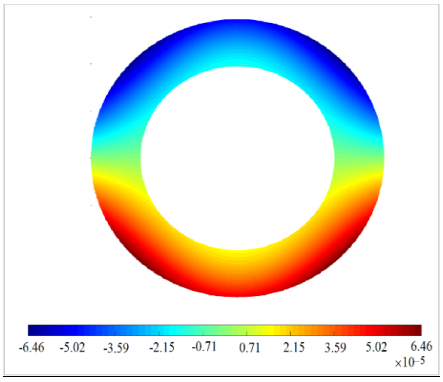

a) ANSYS 3-D *b*) Present

Fig. (4.7). Distribution of Γ_{22} in the section $[90_{40}/25_{40}/90_{20}/30_{40}/90_{20}/45_{40}]$ under (M_2=1 KN.m), a) ANSYS 3D, b) present.

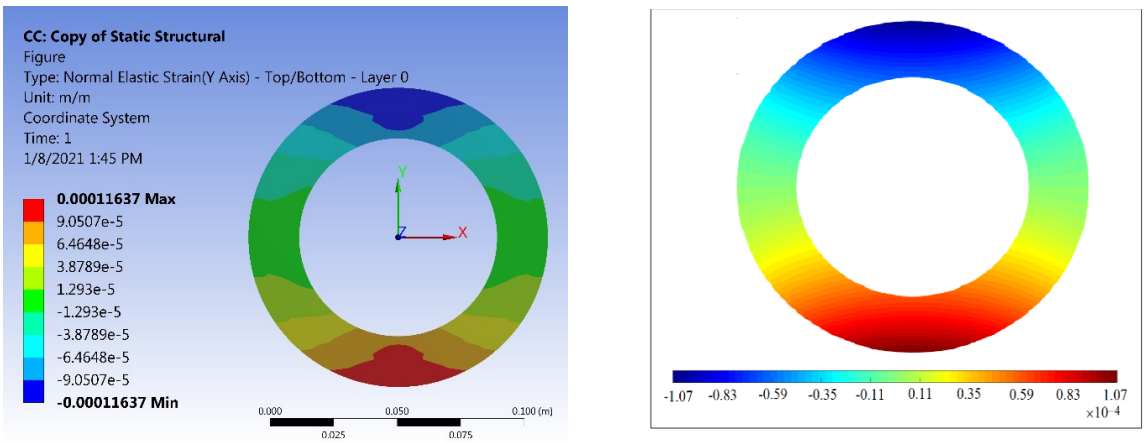

a) ANSYS 3-D *b*) Present

Fig. (4.8). Distribution of Γ_{33} in the section $[90_{40}/25_{40}/90_{20}/30_{40}/90_{20}/45_{40}]$ under ($M_2 = 1$ KN.m), a) ANSYS 3D, b) present.

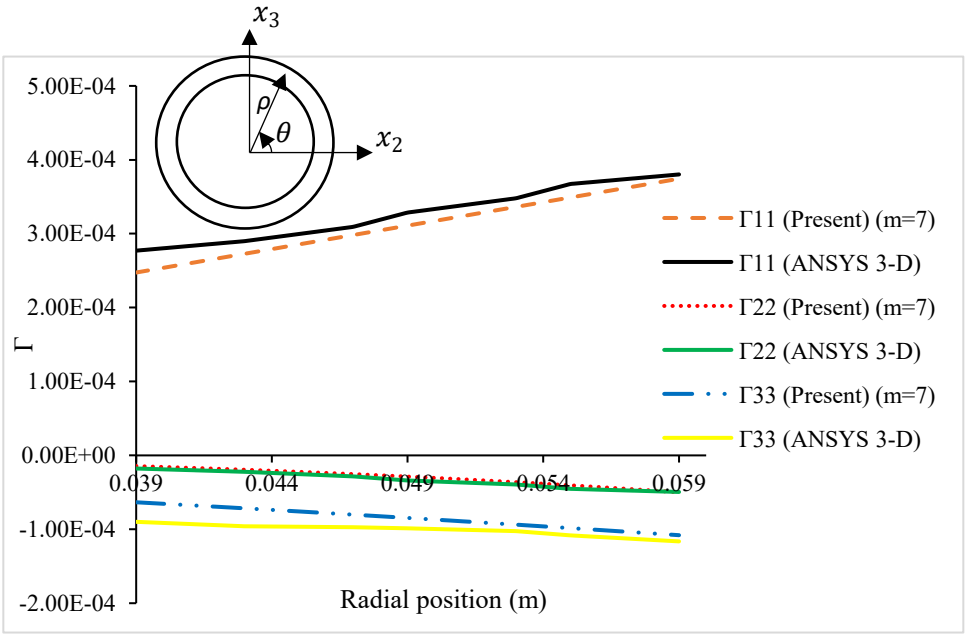

Fig. (4.9). Distribution of Γ_{11}, Γ_{22}, and Γ_{33} through the thickness of $[90_{40}/25_{40}/90_{20}/30_{40}/90_{20}/45_{40}]$ tube at $\theta = 90^{\circ}$ of the circumference under M_2=1 KN.m.

4.5.5.2 Distribution of 3-D strains of $[\pm 60_5]$ tube

The distribution of longitudinal strain Γ_{11}, Γ_{22} (normal strain along x_2), Γ_{33} (normal strain along x_3) and out-of-plane shear strain Γ_{12} through the thickness at $\theta = \frac{\pi}{2}$ of the tube $[\pm 60_5]$ with the material properties and dimensions of the section 4.5.4 under M_2=1 *KN.m* are demonstrated in Fig. (4.10). The order (m=7) of the polynomial is used for the analysis. An excellent correlation between the present method and VABS 3.8 can be observed. It is noted that the tube is meshed with 97800 elements in ANSYS 3D and the cross-section is meshed with 3740 2D elements in VABS 3.8.

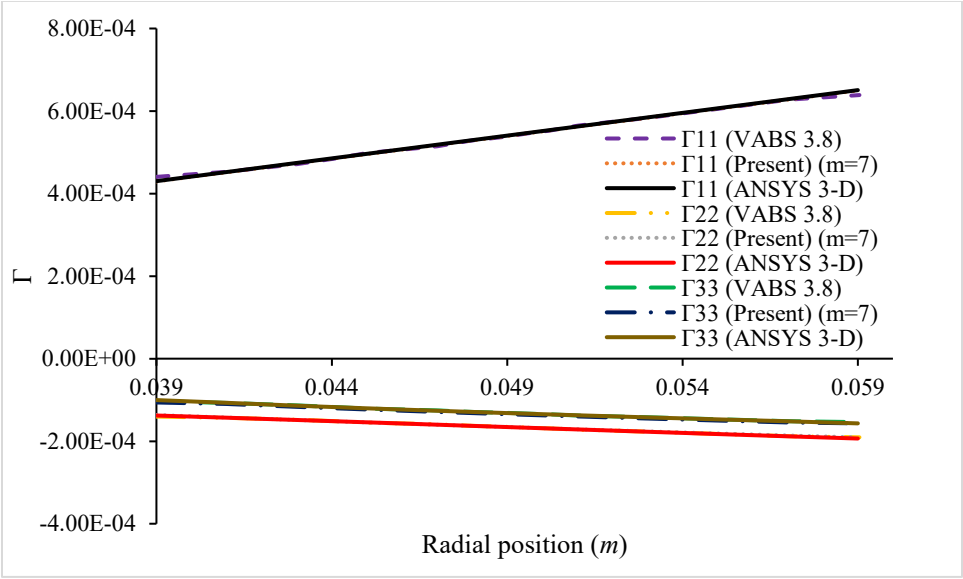

Fig. (4.10). Distribution of Γ_{11}, Γ_{22}, and Γ_{33} through the thickness of $[\pm 60_5]$ tube at $\theta = 90^\circ$ of the circumference under M_2=1 KN.m.

4.5.5.3 Cross-sectional analysis of composite tube

$[(5Harness\ \text{satin})_7 / 90_4 / (\pm 25)_4 / 90_4 / (\pm 35)_4 / 90_4 / (\pm 45)_4]$

The stress analysis of four-point bending of straight composite tube proposed in chapter (3) with lay-up $[(5Harness\ \text{satin})_7 / 90_4 / (\pm 25)_4 / 90_4 / (\pm 35)_4 / 90_4 / (\pm 45)_4]$ is done using Pascal Polynomial dimensional reduction method proposed in this chapter. The material properties, lay-up sequence and loading conditions are reported in section 2.2.2. The distribution of longitudinal strain along x_1 (Γ_{11}), shear strain Γ_{23}, normal strain along x_3 (Γ_{22}), and normal strain along x_3 (Γ_{33}) subjected to bending

moment M_2=-1277 N.*m* are shown in Figs. (4.11-4.14). The obtained strains using the present pascal polynomial dimensional reduction method are compared with ANSYS 3D FEA.

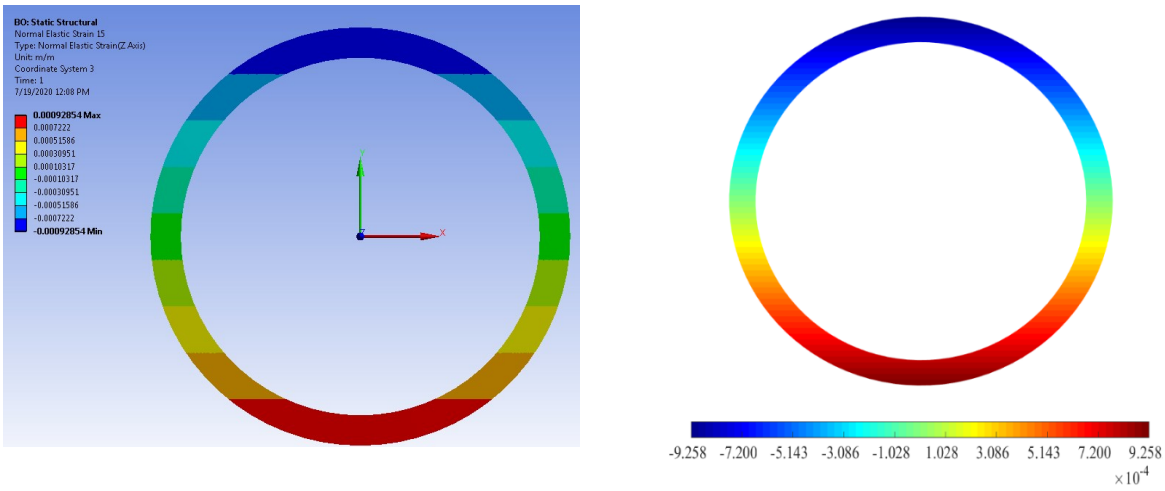

a) *b*)

Fig. (4.11). Distribution of longitudinal strain Γ_{11} in the section of tube $[(5Harness\ \text{satin})_7 / 90_4 / (\pm 25)_4 / 90_4 / (\pm 35)_4 / 90_4 / (\pm 45)_4]$ subjected to M_2=-1277 N.m., *a*) ANSYS 3D, *b*) Present.

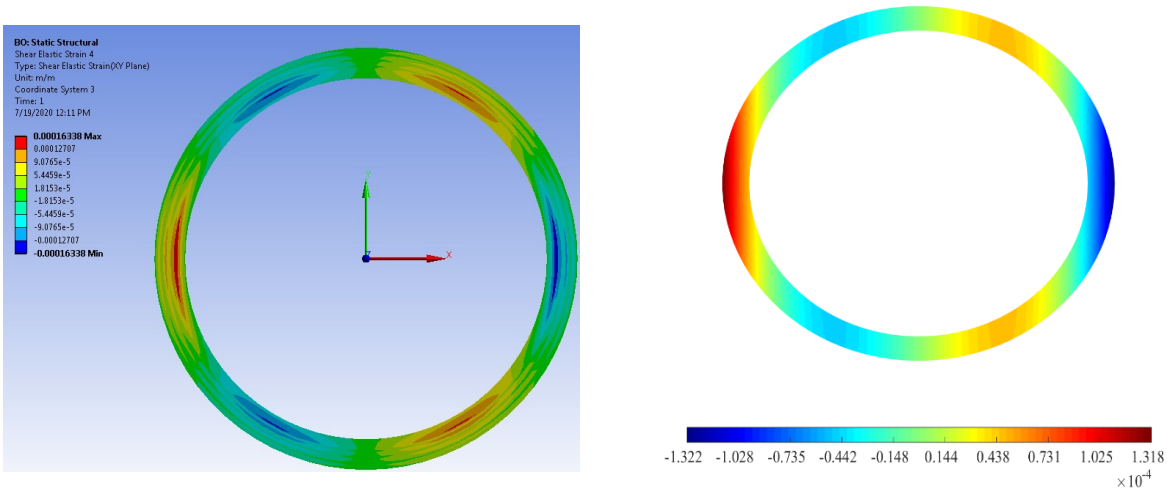

a) *b*)

Fig. (4.12). Distribution of longitudinal strain Γ_{23} in the section of tube $[(5Harness\ \text{satin})_7 / 90_4 / (\pm 25)_4 / 90_4 / (\pm 35)_4 / 90_4 / (\pm 45)_4]$ subjected to M_2=-1277 N.m., *a*) ANSYS 3D, *b*) Present.

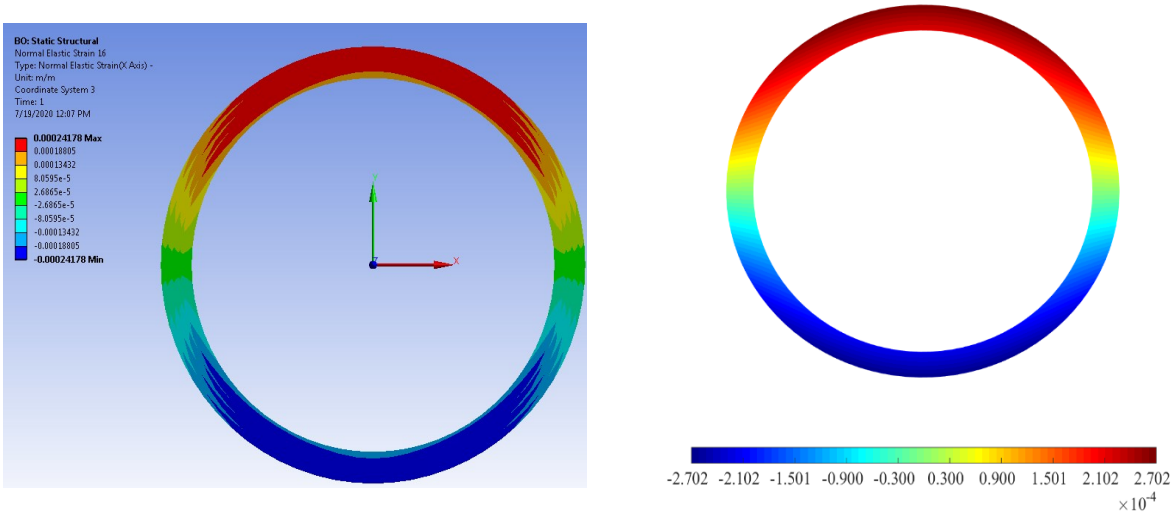

a) *b*)

Fig. (4.13). Distribution of longitudinal strain Γ_{22} in the section of tube $[(5Harness\ \text{satin})_7 / 90_4 / (\pm 25)_4 / 90_4 / (\pm 35)_4 / 90_4 / (\pm 45)_4]$ subjected to M_2=-1277 N.m., *a*) ANSYS 3D, *b*) Present.

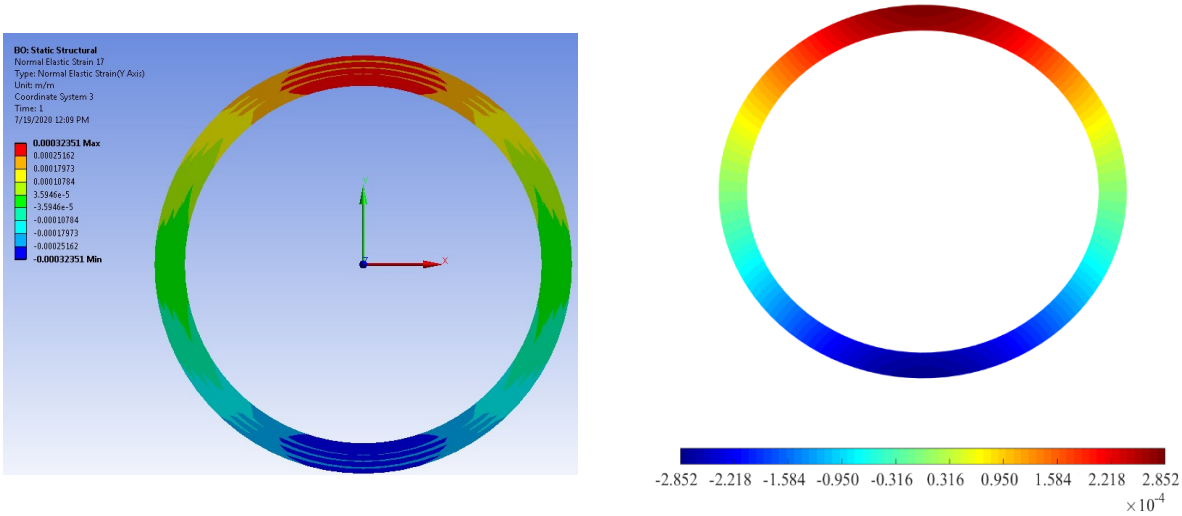

a) *b*)

Fig. (4.14). Distribution of longitudinal strain Γ_{33} in the section of tube $[(5Harness\ \text{satin})_7 / 90_4 / (\pm 25)_4 / 90_4 / (\pm 35)_4 / 90_4 / (\pm 45)_4]$ subjected to M_2=-1277 N.m., *a*) ANSYS 3D, *b*) Present.

The distribution of normal strains Γ_{11} and Γ_{22} at position of $\theta = 90^{\circ}$ of the circumference and outer radius of the tube (location of strain gage shown in Fig. (4.15*a*) of the tube under four-point bending loading subjected to loading F=2P are calculated using the present Pascal polynomial

dimensional reduction method and compared with the experiment presented in chapter (2). At the position, the Γ_{11} is the longitudinal strain and Γ_{22} is the circumferential strain. A good correlation between the present method of solution and the experiment is obtained.

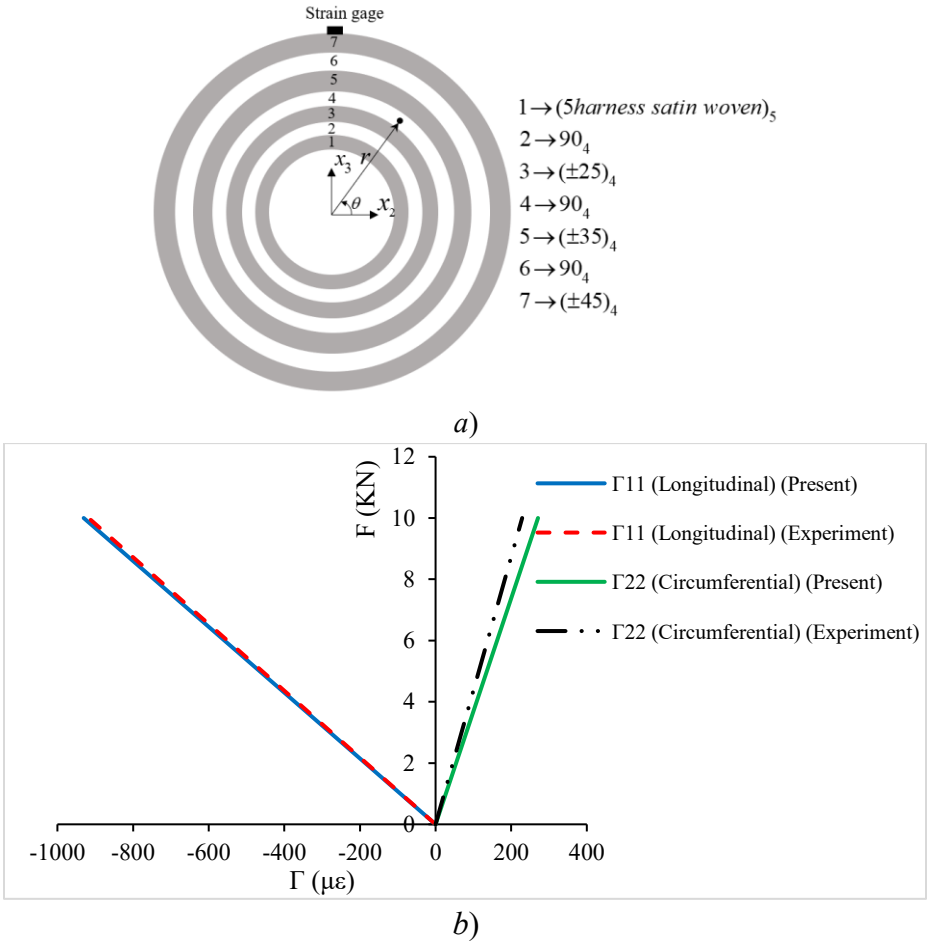

Fig. (4.15), *a*) cross-section of the circular composite tube and the installed strain gage, *b*) Longitudinal and circumferential strains versus load F at $\theta = 90^{\circ}$.

4.6 1-D FE modeling of straight composite tube

$[(5Harness\ \text{satin})_7 / 90_4 / (\pm 25)_4 / 90_4 / (\pm 35)_4 / 90_4 / (\pm 45)_4]$

The deflection of the tubular composite beam calculated using the present polynomial method and 1-D FE (section 4.4) is compared with VABS 3.8 and experimental result. For the experiment, we carried out a test on a composite tube under four-point bending loading (section 2.2.2). The tube was under the load 10 *KN*. The obtained VABS 3.8 stiffness matrix was imported to ANSYS

APDL package to perform 1D FE analysis. In the ANSYS modeling, beam 189 element type was selected which has 3 nodes and 3 degrees of freedom at each node. The boundary conditions are considered as ($\bar{u}=\bar{v}=\bar{w}=0,\ \bar{\varphi}_{x_1}=\bar{\varphi}_{x_3}=0$) at two ends of the beam. The distribution of transverse displacement in the length of the tube is demonstrated in Fig. (4.16), with the experimental point at mid length of the tube. The convergence study shows that the obtained displacement converges with 40 number of 1D elements. It can be seen that a good agreement is obtained.

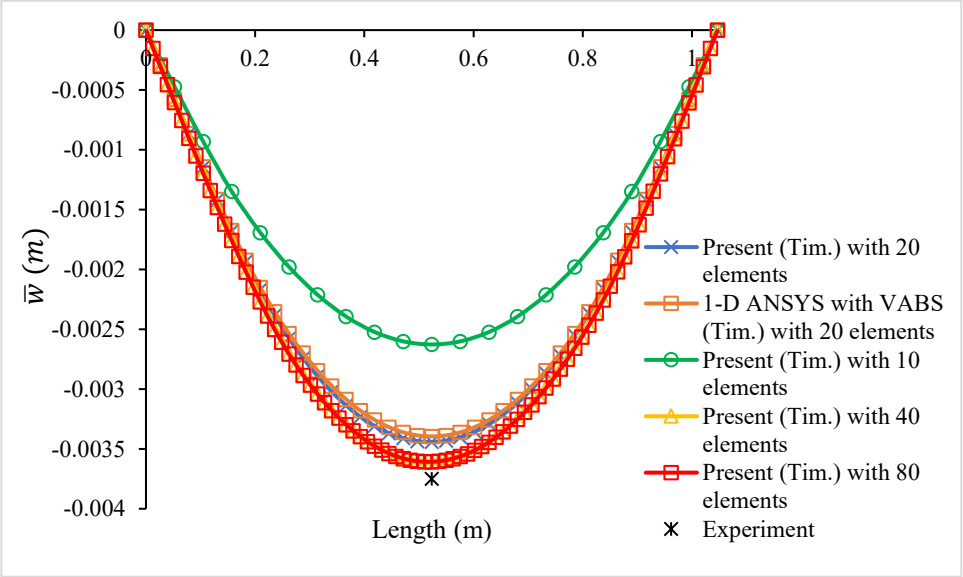

Fig. (4.16). Transverse displacement of tube
$[(5\text{Harness satin})_7 / 90_4 / (\pm 25)_4 / 90_4 / (\pm 35)_4 / 90_4 / (\pm 45)_4]$ under four-point bending loading.

4.7 Parametric study

In the Figs. (4.17-4.19) , we investigated the influence of the fiber angle α on the change of stiffness constants S_{11}, S_{14}, S_{36}, S_{33}, S_{55}, and S_{66} of the composite tubes with lay-up $[\pm\alpha_5]$. The dimensions and material properties are similar to section 4.5.4. It is seen from Fig. (4.17) that as the fiber angle increases, the extensional stiffness (S_{11}) decreases. The change of S_{11} is considerable until the fiber angle of $\alpha = 45^\circ$. The change of extensional-torsional (S_{14}) and torsional-bending (S_{36}) stiffness versus the fiber angle are depicted in Fig. (4.18). At the fiber angle $\alpha = 30^\circ$, the maximum of the S_{14} and S_{36} can be observed. Then, the value of them decrease considerably by $\alpha = 60^\circ$. The variation of torsional and bending stiffness in Fig. (4.19) show that the torsional stiffness (S_{33}) is

maximum at $\alpha = 45^{\circ}$ and the bending stiffness (S_{55} and S_{66}) decreases by increasing the fiber angle.

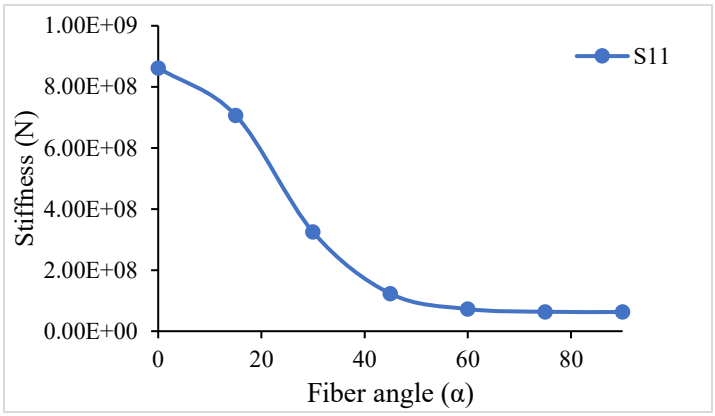

Fig. (4.17). Extensional stiffness (S_{11}) of the composite tube $[\pm\alpha_5]$ versus fiber angle (α).

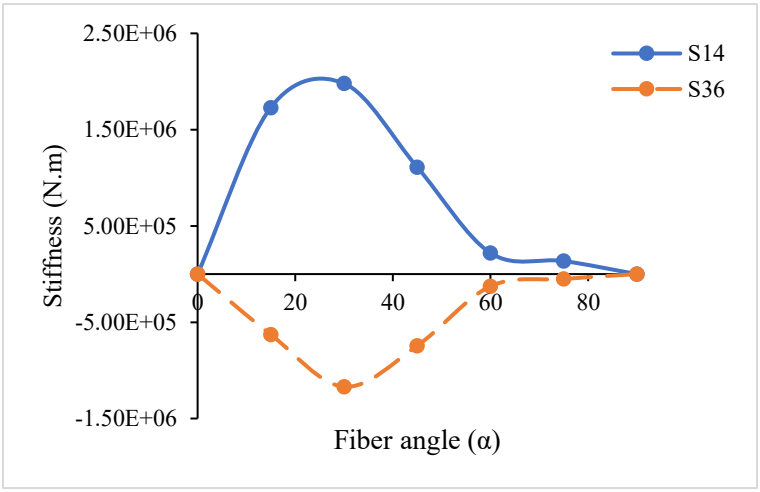

Fig. (4.18). Extensional-torsional (S_{14}) and torsional-bending (S_{36}) stiffness of the composite tube $[\pm\alpha_5]$ versus fiber angle (α).

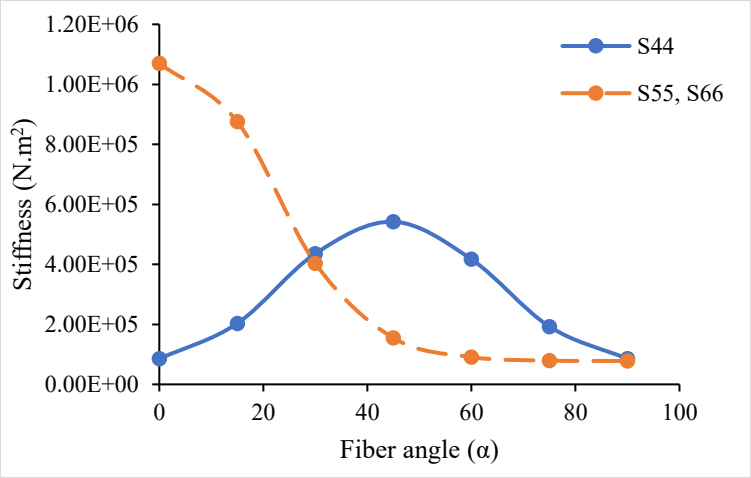

Fig. (4.19). Torsional (S_{44}) and bending (S_{55}, S_{66}) stiffness of the composite tube $[\pm\alpha_5]$ versus fiber angle (α).

4.8 Conclusion

The presented meshless dimensional reduction method for analysis of straight tubes can be studied from two aspects: The accuracy of the simple Pascal polynomial method, and the effect of the lay-up sequence on the need to use refined theory.

It was shown that the simple Pascal polynomial method can provide results that are as accurate as the VABS method and more computationally efficient than 3-D FEA. This has been demonstrated for the determination of the stiffness constants, the through-section strains, and the deflection of beams. This has also been demonstrated for tubes of different lay-up sequences, from simple lay-up sequence such as cross-ply to complicated lay-up sequences with different fiber angle orientations. For example, it has been shown the present cross-sectional analysis can substantially reduce the computational cost compared to 3-D FEM. As such, the present method would be beneficial for structural optimization.

- For tubes made of cross-ply layers *i.e.* $[90_m/0_n]$, there is no significant difference between the stiffness constants obtained using Classical model and Timoshenko model. This is due to the absence of shear coupling terms.
- For straight tubes with the lay-up sequence $[\pm\alpha_5]$, there is no difference between the obtained flexural stiffness of Classical and Timoshenko models.
- In order to obtain sectional stiffness constants of cross-ply tubes, it is not necessary to use higher degree of the polynomial. The polynomial order (m=4) is sufficient.

- For straight tubes with lay-up sequence made of layers of different fiber orientation such as $[45_5/15_5]$, there is a significant difference in the flexural stiffness of Timoshenko and Classical models obtained by both the Pascal polynomial method and VABS 3.8.
- To achieve higher precision of 3D strains for tubes with combination of angle ply layers, the order of applied polynomial needs to be increased, ($m \geq 5$).
- The extensional stiffness (S_{11}) decreases by increasing the fiber angle of a composite tube.
- The magnitude of extensional-torsional (S_{14}) and torsional-bending (S_{36}) of a composite straight tube are maximum at $\alpha = 30^\circ$ of the fiber angle of $[\pm\alpha_5]$ tubes.
- The torsional stiffness (S_{44}) of a straight composite tube is maximum at $\alpha = 45^\circ$ of the fiber angle of $[\pm\alpha_5]$ tubes.
- As the fiber angle increases, the bending stiffness (S_{55} and S_{66}) of a composite tube with lay-up $[\pm\alpha_5]$ decrease.
- The present 1D FE formulation agrees well with 1D FE of ANSYS for a tube with complex lay-up sequence.
- The present method saves computation time considerably. As an example, the analysis of tube of section 4.5.5.1 takes 55 minutes, while the analysis of this tube using Pascal polynomial dimensional reduction method takes only 15 seconds.

5 Chapter 5: Pascal polynomial dimensional reduction method for elliptical tubes

In this chapter, the dimensional reduction method for determining the cross-sectional stiffness constants, strain distribution of composite tubes with elliptical cross-section is presented. The 1D FE solution presented in section 4.4 will be employed to determine transverse deflection of straight elliptical tubes.

5.1 Pascal polynomial dimensional reduction method for elliptical cross-sections

The dimensional reduction procedure using VAM for straight tubes with elliptical section is similar the case of straight tubes presented in chapter (4) except that the angle of layer through the circumference of the tube is not constant and it varies through the circumference. So, this angle should be considered. The matrix [D] in the strain energy for an elliptical tube is considered as follows, see Eq. (3.20).

$$[D] = [T_\beta]^{-1}[T_\alpha]^{-1}[C][T_\alpha]^{-T}[T_\beta]^{-T} \tag{5.1}$$

where [C] is the 6×6 orthotropic material stiffness matrix (Eq. (3.21)) which relates the stresses and strains in the material coordinates e_1, e_2, e_3, [80], $[T_\alpha]$ is the transformation matrix (Eq. (3.22)) that connects the material coordinate system to the coordinate system x_1, y_2 and y_3, and $[T_\beta]$ is the transformation matrix (Eq. (3.23)) which connects the coordinate system x_1, y_2, y_3 to the x_1, x_2, x_3 coordinate system.

It is important that for an elliptical tubular beam the layer angle β changes by the variation of the circumferential angle θ. So, it is important to establish a relation between the circumferential angle θ and the layer angle β. To find this relation, an axillary angle ϕ is defined as shown in Fig. (5.1). The angle ϕ is defined as the counter-clockwise angle between x_2 and y_3. The relation between the layer angle β and this axillary angle ϕ is $\beta = -\pi / 2 + \phi$. It can be shown that the circumferential angle θ is related to the angle ϕ, for the first quadrant, as follows, [86].

$$\phi = \arctan(a^2 / b^2 \tan(\theta)) \tag{5.2}$$

when $\theta = \pi/2$, the use of Eq. (5.2) has uncertainty for the determination of ϕ. There are also complexities for the other quadrants. From geometry considerations, the relationships between ϕ and θ for the whole section can be shown as

$$\phi = \begin{cases} \arctan((\frac{a}{b})^2 \tan(\theta)) & 0 \le \theta < \frac{\pi}{2} \\ \theta & at\ \theta = \frac{\pi}{2} \\ \arctan((\frac{a}{b})^2 \tan(\theta)) + \pi & \frac{\pi}{2} < \theta < \frac{3\pi}{2} \\ \theta & at\ \theta = \frac{3\pi}{2} \\ \arctan((\frac{a}{b})^2 \tan(\theta)) + 2\pi & \frac{3\pi}{2} < \theta < 2\pi \end{cases} \tag{5.3}$$

The relations between ϕ and θ are plotted using Eq. (5.3) in Fig. (5.2). The piecewise function showing the relation between ϕ and θ (Eq. (5.3)) in conjunction with $\beta = -\pi / 2 + \phi$, may be used in calculation of $[T_\beta]$ to calculate the $[D]$ matrix. It is noticed that if Eq. (5.3) is approximated by a polynomial function (*e.g.*, order of 13), the time required for numerical integration later in the analysis is faster using Maple software.

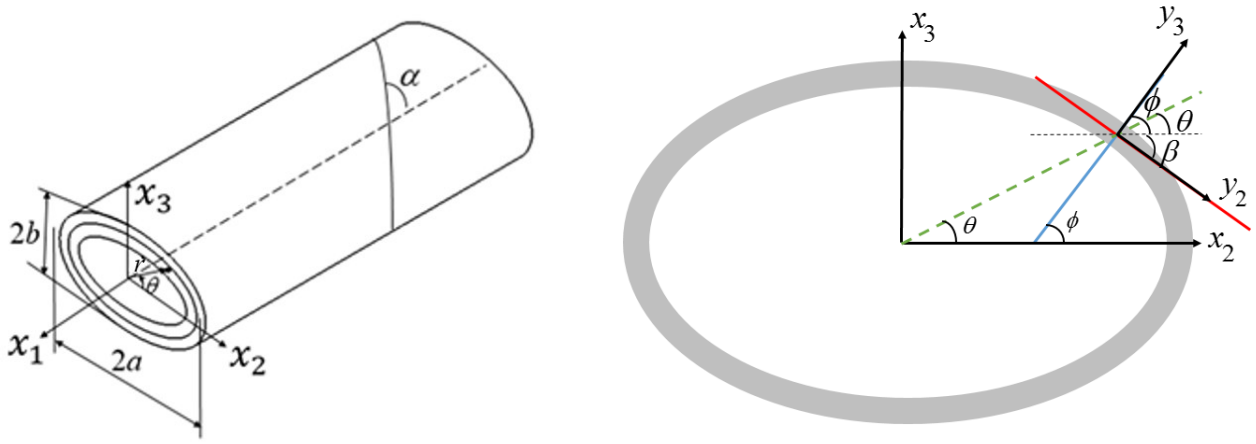

a) *b*)

Fig. (5.1). Coordinate sytem, dimensions, fiber angle and position angle orientation of elliptical composite tube.

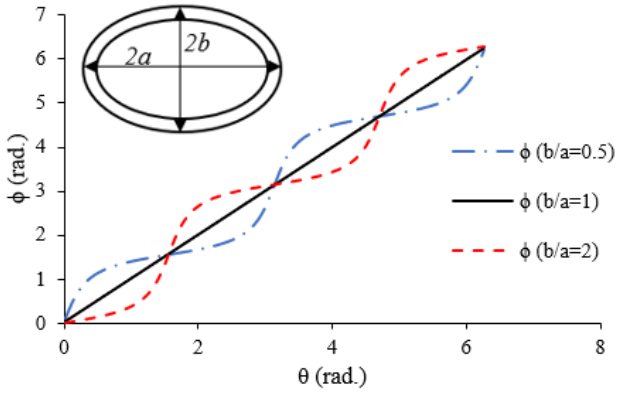

Fig. (5.2). The change of ϕ versus θ for an ellipse with various *b/a*.

5.2 Pascal polynomial dimensional reduction method for unidirectional elliptical tubes

The strain energy of the Eq. (4.1) for a beam with orthotropic material is shown in the Eq. (5.4).

$$
\begin{aligned}
2U = \int_L \iint_R & \left(\left(\left(\bar{\gamma}_{11} + x_3\bar{\kappa}_2 - x_2\bar{\kappa}_3 + \frac{\partial w_1}{\partial x_1} + \left(x_3\frac{\partial w_1}{\partial x_2} - x_2\frac{\partial w_1}{\partial x_3}\right)\right)D_{11} + \left(\frac{\partial w_1}{\partial x_2} - x_3\bar{\kappa}_1 + \frac{\partial w_2}{\partial x_1} + \left(x_3\frac{\partial w_2}{\partial x_2} - x_2\frac{\partial w_2}{\partial x_3}\right)\right)D_{21}\right.\right. \\
& \left.\left. + \left(\frac{\partial w_1}{\partial x_3} + x_2\bar{\kappa}_1 + \frac{\partial w_3}{\partial x_1} + \left(x_3\frac{\partial w_3}{\partial x_2} - x_2\frac{\partial w_3}{\partial x_3}\right)\right)D_{31} + \frac{\partial w_2}{\partial x_2}D_{41} + \left(\frac{\partial w_2}{\partial x_3} + \frac{\partial w_3}{\partial x_2}\right)D_{51} + \frac{\partial w_3}{\partial x_3}D_{61}\right) \right. \\
& \left(\bar{\gamma}_{11} + x_3\bar{\kappa}_2 - x_2\bar{\kappa}_3 + \frac{\partial w_1}{\partial x_1} + \left(x_3\frac{\partial w_1}{\partial x_2} - x_2\frac{\partial w_1}{\partial x_3}\right)\right) + \left(\left(\bar{\gamma}_{11} + x_3\bar{\kappa}_2 - x_2\bar{\kappa}_3 + \frac{\partial w_1}{\partial x_1} + \left(x_3\frac{\partial w_1}{\partial x_2} - x_2\frac{\partial w_1}{\partial x_3}\right)\right)D_{12}\right. \\
& + \left(\frac{\partial w_1}{\partial x_2} - x_3\bar{\kappa}_1 + \frac{\partial w_2}{\partial x_1} + \left(x_3\frac{\partial w_2}{\partial x_2} - x_2\frac{\partial w_2}{\partial x_3}\right)\right)D_{22} + \left(\frac{\partial w_1}{\partial x_3} + x_2\bar{\kappa}_1 + \frac{\partial w_3}{\partial x_1} + \left(x_3\frac{\partial w_3}{\partial x_2} - x_2\frac{\partial w_3}{\partial x_3}\right)\right)D_{32} + \frac{\partial w_2}{\partial x_2}D_{42} \\
& \left. + \left(\frac{\partial w_2}{\partial x_3} + \frac{\partial w_3}{\partial x_2}\right)D_{52} + \frac{\partial w_3}{\partial x_3}D_{62}\right)\left(\frac{\partial w_1}{\partial x_2} - x_3\bar{\kappa}_1 + \frac{\partial w_2}{\partial x_1} + \left(x_3\frac{\partial w_2}{\partial x_2} - x_2\frac{\partial w_2}{\partial x_3}\right)\right) \\
& + \left(\left(\bar{\gamma}_{11} + x_3\bar{\kappa}_2 - x_2\bar{\kappa}_3 + \frac{\partial w_1}{\partial x_1} + \left(x_3\frac{\partial w_1}{\partial x_2} - x_2\frac{\partial w_1}{\partial x_3}\right)\right)D_{13} + \left(\frac{\partial w_1}{\partial x_2} - x_3\bar{\kappa}_1 + \frac{\partial w_2}{\partial x_1} + \left(x_3\frac{\partial w_2}{\partial x_2} - x_2\frac{\partial w_2}{\partial x_3}\right)\right)D_{23}\right. \\
& \left. + \left(\frac{\partial w_1}{\partial x_3} + x_2\bar{\kappa}_1 + \frac{\partial w_3}{\partial x_1} + \left(x_3\frac{\partial w_3}{\partial x_2} - x_2\frac{\partial w_3}{\partial x_3}\right)\right)D_{33} + \frac{\partial w_2}{\partial x_2}D_{43} + \left(\frac{\partial w_2}{\partial x_3} + \frac{\partial w_3}{\partial x_2}\right)D_{53} + \frac{\partial w_3}{\partial x_3}D_{63}\right) \\
& \left(\frac{\partial w_1}{\partial x_3} + x_2\bar{\kappa}_1 + \frac{\partial w_3}{\partial x_1} + \left(x_3\frac{\partial w_3}{\partial x_2} - x_2\frac{\partial w_3}{\partial x_3}\right)\right) + \left(\left(\bar{\gamma}_{11} + x_3\bar{\kappa}_2 - x_2\bar{\kappa}_3 + \frac{\partial w_1}{\partial x_1} + \left(x_3\frac{\partial w_1}{\partial x_2} - x_2\frac{\partial w_1}{\partial x_3}\right)\right)D_{14}\right. \\
& + \left(\frac{\partial w_1}{\partial x_2} - x_3\bar{\kappa}_1 + \frac{\partial w_2}{\partial x_1} + \left(x_3\frac{\partial w_2}{\partial x_2} - x_2\frac{\partial w_2}{\partial x_3}\right)\right)D_{24} + \left(\frac{\partial w_1}{\partial x_3} + x_2\bar{\kappa}_1 + \frac{\partial w_3}{\partial x_1} + \left(x_3\frac{\partial w_3}{\partial x_2} - x_2\frac{\partial w_3}{\partial x_3}\right)\right)D_{34} \\
& \left. + \frac{\partial w_2}{\partial x_2}D_{44} + \left(\frac{\partial w_2}{\partial x_3} + \frac{\partial w_3}{\partial x_2}\right)D_{54} + \frac{\partial w_3}{\partial x_3}D_{64}\right)\frac{\partial w_2}{\partial x_2} + \left(\left(\bar{\gamma}_{11} + x_3\bar{\kappa}_2 - x_2\bar{\kappa}_3 + \frac{\partial w_1}{\partial x_1} + \left(x_3\frac{\partial w_1}{\partial x_2} - x_2\frac{\partial w_1}{\partial x_3}\right)\right)D_{15}\right.
\end{aligned}
\tag{5.4}
$$

$$+\left(\frac{\partial w_1}{\partial x_2}-x_3\overline{\kappa}_1+\frac{\partial w_2}{\partial x_1}+\left(x_3\frac{\partial w_2}{\partial x_2}-x_2\frac{\partial w_2}{\partial x_3}\right)\right)D_{25}+\left(\frac{\partial w_1}{\partial x_3}+x_2\overline{\kappa}_1+\frac{\partial w_3}{\partial x_1}+\left(x_3\frac{\partial w_3}{\partial x_2}-x_2\frac{\partial w_3}{\partial x_3}\right)\right)D_{35}$$

$$+\frac{\partial w_2}{\partial x_2}D_{45}+\left(\frac{\partial w_2}{\partial x_3}+\frac{\partial w_3}{\partial x_2}\right)D_{55}+\frac{\partial w_3}{\partial x_3}D_{65}\Bigg)\left(\frac{\partial w_2}{\partial x_3}+\frac{\partial w_3}{\partial x_2}\right)+\left(\left(\overline{\gamma}_{11}+x_3\overline{\kappa}_2-x_2\overline{\kappa}_3+\frac{\partial w_1}{\partial x_1}+\left(x_3\frac{\partial w_1}{\partial x_2}-x_2\frac{\partial w_1}{\partial x_3}\right)\right)D_{16}\right.$$

$$+\left(\frac{\partial w_1}{\partial x_2}-x_3\overline{\kappa}_1+\frac{\partial w_2}{\partial x_1}+\left(x_3\frac{\partial w_2}{\partial x_2}-x_2\frac{\partial w_2}{\partial x_3}\right)\right)D_{26}+\left(\frac{\partial w_1}{\partial x_3}+x_2\overline{\kappa}_1+\frac{\partial w_3}{\partial x_1}+\left(x_3\frac{\partial w_3}{\partial x_2}-x_2\frac{\partial w_3}{\partial x_3}\right)\right)D_{36}$$

$$\left.+\frac{\partial w_2}{\partial x_2}D_{46}+\left(\frac{\partial w_2}{\partial x_3}+\frac{\partial w_3}{\partial x_2}\right)D_{56}+\frac{\partial w_3}{\partial x_3}D_{66}\right)\frac{\partial w_3}{\partial x_3}\Bigg)dx_3dx_2dx_1$$

where R is the region of the cross-section. In the dimensional reduction method, the VAM is used to perturb the warping field and therefore the strain energy of the beam using the small parameters of the problem. The perturbation is done considering the magnitude of the small terms. These small terms are: ε_{max} is the maximum of the axial strain, h / r_o is the thickness-to- radius ratio and r_o / L radius-to-length ratio. r_o is the mean radius of the elliptical beam cross-section. One can conclude that $h/L \ll 1$. The warping field can be written in the following form, [55].

$$\underset{\varepsilon_{max}}{w_1}=\underset{\varepsilon_{max}}{w_{10}}+\underset{\varepsilon_{max}\frac{h}{L}}{w_{11}}\;;\underset{\varepsilon_{max}}{w_2}=\underset{\varepsilon_{max}}{w_{20}}+\underset{\varepsilon_{max}\frac{h}{L}}{w_{21}}\;;\underset{\varepsilon_{max}}{w_3}=\underset{\varepsilon_{max}}{w_{30}}+\underset{\varepsilon_{max}\frac{h}{L}}{w_{31}} \tag{5.5a}$$

$$\underset{\varepsilon_{max}}{\frac{\partial w_1}{\partial x_i}}=\underset{\varepsilon_{max}}{\frac{\partial w_{10}}{\partial x_i}}+\underset{\varepsilon_{max}\frac{h}{L}}{\frac{\partial w_{11}}{\partial x_i}};\ \underset{\varepsilon_{max}}{\frac{\partial w_2}{\partial x_i}}=\underset{\varepsilon_{max}}{\frac{\partial w_{20}}{\partial x_i}}+\underset{\varepsilon_{max}\frac{h}{L}}{\frac{\partial w_{21}}{\partial x_i}};\ \underset{\varepsilon_{max}}{\frac{\partial w_3}{\partial x_i}}=\underset{\varepsilon_{max}}{\frac{\partial w_{30}}{\partial x_i}}+\underset{\varepsilon_{max}\frac{h}{L}}{\frac{\partial w_{31}}{\partial x_i}}\qquad i=2,\,3 \tag{5.5b}$$

$$\underset{\varepsilon_{max}\frac{h}{L}}{\frac{\partial w_1}{\partial x_1}}=\underset{\varepsilon_{max}\frac{h}{L}}{\frac{\partial w_{10}}{\partial x_1}}+\underset{\varepsilon_{max}(\frac{h}{L})^2}{\frac{\partial w_{11}}{\partial x_1}}\;;\ \underset{\varepsilon_{max}\frac{h}{L}}{\frac{\partial w_2}{\partial x_1}}=\underset{\varepsilon_{max}\frac{h}{L}}{\frac{\partial w_{20}}{\partial x_1}}+\underset{\varepsilon_{max}(\frac{h}{L})^2}{\frac{\partial w_{21}}{\partial x_1}}\;;\ \underset{\varepsilon_{max}\frac{h}{L}}{\frac{\partial w_3}{\partial x_1}}=\underset{\varepsilon_{max}\frac{h}{L}}{\frac{\partial w_{30}}{\partial x_1}}+\underset{\varepsilon_{max}(\frac{h}{L})^2}{\frac{\partial w_{31}}{\partial x_1}} \tag{5.5c}$$

In Eq. (5.5a), the warping displacements w_1, w_2, w_3 are considered to consist of terms of order O (ε_{max}) as (w_{10}, w_{20}, w_{30}) and terms of order O ($\varepsilon_{max}(\frac{h}{L})$) as (w_{11}, w_{21}, w_{31}). Substituting Eq. (5.5) into Eq. (5.4) and collecting the different orders of the strain energy expressions, we collect the expressions up to order $O(\varepsilon_{max}^2)$ which leads to the first approximation of the strain energy. Selecting the expressions up to the order $O(\varepsilon_{max}^2(\frac{h}{L})^2)$, we achieve the second approximation of the strain energy of the beam. First approximation of the strain energy for an anisotropic beam can be written as Eq. (5.6).

$$
\begin{aligned}
2U_0 = \int_L \int_R \int (& \frac{\partial w_{10}}{\partial x_2}\frac{\partial w_{10}}{\partial x_3}D_{32} + \frac{\partial w_{20}}{\partial x_2}\frac{\partial w_{10}}{\partial x_2}D_{24} + D_{56}\frac{\partial w_{30}}{\partial x_3}\frac{\partial w_{30}}{\partial x_2} + D_{35}\frac{\partial w_{10}}{\partial x_3}\frac{\partial w_{20}}{\partial x_3} \\
& + D_{25}\frac{\partial w_{10}}{\partial x_2}\frac{\partial w_{30}}{\partial x_2} + D_{26}\frac{\partial w_{30}}{\partial x_3}\frac{\partial w_{10}}{\partial x_2} + D_{23}\frac{\partial w_{10}}{\partial x_3}\frac{\partial w_{10}}{\partial x_2} + D_{43}\frac{\partial w_{10}}{\partial x_3}\frac{\partial w_{20}}{\partial x_2} + D_{65}\frac{\partial w_{30}}{\partial x_3}\frac{\partial w_{20}}{\partial x_3} \\
& + D_{63}\frac{\partial w_{10}}{\partial x_3}\frac{\partial w_{30}}{\partial x_3} + D_{53}\frac{\partial w_{10}}{\partial x_3}\frac{\partial w_{20}}{\partial x_3} + D_{53}\frac{\partial w_{10}}{\partial x_3}\frac{\partial w_{30}}{\partial x_2} + D_{54}\frac{\partial w_{20}}{\partial x_2}\frac{\partial w_{20}}{\partial x_3} + D_{34}\frac{\partial w_{20}}{\partial x_2}\frac{\partial w_{10}}{\partial x_3} \\
& + D_{52}\frac{\partial w_{10}}{\partial x_2}\frac{\partial w_{20}}{\partial x_3} + D_{52}\frac{\partial w_{10}}{\partial x_2}\frac{\partial w_{30}}{\partial x_2} + D_{42}\frac{\partial w_{10}}{\partial x_2}\frac{\partial w_{20}}{\partial x_2} + D_{62}\frac{\partial w_{10}}{\partial x_2}\frac{\partial w_{30}}{\partial x_3} + D_{36}\frac{\partial w_{30}}{\partial x_3}\frac{\partial w_{10}}{\partial x_3} \\
& + D_{65}\frac{\partial w_{30}}{\partial x_3}\frac{\partial w_{30}}{\partial x_2} + D_{46}\frac{\partial w_{30}}{\partial x_3}\frac{\partial w_{20}}{\partial x_2} + D_{56}\frac{\partial w_{30}}{\partial x_3}\frac{\partial w_{20}}{\partial x_3} + D_{35}\frac{\partial w_{10}}{\partial x_3}\frac{\partial w_{30}}{\partial x_2} + D_{54}\frac{\partial w_{20}}{\partial x_2}\frac{\partial w_{30}}{\partial x_2} \\
& + D_{64}\frac{\partial w_{20}}{\partial x_2}\frac{\partial w_{30}}{\partial x_3} + 2D_{55}\frac{\partial w_{20}}{\partial x_3}\frac{\partial w_{30}}{\partial x_2} + D_{45}\frac{\partial w_{20}}{\partial x_2}\frac{\partial w_{20}}{\partial x_3} + D_{45}\frac{\partial w_{20}}{\partial x_2}\frac{\partial w_{30}}{\partial x_2} + 2D_{21}\frac{\partial w_{10}}{\partial x_2}\bar{\gamma}_{11} \\
& + 2D_{51}\frac{\partial w_{20}}{\partial x_3}\bar{\gamma}_{11} + 2D_{41}\frac{\partial w_{20}}{\partial x_2}\bar{\gamma}_{11} + 2D_{31}\frac{\partial w_{10}}{\partial x_3}\bar{\gamma}_{11} + 2D_{61}\frac{\partial w_{30}}{\partial x_3}\bar{\gamma}_{11} + 2D_{51}\frac{\partial w_{30}}{\partial x_2}\bar{\gamma}_{11} \\
& + x_3{}^2\bar{\kappa}_2{}^2D_{11} + x_2{}^2\bar{\kappa}_3{}^2D_{11} + x_2{}^2\bar{\kappa}_1{}^2D_{33} + x_3{}^2\bar{\kappa}_1{}^2D_{22} + D_{55}\frac{\partial w_{30}{}^2}{\partial x_2} + D_{44}\frac{\partial w_{20}{}^2}{\partial x_2} + D_{66}\frac{\partial w_{30}{}^2}{\partial x_3} \\
& + D_{22}\frac{\partial w_{10}{}^2}{\partial x_2} + D_{55}\frac{\partial w_{20}{}^2}{\partial x_3} + D_{33}\frac{\partial w_{10}{}^2}{\partial x_3} + D_{25}\frac{\partial w_{10}}{\partial x_2}\frac{\partial w_{20}}{\partial x_3} + D_{12}x_3x_2\bar{\kappa}_1\bar{\kappa}_3 + D_{13}x_2x_3\bar{\kappa}_1\bar{\kappa}_2 \\
& + D_{31}x_3x_2\bar{\kappa}_1\bar{\kappa}_2 + D_{21}x_2x_3\bar{\kappa}_1\bar{\kappa}_3 + D_{11}\bar{\gamma}_{11}{}^2 + 2D_{21}\frac{\partial w_{10}}{\partial x_2}x_3\bar{\kappa}_2 - 2D_{21}\frac{\partial w_{10}}{\partial x_2}x_2\bar{\kappa}_3 + 2D_{31}\frac{\partial w_{10}}{\partial x_3}x_3\bar{\kappa}_2 \\
& - 2D_{31}\frac{\partial w_{10}}{\partial x_3}x_2\bar{\kappa}_3 + 2D_{41}\frac{\partial w_{20}}{\partial x_2}x_3\bar{\kappa}_2 - 2D_{41}\frac{\partial w_{20}}{\partial x_2}x_2\bar{\kappa}_3 + 2D_{51}\frac{\partial w_{20}}{\partial x_3}x_3\bar{\kappa}_2 - 2D_{51}\frac{\partial w_{20}}{\partial x_3}x_2\bar{\kappa}_3 \\
& + 2D_{51}\frac{\partial w_{30}}{\partial x_2}x_3\bar{\kappa}_2 - 2D_{51}\frac{\partial w_{30}}{\partial x_2}x_2\bar{\kappa}_3 - 2D_{52}x_3\bar{\kappa}_1\frac{\partial w_{30}}{\partial x_2} - 2D_{62}x_3\bar{\kappa}_1\frac{\partial w_{30}}{\partial x_3} + 2D_{23}x_2\bar{\kappa}_1\frac{\partial w_{10}}{\partial x_2} \\
& + 2D_{33}x_2\bar{\kappa}_1\frac{\partial w_{10}}{\partial x_3} + 2D_{43}x_2\bar{\kappa}_1\frac{\partial w_{20}}{\partial x_2} + 2D_{53}x_2\bar{\kappa}_1\frac{\partial w_{20}}{\partial x_3} + 2x_2\bar{\kappa}_1D_{53}\frac{\partial w_{30}}{\partial x_2} + 2D_{63}x_2\bar{\kappa}_1\frac{\partial w_{30}}{\partial x_3} \\
& + 2D_{11}\bar{\gamma}_{11}x_3\bar{\kappa}_2 - 2D_{11}\gamma_{11}x_2\bar{\kappa}_3 - D_{21}\bar{\gamma}_{11}x_3\bar{\kappa}_1 + D_{31}\bar{\gamma}_{11}x_2\bar{\kappa}_1 - D_{12}\bar{\kappa}_1x_3\bar{\gamma}_{11} - D_{12}\bar{\kappa}_1x_3{}^2\bar{\kappa}_2 - D_{32}x_3x_2\bar{\kappa}_1{}^2 \\
& + D_{13}x_2\bar{\gamma}_{11}\bar{\kappa}_1 - D_{13}x_2{}^2\bar{\kappa}_1\bar{\kappa}_3 - D_{23}x_2x_3\bar{\kappa}_1{}^2 - D_{21}x_3{}^2\bar{\kappa}_2\bar{\kappa}_1 - D_{31}x_2{}^2\bar{\kappa}_3\bar{\kappa}_1 - 2D_{11}x_2x_3\bar{\kappa}_2\bar{\kappa}_3)dx_3dx_2dx_1
\end{aligned}
\tag{5.6}
$$

5.2.1 Pascal polynomial method

Eq. (5.6) consists of derivatives with respect to the coordinate variables x_1, x_2, x_3 of order $O(\varepsilon_{\max}^2)$ of the warping displacement w_{10}, w_{20}, w_{30}, along with the 1D strain variables $\bar{\gamma}_{11}$, $\bar{\kappa}_1$, $\bar{\kappa}_2$, $\bar{\kappa}_3$ and the material constants D_{ij}.

In the VAM, the warping displacements are assumed to be functions of the coordinates x_2 and x_3 only. The VABS uses finite element mesh for the cross-sectional discretization. The displacement for the different type of elements (linear or quadratic) can be assumed, and the degree of accuracy depends on the mesh size. This is the basis for the development of the VABS software. For sections of regular geometry such as circular cross-section, finite element method is not necessary, and a simpler approach can be used. The Pascal polynomial method was introduced in [79]. Here for the elliptical cross section, a similar approach is used. The Pascal polynomials are:

$$\begin{aligned} w_{10}(x_1,x_2,x_3) &= a_1(x_1) + a_2(x_1)x_2 + a_3(x_1)x_3 + a_4(x_1)x_2^2 + a_5(x_1)x_3x_2 + a_6(x_1)x_3^2 \\ w_{20}(x_1,x_2,x_3) &= a_7(x_1) + a_8(x_1)x_2 + a_9(x_1)x_3 + a_{10}(x_1)x_2^2 + a_{11}(x_1)x_3x_2 + a_{12}(x_1)x_3^2 \\ w_{30}(x_1,x_2,x_3) &= a_{13}(x_1) + a_{14}(x_1)x_2 + a_{15}(x_1)x_3 + a_{16}(x_1)x_2^2 + a_{17}(x_1)x_3x_2 + a_{18}(x_1)x_3^2 \end{aligned} \tag{5.7}$$

The warping displacements of the Eq. (5.7), contain unknown coefficients a_1 to a_{18} that need to be determined. The number of the coefficients may depend on the complexity of the section. The determination of these coefficients is done by the minimization of the strain energy of the beam. Substituting the Eq. (5.7) into the strain energy of the Eq. (5.6), the strain energy, which is a function of coordinates x_2, x_3 and Pascal coefficients (a_1 to a_{18}) will be obtained. We consider the material properties for a unidirectional elliptical tube as, [82]

$$\begin{aligned} &E_1 = E_t; E_2 = E_3 = E_p; \nu_{12} = \nu_{13} = \nu_{tp}; \nu_{21} = \nu_{12}E_2 / E_1; \nu_{23} = \nu_p; \\ &\nu_{32} = \nu_{23}E_3 / E_2; \nu_{31} = \nu_{13}E_3 / E_1; G_{12} = G_{13} = G_t; G_{23} = G_p \end{aligned} \tag{5.8}$$

where, $G_p = \dfrac{E_p}{2(1+\nu_p)}$ and p stands for "in-plane" and t strands for "transverse". It can be shown that for the case of tubes made by unidirectional composites (fibers oriented along the axis of the tube), $[D] = [C]$. Substituting Eq. (5.7) into Eq. (5.6), the strain energy can be expressed as follows. The calculation of the strain energy is performed in Maple software.

$$2U_0 = \int_L \iint_R \left(\left(\frac{\left(x_3\bar{\kappa}_2 - x_2\bar{\kappa}_3 + \bar{\gamma}_{11}\right)E_t^2\left(\nu_p - 1\right)}{\nu_p E_t + 2\nu_{tp}^2 E_p - E_t} - \frac{E_p E_t \nu_{tp}}{\nu_p E_t + 2.\nu_{tp}^2 E_p - 1.E_t}\frac{\partial w_2}{\partial x_2} - \frac{E_p E_t \nu_{tp}}{2\nu_{tp}^2 E_p + \nu_p E_t - E_t}\frac{\partial w_3}{\partial x_3} \right) \right.$$
$$\left(x_3\bar{\kappa}_2 - x_2\bar{\kappa}_3 + \bar{\gamma}_{11}\right) + \left(\frac{\partial w_1}{\partial x_2} - x_3\bar{\kappa}_1\right)^2 G_t + \left(\frac{\partial w_1}{\partial x_3} + x_2\bar{\kappa}_1\right)^2 G_t + \left(-\frac{\left(x_3\bar{\kappa}_2 - x_2\bar{\kappa}_3 + \bar{\gamma}_{11}\right)E_p E_t \nu_{tp}}{\nu_p E_t + 2.\nu_{tp}^2 E_p - E_t} \right.$$
$$+ \frac{E_p\left(-E_t + \nu_{tp}^2 E_p\right)}{\left(1+\nu_p\right)\left(\nu_p E_t + 2\nu_{tp}^2 E_p - E_t\right)}\frac{\partial w_2}{\partial x_2} - \frac{E_p\left(\nu_{tp}^2 E_p + \nu_p E_t\right)}{\left(1+\nu_p\right)\left(\nu_p E_t + 2\nu_{tp}^2 E_p - E_t\right)}\frac{\partial w_3}{\partial x_3} \left.\right)\frac{\partial w_2}{\partial x_2} \qquad (5.9)$$
$$+ \frac{1}{2}\frac{\left(\frac{\partial w_2}{\partial x_3} + \frac{\partial w_3}{\partial x_2}\right)^2 E_p}{1+\nu_p} + \left(-\frac{\left(x_3\bar{\kappa}_2 - x_2\bar{\kappa}_3 + \bar{\gamma}_{11}\right)E_p E_t \nu_{tp}}{2\nu_{tp}^2 E_p + \nu_p E_t - E_t} - \right.$$
$$\left. \left. \frac{E_p\left(\nu_{tp}^2 E_p + \nu_p E_t\right)}{\left(1+\nu_p\right)\left(\nu_p E_t + 2\nu_{tp}^2 E_p - E_t\right)}\frac{\partial w_2}{\partial x_2} + \frac{E_p\left(-E_t + \nu_{tp}^2 E_p\right)}{\left(1+\nu_p\right)\left(\nu_p E_t + 2\nu_{tp}^2 E_p - E_t\right)}\frac{\partial w_3}{\partial x_3} \right)\frac{\partial w_3}{\partial x_3} \right) dx_3 dx_2 dx_1$$

The aim is to carry out the integration of Eq. (5.9) in an elliptical region $R = \left\{ (x_2, x_3) \,|\, \frac{x_2^2}{a^2} + \frac{x_3^2}{b^2} \le 1 \right\}$. A change of variable can be considered as in Eq. (5.10).

$$\begin{aligned} x_2 &= a\xi \\ x_3 &= b\eta \end{aligned} \qquad (5.10)$$

where *a* and *b* are major and minor radii of the ellipse. ξ and η are the coordinates in which an ellipse is transformed to a circle and $0 \le \xi \le 1$ and $0 \le \eta \le 1$, where the region of the integration is $\tilde{R} = \left\{ (\xi, \eta) \,|\, \xi^2 + \eta^2 \le 1 \right\}$. The integration of Eq. (5.9) will be as

$$2U_0 = \int_L \iint_R f(x_2, x_3) dx_3 dx_2 dx_1 = \int_L \iint_{\tilde{R}} f(g(\xi,\eta), h(\xi,\eta)) J d\xi d\eta dx_1 \qquad (5.11)$$

Where *J* is the Jacobian, $J = \frac{\partial x_2}{\partial \xi}\frac{\partial x_3}{\partial \eta} - \frac{\partial x_2}{\partial \eta}\frac{\partial x_3}{\partial \xi}$. One can transform the coordinates ξ and η to polar coordinates by substituting $\xi = r\cos(\theta)$ and $\eta = r\sin(\theta)$ where r is a non-dimensional variable ($0 \le r \le 1$) and $0 \le \theta \le 2\pi$. Therefore, the strain energy of the elliptical tube with inner major radius of a_i, inner minor radius b_i, outer major radius a_{out} and outer minor radius b_{out} is written by subtraction of the strain energy of an ellipse rod with the outer radii of (a_{out}, b_{out}) and an imaginary ellipse rod with the radii of (a_i, b_i) with the same material. The strain energy can be expressed as Eq. (5.12).

$$2U_0 = 2\left(\int_{x_1=0}^{L}\int_{r=0}^{1}\int_{\theta=0}^{2\pi} U_0 a_{out} b_{out} r dr d\theta dx_1 - \int_{x_1=0}^{L}\int_{r=0}^{1}\int_{\theta=0}^{2\pi} U_0 a_i b_i r dr d\theta dx_1\right) \tag{5.12}$$

The simplified strain energy of Eq. (5.12) is written in Eq. (5.13).

$$\begin{aligned}
2U_0 = {} & \frac{\pi}{8} a_{out} b_{out} \frac{1}{-E_t + 2\nu_{tp}^2 E_p + \nu_p^2 E_t + 2\nu_p \nu_{tp}^2 E_p} \Big(4G_t b_{out}^2 \bar{\kappa}_1^2 \nu_p \nu_{tp}^2 E_p + 4G_t a_{out}^2 \bar{\kappa}_1^2 \nu_p \nu_{tp}^2 E_p \\
& + 16 G_t a_4^2 a_{out}^2 \nu_p \nu_{tp}^2 E_p - 8 G_t a_5 b_{out}^2 \bar{\kappa}_1 \nu_{tp}^2 E_p - 4 G_t a_5 b_{out}^2 \bar{\kappa}_1 \nu_p^2 E_t + 8 G_t a_5 a_{out}^2 \bar{\kappa}_1 \nu_{tp}^2 E_p + 4 G_t a_5 a_{out}^2 \bar{\kappa}_1 \nu_p^2 E_t \\
& + 4 G_t a_5^2 b_{out}^2 \nu_p \nu_{tp}^2 E_p + 4 G_t a_5^2 a_{out}^2 \nu_p \nu_{tp}^2 E_p + 16 G_t a_6^2 b_{out}^2 \nu_p \nu_{tp}^2 E_p - 16 E_t E_p \nu_{tp} a_8 \bar{\gamma}_{11} \nu_p + 8 E_t E_p \nu_{tp} a_{10} a_{out}^2 \bar{\kappa}_3 \\
& - 4 E_t E_p \nu_{tp} a_{11} b_{out}^2 \bar{\kappa}_2 - 16. E_t E_p \nu_{tp} a_{15} \bar{\gamma}_{11} \nu_p + 4 E_p a_{11} a_{out}^2 a_{16} \nu_p E_t + 4 E_t E_p \nu_{tp} a_{17} a_{out}^2 \bar{\kappa}_3 - 8 E_p a_{17} a_{out}^2 \nu_p E_t a_{10} \\
& + 4 E_p a_{12} b_{out}^2 a_{17} \nu_p E_t - 8 E_t E_p \nu_{tp} a_{18} b_{out}^2 \bar{\kappa}_2 - 8 E_p a_{18} b_{out}^2 \nu_p E_t a_{11} + 8 E_t^2 \bar{\gamma}_{11}^2 \nu_p^2 - 8 E_t^2 \bar{\gamma}_{11}^2 - 8 E_p E_t \nu_{tp} b_{out}^2 \bar{\kappa}_2 \nu_p a_{18} \\
& + 4 E_p E_t \nu_{tp} a_{out}^2 \bar{\kappa}_3 \nu_p a_{17} - 4 E_p E_t \nu_{tp} b_{out}^2 \bar{\kappa}_2 \nu_p a_{11} + 8 E_p E_t \nu_{tp} a_{out}^2 \bar{\kappa}_3 \nu_p a_{10} - 8 G_t a_5 b_{out}^2 \bar{\kappa}_1 \nu_p \nu_{tp}^2 E_p \\
& + 8 G_t a_5 a_{out}^2 \bar{\kappa}_1 \nu_p \nu_{tp}^2 E_p - 2 G_t b_{out}^2 \bar{\kappa}_1^2 E_t - 2 G_t a_{out}^2 \bar{\kappa}_1^2 E_t + 2 E_t^2 b_{out}^2 \bar{\kappa}_2^2 \nu_p^2 + 2 E_t^2 a_{out}^2 \bar{\kappa}_3^2 \nu_p^2 \\
& + 16 G_t a_2^2 \nu_{tp}^2 E_p + 8 G_t a_2^2 \nu_p^2 E_t + 16 G_t a_3^2 \nu_{tp}^2 E_p + 8 G_t a_3^2 \nu_p^2 E_t + 8 a_8^2 \nu_{tp}^2 E_p^2 - 8 G_t a_3^2 E_t \\
& - 8 G_t a_2^2 E_t - 2 E_t^2 a_{out}^2 \bar{\kappa}_3^2 - 2 E_t^2 b_{out}^2 \bar{\kappa}_2^2 + 8 a_{15}^2 \nu_{tp}^2 E_p^2 - 4 E_p a_{14}^2 E_t - 8 E_p a_{15}^2 E_t \\
& - 8 E_p a_8^2 E_t + 8 a_9^2 \nu_{tp}^2 E_p^2 - 4 E_p a_9^2 E_t + 8 a_{14}^2 \nu_{tp}^2 E_p^2 - 8 G_t a_4^2 a_{out}^2 E_t - 2 G_t a_5^2 a_{out}^2 E_t \\
& - 2 G_t a_5^2 b_{out}^2 E_t - 8 G_t a_6^2 b_{out}^2 E_t + 4 E_p a_9^2 \nu_p E_t - 8 E_p a_{10}^2 a_{out}^2 E_t + 8 E_p^2 a_{10}^2 a_{out}^2 \nu_{tp}^2 \\
& - E_p a_{11}^2 a_{out}^2 E_t + 2 a_{11}^2 a_{out}^2 \nu_{tp}^2 E_p^2 - 2 E_p a_{11}^2 b_{out}^2 E_t + 2 E_p^2 a_{11}^2 b_{out}^2 \nu_{tp}^2 - 4 E_p a_{12}^2 b_{out}^2 E_t \\
& + 8 a_{12}^2 b_{out}^2 \nu_{tp}^2 E_p^2 + 4 E_p a_{14}^2 \nu_p E_t + 16 a_9 a_{14} \nu_{tp}^2 E_p^2 - 8 E_p a_9 a_{14} E_t - 16 a_{15} \nu_{tp}^2 E_p^2 a_8 \\
& - 4 E_p a_{16}^2 a_{out}^2 E_t + 8 a_{16}^2 a_{out}^2 \nu_{tp}^2 E_p^2 - E_p a_{17}^2 b_{out}^2 E_t + 2 a_{17}^2 b_{out}^2 \nu_{tp}^2 E_p^2 - 2 E_p a_{17}^2 a_{out}^2 E_t \\
& + 2 E_p^2 a_{17}^2 a_{out}^2 \nu_{tp}^2 - 8 E_p a_{18}^2 b_{out}^2 E_t + 8 E_p^2 a_{18}^2 b_{out}^2 \nu_{tp}^2 + 4 G_t a_{out}^2 \bar{\kappa}_1^2 \nu_{tp}^2 E_p + 2 G_t a_{out}^2 \bar{\kappa}_1^2 \nu_p^2 E_t \\
& + 4 G_t b_{out}^2 \bar{\kappa}_1^2 \nu_{tp}^2 E_p + 2 G_t b_{out}^2 \bar{\kappa}_1^2 \nu_p^2 E_t + 16 G_t a_2^2 \nu_p \nu_{tp}^2 E_p + 16 G_t a_3^2 \nu_p \nu_{tp}^2 E_p + 16 G_t a_4^2 a_{out}^2 \nu_{tp}^2 E_p \\
& 4 G_t a_5^2 b_{out}^2 \nu_{tp}^2 E_p + 2 G_t a_5^2 b_{out}^2 \nu_p^2 E_t + 4 G_t a_5^2 a_{out}^2 \nu_{tp}^2 E_p + 2 G_t a_5^2 a_{out}^2 \nu_p^2 E_t + 4 G_t a_5 b_{out}^2 \bar{\kappa}_1 E_t \\
& - 4 G_t a_5 a_{out}^2 \bar{\kappa}_1 E_t + 16 G_t a_6^2 b_{out}^2 \nu_{tp}^2 E_p + 8 G_t a_6^2 b_{out}^2 \nu_p^2 E_t - 16 E_t E_p \nu_{tp} a_8 \bar{\gamma}_{11} + E_p a_{11}^2 a_{out}^2 \nu_p E_t \\
& + 4 E_p a_{12}^2 b_{out}^2 \nu_p E_t + 8 E_p a_9 a_{14} \nu_p E_t - 16 E_t E_p \nu_{tp} a_{15} \bar{\gamma}_{11} - 16 E_p a_{15} \nu_p E_t a_8 + 4 E_p a_{16}^2 a_{out}^2 \nu_p E_t \\
& + 8 a_{11} a_{out}^2 a_{16} \nu_{tp}^2 E_p^2 - 4 E_p a_{11} a_{out}^2 a_{16} E_t + E_p a_{17}^2 b_{out}^2 \nu_p E_t - 8 E_p^2 a_{17} a_{out}^2 \nu_{tp}^2 a_{10} + 8 a_{12} b_{out}^2 a_{17} \nu_{tp}^2 E_p^2 \\
& + 8 G_t a_4^2 a_{out}^2 \nu_p^2 E_t - 4. E_p a_{12} b_{out}^2 a_{17} E_t - 8. E_p^2 a_{18} b_{out}^2 \nu_{tp}^2 a_{11} \Big) \\
& - \frac{\pi}{8} a_i b_i \frac{1}{-E_t + 2\nu_{tp}^2 E_p + \nu_p^2 E_t + 2\nu_p \nu_{tp}^2 E_p} \Big(4 G_t a_i^2 \bar{\kappa}_1^2 \nu_p \nu_{tp}^2 E_p + 4 G_t b_i^2 \bar{\kappa}_1^2 \nu_p \nu_{tp}^2 E_p \\
& + 16 G_t a_4^2 a_i^2 \nu_p \nu_{tp}^2 E_p + 8 G_t a_5 a_i^2 \bar{\kappa}_1 \nu_{tp}^2 E_p + 4 G_t a_5 a_i^2 \bar{\kappa}_1 \nu_p^2 E_t - 8 G_t a_5 b_i^2 \bar{\kappa}_1 \nu_{tp}^2 E_p - 4 G_t a_5 b_i^2 \bar{\kappa}_1 \nu_p^2 E_t \\
& + 4 G_t a_5^2 a_i^2 \nu_p \nu_{tp}^2 E_p + 4 G_t a_5^2 b_i^2 \nu_p \nu_{tp}^2 E_p + 16 G_t a_6^2 b_i^2 \nu_p \nu_{tp}^2 E_p - 16 E_t E_p \nu_{tp} a_8 \bar{\gamma}_{11} \nu_p + 8 E_t E_p \nu_{tp} a_{10} a_i^2 \bar{\kappa}_3 \\
& - 4 E_p E_t \nu_{tp} b_i^2 \bar{\kappa}_2 a_{11} - 16 E_t E_p \nu_{tp} a_{15} \bar{\gamma}_{11} \nu_p + 4 E_p a_{11} a_i^2 a_{16} \nu_p E_t + 4 E_t E_p \nu_{tp} a_{17} a_i^2 \bar{\kappa}_3 - 8 E_p a_{17} a_i^2 \nu_p E_t a_{10}
\end{aligned} \tag{5.13}$$

$$+4E_p a_{12} b_i^2 a_{17} \nu_p E_t - 8E_p E_t \nu_{tp} b_i^2 \bar{\kappa}_2 a_{18} - 8E_p a_{18} b_i^2 \nu_p E_t a_{11} + 8E_t^2 \bar{\gamma}_{11}^2 \nu_p^2 - 8E_t^2 \bar{\gamma}_{11}^2$$
$$+4E_p E_t \nu_{tp} a_i^2 \bar{\kappa}_3 \nu_p a_{17} - 4E_p E_t \nu_{tp} b_i^2 \bar{\kappa}_2 \nu_p a_{11} + 8E_p E_t \nu_{tp} a_i^2 \bar{\kappa}_3 \nu_p a_{10} - 8G_t a_5 b_i^2 \bar{\kappa}_1 \nu_p \nu_{tp}^2 E_p$$
$$+8G_t a_5 a_i^2 \bar{\kappa}_1 \nu_p \nu_{tp}^2 E_p - 2G_t b_i^2 \bar{\kappa}_1^2 E_t - 2G_t a_i^2 \bar{\kappa}_1^2 E_t + 2E_t^2 b_i^2 \bar{\kappa}_2^2 \nu_p^2 + 2E_t^2 a_i^2 \bar{\kappa}_3^2 \nu_p^2 + 16G_t a_2^2 \nu_{tp}^2 E_p$$
$$+8G_t a_2^2 \nu_p^2 E_t + 16G_t a_3^2 \nu_{tp}^2 E_p + 8G_t a_3^2 \nu_p^2 E_t + 8a_8^2 \nu_{tp}^2 E_p^2 - 8G_t a_3^2 E_t - 8G_t a_2^2 E_t - 2E_t^2 a_i^2 \bar{\kappa}_3^2$$
$$-2E_t^2 b_i^2 \bar{\kappa}_2^2 + 8a_{15}^2 \nu_{tp}^2 E_p^2 - 4E_p a_{14}^2 E_t - 8E_p a_{15}^2 E_t - 8E_p a_8^2 E_t + 8a_9^2 \nu_{tp}^2 E_p^2 - 4E_p a_9^2 E_t$$
$$+8a_{14}^2 \nu_{tp}^2 E_p^2 - 8G_t a_4^2 a_i^2 E_t - 2G_t a_5^2 b_i^2 E_t - 2G_t a_5^2 a_i^2 E_t - 8G_t a_6^2 b_i^2 E_t + 4E_p a_9^2 \nu_p E_t$$
$$-8E_p a_{10}^2 a_i^2 E_t + 8E_p^2 a_{10}^2 a_i^2 \nu_{tp}^2 - E_p a_{11}^2 a_i^2 E_t + 2a_{11}^2 a_i^2 \nu_{tp}^2 E_p^2 - 2E_p a_{11}^2 b_i^2 E_t + 2E_p^2 a_{11}^2 b_i^2 \nu_{tp}^2$$
$$-4E_p a_{12}^2 b_i^2 E_t + 8a_{12}^2 b_i^2 \nu_{tp}^2 E_p^2 + 4E_p a_{14}^2 \nu_p E_t + 16a_9 a_{14} \nu_{tp}^2 E_p^2 - 8E_p a_9 a_{14} E_t - 16a_{15} \nu_{tp}^2 E_p^2 a_8$$
$$-4E_p a_{16}^2 a_i^2 E_t + 8a_{16}^2 a_i^2 \nu_{tp}^2 E_p^2 - E_p a_{17}^2 b_i^2 E_t + 2a_{17}^2 b_i^2 \nu_{tp}^2 E_p^2 2E_p^2 a_{17}^2 a_i^2 \nu_{tp}^2 - 2E_p a_{17}^2 a_i^2 E_t$$
$$+8E_p^2 a_{18}^2 b_i^2 \nu_{tp}^2 - 8E_p a_{18}^2 b_i^2 E_t - 8E_p E_t \nu_{tp} b_i^2 \bar{\kappa}_2 \nu_p a_{18} + 2G_t b_i^2 \bar{\kappa}_1^2 \nu_p^2 E_t + 4G_t b_i^2 \bar{\kappa}_1^2 \nu_{tp}^2 E_p$$
$$+2G_t a_i^2 \bar{\kappa}_1^2 \nu_p^2 E_t + 4G_t a_i^2 \bar{\kappa}_1^2 \nu_{tp}^2 E_p + 16G_t a_2^2 \nu_p \nu_{tp}^2 E_p + 16G_t a_3^2 \nu_p \nu_{tp}^2 E_p + 16G_t a_4^2 a_i^2 \nu_{tp}^2 E_p$$
$$+8G_t a_4^2 a_i^2 \nu_p^2 E_t + 4G_t a_5^2 b_i^2 \nu_{tp}^2 E_p + 2G_t a_5^2 b_i^2 \nu_p^2 E_t + 4G_t a_5^2 a_i^2 \nu_{tp}^2 E_p + 2G_t a_5^2 a_i^2 \nu_p^2 E_t$$
$$+4G_t a_5 b_i^2 \bar{\kappa}_1 E_t - 4G_t a_5 a_i^2 \bar{\kappa}_1 E_t + 16G_t a_6^2 b_i^2 \nu_{tp}^2 E_p + 8G_t a_6^2 b_i^2 \nu_p^2 E_t - 16E_t E_p \nu_{tp} a_8 \gamma_{11}$$
$$+E_p a_{11}^2 a_i^2 \nu_p E_t + 4E_p a_{12}^2 b_i^2 \nu_p E_t + 8E_p a_9 a_{14} \nu_p E_t - 16E_t E_p \nu_{tp} a_{15} \bar{\gamma}_{11} - 16E_p a_{15} \nu_p E_t a_8$$
$$+4E_p a_{16}^2 a_i^2 \nu_p E_t + 8a_{11} a_i^2 a_{16} \nu_{tp}^2 E_p^2 - 4E_p a_{11} a_i^2 a_{16} E_t + E_p a_{17}^2 b_i^2 \nu_p E_t - 8E_p^2 a_{17} a_i^2 \nu_{tp}^2 a_{10}$$
$$+8a_{12} b_i^2 a_{17} \nu_{tp}^2 E_p^2 - 4E_p a_{12} b_i^2 a_{17} E_t - 8E_p^2 a_{18} b_i^2 \nu_{tp}^2 a_{11})$$

The procedure of VAM is to minimize the strain energy of Eq. (5.13) with respect to unknown warping. So, the strain energy is minimized with respect to each Pascal coefficient as

$$\frac{\partial U_0}{\partial a_i} = 0, \; i=1..18 \tag{5.14}$$

Eq. (5.14), leads to a system of algebraic equations with nine equations and nine variables. By solving Eq. (5.14) and substituting into Eq. (5.13), we have

$$2U_0 = \pi E_t (a_{out} b_{out} - a_i b_i) \bar{\gamma}_{11}^2 + \left(-\pi a_{out} b_{out} \left(-\frac{1}{4} \frac{G_t B_2^2 a_{out}^2}{B_1^2} - \frac{1}{2} \frac{G_t B_2 b_{out}^2}{B_1} + \frac{1}{2} \frac{G_t B_2 a_{out}^2}{B_1} - \frac{1}{4} \frac{G_t B_2^2 b_{out}^2}{B_1^2} - \frac{1}{4} G_t b_{out}^2 - \frac{1}{4} G_t a_{out}^2 \right) \right.$$
$$\left. + \pi a_i b_i \left(-\frac{1}{2} \frac{G_t B_2 b_i^2}{B_1} + \frac{1}{2} \frac{G_t B_2 a_i^2}{B_1} - \frac{1}{4} \frac{G_t B_2^2 b_i^2}{B_1^2} - \frac{1}{4} \frac{G_t B_2^2 a_i^2}{B_1^2} - \frac{1}{4} G_t b_i^2 - \frac{1}{4} G_t a_i^2 \right) \right) \bar{\kappa}_1^2 + \frac{\pi}{4} E_t (a_{out} b_{out}^3 - a_i b_i^3) \bar{\kappa}_2^2$$
$$+ \frac{\pi}{4} E_t (a_{out}^3 b_{out} - a_i^3 b_i) \tag{5.15}$$
$$B_1 = -a_{out} b_{out}^3 - a_{out}^3 b_{out} + a_i b_i^3 + a_i^3 b_i; \; B_2 = a_i^3 b_i - a_o^3 b_o + a_o b_o^3 - a_i b_i^3$$

Collecting the coefficients of $\bar{\gamma}_{11}^{\,2}$ results in $\bar{S}_{11}$, coefficients of $\bar{\kappa}_1^{\,2}, \bar{\kappa}_2^{\,2}$, and $\bar{\kappa}_3^{\,2}$ lead to $\bar{S}_{22}$, $\bar{S}_{33}$ and $\bar{S}_{44}$, respectively, as in Eq. (5.16).

$$\begin{aligned}
\bar{S}_{11} &= E_t \pi (a_{out} b_{out} - a_i b_i) \\
\bar{S}_{22} &= \pi \frac{G_t}{B_1} \left(a_i^{\,4} b_i^{\,4} - a_o^{\,3} b_o a_i b_i^{\,3} + a_o^{\,4} b_o^{\,4} - a_i^{\,3} b_i a_o b_o^{\,3} \right) \\
\bar{S}_{33} &= \frac{\pi}{4} E_t (a_{out} b_{out}^{\,3} - a_i b_i^{\,3}) \\
\bar{S}_{44} &= \frac{\pi}{4} E_t (a_{out}^{\,3} b_{out} - a_i^{\,3} b_i)
\end{aligned} \tag{5.16}$$

The stiffness constants $\bar{S}_{11}$, $\bar{S}_{33}$ and $\bar{S}_{44}$ are the same as those from strength of materials. However, there is a difference in the torsional stiffness ($\bar{S}_{22}$) of Eq. (5.16) and strength of materials. The torsional stiffness of a unidirectional tube using the strength of materials is as the following, [87].

$$\bar{S}_{22}\Big|_{strength \text{ of mat.}} = G_{12} \left(\frac{\pi (a_o)^3 (b_o)^3}{(a_o)^2 + (b_o)^2} - \frac{\pi (a_{in})^3 (b_{in})^3}{(a_{in})^2 + (b_{in})^2} \right) \tag{5.17}$$

This difference will be investigated in section 5.4.2 where we will compare the obtained $\bar{S}_{22}$ of the Present Pascal polynomial dimensional reduction method and the obtained values of strength of materials approach.

5.3 Pascal polynomial dimensional reduction method for elliptical tubes with arbitrary lay-up

For elliptical tubes with arbitrary lay-up, the matrices of Eq. (4.20) will be modified to Eq. (5.18).

$$\begin{aligned}
\Lambda_1 &= \sum_{i=1}^{n} \left(\left(\int_{\theta=0}^{2\pi} \int_{r=0}^{1} ([\Gamma_\varepsilon]^T [D^i] [\Gamma_\varepsilon] r a_{i+1} b_{i+1} dr d\theta \right) - \left(\int_{\theta=0}^{2\pi} \int_{r=0}^{1} ([\Gamma_\varepsilon]^T [D^i] [\Gamma_\varepsilon] r a_i b_i dr d\theta \right) \right) \\
\Lambda_2 &= \sum_{i=1}^{n} \left(\left(\int_{\theta=0}^{2\pi} \int_{r=0}^{1} [\Gamma_h W]^T [D^i] [\Gamma_h W] a_{i+1} b_{i+1} r dr d\theta \right) - \left(\int_{\theta=0}^{2\pi} \int_{r=0}^{1} [\Gamma_h W]^T [D^i] [\Gamma_h W] a_i b_i r dr d\theta \right) \right) \\
\Lambda_3 &= \sum_{i=1}^{n} \left(\left(\int_{\theta=0}^{2\pi} \int_{r=0}^{1} [\Gamma_h W]^T [D^i] [\Gamma_\varepsilon] a_{i+1} b_{i+1} r dr d\theta \right) - \left(\int_{\theta=0}^{2\pi} \int_{r=0}^{1} [\Gamma_h W]^T [D^i] [\Gamma_\varepsilon] a_i b_i r dr d\theta \right) \right)
\end{aligned} \tag{5.18}$$

$$\Lambda_4 = \sum_{i=1}^{n}\left((\int_{\theta=0}^{2\pi}\int_{r=0}^{1} [\Gamma_h W]^T [D^i][\Gamma_l W] a_{i+1} b_{i+1} r dr d\theta) - (\int_{\theta=0}^{2\pi}\int_{r=0}^{1} [\Gamma_h W]^T [D^i][\Gamma_l W] a_i b_i r dr d\theta) \right)$$

$$\Lambda_5 = \sum_{i=1}^{n}\left((\int_{\theta=0}^{2\pi}\int_{r=0}^{1} [\Gamma_l W]^T [D^i][\Gamma_\varepsilon] a_{i+1} b_{i+1} r dr d\theta) - (\int_{\theta=0}^{2\pi}\int_{r=0}^{1} [\Gamma_l W]^T [D^i][\Gamma_\varepsilon] a_i b_i r dr d\theta) \right)$$

$$\Lambda_6 = \sum_{i=1}^{n}\left((\int_{\theta=0}^{2\pi}\int_{r=0}^{1} [\Gamma_l W]^T [D^i][\Gamma_l W] a_{i+1} b_{i+1} r dr d\theta) - (\int_{\theta=0}^{2\pi}\int_{r=0}^{1} [\Gamma_l W]^T [D^i][\Gamma_l W] a_i b_i r dr d\theta) \right)$$

where each of the expressions above consist of subtraction of the area of the transformed ellipse with the major and minor radius of a_{i+1} and b_{i+1} from the area of the transformed ellipse with the major and minor radius of a_i and b_i. In Eq. (5.18), the relations Eq. (3.22) and Eq. (3.23) with the help of Eq. (5.3) are used to take into account the change of the angle of the fiber through the circumference of the elliptical section.

5.4 Stress analysis of elliptical composite tubular beams using meshless dimensional reduction method

A program in Maple 15 named AMESM (Analytical Meshless Elliptical Sectional Method) is developed in order to validate the present method of solution for elliptical tubes. Different elliptical sections with different minor to major radius ratios (b/a) are examined and compared with the literature, VABS 3.8 (the latest version of VABS tool), experiment, and Strength of materials. The parametric study is performed to investigate the effect of lay-up sequence as well as aspect ratio on the cross-sectional stiffness constants and the transverse displacement of the tube under four-point bending loading.

5.4.1 Validation

First, elliptical tubes made by IM6/3501-6 graphite/epoxy with material properties of E_{11}=24.8 Msi (170 GPa), $E_{22}=E_{33}$=1.41 Msi (9.72 GPa), $G_{12}=G_{23}=G_{13}$=0.9 Msi (6.20 GPa), $\nu_{12}=\nu_{23}=\nu_{13}$=0.329 with the thickness of each layer of 0.0052 *in*, with the lay-up sequence $[\pm 45_2/0_2/\pm 45]_s$ is studied and results are compared with those of reference [71]. The elliptical cross-section has a ratio of major to minor radii of 0.75. The cross-section of the tube is demonstrated in Fig. (5.3). The bending stiffness of the elliptical tube with various major axes obtained from the present method are compared to those obtained by [71] in Fig. (5.4). The

obtained bending stiffness by the present method (Timoshenko beam model) with order (m=4) agrees well with that obtained by an analytical method, [71].

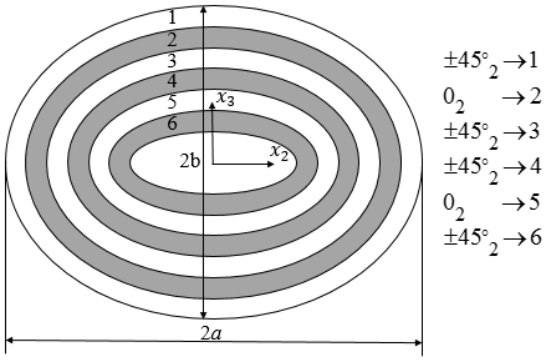

Fig. (5.3). Cross-section of an elliptical tube with lay-up $[\pm 45_2/0_2/\pm 45]_s$.

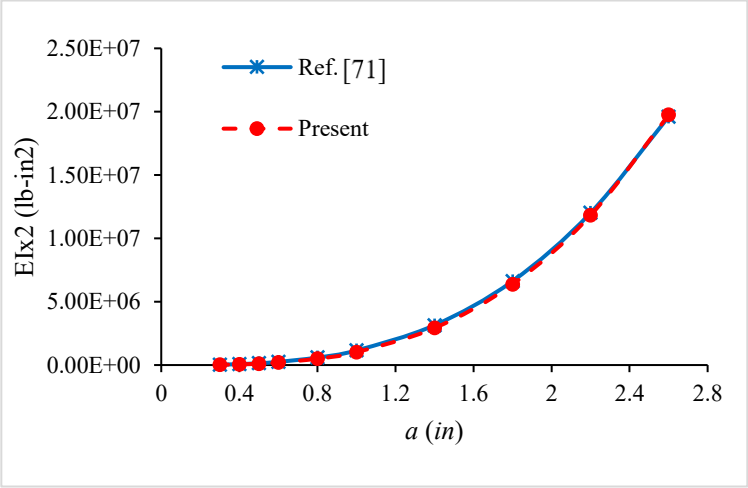

Fig. (5.4). Comparison of bending stiffness of composite elliptical tubes with b/a=0.75, $[\pm 45_2/0_2/\pm 45]_s$.

5.4.2 Analysis for unidirectional elliptical tube

The difference between the obtained $\bar{S}_{22}$ of Eq. (5.16) obtained through Pascal polynomial method and (5.17) obtained through mechanics of materials approach is studied. To do so, a composite Carbon/PEEK tube with E_1 = 138.3 *GPa*, $E_2 = E_3$ = 10.2 *GPa*, $\nu_{12} = \nu_{13} = 0.31$, $\nu_{23} = 0.33$ and $G_{12} = G_{13} = G_{23}$ = 5.56 *GPa,* [2] is studied. We used this composite material in all the following composite case studies throughout this section unless other properties are mentioned.

The torsional stiffness of elliptical unidirectional $[0]_2$ tubes with the thickness of each layer 1 *mm* (total thickness of 2 *mm*), and (a = 0.06 *m*) with different *b/a* ratios using Eq. (5.16) and Eq. (5.17)

are shown in Fig. (5.5). We used the thickness of 1 *mm* for a layer in all the composite cases throughout this chapter unless the other thickness is mentioned. It can be seen that even though the expressions for the twisting coefficients are different, their values are practically the same.

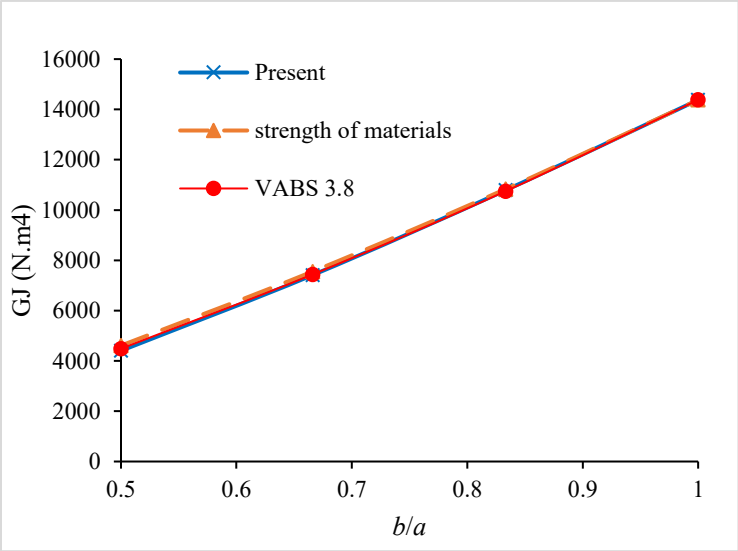

Fig. (5.5). Torsional stiffness change versus minor to major axes ratio of elliptical unidirectional tubes, (a = 0.06 m).

5.4.3 Analysis for [90/0] elliptical tube

The change of torsional and bending stiffness of [90/0] elliptical tubes versus b/a are demonstrated in Figs. (5.6), and (5.7), respectively. As expected, by increasing the b/a ratio, the torsional and the bending stiffness increase. Moreover, only the diagonal stiffness constants are non-zero. It is noted for the case of [90/0] tubes, the common Classical and Timoshenko beam model stiffness constants are identical.

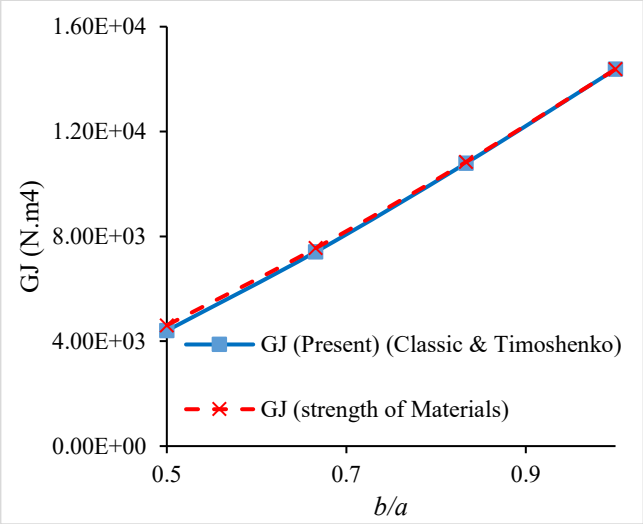

Fig. (5.6). Torsional stiffness change versus minor to major axes ratio of elliptical [90/0] tubes, a=0.06 m.

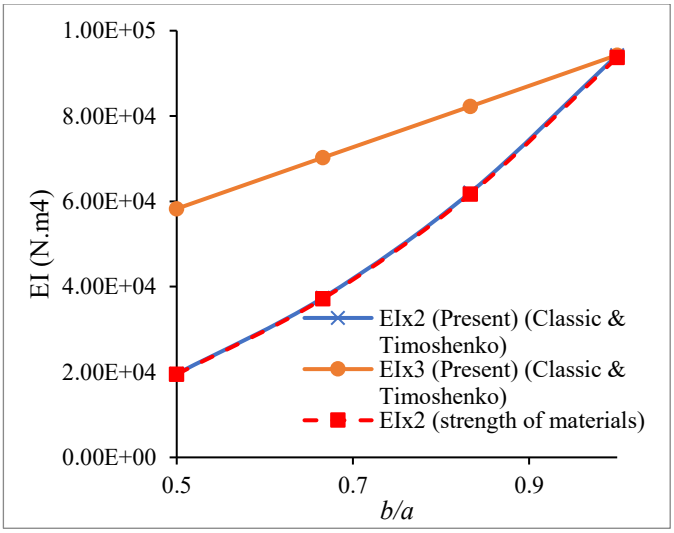

Fig. (5.7). Bending stiffness change versus minor to major axes ratio of elliptical [90/0] tubes, a=0.06 m.

5.4.4 Elliptical tubes containing off-axis fibers

In order to investigate the capability of the Pascal polynomial method to handle elliptical tubes with complex lay-up sequences, CUS (Circumferentially Uniform Stiffness) tubes made of lay-up sequences [0/α] are examined. These lay-up sequences will give rise to couplings among different modes such as axial-torsion or shear-bending. The results obtained from the present Pascal polynomial method for both the Classical and Timoshenko beam models will be compared with those obtained from VABS, and Strength of Materials. Stiffness constants for laminates having α = 0°, 15°, 30°, 45°, 60°, 90° were determined. Values of the stiffness constants for two cases (α = 30° and α = 60°) are shown in Tables (5.1) and (5.2). The cross-section of these tubes is meshed by 2560 elements in VABS 3.8. It can be observed that the off-diagonal stiffness constants are non-zero when the tube is angle-ply. Comparing the tables (5.1) and (5.2), one can see that there is a significant increase in the absolute values of shear couplings as S_{14}, S_{25} and S_{36} as the angle α decreases from 60° to 30°.

Table (5.1). Stiffness constants of CUS elliptical tube, [0/30], a=0.06 m.

(non-zero stiffness constants)	b/*a*	Beam theory	S_{11} ($\times 10^7$) (N)	S_{22} ($\times 10^6$) (N)	S_{33} ($\times 10^6$) (N)	S_{14} ($\times 10^5$) (N.m)	S_{25} ($\times 10^5$) (N.m)	S_{36} ($\times 10^5$) (N.m)	S_{44} ($\times 10^3$) ($N.m^2$)	S_{55} ($\times 10^4$) ($N.m^2$)	S_{66} ($\times 10^4$) ($N.m^2$)
Present	½	**(Cl.)**	5.336	-	-	-2.859	-	-	10.740	2.222	6.746
		(Tim.)	5.336	5.409	2.154	-2.859	1.497	1.607	10.740	2.636	7.946

VABS 3.8		**(Cl.)**	5.433	-	-	-2.759	-	-	10.913	2.266	6.798
		(Tim.)	5.433	5.302	1.717	-2.759	1.426	1.209	10.913	2.650	7.650
Present	**2/3**	**(Cl.)**	5.950	-	-	-3.901	-	-	18.094	4.264	8.054
		(Tim.)	5.950	4.552	2.797	-3.901	1.931	1.825	18.094	5.016	9.244
VABS 3.8		**(Cl.)**	5.959	-	-	-3.739	-	-	18.040	4.280	8.006
		(Tim.)	5.959	5.208	2.713	-3.739	1.934	1.698	18.040	4.998	9.069
Present	**5/6**	**(Cl.)**	6.570	-	-	-4.933	-	-	26.323	7.038	9.376
		(Tim.)	6.570	4.858	4.183	-4.933	2.389	2.558	26.323	8.214	10.940
VABS 3.8		**(Cl.)**	6.524	-	-	-4.683	-	-	26.014	7.055	9.318
		(Tim.)	6.524	5.048	3.747	-4.683	2.436	2.154	26.014	8.321	10.556
Present	**1**	**(Cl.)**	7.224	-	-	-5.990	-	-	35.084	10.704	10.704
		(Tim.)	7.224	4.877	4.877	-5.990	2.945	2.945	35.084	12.483	12.483
VABS 3.8		**(Cl.)**	7.151	-	-	-5.728	-	-	34.790	10.721	10.721
		(Tim.)	7.151	4.871	8.807	-5.728	2.943	2.694	34.790	12.481	12.231

Table (5.2). Stiffness constants of CUS elliptical tube, [0/60], a=0.06 m.

(non-zero stiffness constants)	**b/*a***	**Beam theory**	S_{11} $(\times 10^7)$ ***(N)***	S_{22} $(\times 10^6)$ ***(N)***	S_{33} $(\times 10^6)$ ***(N)***	S_{14} $(\times 10^4)$ ***(N.m)***	S_{25} $(\times 10^4)$ ***(N.m)***	S_{36} $(\times 10^4)$ ***(N.m)***	S_{44} $(\times 10^3)$ ***($N.m^2$)***	S_{55} $(\times 10^4)$ ***($N.m^2$)***	S_{66} $(\times 10^4)$ ***($N.m^2$)***
Present	**½**	**(Cl.)**	4.109	-	-	-2.323	-	-	6.443	1.964	5.828
		(Tim.)	4.109	2.859	1.223	-2.323	1.059	1.126	6.443	1.968	5.839
VABS 3.8		**(Cl.)**	4.216	-	-	-2.214	-	-	6.566	1.995	5.991
		(Tim.)	4.216	3.200	1.044	-2.214	1.150	0.972	6.566	1.999	6.000
Present	**2/3**	**(Cl.)**	4.581	-	-	-3.143	-	-	10.431	3.754	7.040
		(Tim.)	4.581	2.875	1.866	-3.143	1.488	1.532	10.431	3.761	7.052
VABS 3.8		**(Cl.)**	4.617	-	-	-2.996	-	-	10.869	3.775	7.071
		(Tim.)	4.617	3.146	1.648	-2.996	1.554	1.364	10.869	3.783	7.083
Present	**5/6**	**(Cl.)**	5.053	-	-	-3.944	-	-	14.685	6.229	8.251
		(Tim.)	5.053	2.921	2.448	-3.944	1.914	1.931	14.685	6.242	8.266
VABS 3.8		**(Cl.)**	5.053	-	-	-3.760	-	-	15.703	6.230	8.215
		(Tim.)	5.053	3.050	2.281	-3.760	1.954	1.738	15.703	6.243	8.228
Present	**1**	**(Cl.)**	5.522	-	-	-4.761	-	-	21.039	9.457	9.457
		(Tim.)	5.522	2.934	2.934	-4.761	2.353	2.353	21.039	9.476	9.476
VABS 3.8		**(Cl.)**	5.522	-	-	-4.589	-	-	20.985	9.460	9.460
		(Tim.)	5.522	2.943	2.918	-4.589	2.357	2.167	20.985	9.479	9.476

In the above tables, the bending stiffness constants are $S_{55} \equiv (EI)_{x_2}$ and $S_{66} \equiv (EI)_{x_3}$. One may make a simple approximation for the bending stiffness constant using the Strength of Materials approach [76] in the following Eqs. (5.19) where n is the number of layers.

$$(EI)_{x_2} = \sum_{i=1}^{n} \left(\frac{\pi}{4} \frac{E_1^i}{\cos^4 \alpha^i + \frac{E_1^i \sin^2 \alpha^i \cos^2 \alpha^i}{G_{12}^i} + \frac{E_1^i \sin^4 \alpha^i}{E_2^i}} \cdot \left(a_o^i (b_o^i)^3 - a_{in}^i (b_{in}^i)^3 \right) \right), i=1..n \qquad (5.19)$$

Figs. (5.8) and (5.9) show the variations of the bending stiffness constants with respect to the variation of the angle α using Present polynomial method, VABS, and strength of materials approach of Eq. (5.19).

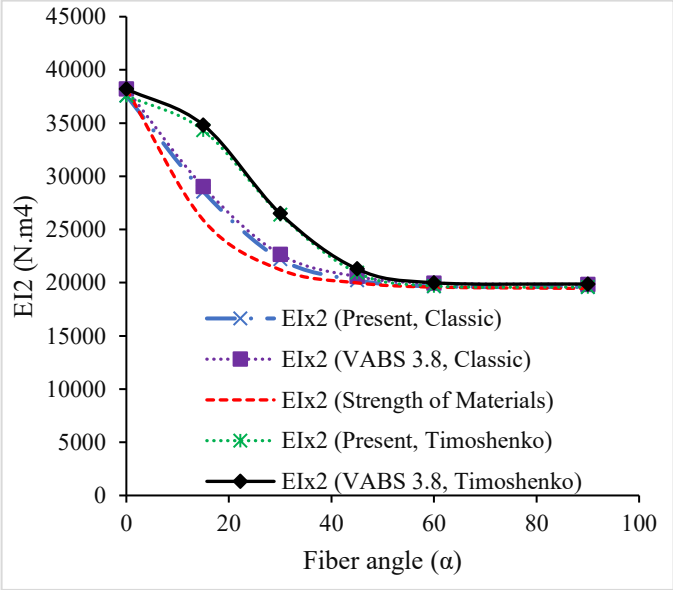

Fig. (5.8). The change of $(EI)_{x_2}$ versus the fiber angle of the elliptical tube $[0/\alpha]$ with b/a=0.5, a=0.06 m.

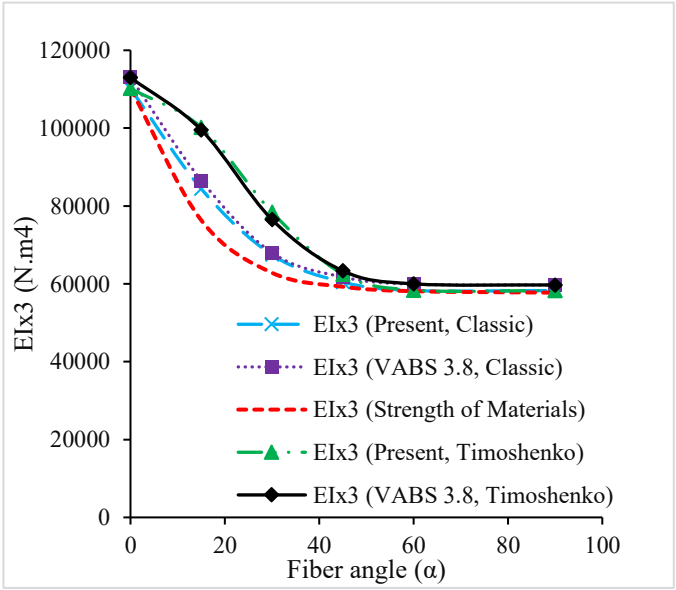

Fig. (5.9). The change of $(EI)_{x_3}$ versus the fiber angle of the elliptical tube $[0/\alpha]$ with b/a=0.5, a=0.06 m.

The following can be observed:

- Values obtained from Pascal polynomial solutions agree with those obtained from VABS solution.
- $(EI)_{x3}$ is larger than $(EI)_{x2}$ for $b/a < 1.0$, but the two stiffness constants are the same at $b/a = 1$ (circular shape). This is to be expected.
- Variation of the angle α only has significant effect on the stiffness constants for the range $0^o < \alpha < 60^o$. Above 60°, variation of α has negligible effect on the stiffness constants.

- For α < 60°, the bending stiffness constants obtained from Classical model are significantly smaller than those obtained from the Timoshenko model.
- The Strength of Material solution provides smaller stiffness constants than either the Classical model or the Timoshenko model. This can be due to the fact that the Strength of Material solution does not take into account the shear coupling between the 0° and α layers.

Tubes with elliptical cross-section can be useful for torsional applications. The torsional stiffness constants are shown as S_{44} in Tables (5.1) and (5.2). A simple approximation for the torsional stiffness may be obtained using Strength of Materials approach as shown in Eq. (5.20), [19]. Fig. (5.10) shows the variation of the torsional stiffness with the variation of the angle α in the lay-up [0/α]. The following can be observed:

$$GJ=\sum_{i=1}^{n}\left(\pi\left(\frac{G_{12}^{i}}{\cos^{4}\alpha^{i}+\sin^{4}\alpha^{i}+2\left(2\frac{G_{12}^{i}\left(1+2\nu_{12}^{i}\right)}{E_{1}^{i}}+2\frac{G_{12}^{i}}{E_{2}^{i}}-1\right)\sin^{2}\alpha^{i}\cos^{2}\alpha^{i}}\right)\left(\frac{(a_{o}^{i})^{3}(b_{o}^{i})^{3}}{(a_{o}^{i})^{2}+(b_{o}^{i})^{2}}-\frac{(a_{in}^{i})^{3}(b_{in}^{i})^{3}}{(a_{in}^{i})^{2}+(b_{in}^{i})^{2}}\right)\right) \tag{5.20}$$

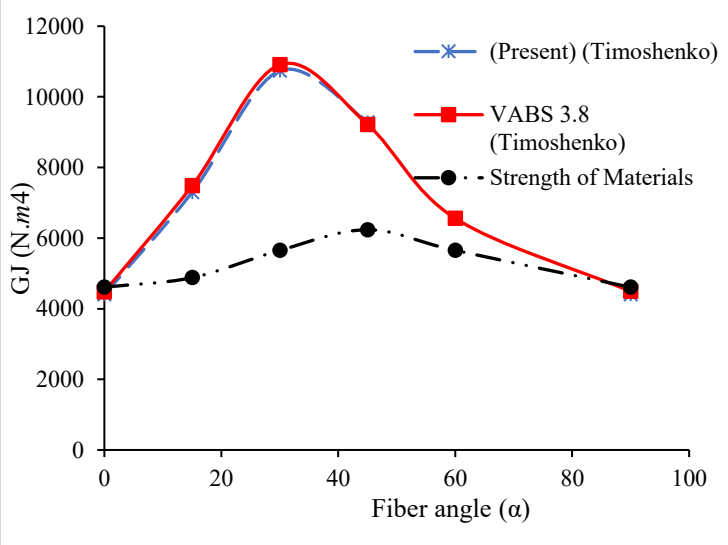

Fig. (5.10). The change of torsional stiffness GJ versus the winding angle of the elliptical tube $[0/\alpha]$ with *b/a=0.5*.

- The torsional stiffness from Strength of Materials approach are less than those obtained using Pascal or VABS. This can be due to the fact that Strength of Materials approach does not take into account the coupling between the 0^o and α layers.

The maximum value of torsional stiffness from Strength of Materials occurs at $\alpha = 45^o$ while that obtained from VABS, or Pascal occur at an angle $\alpha = 30^o$. This is due to the coupling between the α layers and the 0^o, which is not taken into account in the Strength of Materials solution.

5.4.5 1D analysis of tubes under four-point bending loading

The 1D FE analysis of [0/60] (total thickness 2 mm) for two values of (b/a) is performed using the solution presented in section 4.4 and displacement results are compared with those obtained using VABS in combination with ANSYS 1D FE solution. The tubes have (a=0.06 m). The loading conditions of the tubes are illustrated in Fig. (5.11) where the beams have the simply supported boundary condition and subjected to the loadings 2P. The displacements of two ends are restricted in three directions and they can only rotate about x_2. The beams are 1 m long (L=1 m). The transverse displacement distribution ($\overline{w}$) through the length of the elliptical tubes under four-point bending loading are demonstrated in Fig. (5.12). It is noted that in the ANSYS 1D FE solution, we used the element beam 189 which has three nodes and 6 degrees of freedom at each node, [88]. In both the present 1D solution as well as 1D ANSYS FE, the number of elements is 40 and the transverse displacement is converged with this number of elements. The order (m=4) is used for the cross-sectional analysis in the Pascal polynomial method. The presented cross-sectional analysis has the similar computational time compared to VABS without considering preprocessing time including meshing of the cross-section while the present method is simple-input, and the modeling and mesh procedure can be eliminated. Moreover, the same computational time for 1D analysis compared to the VABS is obtained.

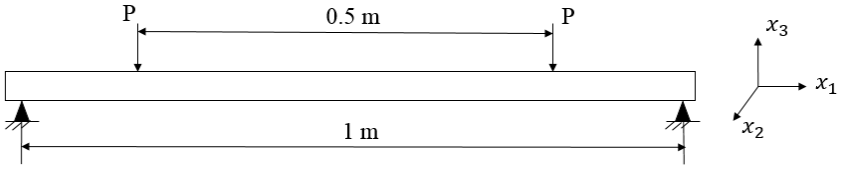

Fig. (5.11). Schematic of four point bending of elliptical tubes under loading 2P.

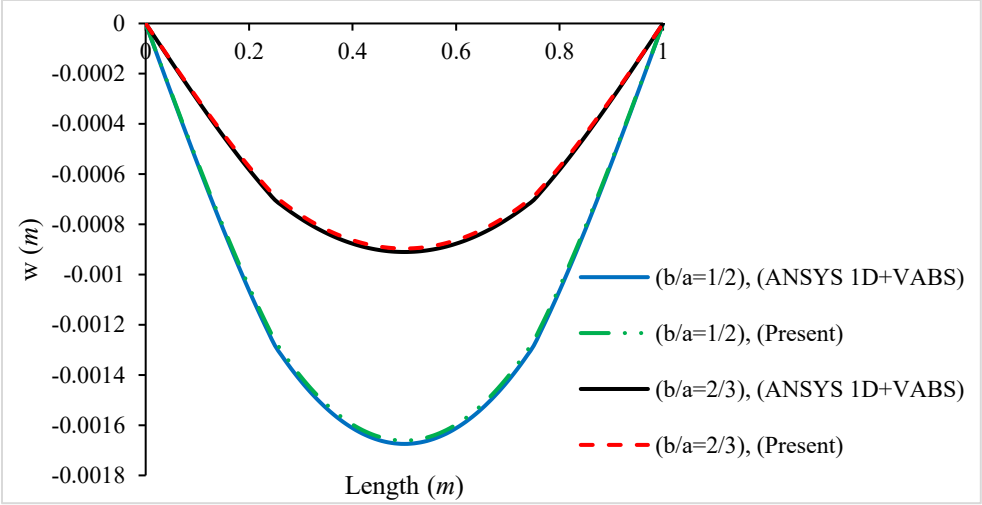

Fig. (5.12). Transverse displacement of three composite tubes under four-point bending loading, (a=0.06 m), (P=1 KN).

5.4.6 3D strain distribution in an elliptical tube with *b*/*a*=2/3 under pure bending

The recovery analysis can be carried out to determine the 3D strains in the cross-section of the elliptical tube under arbitrary loading. The ability of the dimensional reduction method to determine the strain or stress distribution in the cross-section of the beam makes it to be an efficient method compared to 3D FEM, [49]. Fig. (5.13) illustrates the distribution of 3D strains Γ_{11}, Γ_{12}, Γ_{22} and Γ_{33} where Γ_{11} is the normal strain along x_1, Γ_{22} is the normal strain along x_2, Γ_{33} is the normal strain along x_3, and Γ_{12} is the shear strain. The tube is subjected to pure bending moment of M_2=1 KN.m. The obtained strains using the present method are compared with VABS 3.8.

In the VABS 3.8, first the cross-section of the elliptical tube is modelled, then the lay-up sequence is defined, next the modelled mold lines of the cross-section is divided into different segments and then it is meshed with quadrilateral 8-noded elements. The number of elements is 2558. While in the present method, it is not necessary to create mesh over the cross-section which can make the present method to be more straightforward than VABS.

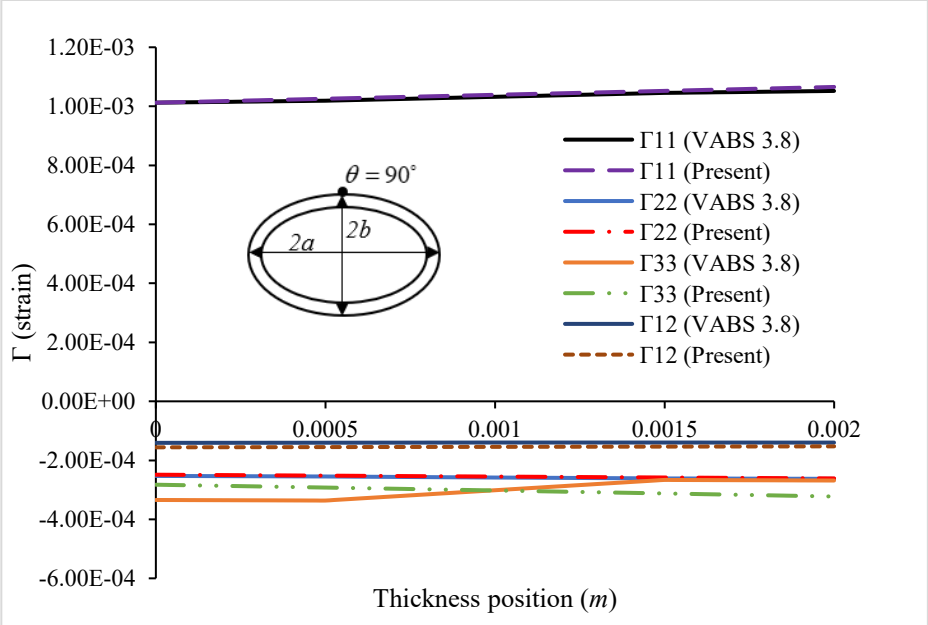

Fig. (5.13). Distribution of 3D strains at $\theta = 90^{\circ}$ of the elliptical tube with [0/60] with b/a=2/3.

5.5 Conclusion

An analytical meshless method for cross-sectional analysis of composite elliptical tubes subjected to bending loadings is provided. Utilizing Pascal polynomials in the polar coordinates, the warping functions of the beam are evaluated where there is no need to generate mesh of the cross-section.

- The main difference between the analysis for beams with elliptical cross-section and for those of circular section is the change of the radial distance along the circumferential direction, and a new procedure has been introduced to handle this.
- The method not only provide the traditional sectional stiffness constants such as along the axial direction, twisting and bending, but also the coupling stiffness constants between different modes.
- The effect of different ratios between major/minor axes, and the effect of lay-up sequences, are studied.
- The global behavior of elliptical composite tubes as well as the strains can be predicted. The present method of solution is computationally more efficient than 3D FE solution for elliptical composite beams.

6 Chapter 6: Stress analysis of initially curved composite beams

6.1 Introduction

The analysis of initially curved beams has been done before by a few researchers [56, 57, 59, 60]. These are mainly for isotropic materials, [56, 57]. Zupan and Saje [56] used FE for initially curved and twisted beams with small deformations. Tabarrok et al. [57] provided a set of governing equations for initially curved and twisted beams made of isotropic materials. For tubes made of composite materials, Yazdani [21] applied a displacement-based method to analyze orthotropic single layered curved tubes under pure bending moment. These techniques have shortcomings, the methods are restricted to beams with isotropic material, or rectangular cross-section. For the analysis of initially curved orthotropic tubes the investigators analyzed the tubes only subjected to pure bending moment.

There is the possibility to use VAM for the analysis of initially curved tubes. The development of the relevant equations has been given in chapter 3. Using the procedure in chapter 3, with VABS, one can obtain the stiffness coefficients for the initially curved beam. These stiffness coefficients can be used for the analysis of beam under pure bending, or four-point bending loading. First, we validate the presented method (meshless Pascal polynomial-based method) with VABS 3.8 and the literature for the cross-sectional stiffness constants of isotropic rectangular sections. Then, we compared the strains of the isotropic and unidirectional rectangular beams with ANSYS 3D under pure bending moment. In the next step, we validate the present meshless method for the case of isotropic and orthotropic tubes.

For the case where there are boundary conditions (general load case), in addition to the 2D sectional analysis, 1D analysis using FE needs to be done. In this case, curvilinear coordinates need to be done for the development of the individual elements ([61, 62]). However, development of elements using curvilinear coordinates is very complex. It was suggested by Kovvali and Hodges [89] that the equivalent stiffness coefficients obtained from straight elements could be used to model the curved structure, as long as there are sufficient number of straight elements to model the curved geometry. Moreover, it is suggested by Hodges that it would be more efficient to be as close as possible to the real structure. So that one can use the initially curved cross-sectional stiffness matrix to model a curved beam with straight (piecewise cartesian) elements. One part of this chapter would be to evaluate the accuracy of this procedure. The results from the

1D straight finite elements will be compared against the result obtained from the ANSYS 3D analysis for the whole structure. For determining the transverse displacement of beams under transverse loading, we bring in the elasticity solution for determination of displacement of initially curved beam with isotropic and rectangular cross-section under tip loading proposed by Timoshenko [90]. The presented 1D FE solution for initially curved rectangular section is compared with elasticity solution and then we examined the method for initially curved composite tubes under tip loading and four-point bending loading. The solution is compared with ANSYS 3D FEM. The effect of initial curvature on the stiffness constants, and deflection of the composite tubes are investigated.

6.2 Treatment of the initially curved beam using VAM, VABS and Pascal polynomial to obtain equivalent stiffness coefficients

In this section, the validation is done regarding the cross-sectional dimensional reduction method using Pascal polynomials as well as VABS 3.8 modeling. To do so, we perform the validation with the available cases in the literature. Then, we performed the validation of strains distribution obtained using Pascal polynomials dimensional reduction method with those obtained via ANSYS 3D FEM. In following, we do the cross-sectional analysis of unidirectional rectangular sections using the presented method and VABS 3.8. In the next step, we perform the validation of the present method for the case of isotropic, unidirectional, cross-ply, and angle ply **tubes** with VABS 3.8. Also, the strain distribution of a tube with a complex lay-up is presented and compared with ANSYS 3D.

6.2.1 Isotropic square section

As the first case study, curved aluminum beams with square section are studied. The obtained sectional stiffness constants are compared with Yu et al. [48]. The section has dimensions 0.5 *in* × 0.5 *in* with Young modulus $E = 2.6 \times 10^7$ psi (179 GPa) and $\nu = 0.3$. Tables (6.1) and (6.2) show the obtained stiffness constants for curved beams with k_2=0.05 1/*in* and k_2=0.1 (1/*in*) by the present Pascal polynomial method, Borri et al. [91] who provided a constitutive equations for cross-sectional analysis of beams based on FEM, Yu et al. [48], and VABS 3.8 version 2019. In Yu et al. [48] they used VABS provided in 2002 for cross-sectional analysis. They meshed the square section with 8×8 quadrilateral elements (a total of 675 degrees of freedom). The cross-section is meshed with 1059 elements in VABS 3.8. A good agreement between the present polynomial

based method and other references is observed. Comparing the stiffness constants of the straight beams reported in Chapter (4) and curved beams in Table (6.1), one can observe that when an isotropic straight beam becomes curved, two stiffness constants are added to the beam stiffness constants as extensional-bending (S_{15}) and shear-torsion (S_{24}). When the curvature of the beam increases, the magnitude of these two stiffness constants increases. Comparison of Tables (6.1) and (6.2) shows that increasing the initial curvature, increases the magnitude of extension-bending (S_{15}) and shear-torsion (S_{24}) of a beam. While the other stiffness constants remain the same. There is a difference between VABS 3.8 and the other results. This can be because of an update in its formulation. The physical meaning of extension-bending (S_{15}) is considerable for initially curved beams which can be figured out from Eq. (3.66). This means that when a curved beam is under bending moment, the longitudinal strain of the reference line is non-zero. The Classical stiffness matrix up to 2nd order does not take into account the effect of transverse shear. This stiffness matrix which is obtained through Eq. (3.42) is more accurate compared to Classical stiffness matrix obtained by first approximation of strain energy of the beam. The Cross-sectional stiffness matrix up to 2nd order will be used for 1D FE analysis of curved tubes.

Table (6.1). Stiffness constants of isotropic beam with square cross-section with initial curvature (k_2=0.05 (1/*in*)).

S	**Borri et al. [91]**	**Yu et al. [48]**	**VABS 3.8 Classic (2nd order)**	**VABS 3.8 (Timoshenko)**	**Present Classic (2nd order)**	**Present (Timoshenko)**
S_{11} (lb)	6.500×10^6	6.500×10^6	6.500×10^6	6.500×10^6	6.490×10^6	6.490×10^6
S_{15} (lb.in)	-9.340×10^3	-8.800×10^3	-9.330×10^3	-9.330×10^3	-8.800×10^3	-8.800×10^3
S_{22} (lb)	2.070×10^6	2.070×10^6	-	2.070×10^6	-	2.060×10^6
S_{24} (lb.in)	2.120×10^3	2.120×10^3	-	1.490×10^3	-	2.170×10^3
S_{33} (lb)	2.070×10^6	2.070×10^6	-	2.070×10^6	-	2.070×10^6
S_{44} ($lb.in^2$)	8.790×10^4	8.790×10^4	8.780×10^4	8.780×10^4	8.780×10^4	8.780×10^4
S_{55} ($lb.in^2$)	1.350×10^5	1.350×10^5	1.350×10^5	1.350×10^5	1.350×10^5	1.350×10^5
S_{66} ($lb.in^2$)	1.350×10^5	1.350×10^5	1.350×10^5	1.350×10^5	1.350×10^5	1.350×10^5

Table (6.2). Stiffness constants of isotropic beam with square cross-section with initial curvature, (k_2=0.1 (1/*in*)).

S	**Borri et al. [91]**	**Yu et al. [48]**	**VABS 3.8 Classic (2nd order)**	**VABS 3.8 (Timoshenko)**	**Present Classic (2nd order)**	**Present (Timoshenko)**
S_{11} (lb)	6.500×10^6	6.500×10^6	6.500×10^6	6.500×10^6	6.490×10^6	6.490×10^6
S_{15} (lb.in)	-1.870×10^4	-1.760×10^4	-1.760×10^4	-1.860×10^4	-1.750×10^4	-1.750×10^4
S_{22} (lb)	2.070×10^6	2.070×10^6	-	2.070×10^6	-	2.060×10^6
S_{24} (lb.in)	4.360×10^3	4.520×10^3	-	2.990×10^3	-	4.360×10^3
S_{33} (lb)	2.070×10^6	2.070×10^6	-	2.070×10^6	-	2.070×10^6

S_{44} ($lb.in^2$)	8.790×10^4	8.790×10^4	8.780×10^4	8.780×10^4	8.780×10^4	8.780×10^4
S_{55} ($lb.in^2$)	1.350×10^5	1.350×10^5	1.350×10^5	1.350×10^5	1.350×10^5	1.350×10^5
S_{66} ($lb.in^2$)	1.350×10^5	1.350×10^5	1.350×10^5	1.350×10^5	1.350×10^5	1.350×10^5

In the cross-sectional analysis, one can perform the recovery analysis to obtain the 3D strains in the cross-section. This is an advantage of the cross-sectional analysis compared to the 3D analysis. For instance, the distribution of the normal and shear strains in the aluminum beam with initial curvature k_2=0.1 (1/*in*) and square section with the reported dimensions and material properties under bending moment M_2=1 *lb.in* are illustrated in Figs. (6.1-6.4).

The obtained strains from the present polynomial based method are compared with ANSYS 3D FEA. The ANSYS modeling is performed in such a way that the curved beam is under pure bending moment at one side and clamped (fixed) at the other side. The element SOLID 185 has been used for the analysis. It is noted that the curved beam is meshed with 50400 3D elements. A very good correlation between the present solution and ANSYS 3D is observed. The maximum of 4.76% difference between the Pascal polynomial solution and ANSYS 3D is observed for shear strain Γ_{23}. The other shear stains Γ_{12} and Γ_{13} are very small compared to the other shear strain (Γ_{23}).

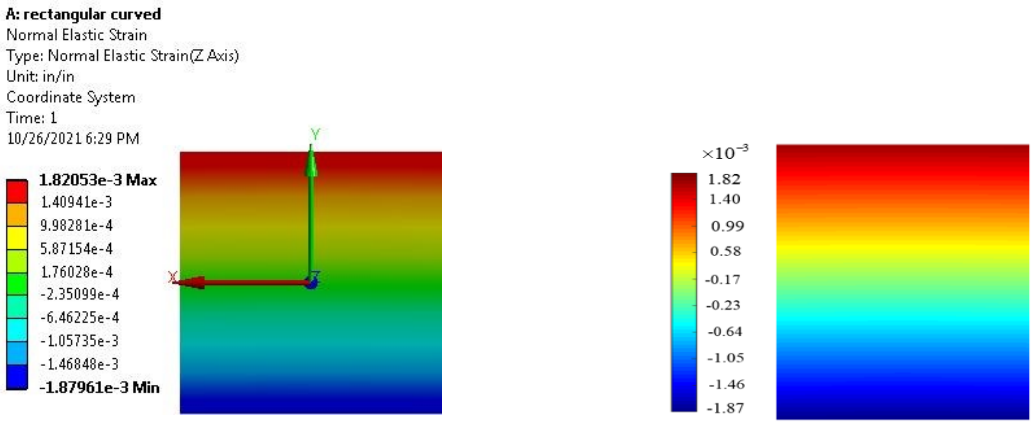

a) ANSYS 3D *b*) Present

Fig. (6.1). Distribution of Γ_{11} in the section of the rectangular aluminum curved beam k_2=0.1 (1/*in*), *a*) ANSYS 3D, *b*) Present

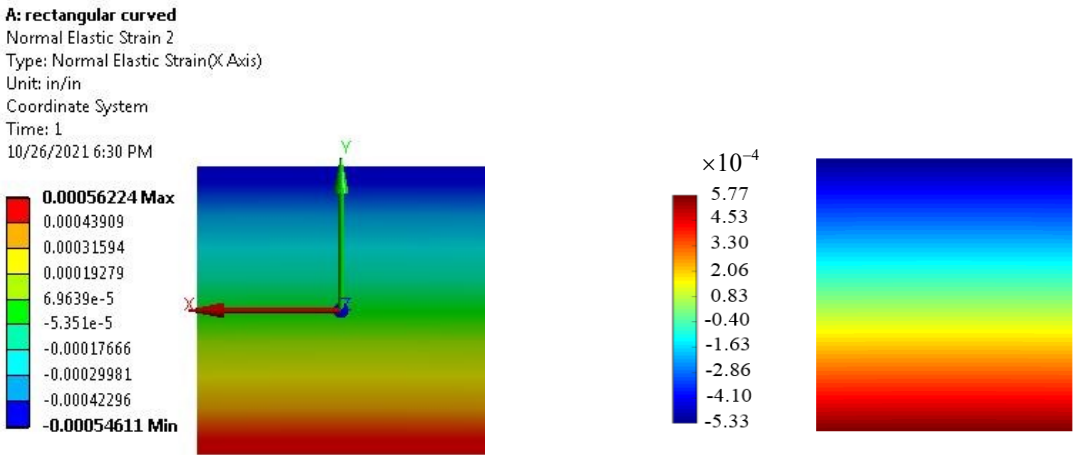

a) ANSYS 3D *b*) Present

Fig. (6.2). Distribution of Γ_{22} in the section of the rectangular aluminum curved beam k_2=0.1 (1/*in*), *a*) ANSYS 3D, *b*) Present.

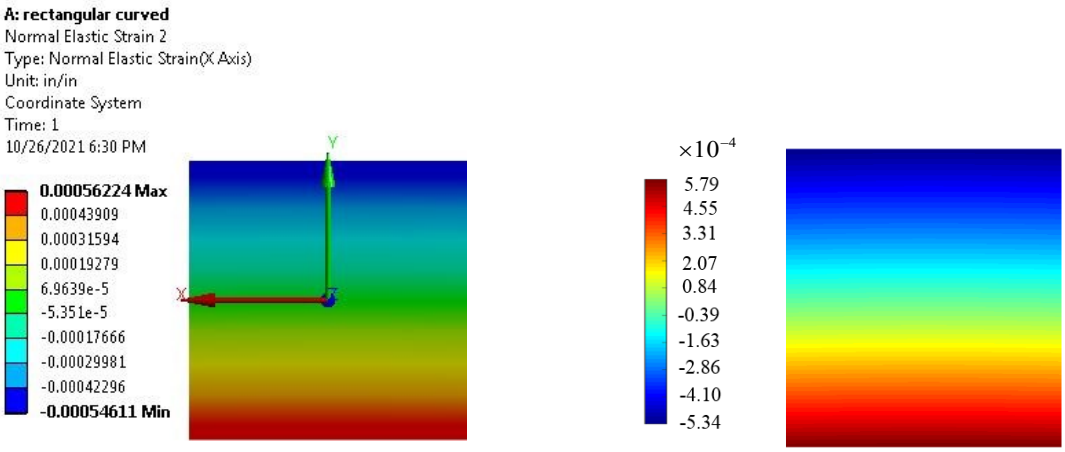

a) ANSYS 3D *b*) Present

Fig. (6.3). Distribution of Γ_{33} in the section of the rectangular aluminum curved beam k_2=0.1 (1/*in*), *a*) ANSYS 3D, *b*) Present.

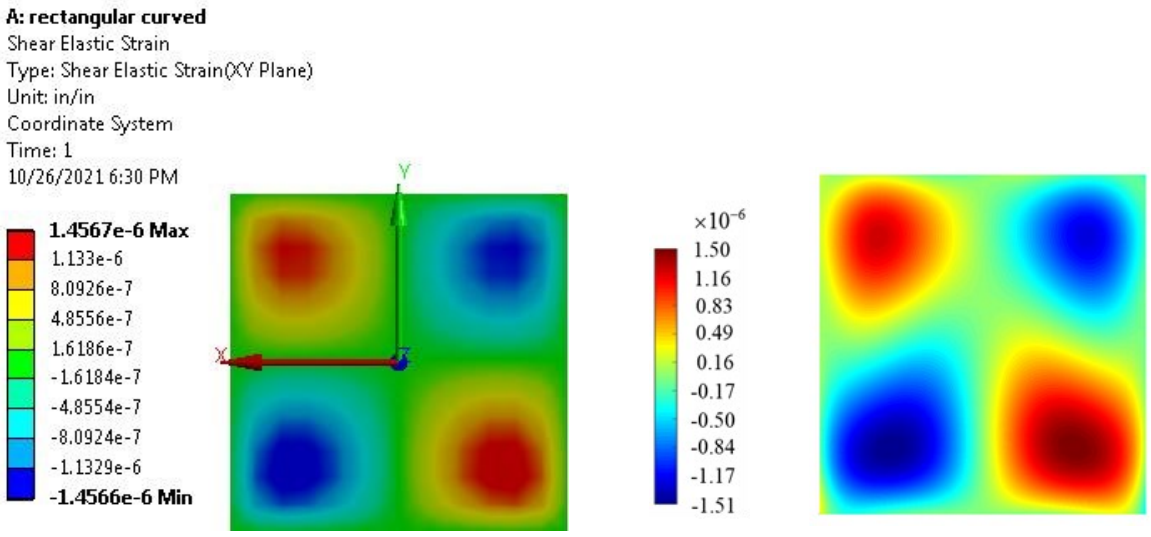

a) ANSYS 3D *b*) Present

Fig. (6.4). Distribution of Γ_{23} in the section of the rectangular aluminum curved beam k_2=0.1 (1/*in*), *a*) ANSYS 3D, *b*) Present.

In order to observe the effect of initial curvature on the accuracy and variation of longitudinal strain through the thickness, we plotted the strain distribution for rectangular sections with the mentioned material properties and dimensions for different values of initial curvatures in Fig. (6.5). It is observed that for the case of straight beam (k_2=0), the longitudinal strain variation is linear. While as the initial curvature increases, this strain distribution varies non-linearly.

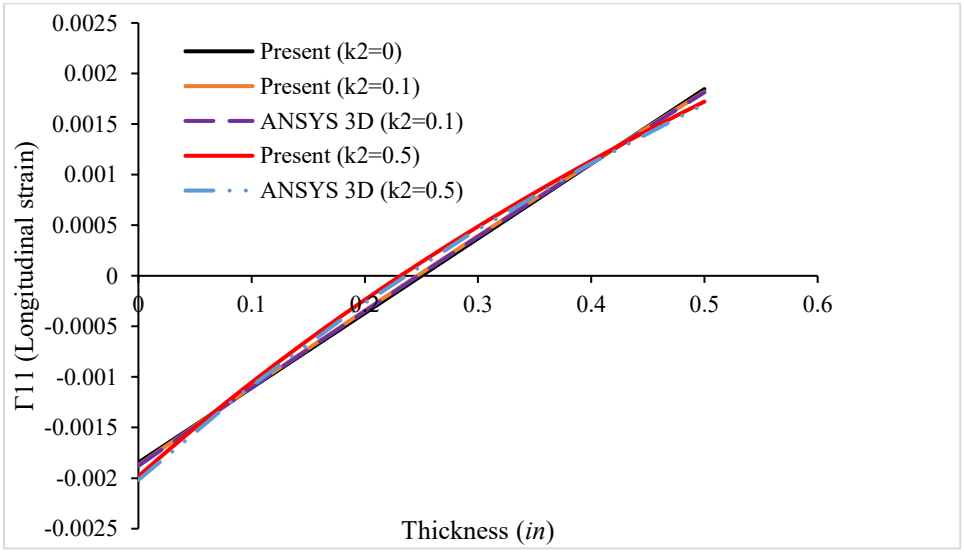

Fig. (6.5). distribution of longitudinal strain through the thickness of curved beams with rectangular cross-section with various initial curvatures (E=2.6× 10^7 psi, ν=0.3).

6.2.2 Unidirectional square section

A square section with dimensions of (0.5 *in*×0.5 *in*) with material properties E_1=21.5× 10^6 psi (1.48 GPa), E_2=1.46× 10^6 psi (10 GPa), v_{12}=0.3, v_{13}=0.3, v_{23}=0.3, G_{12}= G_{13}= G_{23}=0.81× 10^6 *psi* (5.58 GPa) is studied. The obtained cross-sectional stiffness constants of the prismatic and curved unidirectional square sections with k_2=0.1 *1/in* are shown in Table (6.3). It is observed that two stiffness constants will be added to the prismatic ones as S_{15} and S_{24}. The values of the obtained stiffness constants by the polynomial method with (*m*=7) agree well with VABS 3.8.

Table (6.3). Stiffness constants of unidirectional square cross-section with (k_2=0.1 1/*in*).

S	**VABS 3.8** Classic (2nd order)	**VABS 3.8** (Timoshenko)	**Present** Classic (2nd order)	**Present** (Timoshenko)
S_{11} **(lb)**	*5.376*× 10^6	*4.327*× 10^6	5.376 × 10^6	*4.264*× 10^6
S_{15} **(lb.in)**	*-1.456*× 10^4	*-1.233*× 10^4	*-1.456*× 10^4	*-1.228*× 10^4
S_{22} **(lb)**	-	*1.678*× 10^5	-	*1.697*× 10^5
S_{24} **(lb.in)**	-	*1.425*× 10^2	-	*2.482*× 10^2
S_{33} **(lb)**	-	*1.675*× 10^5	-	*1.664*× 10^5
S_{44} **(lb.in^2)**	7.118 × 10^3	*7.119*× 10^3	*7.119*× 10^3	7.174 × 10^3
S_{55} **(lb.in^2)**	*1.116*× 10^5	*1.116*× 10^5	*1.120*× 10^5	*1.120*× 10^5
S_{66} **(lb.in^2)**	*1.116*× 10^5	*1.114*× 10^5	*1.120*× 10^5	*1.110*× 10^5

6.2.3 Tubular isotropic section

The next case study is the tubular curved and straight aluminum beams. The tubes have inner and outer radii r_i=0.049 *m* and r_o=0.059 *m* and material properties *E*=69.7 *GPa* and *v*=0.3. The stiffness constants of this section for straight and curved beams are reported in Table (6.4). It is seen that two values of S_{15} and S_{24} are added to the straight tube stiffness constants. Moreover, it is observed that there is a good agreement between the presented polynomial based method (with *m*=4) and VABS 3.8. It is noted that the tubular cross-section is meshed with 2891 elements whereas there is no need to mesh the cross-section with the presented polynomial method. The generated mesh of the cross-section with VABS 3.8 is shown in Fig. (6.6). The values for extension-bending stiffness (S_{15}) of Classical beam model up to 2nd order and Timoshenko are different. This difference can affect the distribution of normal strains of the tube in the recovery analysis.

Table (6.4). Stiffness constants of aluminum tubular cross-section with initial curvature.

Beam type	***Straight***		***k_2=0.1 (1/m)***			
S	**VABS 3.8 (Timoshenko)**	**Present (Timoshenko)**	**VABS 3.8 Classic (2nd order)**	**VABS 3.8 (Timoshenko)**	**Present Classic (2nd order)**	**Present (Timoshenko)**
S_{11}	2.364×10^{8}	2.365×10^{8}	2.364×10^{8}	2.364×10^{8}	2.365×10^{8}	2.365×10^{8}
S_{15}	0	0	-4.520×10^{4}	-5.543×10^{4}	-4.517×10^{4}	-5.515×10^{4}
S_{24}	0	0	-	8.538×10^{3}	-	8.342×10^{3}
S_{22}	4.605×10^{7}	4.724×10^{7}	-	4.605×10^{7}	-	4.725×10^{7}
S_{33}	4.605×10^{7}	4.720×10^{7}	-	4.605×10^{7}	-	4.718×10^{7}
S_{44}	2.674×10^{5}	2.677×10^{5}	2.674×10^{5}	2.674×10^{5}	2.677×10^{5}	2.677×10^{5}
S_{55}	3.475×10^{5}	3.476×10^{5}	3.475×10^{5}	3.475×10^{5}	3.476×10^{5}	3.476×10^{5}
S_{66}	3.475×10^{5}	3.483×10^{5}	3.475×10^{5}	3.475×10^{5}	3.483×10^{5}	3.483×10^{5}

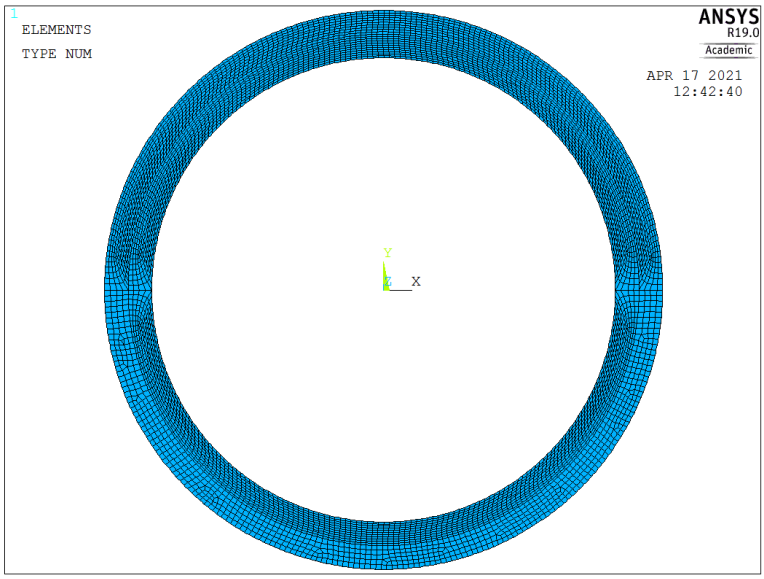

Fig. (6.6). The generated tubular section mesh in VABS 3.8.

The normal strains of the studied aluminum tube with k_2=0.1 (1/m) using Timoshenko-Like beam model subjected to the bending moment M_2=1 KN.m are shown in Figs. (6.7-6.9). The obtained strains are compared with ANSYS 3D FEM. The tube is under pure bending moment at one side and clamed at the other side in ANSYS 3D solution. The mesh is refined to 1794460 number of 3D elements. A good agreement between the present solution and ANSYS 3D is observed. The maximum difference between the Pascal polynomial solution and ANSYS 3D is 10.7% for Γ_{22}. It is noted that the values of Γ_{12} and Γ_{13} are zero for the tube under pure bending moment. The distribution of normal strains at $\theta = 90^{\circ}$ of the tube has been demonstrated in Fig. (6.10). A good

agreement for normal strains has been obtained for this tube, there is a difference between the present method and ANSYS 3D for shear strain Γ_{23} in which the maximum of Γ_{23} is negligible compared to the normal strains.

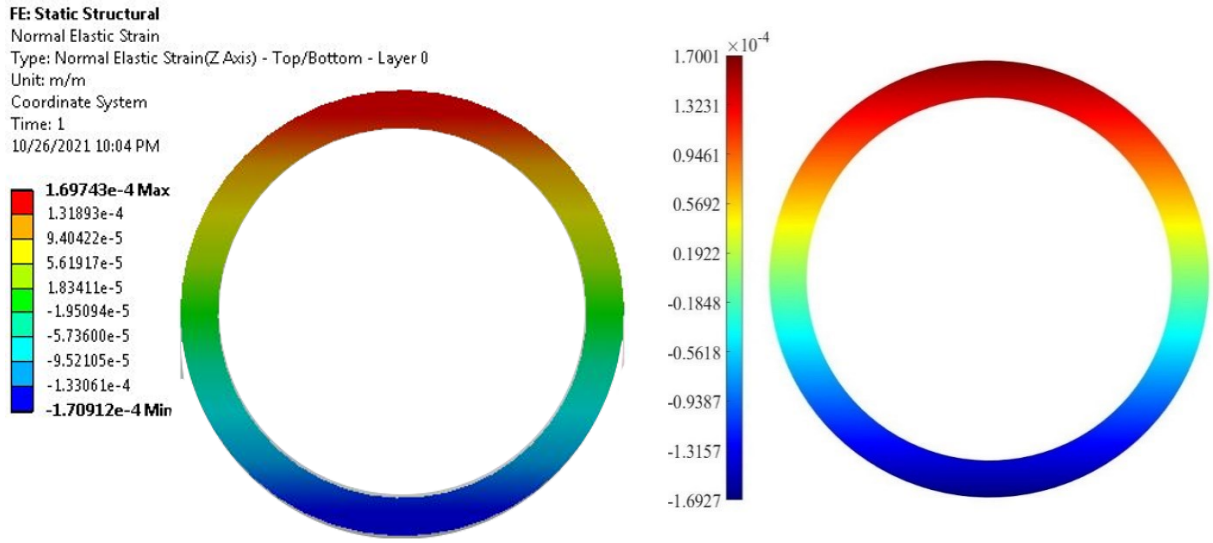

a) ANSYS 3D *b*) Present

Fig. (6.7). Distribution of Γ_{11} in the section of the tubular aluminum curved beam k_2=0.1 1/*m*, *a*) ANSYS 3D, *b*) Present

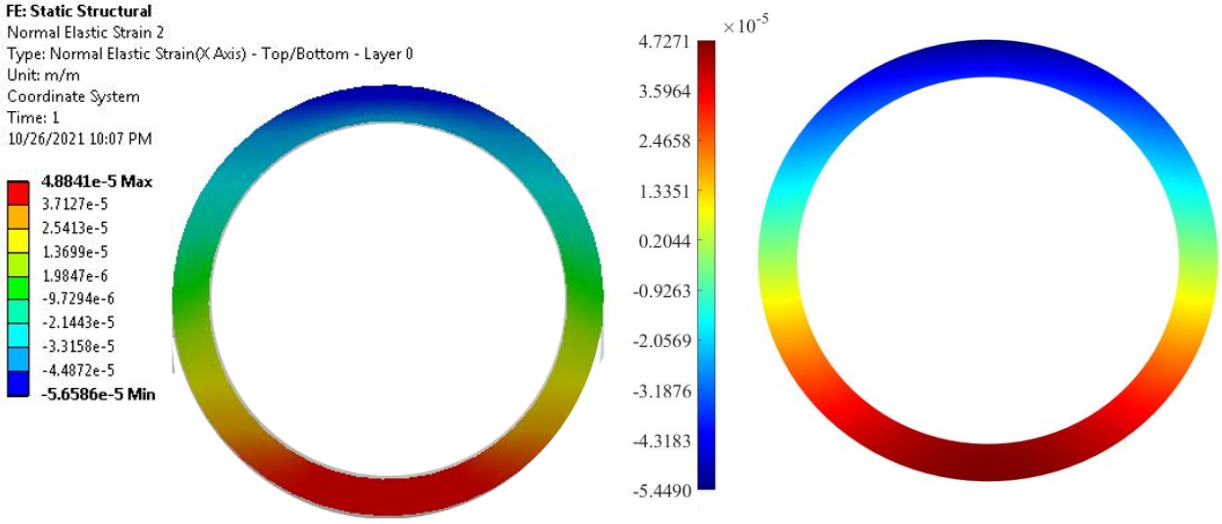

a) ANSYS 3D *b*) Present

Fig. (6.8). Distribution of Γ_{22} in the section of the tubular aluminum curved beam k_2=0.1 1/*m*, *a*) ANSYS 3D, *b*) Present.

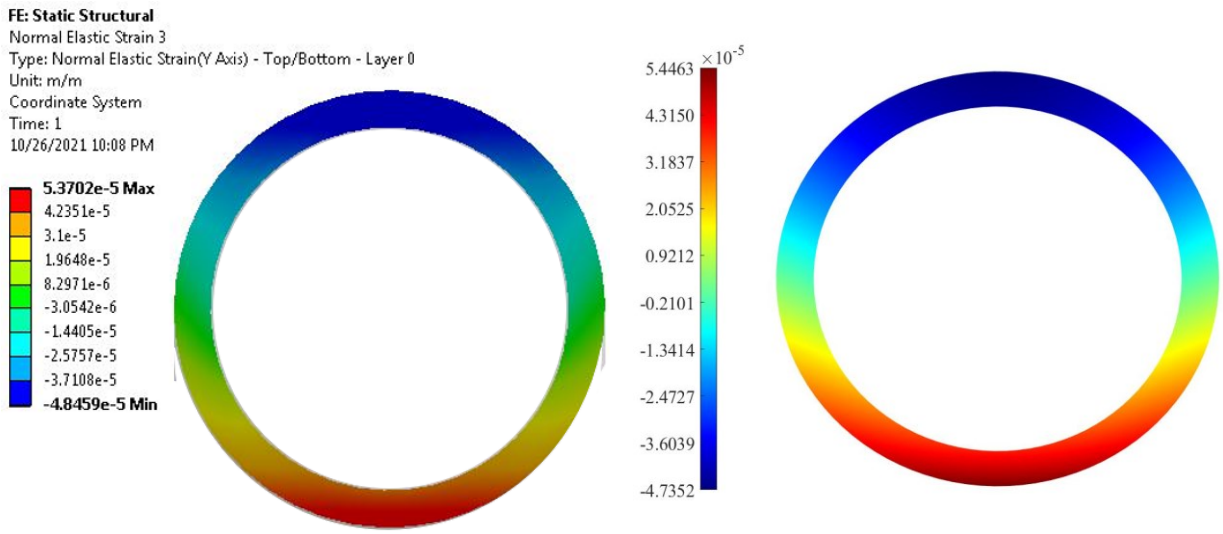

a) ANSYS 3D *b*) Present

Fig. (6.9). Distribution of Γ_{33} in the section of the tubular aluminum curved beam k_2=0.1 1/*m*, *a*) ANSYS 3D, *b*) Present.

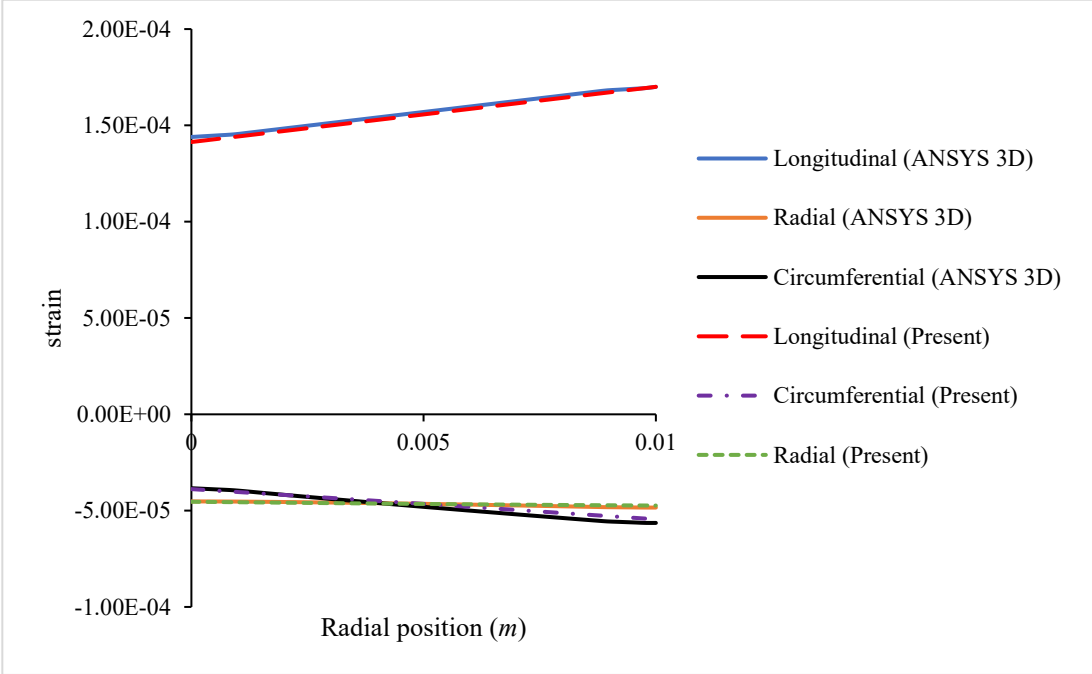

Fig. (6.10). Distribution of strains at $\theta = 90^{\circ}$ of the isotropic curved tube with, r_i=*0.049 m and* r_o=*0.059 m,* k_2=0.1 1/*m*.

To observe the effect of initial curvature on strains distribution of curved tubes, we studied two isotropic tubes with initial radius of curvatures of *R*=2 *m* and 10 *m* with the same material properties and cross-section dimensions. The longitudinal Γ_{11}, circumferential and radial strains at

$\theta = 90^{\circ}$ of the section are investigated. It can be observed from Fig. (6.11) that by changing the initial curvature, there is no significant change in the longitudinal strain Γ_{11}. While as the radius of initial curvature decreases from 10 m to 2 m, the distribution of circumferential Γ_{22} and radial strains Γ_{33} at this position change noticeably.

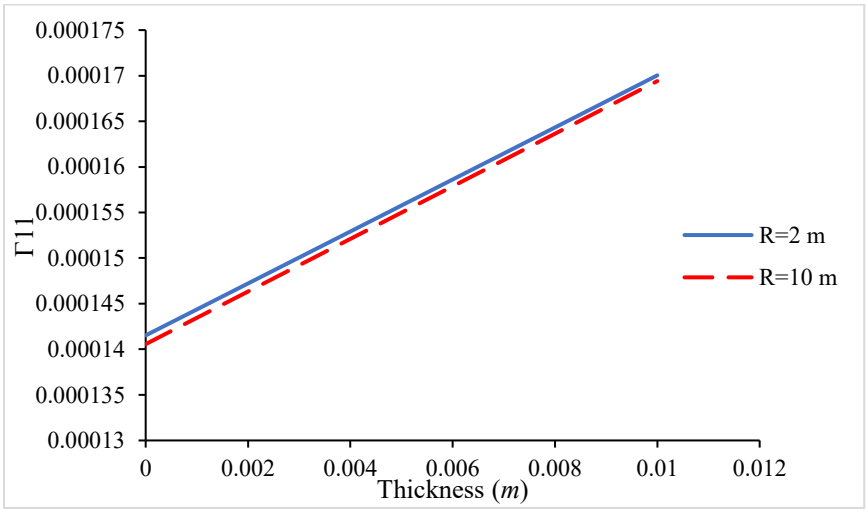

a) Distribution of Γ_{11}

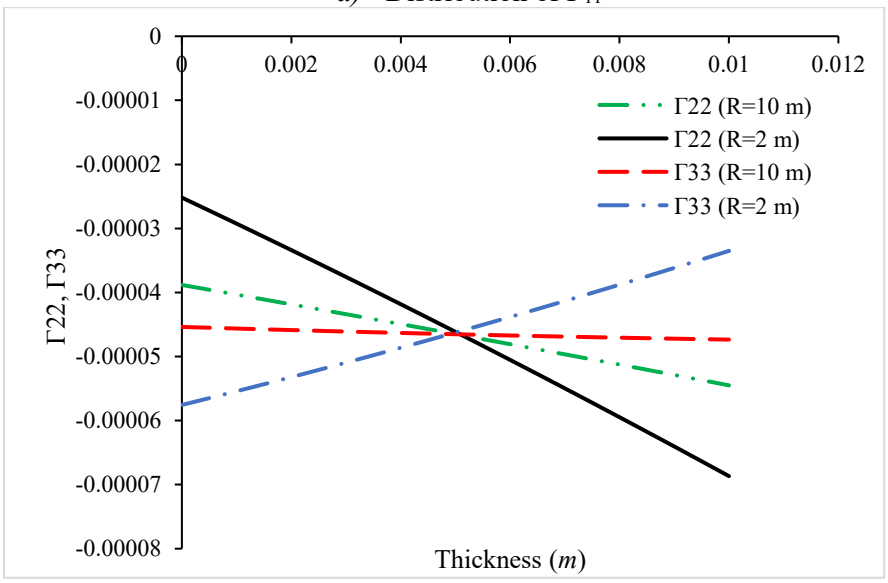

b) Distribution of Γ_{22} and Γ_{33}

Fig. (6.11). Distribution of strains *a*) Γ_{11}, *b*) Γ_{22} and Γ_{33} at $\theta = 90^{\circ}$ of the isotropic curved tube with, r_i=0.049 m and r_o=0.059 m, for two values of k_2=0.1 and 0.5 $1/m$.

6.2.4 Tubular orthotropic sections

Unidirectional $[0]_{10}$, $[90]_{10}$ and cross-ply tubes

Initially curved beams with tubular sections stiffness constants with inner and outer radii r_i=0.049 m, r_o=0.059 m, and material properties E_1=138 GPa, E_2=10.5 GPa, v_{12}=0.3, v_{13}=0.31, v_{23}=0.33, G_{12}= G_{13}= G_{23}=5.57 GPa are studied. The thickness of each layer is 1 mm. These cross-sectional dimensions and material properties are used for composite tubular beams in the following cross-sections in this chapter unless the other material properties or dimensions are mentioned. The obtained stiffness constants of unidirectional $[0]_{10}$ and $[90]_{10}$ curved tubes are calculated and compared with VABS 3.8 in the Tables (6.5) and (6.6), respectively. It is seen that the values of S_{11}, S_{15}, S_{55} and S_{66} decrease by changing the fiber angle of the curved tube from $[0]_{10}$ to $[90]_{10}$.

Table (6.5). Stiffness constants of $[0]_{10}$ tubular cross-section, (r_i=0.049 m and r_o=0.059 m, k_2=0.1 (1/m)).

S	VABS 3.8 Classic (2nd order)	VABS 3.8 (Timoshenko)	Present Classic (2nd order)	Present (Timoshenko)
S_{11}	4.682×10^8	4.524×10^8	4.670×10^8	4.670×10^8
S_{15}	-9.019×10^4	-1.082×10^5	-8.916×10^4	-8.916×10^4
S_{22}	-	9.422×10^6	-	1.003×10^7
S_{24}	-	2.089×10^3	-	1.968×10^3
S_{33}	-	9.420×10^6	-	9.789×10^6
S_{44}	5.558×10^4	5.558×10^4	5.563×10^4	5.563×10^4
S_{55}	6.826×10^5	6.826×10^5	6.876×10^5	6.876×10^5
S_{66}	6.826×10^5	6.826×10^5	6.973×10^5	6.973×10^5

Table (6.6). Stiffness constants of $[90]_{10}$ tubular cross-section, (r_i=0.049 m and r_o=0.059 m, k_2=0.1 ($1/m$)).

S	VABS 3.8 Classic (2nd order)	VABS 3.8 (Timoshenko)	Present Classic (2nd order)	Present (Timoshenko)
S_{11}	3.574×10^7	3.574×10^7	3.586×10^7	3.586×10^7
S_{15}	-5.391×10^3	-5.518×10^3	-5.216×10^3	-5.534×10^3
S_{22}	-	9.577×10^6	-	9.814×10^6
S_{24}	-	2.055×10^3	-	2.114×10^3
S_{33}	-	9.577×10^6	-	9.801×10^6
S_{44}	5.558×10^4	5.558×10^4	5.563×10^4	5.563×10^4
S_{55}	5.254×10^4	5.258×10^4	5.258×10^4	5.258×10^4
S_{66}	5.254×10^4	5.258×10^4	5.268×10^4	5.268×10^4

The cross-sectional stiffness constants of composite tubes with lay-up $[90_5/0_5]$ for two values of k_2=0.1 and 0.5 $1/m$ have been calculated and reported in Tables (6.7-6.8) using the present method and VABS 3.8. Comparison of stiffness constants of tubes with k_2=0.1 and 0.5 $1/m$ shows that by

changing the curvature from 0.1 to 0.5, the value of S_{11} (Timoshenko) decreases, while the magnitude of S_{15} increases, while the value of S_{55} reduces slightly. Also, a good correlation between the present method and VABS 3.8 is observed.

Table (6.7). Stiffness constants of $[90_5/0_5]$ tubular cross-section, (r_i=0.049 m and r_o=0.059 m, k_2=0.1 $(1/m)$).

S	**VABS 3.8 Classic (2nd order)**	**VABS 3.8 (Timoshenko)**	**Present Classic (2nd order)**	**Present (Timoshenko)**
S_{11}	2.631×10^8	2.606×10^8	2.630×10^8	2.605×10^8
S_{15}	-4.492×10^4	-4.667×10^4	-5.105×10^4	-4.693×10^4
S_{22}	-	1.023×10^7	-	1.033×10^7
S_{24}	-	1.940×10^3	-	2.664×10^3
S_{33}	-	1.024×10^7	-	1.040×10^7
S_{44}	5.558×10^4	5.558×10^4	5.518×10^4	5.518×10^4
S_{55}	4.156×10^5	4.156×10^5	4.160×10^5	4.160×10^5
S_{66}	4.155×10^5	4.155×10^5	4.160×10^5	4.163×10^5

Table (6.8). Stiffness constants of $[90_5/0_5]$ tubular cross-section, (r_i=0.049 m and r_o=0.059 m, k_2=0.5 $(1/m)$).

S	**VABS 3.8 Classic (2nd order)**	**VABS 3.8 (Timoshenko)**	**Present Classic (2nd order)**	**Present (Timoshenko)**
S_{11}	2.632×10^8	1.944×10^8	2.631×10^8	2.005×10^8
S_{15}	-2.247×10^5	-1.753×10^5	-2.554×10^5	-1.806×10^5
S_{22}	-	9.598×10^6	-	1.034×10^7
S_{24}	-	1.032×10^4	-	1.427×10^4
S_{33}	-	9.614×10^6	-	1.041×10^7
S_{44}	5.558×10^4	5.561×10^4	5.520×10^4	5.562×10^4
S_{55}	4.029×10^5	4.028×10^5	4.164×10^5	4.165×10^5
S_{66}	4.023×10^5	4.018×10^5	4.162×10^5	4.137×10^5

Angle-ply tubes

To study the cross-sectional properties of the angle-ply curved tubes, a $[30]_{10}$ and $[0_5/45_5]$ tubes are considered. In Table (6.9), the cross-sectional stiffness constants of the curved $[30]_{10}$ tubes are reported. It is seen that the additional stiffness constants S_{14}, S_{25}, S_{36} and S_{45} are added to the section properties of the angle-ply curved tube compared to unidirectional. Moreover, it can be seen that the obtained S_{55} and S_{66} of the Classical beam model (up to second order of the strain energy) are smaller than the Timoshenko beam model results.

Table (6.9). Stiffness constants of $[30]_{10}$ tubular cross-section, (r_i=0.049 *m* and r_o=0.059 *m*, k_2=0.1 (*1/m*)).

S	VABS 3.8 Classic (2nd order)	VABS 3.8 (Timoshenko)	Present Classic (2nd order)	Present (Timoshenko)
S_{11}	1.723×10^{8}	1.727×10^{8}	1.748×10^{8}	1.761×10^{8}
S_{14}	-4.029×10^{6}	-4.037×10^{6}	-4.175×10^{6}	-4.156×10^{6}
S_{15}	-5.415×10^{4}	-5.468×10^{4}	-5.354×10^{4}	-5.584×10^{4}
S_{22}	-	3.115×10^{7}	-	3.017×10^{7}
S_{24}	-	7.579×10^{3}	-	8.367×10^{3}
S_{25}	-	2.078×10^{6}	-	2.046×10^{6}
S_{33}	-	3.121×10^{7}	-	2.990×10^{7}
S_{36}	-	2.075×10^{6}	-	2.014×10^{6}
S_{44}	1.750×10^{5}	1.753×10^{5}	1.755×10^{5}	1.786×10^{5}
S_{45}	1.647×10^{3}	1.228×10^{3}	1.603×10^{3}	1.903×10^{3}
S_{55}	1.189×10^{5}	2.576×10^{5}	1.150×10^{5}	2.544×10^{5}
S_{66}	1.190×10^{5}	2.571×10^{5}	1.157×10^{5}	2.540×10^{5}

The 3D strains of a curved section with lay-up of $[30]_{10}$ subjected to the moment of M_2=1 KN.m is calculated and compared with ANSYS 3D FEA, Figs. (6.12-6.16). The obtained strains agree well with ANSYS 3D FEA.

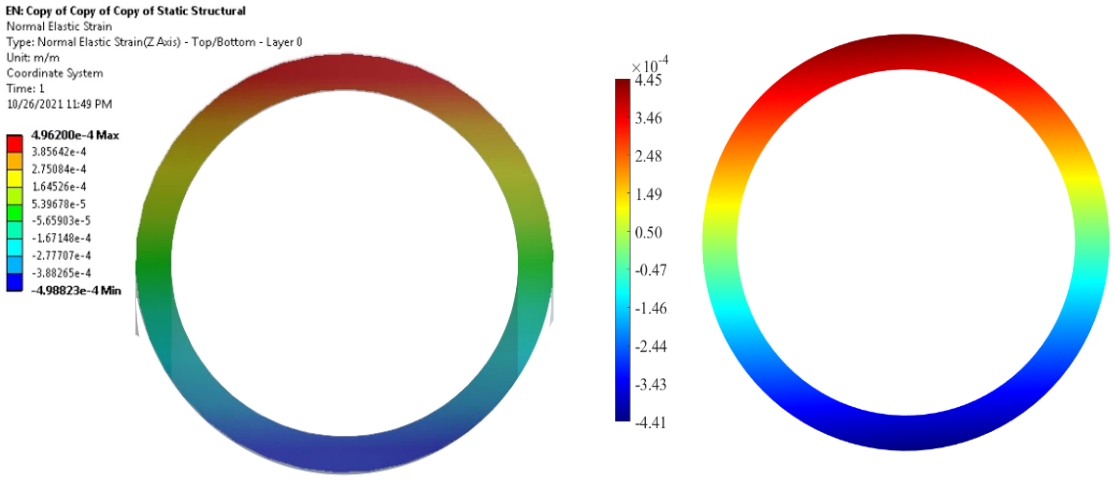

a) ANSYS 3D *b*) Present

Fig. (6.12). Distribution of Γ_{11} in the section of the tubular $[30]_{10}$ curved beam k_2=0.1 1/*m*, *a*) ANSYS 3D, *b*) Present

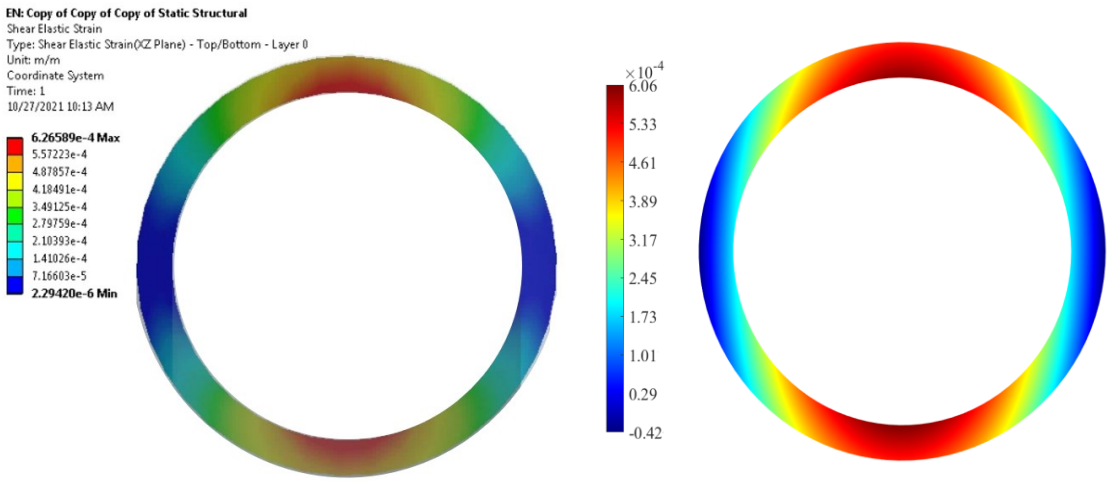

a) ANSYS 3D *b*) Present

Fig. (6.13). Distribution of Γ_{12} in the section of the tubular $[30]_{10}$ curved beam k_2=0.1 1/*m*, *a*) ANSYS 3D, *b*) Present.

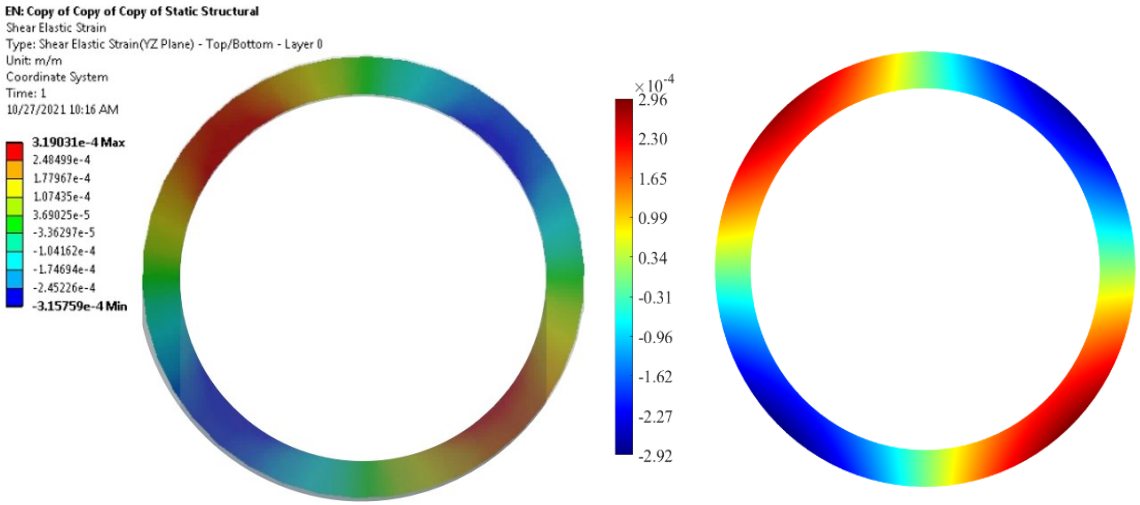

a) ANSYS 3D *b*) Present

Fig. (6.14). Distribution of Γ_{13} in the section of the tubular $[30]_{10}$ curved beam k_2=0.1 1/*m*, *a*) ANSYS 3D, *b*) Present.

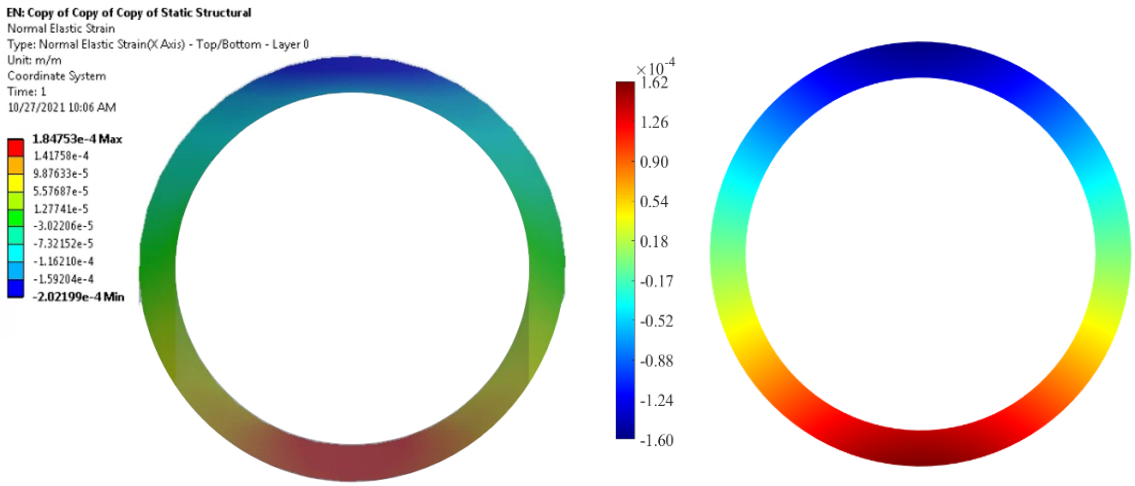

a) ANSYS 3D *b*) Present

Fig. (6.15). Distribution of Γ_{22} in the section of the tubular $[30]_{10}$ curved beam k_2=0.1 1/*m*, *a*) ANSYS 3D, *b*) Present.

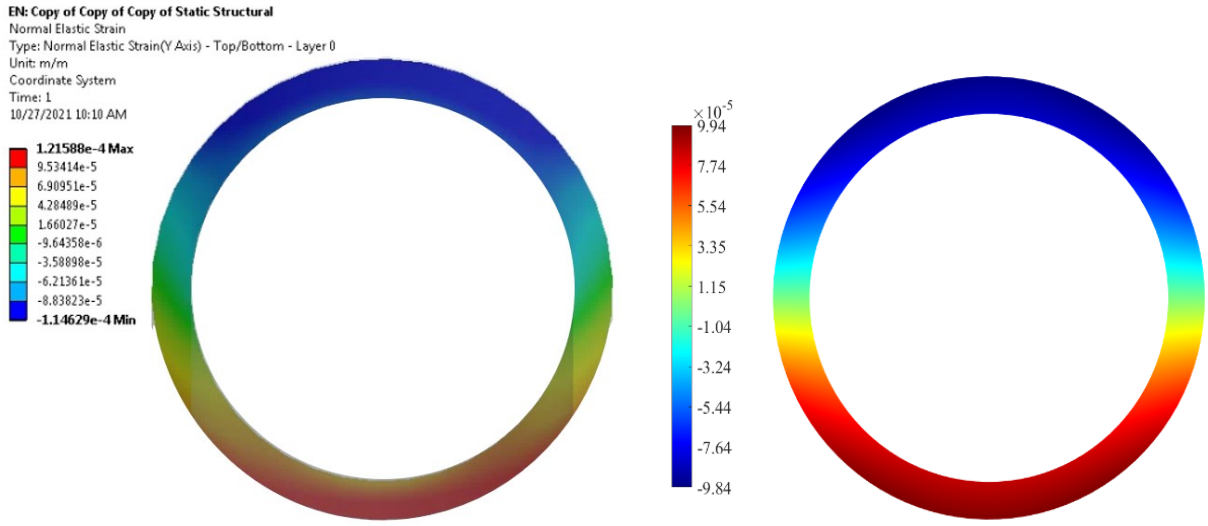

a) ANSYS 3D *b*) Present

Fig. (6.16). Distribution of Γ_{33} in the section of the tubular $[30]_{10}$ curved beam k_2=0.1 1/*m*, *a*) ANSYS 3D, *b*) Present.

The cross-sectional stiffness constants of curved tubes $[0_5/45_5]$ with initial curvatures of k_2=*0.05* (*1/m*) and k_2=*0.1* (*1/m*) are reported in the Table (6.10). A good agreement between the obtained stiffness constants of the present method and the VABS 3.8 is observed for the complex lay-ups. Moreover, it can be observed that there is not a substantial difference in the S_{55} and S_{66} of the obtained Classical beam model (up to the second order of the strain energy) and the Timoshenko stiffness constants.

Table (6.10). Stiffness constants of $[0_5/45_5]$ tubular cross-section, (r_i=0.049 *m* and r_o=0.059 *m*).

Curvature	k_2=0.05 (1/m)		k_2=0.1 (1/m)			
S	**VABS 3.8 (Timoshenko)**	**Present (Timoshenko)**	**VABS 3.8 Classic (2nd order)**	**VABS 3.8 (Timoshenko)**	**Present Classic (2nd order)**	**Present (Timoshenko)**
S_{11}	2.610×10^{8}	2.617×10^{8}	2.612×10^{8}	2.607×10^{8}	2.612×10^{8}	2.620×10^{8}
S_{14}	-1.109×10^{6}	-1.145×10^{6}	-1.112×10^{6}	-1.113×10^{6}	-1.114×10^{6}	-1.149×10^{6}
S_{15}	-3.873×10^{4}	-4.417×10^{4}	-6.167×10^{4}	-7.694×10^{4}	-6.039×10^{4}	-8.870×10^{4}
S_{22}	1.738×10^{7}	1.669×10^{7}	-	1.730×10^{7}	-	1.669×10^{7}
S_{24}	2.627×10^{3}	2.968×10^{3}	-	5.200×10^{3}	-	5.951×10^{3}
S_{25}	4.910×10^{5}	4.950×10^{5}	-	4.903×10^{5}	-	4.955×10^{5}
S_{33}	1.739×10^{7}	1.679×10^{7}	-	1.730×10^{7}	-	1.681×10^{7}
S_{36}	4.868×10^{5}	4.944×10^{5}	-	4.871×10^{5}	-	4.939×10^{5}
S_{44}	1.242×10^{5}	1.268×10^{5}	1.243×10^{5}	1.243×10^{5}	1.268×10^{5}	1.269×10^{5}
S_{45}	7.263×10^{2}	7.285×10^{2}	1.592×10^{3}	1.455×10^{3}	1.583×10^{3}	1.459×10^{3}
S_{55}	3.564×10^{5}	3.570×10^{5}	3.417×10^{5}	3.556×10^{5}	3.426×10^{5}	3.573×10^{5}
S_{66}	3.561×10^{5}	3.575×10^{5}	3.417×10^{5}	3.553×10^{5}	3.428×10^{5}	3.574×10^{5}

The cross-sectional analysis of a tubular section with complex lay-up $[90_{40}/60_{60}/\text{-}60_{60}]$ is performed. This tube has the inner and outer diameters of D_i=78 *mm* and D_o=110 *mm*, respectively. The thickness of each ply is 0.1 *mm*. In Table (6.11), the cross-sectional stiffness constants of this tube with two values of initial curvature k_2=0.1 1/*m* and k_2=0.5 1/*m* are demonstrated. The polynomial order (*m*=7) is employed for the analysis. The distribution of 3D strains in the curved tube with initial curvature of k_2=0.5 1/*m* is illustrated in Figs. (6.17-6.19). The total number of elements for analysis of this tube in ANSYS is 1924640. The total computational time for analysis of this tube in ANSYS is 1 hour and 45 minutes. The required time for calculation of stiffness constants and the strains using the Pascal polynomial dimensional reduction method is 30 minutes. It is noted that the Pascal polynomial solution is performed in Maple 19 software. Maple uses only one cores of the CPU. The programming in other programming software (*e.g.* C++) may reduce the computational time considerably with respect to MAPLE.

Table (6.11). Stiffness constants of $[90_{40}/60_{60}/\text{-}60_{60}]$ tubular cross-section, (D_i=78 *mm* and D_o=110 *mm*).

Beam type	k_2=0.1 (1/m)		k_2=0.5 (1/m)			
S	**VABS 3.8 (Timoshenko)**	**Present (Timoshenko)**	**VABS 3.8 Classic (2nd order)**	**VABS 3.8 (Timoshenko)**	**Present Classic (2nd order)**	**Present (Timoshenko)**
S_{11}	6.067×10^{7}	6.098×10^{7}	6.069×10^{7}	6.073×10^{7}	6.101×10^{7}	6.116×10^{7}
S_{14}	-6.899×10^{4}	-7.387×10^{4}	-6.917×10^{4}	-6.949×10^{4}	-7.395×10^{4}	-6.745×10^{4}
S_{15}	-1.024×10^{4}	-1.033×10^{4}	-4.243×10^{4}	-5.132×10^{4}	-4.369×10^{4}	-5.138×10^{4}

S_{22}	5.255×10^{7}	5.420×10^{7}	-	5.248×10^{7}	-	5.403×10^{7}
S_{24}	-3.813×10^{3}	-1.229×10^{3}	-	-1.856×10^{4}	-	-6.593×10^{4}
S_{25}	1.455×10^{4}	1.560×10^{4}	-	1.466×10^{4}	-	1.568×10^{4}
S_{33}	5.222×10^{7}	5.340×10^{7}	-	5.216×10^{7}	-	5.410×10^{7}
S_{36}	1.035×10^{4}	1.587×10^{4}	-	1.031×10^{4}	-	1.594×10^{4}
S_{44}	2.580×10^{5}	2.622×10^{5}	2.580×10^{5}	2.583×10^{5}	2.620×10^{5}	2.377×10^{5}
S_{55}	6.738×10^{4}	6.823×10^{4}	6.736×10^{4}	6.738×10^{4}	6.827×10^{4}	6.829×10^{4}
S_{66}	6.732×10^{4}	6.823×10^{4}	6.727×10^{4}	6.726×10^{4}	6.827×10^{4}	6.801×10^{4}

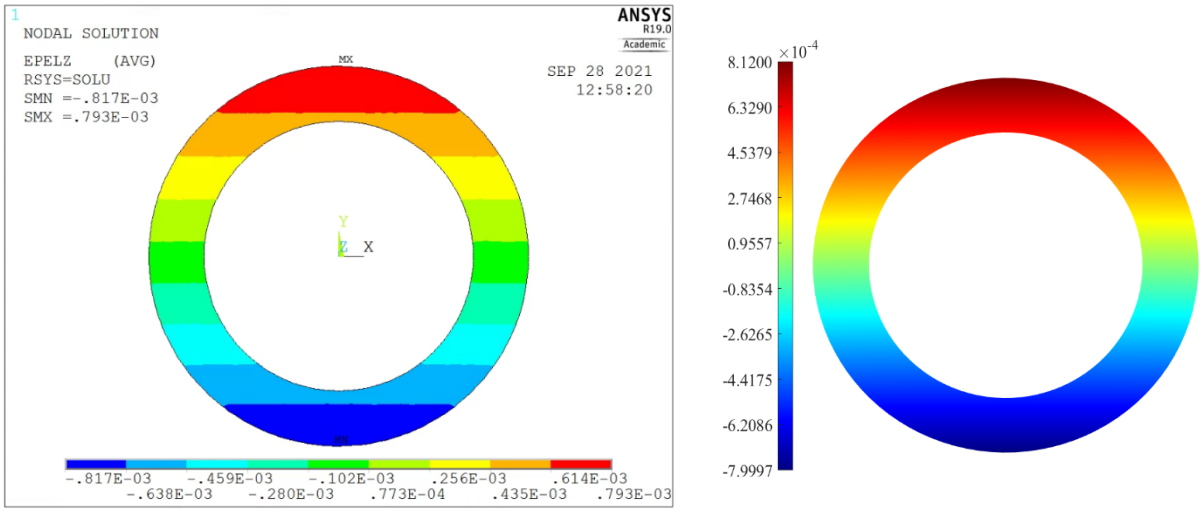

a) VABS 3.8 *b*) Present

Fig. (6.17). Distribution of Γ_{11} in the section of the tubular [90_{40}/-60_{60}/60_{60}] curved beam with k_2=0.5 1/*m*, *a*) VABS 3.8, *b*) Present.

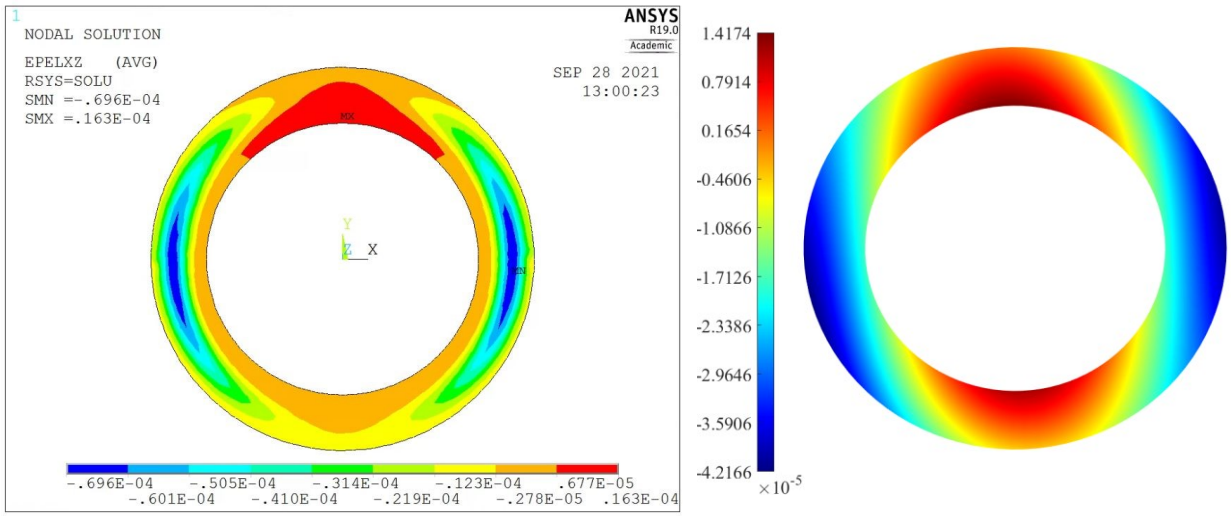

a) VABS 3.8 *b*) Present

Fig. (6.18). Distribution of $2\Gamma_{12}$ in the section of the tubular [90_{40}/-60_{60}/60_{60}] curved beam with k_2=0.5 1/*m*, *a*) VABS 3.8, *b*) Present.

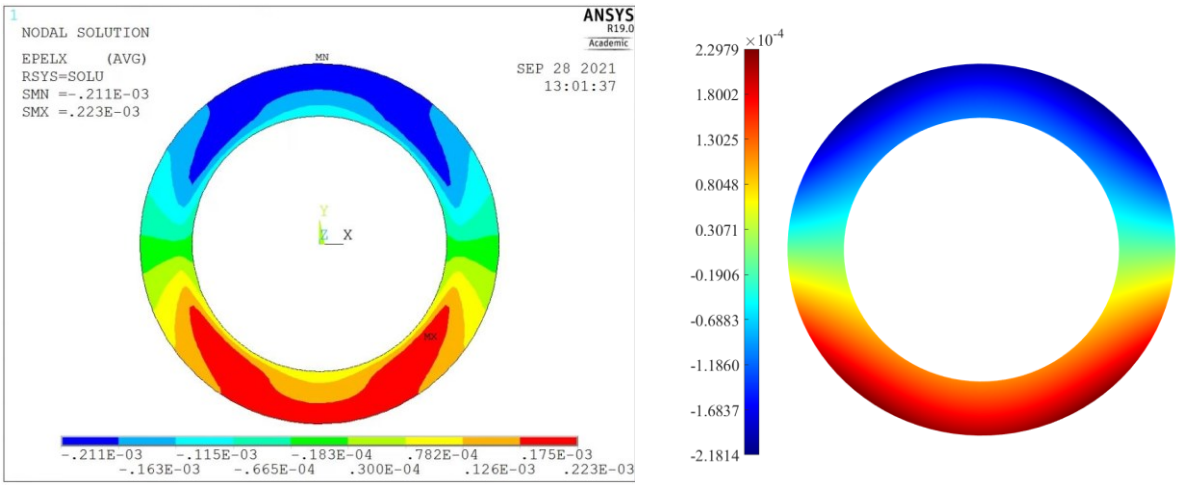

a) VABS 3.8 *b*) Present

Fig. (6.19). Distribution of Γ_{22} in the section of the tubular $[90_{40}/\text{-}60_{60}/60_{60}]$ curved beam with k_2=0.5 1/*m*, *a*) VABS 3.8, *b*) Present.

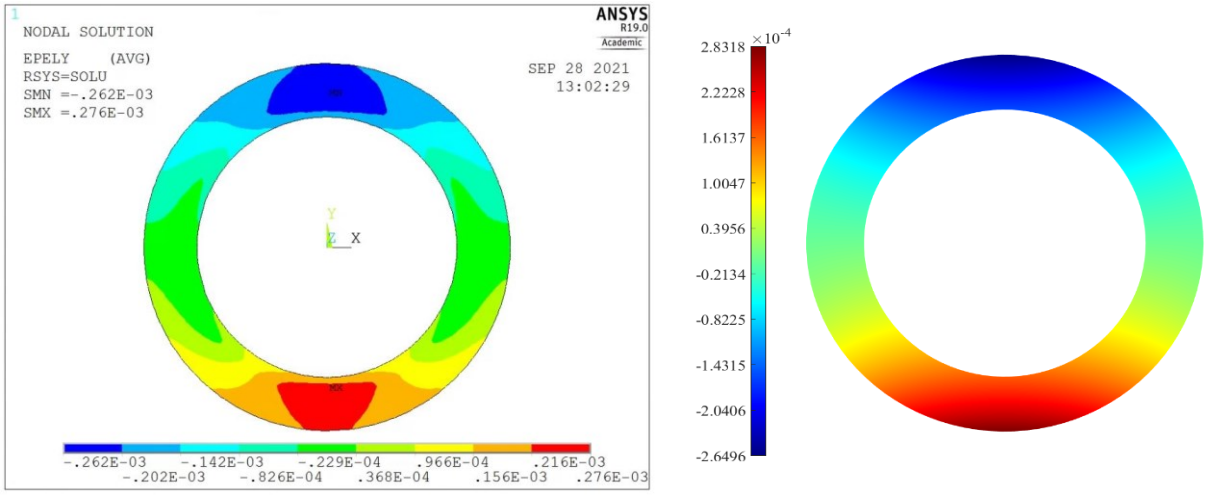

a) VABS 3.8 *b*) Present

Fig. (6.20). Distribution of Γ_{33} in the section of the tubular $[90_{40}/\text{-}60_{60}/60_{60}]$ curved beam with k_2=0.5 1/*m*, *a*) VABS 3.8, *b*) Present.

Distribution of normal strains such as longitudinal strain, circumferential strain and radial strain at the circumference angle of $\theta = 90^{\circ}$ of the tube $[90_{40}/\text{-}60_{60}/60_{60}]$ with initial curvature k_2=0.5 1/*m* is shown in Fig. (6.21*a*). A good agreement between the present method and VABS 3.8 is observed. The distribution of shear strain ($2\Gamma_{12}$) is shown in Fig. (6.21*b*) in which some difference between the VABS and the present solution is observed. Increasing the polynomial order may

reduce this difference. The distribution of other shear strains $2\Gamma_{13}$ and $2\Gamma_{23}$ are negligible compared to the other strains at this circumferential position.

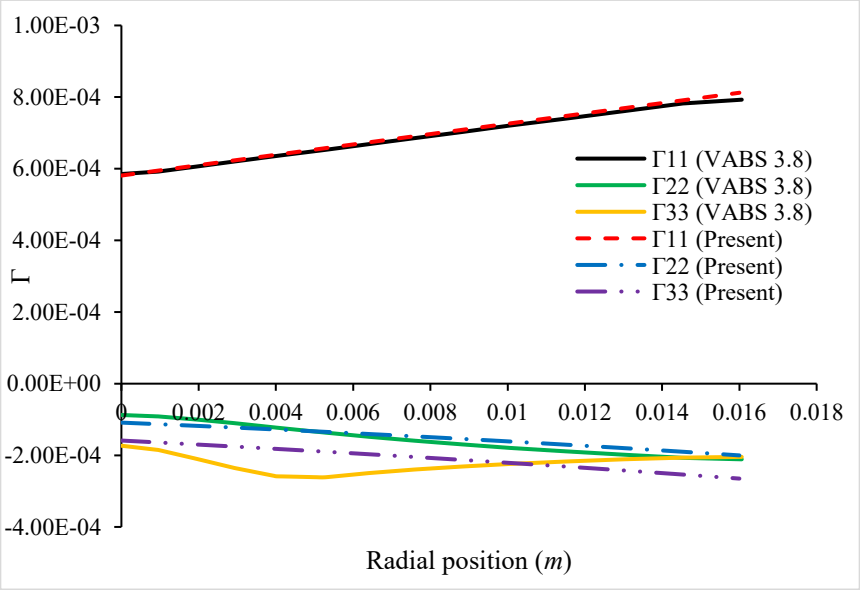

a)

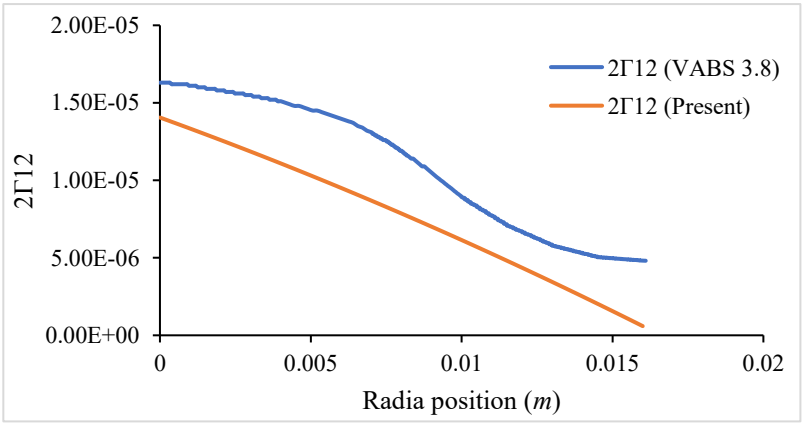

b)

Fig. (6.21). *a*) Normal strains, *b*) shear strain, through the radial position of tube with lay-up $[90_{40}/\text{-}60_{60}/60_{60}]$ and (k_2=0.5 1/*m*) at $\theta = 90^{\circ}$ of the circumference.

6.3 1D analysis using straight elements to model a curved beam

In this section, a 1D FE solution is provided for determining the global behavior of beams under complex loadings. In the presented curved beam solution, we model the beam with straight elements (piecewise Cartesian). The modeling can be performed using two ways. The first

modeling can be done by setting k_2=0 to obtain the cross-sectional stiffness matrix. The second way, one can set $k_2 \neq 0$ for obtaining the cross-sectional stiffness matrix. In both the ways, we should model with sufficiently large number of elements to have convergence.

6.3.1 1D analysis of initially curved beams

In order to study the global behavior of the orthotropic curved beam, a simple 1D FE solution is developed. Using the stiffness matrix of Eq. (3.42), the one-dimensional strain energy can be constructed as Eq. (6.1).

$$2U^e = \int_{L_e} \left\{ \zeta^T [Y_1] \zeta \right\} dx_1 \tag{6.1}$$

$[Y_1]$ is the classical cross-sectional stiffness matrix up to the second order of the strain energy which considers the initial curvature. ζ is the strain vector of the reference line. $\zeta = \left[\bar{\gamma}_{11} \quad \bar{\kappa}_1 \quad \bar{\kappa}_2 \quad \bar{\kappa}_3 \right]^T$ and L_e is the element length. We define a global coordinate ($\bar{x}, \bar{y}, \bar{z}$) for the beam element. The beam element has the local coordinate (x_1, x_2, x_3). Fig. (6.22) shows the beam element in space. The element has 6 degrees of freedom at each node including three displacements (u, v and w) and three cross-sectional rotations ($\omega_{x_1}, \omega_{x_2}, \omega_{x_3}$) in the local coordinate (x_1, x_2 and x_3), respectively. Hence, twelve degrees of freedom for the element is considered.

The following polynomials for the approximation of the degree of freedom in the beam local coordinate is used, [84].

$$u = \bar{\alpha}_1 + \bar{\alpha}_2 x_1 \tag{6.2a}$$

$$v = \bar{\alpha}_3 + \bar{\alpha}_4 x_1 + \bar{\alpha}_5 x_1^2 + \bar{\alpha}_6 x_1^3 \tag{6.2b}$$

$$w = \bar{\alpha}_7 + \bar{\alpha}_8 x_1 + \bar{\alpha}_9 x_1^2 + \bar{\alpha}_{10} x_1^3 \tag{6.2c}$$

$$\omega_{x_1} = \bar{\alpha}_{11} + \bar{\alpha}_{12} x_1 \tag{6.2d}$$

$$\omega_{x_2} = -\bar{\alpha}_8 - 2\bar{\alpha}_9 x_1 - 3\bar{\alpha}_{10} x_1^2 \tag{6.2e}$$

$$\omega_{x_3} = \bar{\alpha}_4 + 2\bar{\alpha}_5 x_1 + 3\bar{\alpha}_6 x_1^2 \tag{6.2f}$$

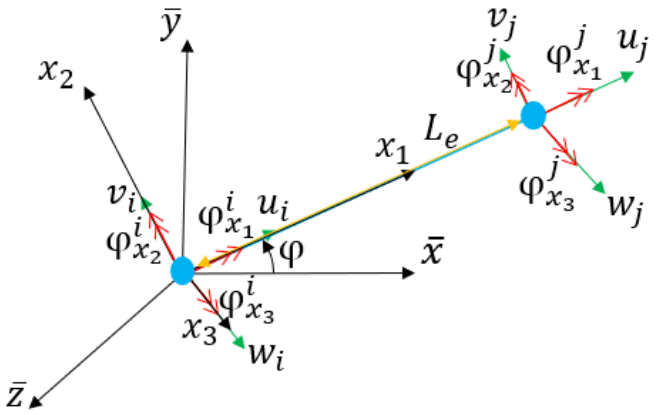

Fig. (6.22). Presentation of the beam element with two nodes in space.

For a Timoshenko beam model, the 1D generalized strain components in the local coordinate are as follows.

$$\begin{Bmatrix} \bar{\gamma}_{11} \\ \bar{\kappa}_1 \\ \bar{\kappa}_2 \\ \bar{\kappa}_3 \end{Bmatrix} = \begin{Bmatrix} u' \\ \omega'_{x_1} \\ \omega'_{x_2} \\ \omega'_{x_3} \end{Bmatrix} \tag{6.3}$$

The unknowns $(\bar{\alpha}_1, \bar{\alpha}_2, ..., \bar{\alpha}_{12})$ in the Eq. (6.2) are expressed in terms of nodal displacement vector $\boldsymbol{\delta}$ by substituting u, v, w, ω_{x_1} , ω_{x_2} and ω_{x_3} at the nodes of the beam element in the local coordinate. We have:

$$\boldsymbol{\delta} = [\tilde{N}]_{12\times12}\bar{\boldsymbol{\alpha}} \text{ or } \bar{\boldsymbol{\alpha}} = [\tilde{N}]^{-1}\boldsymbol{\delta} \tag{6.4}$$

where $\bar{\boldsymbol{\alpha}} = [\bar{\alpha}_1, \bar{\alpha}_2, ..., \bar{\alpha}_{12}]^T$, $\boldsymbol{\delta} = [u^i \ v^i \ w^i \ \omega^i_{x_1} \ \omega^i_{x_2} \ \omega^i_{x_3} \ u^j \ v^j \ w^j \ \omega^j_{x_1} \ \omega^j_{x_2} \ \omega^j_{x_3}]^T$. The matrix $[\tilde{N}]$ contains the nodal local coordinates. The strain vector $\boldsymbol{\zeta}$ can be expressed in terms of $\bar{\boldsymbol{\alpha}}$ using Eqs. (6.2-6.3) as follows.

$$\boldsymbol{\zeta} = [\tilde{B}]_{6\times12}\bar{\boldsymbol{\alpha}} \tag{6.5}$$

where the matrix $[\tilde{B}]$ is a function of x_1. The strain vector $\boldsymbol{\zeta}$ can be represented in terms of the nodal displacement vector $\boldsymbol{\delta}$ in the local coordinate using Eq. (6.5).

$$\boldsymbol{\zeta} = [\tilde{B}][\tilde{N}]^{-1}\boldsymbol{\delta} = [B]\boldsymbol{\delta} \tag{6.6}$$

The next step is to transform the element load vector $\boldsymbol{f} = [f_1^i \; f_2^i \; f_3^i \; m_{x_1}^i \; m_{x_2}^i \; m_{x_3}^i \; f_1^j \; f_2^j \; f_3^j \; m_{x_1}^j \; m_{x_2}^j \; m_{x_3}^j \;]^T$ and the element displacement vector $\boldsymbol{\delta}$ in the global coordinate system so that the individual elements can be combined in the assembly process. Consider a beam element at an arbitrary orientation described by an angle φ, measured counter-clockwise from the horizontal, and a global coordinate system (Fig. (6.22)). The loads and displacements in the global coordinate system can be related to the loads and displacements in the element coordinate system.

$$\boldsymbol{\delta} = [\hat{\lambda}]\bar{\boldsymbol{\delta}} \tag{6.7a}$$

$$\boldsymbol{f} = [\hat{\lambda}]\bar{\boldsymbol{f}} \tag{6.7b}$$

The hat in Eq. (6.7) indicates that loads and displacements in global coordinates. The transformation matrix $[\hat{\lambda}]$ is given by, [34]

$$\begin{Bmatrix} [f^i]_{6\times1} \\ [f^j]_{6\times1} \end{Bmatrix} = \begin{bmatrix} [\tilde{\lambda}]_{3\times3} & O_{3\times3} & O_{3\times3} & O_{3\times3} \\ O_{3\times3} & [\tilde{\lambda}]_{3\times3} & O_{3\times3} & O_{3\times3} \\ O_{3\times3} & O_{3\times3} & [\tilde{\lambda}]_{3\times3} & O_{3\times3} \\ O_{3\times3} & O_{3\times3} & O_{3\times3} & [\tilde{\lambda}]_{3\times3} \end{bmatrix} \begin{Bmatrix} [\bar{f}^i]_{6\times1} \\ [\bar{f}^j]_{6\times1} \end{Bmatrix} \equiv [\hat{\lambda}] \begin{Bmatrix} [\bar{f}^i]_{6\times1} \\ [\bar{f}^j]_{6\times1} \end{Bmatrix} \tag{6.8}$$

where,

$$[\tilde{\lambda}] = \begin{bmatrix} \cos\varphi_{\bar{x}x_1} & \cos\varphi_{\bar{y}x_1} & \cos\varphi_{\bar{z}x_1} \\ \cos\varphi_{\bar{x}x_2} & \cos\varphi_{\bar{y}x_2} & \cos\varphi_{\bar{z}x_2} \\ \cos\varphi_{\bar{x}x_3} & \cos\varphi_{\bar{y}x_3} & \cos\varphi_{\bar{z}x_3} \end{bmatrix} \tag{6.9}$$

The element stiffness matrix transformed to global coordinates is obtained as

$$[\bar{k}] = [\hat{\lambda}]^T[k][\hat{\lambda}] \tag{6.10}$$

$[\bar{k}]$ is the element stiffness matrix in the global coordinates. The nodal displacement vector in the global coordinate is achieved as follows.

$$\bar{\boldsymbol{\delta}} = [\bar{k}^e]^{-1}\bar{\boldsymbol{f}} \tag{6.11}$$

6.3.2 Elasticity solution for bending of a curved beam with rectangular section by a force at the end ([90])

A bar of a narrow rectangular cross-section and with a circular axis is considered at the lower end and bent by a force *P* applied at the upper end in the radial direction, Fig. (6.23). The bending moment at any cross-section *mn*, is proportional to $\sin(\theta)$, and the normal stress σ_θ, according to elementary theory of the bending of curved beams, is proportional to the bending moment. The stress function ϕ satisfies the equation below, [90].

$$\left(\frac{\partial^2}{\partial r^2}+\frac{1}{r}\frac{\partial}{\partial r}+\frac{1}{r^2}\frac{\partial^2}{\partial \theta^2}\right)\left(\frac{\partial^2 \phi}{\partial r^2}+\frac{1}{r}\frac{\partial \phi}{\partial r}+\frac{1}{r^2}\frac{\partial^2 \phi}{\partial \theta^2}\right)=0 \tag{6.12}$$

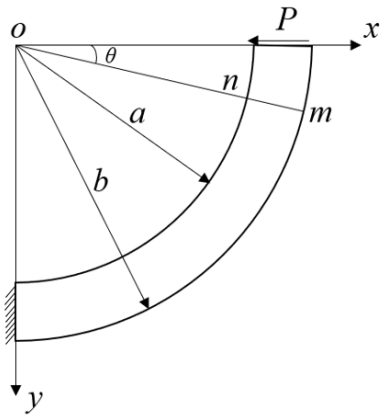

Fig. (6.23) curved beam under tip loading, [90].

This equation is proportional to $\sin(\theta)$, and $\phi = f(r)\sin(\theta)$. The general solution of the differential equation is

$$f(r) = Ar^3 + B\frac{1}{r} + Cr + Dr\log r \tag{6.13}$$

Where A, B, C, and D are constants of integration, which are determined from boundary conditions. Using the stress functions, we find the following expressions for the stress components.

$$\sigma_r = \frac{1}{r}\frac{\partial \phi}{\partial r} + \frac{1}{r^2}\frac{\partial^2 \phi}{\partial \theta^2} = (2Ar - \frac{2B}{r^3} + \frac{D}{r})\sin(\theta)$$
$$\sigma_\theta = \frac{\partial^2 \phi}{\partial r^2} = (6Ar + \frac{2B}{r^3} + \frac{D}{r})\sin(\theta) \quad (6.14)$$
$$\tau_{r\theta} = -\frac{\partial}{\partial r}(\frac{1}{r}\frac{\partial \phi}{\partial \theta}) = -(2Ar - \frac{2B}{r^3} + \frac{D}{r})\cos(\theta)$$

From conditions that the outer and inner boundaries of the curved bar are free from external forces, at $r=a$ and $r=b$ we have $\sigma_r = \tau_{r\theta} = 0$. The other condition is that the sum of the shearing forces distributed over the upper of the bar should equal the force P. Applying the boundary conditions, the following stress components for upper end of the bar, $\theta = 0$ will be as follows.

$$\sigma_\theta = 0$$
$$\tau_{r\theta} = \frac{-P}{N}[r + \frac{a^2 b^2}{r^3} - \frac{1}{r}(a^2 + b^2)] \quad (6.15)$$

For the lower end, $\theta = \frac{\pi}{2}$, we have $\tau_{r\theta} = 0$ and $\sigma_\theta = \frac{P}{N}(3r - \frac{a^2 b^2}{r^3} - (a^2 + b^2)\frac{1}{r})$ and,

$N = a^2 - b^2 + (a^2 + b^2)\log(b/a)$. The displacements produced by the force P can be obtained using the strain displacement relations ($\varepsilon_r = \partial u_r / \partial r$, $\varepsilon_\theta = u_r / r + \partial u_\theta / (r\partial\theta)$, and $\gamma_{r\theta} = \partial u_r / (r\partial\theta) + \partial u_\theta / \partial r - u_\theta / r$) as well as Hooke's law, we have

$$\frac{\partial u_r}{\partial r} = \frac{\sin(\theta)}{E}[2Ar(1-3u_\theta) - \frac{2B}{r^3}(1+u_\theta) + \frac{D}{r}(1-u_\theta)]$$
$$\frac{\partial u_\theta}{\partial r} = r\varepsilon_\theta - u_r \quad (6.16)$$
$$\gamma_{r\theta} = \frac{\partial u_r}{r\partial\theta} + \frac{\partial u_\theta}{\partial r} - \frac{u_\theta}{r}$$

Where, $A = \frac{P}{2N}$, B=-$\frac{Pa^2 b^2}{2N}$, D=-$\frac{P}{N}(a^2 + b^2)$. Solving the differential equations, leads to the following displacement $(u)_{\theta=0}$ as

$$(u_r)_{\theta=0} = \frac{-P\pi(a^2 + b^2)}{E[(a^2 - b^2) + (a^2 + b^2)\log(b/a)]} \quad (6.17)$$

6.3.3 Validation of the presented 1D solution for beams with rectangular section by a force at the end

To validate the present method of solution for initially curved beams with rectangular section, the transverse displacement ($\bar{W}$), longitudinal displacement ($\bar{u}$) of a cantilever initially curved beam with isotropic rectangular section subjected to a tip loading proposed by Tang et. al. [92] is calculated which is based on Euler-Bernoulli beam theory and 1D FEM for the solution. Moreover, the elasticity solution presented in previous section Eq. (6.17) is also used for validation purpose. The rectangular cross-section and its dimensions are represented in Fig. (6.24). Moreover, the cross-sectional stiffness constants are calculated using VABS 3.8 and imported to ANSYS-APDL 19 to perform 1D FE analysis of the beam. The Timoshenko beam model of curved beams is used for cross-sectional analysis in VABS 3.8 so that the effect of shear and curvature are taken into account while the presented solution is based on the Classical beam model. It is noted that the ANSYS-APDL has only the Timoshenko beam element. Moreover, comparing the presented Classical beam solution gives us the range of validity of the present solution. In ANSYS APDL, the element type beam 188 has been used for the modeling. The element has two nodes and 6 degrees of freedom at each node, [88]. Also, the element is based on Timoshenko beam theory. Fig. (6.25) shows the curved beam and loading condition. The beam is clamped at one side where all the displacements and rotations are zero and subjected to a tip loading at the other side in both the present and ANSYS solutions. The beam has a width of b=1 *in* and height of h=1 *in.* The tip loading value is P=-1 *lb*. The beam has Young modulus E=10.5e6 psi and poisson's ration v=0.3.

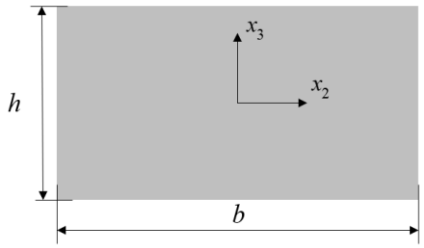

Fig. (6.24). Cross-section of rectangular curved beam with width b and height h, (b=1 *in*, and h=1 *in*).

The obtained transverse displacements of different beams with different slenderness ratios R/h are evaluated. To obtain the cross-sectional stiffness constants of the rectangular section of curved beams using the present method, the Pascal polynomials with order (m=4) are used in the Cartesian

coordinates. For 1D FE solution, we used the presented solution in section 6.3.1. Table (6.12) shows the obtained displacements of the beam. Moreover, ANSYS 3D solution is used for validation in which the element type Solid 185 is used. For the beam with *R/h*=4, the number of 3D elements is 3242529, for *R/h*=10 the number of elements is 1004800. For *R/h*=20, the number of elements is 251600. It is noted that $(u_r)_{\theta=0}$ of Eq. (6.17) is equivalent to $\bar{W}$ of 1D solution at tip of the beam Eq. (6.25).

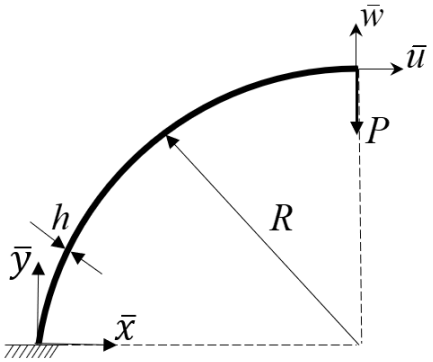

Fig. (6.25). Initially curved beam under tip loading *P*.

Table (6.12). Comparison of the obtained displacements of the present method for an isotropic curved beam with rectangular section, *b*=1 *in* and *h*=1 *in*, *E*=10.5e6 psi, *v*=0.3.

Slenderness ratio (*R/h*)	$\bar{u}$ ([92])	$\bar{w}$ ([92])	$\bar{u}$ (Present)	$\bar{w}$ (Present)	$\bar{u}$ (VABS+ ANSYS 1D)	$\bar{w}$ (VABS+ANSYS 1D)	$\bar{u}$ (ANSYS 3D)	$\bar{w}$ (ANSYS 3D)	$\bar{w}$ (Eq. (6.17))
2	-	-	4.480e-6	-7.634e-6	4.810e-6	-8.240e-6	4.722e-6	-7.310e-6	-7.435e-6
4	3.638e-5	-5.774e-5	3.620e-5	-5.741e-5	3.701e-5	-5.951e-5	3.679e-5	-5.753e-5	-5.797e-5
10	5.709e-4	-8.983e-4	5.707e-4	-8.971e-4	5.722e-4	-9.015e-4	5.710e-4	-8.962e-4	-8.989e-4
20	4.570e-3	-7.182e-3	4.571e-3	-7.176e-3	4.571e-3	-7.181e-3	4.567e-3	-7.173e-3	-7.183e-3
50	7.142e-2	-1.122e-1	7.147e-1	-1.121e-1	7.138e-2	-1.120e-1	7.139e-2	-1.121e-2	-1.122e-1
100	5.714e-1	-8.976e-1	5.719e-1	-8.975e-1	5.710e-1	-8.960e-1	5.712e-1	-8.973e-1	-8.983e-1

The transverse and longitudinal displacement distributions of the beams with rectangular section under loading conditions of Fig. (6.25) with different slenderness ratios (*R/h*) are demonstrated in Figs. (6.26) and (6.27). Two solutions for determining the deflections are provided in which first

the solution is done when the k_2 in the cross-sectional stiffness matrix is set to zero, and second the k_2 is non-zero and is equal to the geometrical curvature of the beam. There is no difference between two situations. Comparison of the present work and VABS 3.8 shows that the present method agrees with (VABS+ANSYS 1D) for R/h=4 and R/h=10. One can say that for determining the deflections of a curved beam with isotropic material, one can use the straight cross-sectional stiffness matrix to model a curved beam. This conclusion was also made by Kovvali and Hodges [89]. The number of 1D elements in all the present and (VABS+1D FE ANSYS) is 30. As the slenderness ratio increases the difference between the present method and VABS decreases. The slight deference between the present method which is based on the Classical beam model and the (VABS+ANSYS 1D), which is based on Timoshenko beam solution, for (R/h=4) is due to the effect of transverse shear.

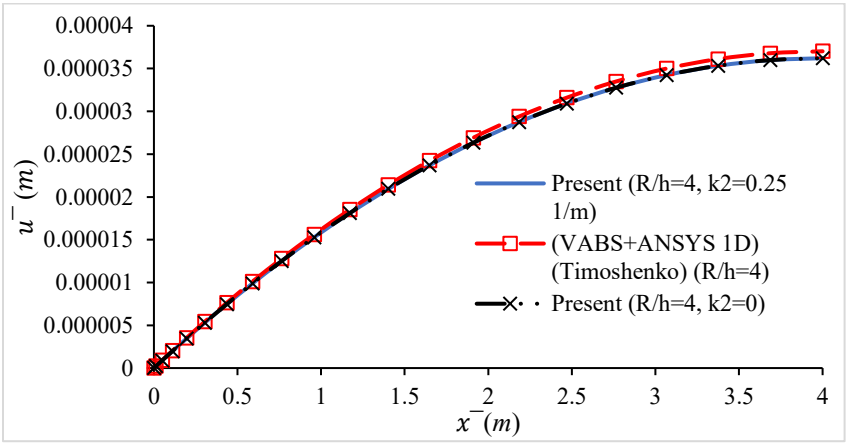

a)

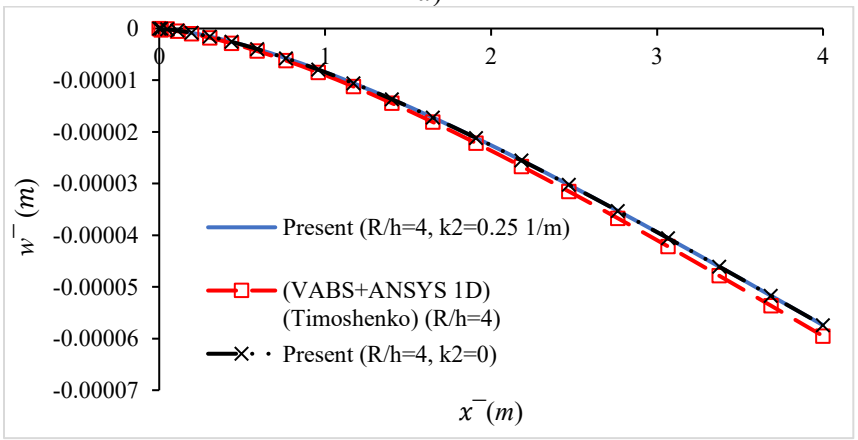

b)

Fig. (6.26). *a*) longitudinal displacement $\bar{u}$, *b*) transverse displacement $\bar{w}$ of the beam with rectangular section under tip loading with (*R/h*=4).

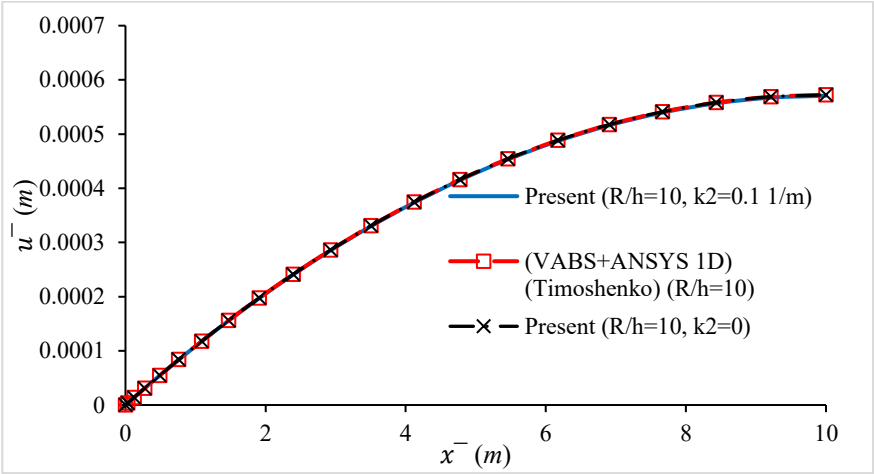

a)

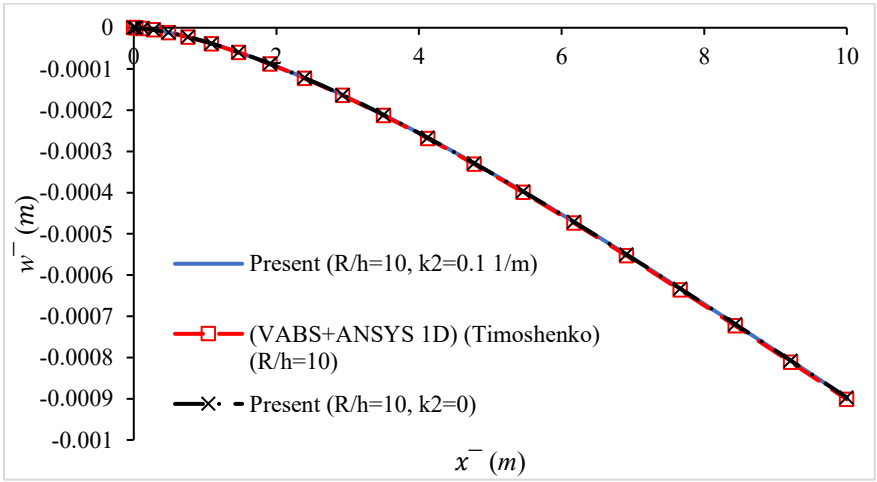

b)

Fig. (6.27). *a*) longitudinal displacement $\bar{u}$, *b*) transverse displacement $\bar{w}$ of the beam with rectangular section under tip loading with (*R/h*=10).

6.3.4 Present 1D curved beam solution for tubular cross-sections under tip loading

The effect of initial curvature for the analysis of composite tubes has two aspects. The first aspect is that the initial curvature changes the values of extensional stiffness, bending stiffness, and extension-bending stiffness. The study on the effect of these stiffness constants show that the

bending stiffness has substantial effect on the 1D behavior of the beam. The second aspect is that all the values of stiffness constants affect more the distribution of strain in the tubes, subjecting to bending moment. To show the effect of initial curvature on the 1D longitudinal and transverse displacements of tubes, we analyzed composite tubes [$-\alpha_5/\alpha_5$] with different levels of initial curvature. The tubes are subjected to tip loading of Fig. (6.25) with the value of P=-100 *N*. The tubes have dimensions explained in the beginning of section 6.2.4. Moreover, the obtained displacements of the present solution are compared with ANSYS 3D. It is noted that we used the 4×4 Classical cross-sectional stiffness matrix (up to second order of the strain energy) which takes into account the initial curvature in the cross-sectional stiffness matrix ($k_2 \neq 0$) and Classical stiffness matrix of the straight tube in which the initial curvature is not considered in the cross-sectional stiffness matrix ($k_2 = 0$). In ANSYS 3D, we used element Solid 185 for the analysis. In ANSYS 3D modeling, the one side ring surface of the tube is fixed (all the displacements and rotations) and the other side is under tip loading on the ring surface. Moreover, for the tubes with k_2=0.5 1/*m*, the tubes are meshed with 1461960 elements and for tubes with k_2=1 1/*m*, we meshed the tubes with 730980 elements in ANSYS 3D solution. The tube [$-45_5/45_5$] is subjected to tip loading P=-100 N at one side and clamped at the other side as shown in Fig. (6.28). The longitudinal and transverse displacements of the tube are illustrated in Fig. (6.29). The change of tip longitudinal and transverse deflection of composite tubes [$-\alpha_5/\alpha_5$] under loading with different levels of initial curvature and various fiber angles are shown in Figs. (6.30) and (6.31).

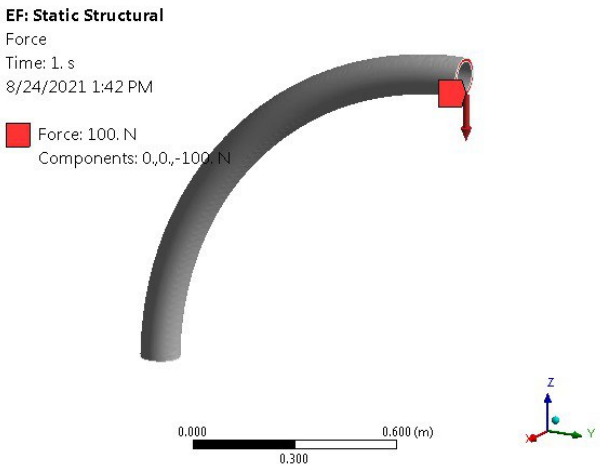

Fig. (6.28) Modeling of initially curved (R=1 *m*) composite tube [$-45_5/45_5$] under tip loading P=100 N.

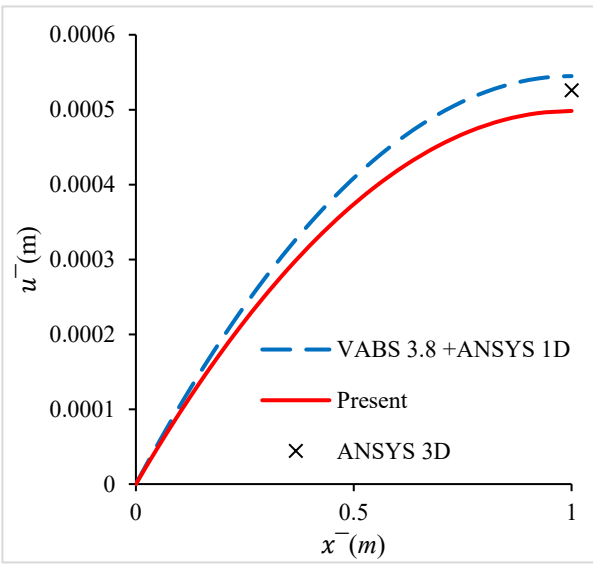

a) Longitudinal

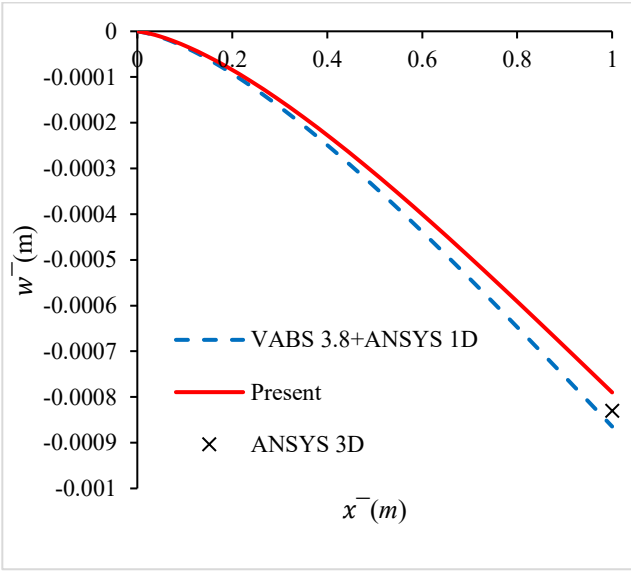

b) Transverse

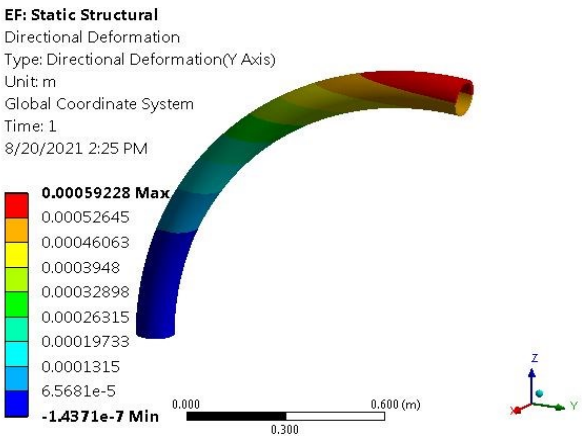

c) ANSYS 3D, longitudinal ($\bar{u}$)

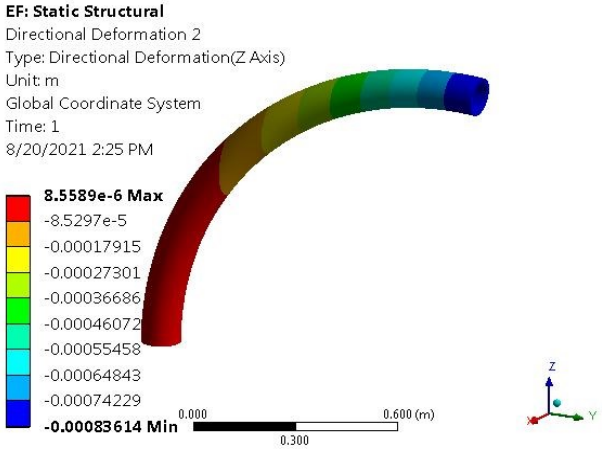

d) transverse ($\bar{w}$)

Fig. (6.29). The obtained displacements *a*) Longitudinal, *b*) Transverse, of [-45$_5$/45$_5$] tube under tip loading P=100 N using the present, VABS 3.8+ANSYS 1D, and *c*,*d*) ANSYS 3D, (R_i=49 mm, R_o=59 mm, P=-100 N).

It can be observed from Fig. (6.30) that as the initial curvatures changes two times from 0.5 to 1, the values of longitudinal tip displacements decrease by 6 to 8 times. Moreover, it can be observed from Fig. (6.31) that by increasing the initial curvature from 0.5 to 1, the transverse deflections decrease by 6 to 7 times. Additionally, for a certain value of initial curvature, by increasing the fiber angle, the magnitudes of longitudinal and transverse deflections increase. For the fiber angles more than α=50°, the increase in the displacements is more. In the Fig. (6.31) the obtained

transverse displacements of the present solution are shown for two cases when the initial curvature has been considered ($k_2 \neq 0$) in the stiffness matrix and when the initial curvature is not taken into account ($k_2 = 0$). In both the analyses the number of elements is 50.

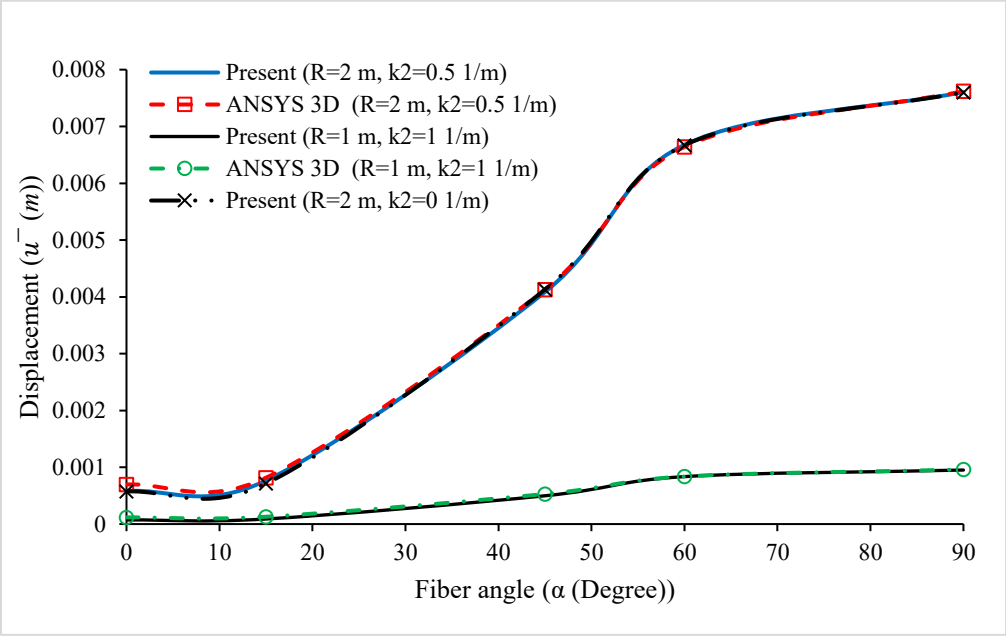

Fig. (6.30). Variation of longitudinal displacement ($\bar{u}$) at tip point of composite tubes [-α5/α5] under tip loading versus fiber angle for various levels of initial curvature, (R_i=49 *mm*, R_o=59 *mm*, *P*=100 *N*).

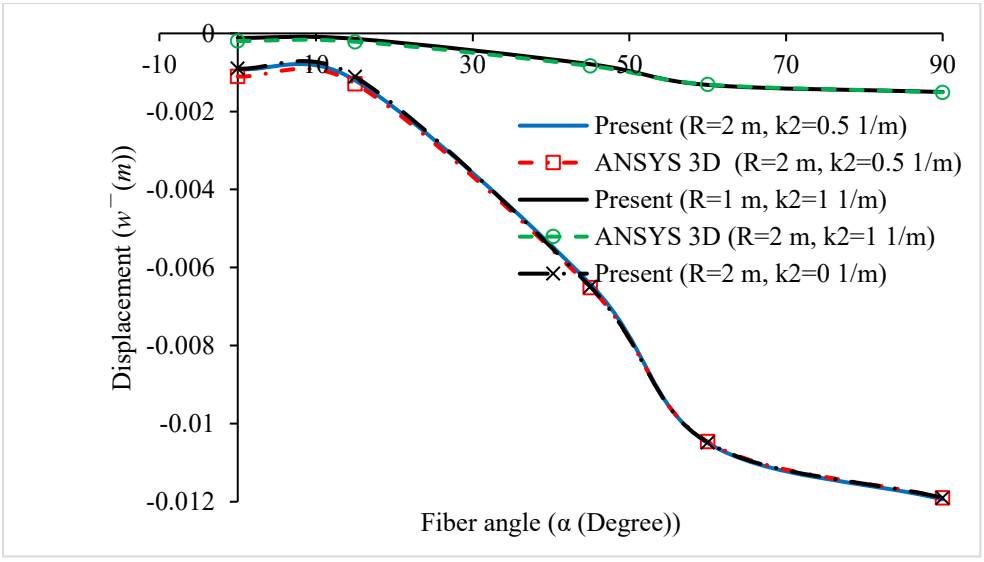

Fig. (6.31). Variation of transverse displacement ($\bar{w}$) at tip point of composite tubes [-α5/α5] under tip loading versus fiber angle for various levels of initial curvature, (R_i=49 *mm*, R_o=59 *mm*, *P*=100 *N*).

6.3.5 Presented 1D solution for initially curved tubes under four-point bending loading

Initially curved composite tubes under four-point bending are the subject of interest in the helicopter industry. The cross-tubes for landing gear of helicopters are the initially curved tubes. The analysis of initially curved composite tubes under four-point bending loading is a complex task. In this section, we analyzed displacements of initially curved tubes under four-point bending loading. Tubes with cross-ply, and $[-\alpha_5/\alpha_5]$ with aforementioned inner and outer diameters (section 6.2.4) and radius of curvature R=2.5 m under four-point bending loading and simply supported-simply supported boundary conditions are analyzed using the presented method and ANSYS 3D. Fig. (6.32) shows the loading and boundary conditions.

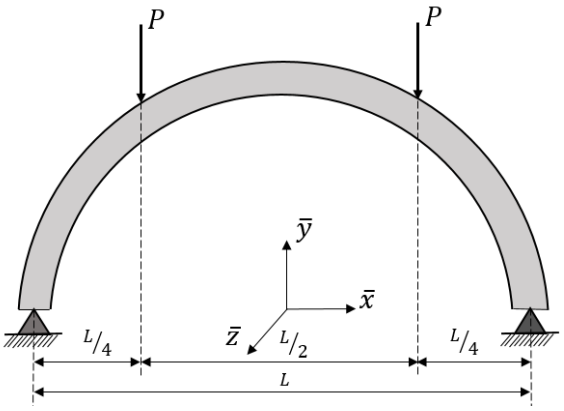

Fig. (6.32). Four-point bending of the initially curved beam.

Fig. (6.33) demonstrates transverse displacement distribution of simply supported-simply supported tube with $[90_5/0_5]$ lay-up sequence. The solution is done with 50, 100 and 200 elements and it is converged with 100 elements. The obtained displacement is compared with ANSYS 3D (with 74670 3D elements (Solid 185)). In both the present 1D solution and ANSYS 3D, the displacements at the ends are restricted, and the rotation is free about $\bar{z}$ coordinate.

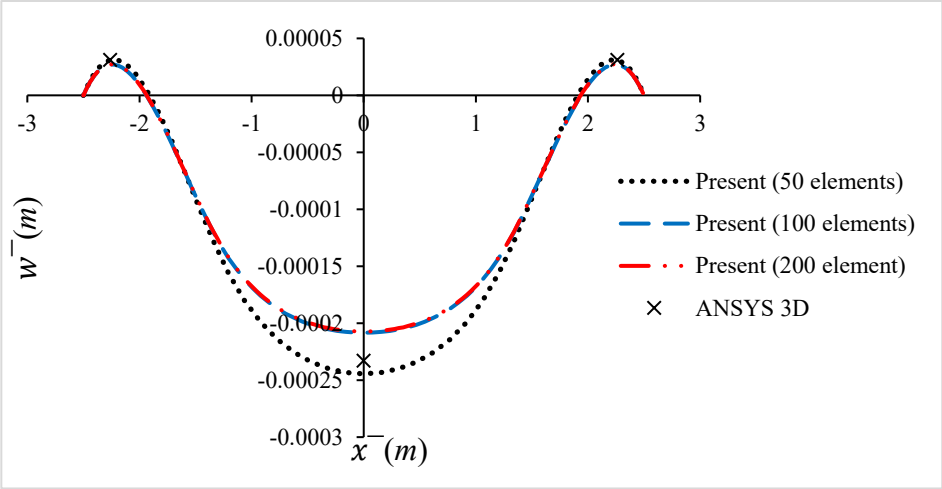

a) Present, ANSYS 3D (at mid-span)

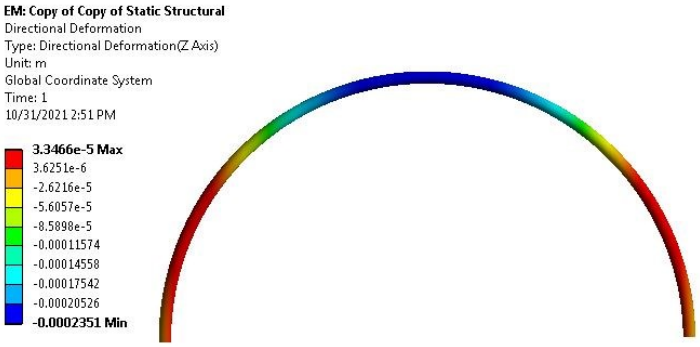

b) ANSYS 3D

Fig. (6.33). Transverse displacement distribution of simply supported-simply supported curved tube [$90_5/0_5$] under four-point bending loading, *a*) Present, ANSYS 3D (at mid-span), *b*) ANSYS 3D (P=-500 N), (D_o=118 mm, D_i=98 mm, R=2.5 m).

Tubes with [-α_5/α_5]

The transverse displacements obtained through the present solution (Classical beam model up to 2nd order of strain energy) for [-α_5/α_5] tubes under four-point bending loading (P=-500 N) and simply-supported are reported in Figs. (6.34-6.35). The analyses have been done for initially curved tubes with straight (k_2=0) and curved ($k_2 \neq 0$) of the cross-sectional stiffness matrix. The analyses have been done with 100 number of elements. Increasing the fiber angle of the tube, increases the transverse deflection of the tubes. The percentage difference between the Classical

up to 2nd order and ANSYS 3D for [-15$_5$/15$_5$] is 15%. This difference for VABS+ANSYS 1D which uses Timoshenko beam model is 10%. The percentage difference between Classical up to 2nd order and ABSYS 3D for tubes with [-60$_5$/60$_5$] is 6.25% while this difference between VABS+ANSYS 1D and ANSYS 3D is 3.75%. By increasing the fiber angle, the difference between the Classical up to 2nd order and ANSYS 3D decreases which is due to the effect of shear. Comparison of VABS+ANSYS 1D which uses Timoshenko and Classical up to 2nd order shows that the transverse shear will have more effect for lower fiber angles of the tube.

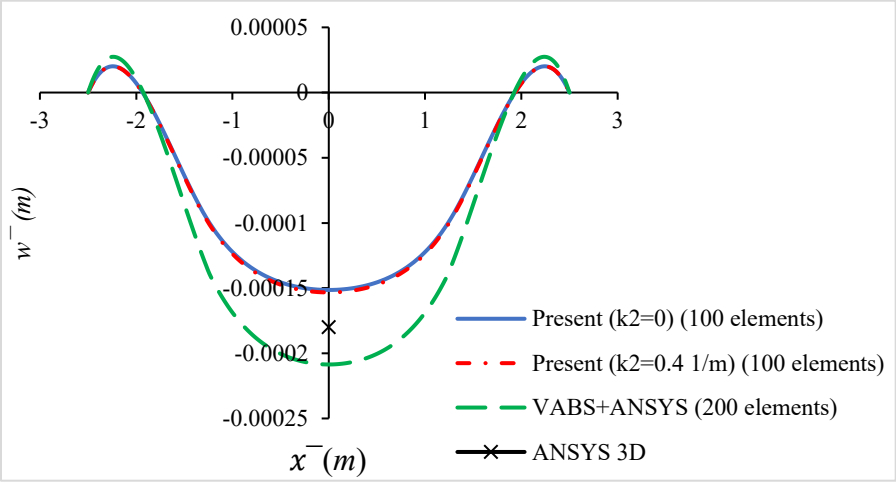

Fig. (6.34). Transverse displacement distribution of simply supported-simply supported curved tube [-15$_5$/15$_5$] under four-point bending loading, (P=-500 N), (D_o=118 mm, D_i=98 mm, R=2.5 m).

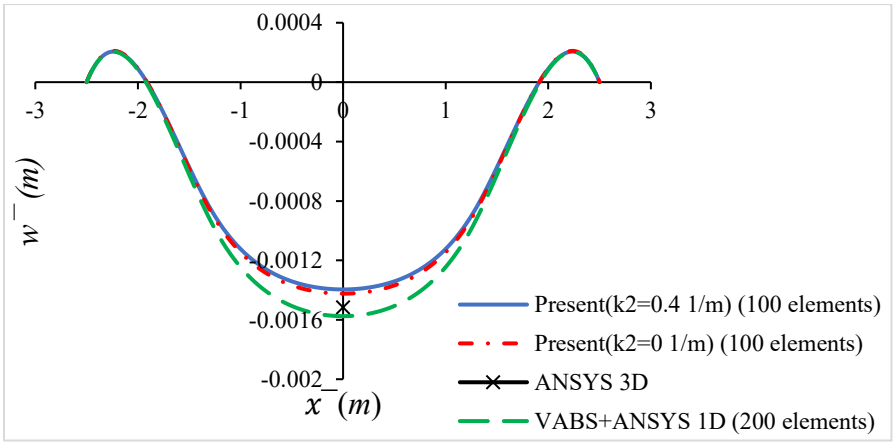

Fig. (6.35). Transverse displacement distribution of simply supported-simply supported curved tube [-60$_5$/60$_5$] under four-point bending loading, (P=-500 N), (D_o=118 mm, D_i=98 mm, R=2.5 m).

6.4 Investigating the location of tension center (Neutral axes)

The neutral axes or the tension center (X,Y) is defined as the point of the cross-section through which no bending deformation will occur when an axial force applied at this point [40]. Fig. (6.36) shows the cross-section of a tube with its tension center point.

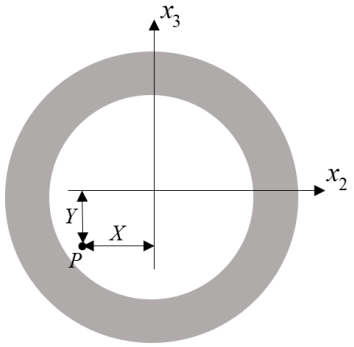

Fig. (6.36). Cross-section of a tube with initial curvature and its tension center point.

For the applied axial force F_1 at the point P. The moments induced by this force are

$$\begin{aligned} M_{x_2} &= -F_1 Y \\ M_{x_3} &= F_1 X \end{aligned} \tag{6.18}$$

We look for the positions where $\kappa_2 = \kappa_3 = 0$. From the cross-section constitutive relation as Eq. (3.42), we have.

$$\begin{Bmatrix} \gamma_{11} \\ \kappa_1 \\ \kappa_2 \\ \kappa_3 \end{Bmatrix} = \begin{bmatrix} P_{11} & P_{12} & P_{13} & P_{14} \\ P_{12} & P_{22} & P_{23} & P_{24} \\ P_{13} & P_{23} & P_{33} & P_{34} \\ P_{14} & P_{24} & P_{34} & P_{44} \end{bmatrix} \begin{Bmatrix} F_1 \\ M_1 \\ M_2 \\ M_3 \end{Bmatrix} \tag{6.19}$$

Where the matrix [P] is the cross-sectional flexibility matrix and is $[P] = [Y_1]^{-1}$. The matrix $[Y_1]$ is the classical stiffness matrix (up to second order) obtained from Eq. (3.42). Using the Eq. (6.19), the following relation is obtained.

$$\begin{aligned} \kappa_2 &= P_{13}F_1 + P_{33}M_2 + P_{34}M_3 = 0 \\ \kappa_3 &= P_{14}F_1 + P_{34}M_2 + P_{44}M_3 = 0 \end{aligned} \tag{6.20}$$

Substitution of Eq. (6.19) into Eq. (6.20) and solving X and Y leads to the following relations which are the coordinates of the location of tension center of a curved beam.

$$X = \frac{P_{13}P_{34} - P_{14}P_{33}}{P_{33}P_{44} - P_{34}^2}$$
$$Y = \frac{P_{13}P_{44} - P_{14}P_{34}}{P_{33}P_{44} - P_{34}^2} \tag{6.21}$$

6.4.1 Strength of materials (rectangular section, [93])

The location of neutral axes of rectangular sections with height *h*, width *b*, curvature center C (see Fig. (6.37) using the strength of materials method is as follows.

$$R = \frac{h}{\ln(\frac{r_2}{r_1})} \tag{6.22}$$

where, *R* is the radius of location of neutral axis r_1 and r_2 are the distances of edges of cross-section from curvature center.

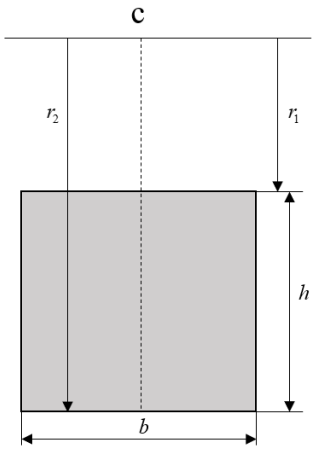

Fig. (6.37). Radius of neutral axis for a rectangular section.

The location of neutral axis of rectangular sections with various radius of curvature of beam reported in section 6.3.3 have been shown in Table (6.13). A good correlation between the present method and strength of materials is observed. As the radius of curvature increases, the location of neutral axis becomes close to the centroid of the cross-section.

Table (6.13). Location of neutral axis of rectangular sections with various values of initial curvatures, (b=1 *in*, h=1 *in*).

R/h	Strength of materials (Eq. (6.22)) (Y (*in*))	Eq. (6.21) (Y (*in*))
2	0.0423	0.0424
4	0.0209	0.0209
10	0.0083	0.0083
20	0.0041	0.0041
50	0.0016	0.0016
100	0.0008	0.0008

6.4.2 Tubular orthotropic section ([-α_5/α_5])

Fig. (6.38) shows the change of location of neutral axes of composite tube [-α_5/α_5] for different values of initial curvature. It is seen that the location of tension center has the maximum distance from the center of the cross-section for the case of $\alpha = 15^{\circ}$.

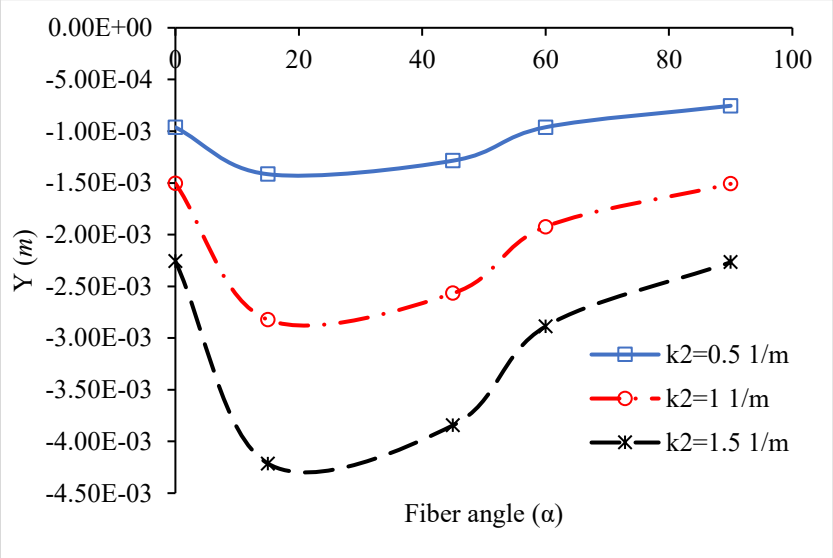

Fig. (6.38). The Y coordinate of the location of tension center of composite tubes [-α_5/α_5] versus initial curvature k_2, (outer diameter D_o=118 *mm*, and inner diameter D_i=98 *mm*).

6.5 Influence of initial curvature

The initial curvature has influences on the obtained cross-sectional stiffness matrix of composite beam and therefore on the strain distributions of the composite beam under loading. This affects the global 1D behavior of composite tube. To study the effect of initial curvature we first aim to

observe the effect of initial curvature on the strain energy and consequently on the cross-sectional stiffness constants of the beam. We first start with a simple case of a beam with isotropic material and rectangular cross-section. Then, we will study the effect of initial curvature on the more complex cases such as isotropic and orthotropic tubular curved beams.

6.5.1 Effect of initial curvature on the stiffness constants of an isotropic rectangular cross-section

As presented in chapter (3), the first approximation of the strain energy in the VAM comes from keeping the terms up to order O ($\varepsilon_{\max}^2$). One can write the first approximation of the strain energy (Classical beam model) for an orthotropic beam with rectangular cross-section as the following format.

$$
\begin{aligned}
2U_0 = \int_L \iint_\Omega \Bigg(& \left(\frac{\partial w_{10}}{\partial x_2} D_{22} + \frac{\partial w_{10}}{\partial x_3} D_{32} + \frac{\partial w_{20}}{\partial x_2} D_{42} + \left(\frac{\partial w_{20}}{\partial x_3} + \frac{\partial w_{30}}{\partial x_2} \right) D_{52} + \frac{\partial w_{30}}{\partial x_3} D_{62} \right) \frac{\partial w_{10}}{\partial x_2} \\
& + \left(\frac{\partial w_{10}}{\partial x_2} D_{23} + \frac{\partial w_{10}}{\partial x_3} D_{33} + \frac{\partial w_{20}}{\partial x_2} D_{43} + \left(\frac{\partial w_{20}}{\partial x_3} + \frac{\partial w_{30}}{\partial x_2} \right) D_{53} + \frac{\partial w_{30}}{\partial x_3} D_{63} \right) \frac{\partial w_{10}}{\partial x_3} \\
& + \left(\frac{\partial w_{10}}{\partial x_2} D_{24} + \frac{\partial w_{10}}{\partial x_3} D_{34} + \frac{\partial w_{20}}{\partial x_2} D_{44} + \left(\frac{\partial w_{20}}{\partial x_3} + \frac{\partial w_{30}}{\partial x_2} \right) D_{54} + \frac{\partial w_{30}}{\partial x_3} D_{64} \right) \frac{\partial w_{20}}{\partial x_2} \\
& + \left(\frac{\partial w_{10}}{\partial x_2} D_{25} + \frac{\partial w_{10}}{\partial x_3} D_{35} + \frac{\partial w_{20}}{\partial x_2} D_{45} + \left(\frac{\partial w_{20}}{\partial x_3} + \frac{\partial w_{30}}{\partial x_2} \right) D_{55} + \frac{\partial w_{30}}{\partial x_3} D_{65} \right) \left(\frac{\partial w_{20}}{\partial x_3} + \frac{\partial w_{30}}{\partial x_2} \right) \\
& + \left(\frac{\partial w_{10}}{\partial x_2} D_{26} + \frac{\partial w_{10}}{\partial x_3} D_{36} + \frac{\partial w_{20}}{\partial x_2} D_{46} + \left(\frac{\partial w_{20}}{\partial x_3} + \frac{\partial w_{30}}{\partial x_2} \right) D_{56} + \frac{\partial w_{30}}{\partial x3} D_{66} \right) \frac{\partial w_{30}}{\partial x_3} \\
& + \frac{1}{\sqrt{\lambda}} \left(2 \frac{\partial w_{10}}{\partial x_2} D_{21} + 2 \frac{\partial w_{10}}{\partial x_3} D_{31} + 2 \frac{\partial w_{20}}{\partial x_2} D_{41} + \left(2 \frac{\partial w_{20}}{\partial x_3} + 2 \frac{\partial w_{30}}{\partial x_2} \right) D_{51} + 2 \frac{\partial w_{30}}{\partial x_3} D_{61} \right) \\
& \left(\gamma_{11} + x_3 \bar{\kappa}_2 - x_2 \bar{\kappa}_3 \right) - \frac{1}{\sqrt{\lambda}} \left(2 \frac{\partial w_{10}}{\partial x_2} D_{22} + 2 \frac{\partial w_{10}}{\partial x_3} D_{32} + 2 \frac{\partial w_{20}}{\partial x_2} D_{42} + \left(2 \frac{\partial w_{20}}{\partial x_3} + 2 \frac{\partial w_{30}}{\partial x_2} \right) D_{52} \right. \\
& \left. + 2 \frac{\partial w_{30}}{\partial x_3} D_{62} \right) + \frac{1}{\sqrt{\lambda}} \left(2 \frac{\partial w_{10}}{\partial x_2} D_{23} + 2 \frac{\partial w_{10}}{\partial x_3} D_{33} + 2 \frac{\partial w_{20}}{\partial x_2} D_{43} + \left(2 \frac{\partial w_{20}}{\partial x_3} + 2 \frac{\partial w_{30}}{\partial x_2} \right) D_{53} + 2 \frac{\partial w_{30}}{\partial x_3} D_{63} \right) x_2 \bar{\kappa}_1 \\
& + \frac{1}{\sqrt{\lambda}} \left(\bar{\gamma}_{11} + x_3 \bar{\kappa}_2 - x_2 \bar{\kappa}_3 \right) D_{11} - \frac{1}{\sqrt{\lambda}} x_3 \bar{\kappa}_1 D_{21} + \frac{1}{\sqrt{\lambda}} x_2 \bar{\kappa}_1 D_{31} + \frac{1}{\sqrt{\lambda}} \left(\bar{\gamma}_{11} + x_3 \bar{\kappa}_2 - x_2 \bar{\kappa}_3 \right) D_{11} \\
& - \frac{1}{\sqrt{\lambda}} x_3 \bar{\kappa}_1 D_{21} + \frac{1}{\sqrt{\lambda}} x_2 \bar{\kappa}_1 D_{31} \Bigg) dx_3 dx_2 dx_1
\end{aligned}
\tag{6.23}
$$

The beam strain energy for a beam **with isotropic material and rectangular cross-section** with initial curvature k_2 can be written as follows.

$$2U_0 = \int_L \iint_\Omega \Big(\frac{1}{2}\frac{\left(\frac{\partial w_{10}}{\partial x_2}\right)^2 E}{1+\nu} + \frac{1}{2}\frac{\left(\frac{\partial w_{10}}{\partial x_3}\right)^2 E}{1+\nu} + \frac{1}{2\nu^2+\nu-1} E\left(\frac{\partial w_{20}}{\partial x_2}(\nu-1) - \frac{\partial w_{30}}{\partial x_3}\nu\right)\left(\frac{\partial}{\partial x_2} w_{20}\right) + \frac{1}{2}\frac{\left(\frac{\partial w_{20}}{\partial x_3} + \frac{\partial w_{30}}{\partial x_2}\right)^2 E}{1+\nu}$$
$$- \frac{1}{2\nu^2+\nu-1}\frac{\partial w_{20}}{\partial x_2}\nu E + \frac{1}{2\nu^2+\nu-1}\frac{\partial w_{30}}{\partial x_3}(\nu-1) E\frac{\partial w_{30}}{\partial x_3} - \frac{\left(\nu^2+\frac{1}{2}\nu-\frac{1}{2}\right)\left(\frac{\partial w_{20}}{\partial x_2}+\frac{\partial w_{30}}{\partial x_3}\right)\nu E\left(x_3\bar{\kappa}_2 - x_2\bar{\kappa}_3 + \bar{\gamma}_{11}\right)}{(1+\nu)^2(k_2x_3+1)\left(\nu-\frac{1}{2}\right)^2} \quad (6.24)$$
$$- \frac{1}{(1+\nu)(k_2x_3+1)}\frac{\partial w_{10}}{\partial x_2} E x_3\bar{\kappa}_1 + \frac{1}{(1+\nu)(k_2x_3+1)}\frac{\partial w_{10}}{\partial x_3} E x_2\bar{\kappa}_1 + \frac{\left(x_3\bar{\kappa}_2 - x_2\bar{\kappa}_3 + \bar{\gamma}_{11}\right)^2(\nu-1)E}{(k_2x_3+1)^2(2\nu^2+\nu-1)}$$
$$+ \frac{1}{2}\frac{{x_3}^2{\bar{\kappa}_1}^2 E}{(k_2x_3+1)^2(1+\nu)} + \frac{1}{2}\frac{{x_2}^2{\bar{\kappa}_1}^2 E}{(k_2x_3+1)^2(1+\nu)}\Big) dx_3 dx_2 dx_1$$

The warping functions can be discretized using the Pascal Polynomials as follows.

$$w_k(x_1, x_2, x_3) = [W(x_2, x_3)]\boldsymbol{V}_k(x_1) \quad (6.25)$$

$W(x_2, x_3)$ includes Pascal polynomials and $\boldsymbol{V}_k(x_1)$ consists of unknown coefficients which is a function of axial coordinate and should be determined. The Pascal polynomials in the Cartesian coordinates may be defined as follows.

$$W(x_2, x_3) = 1 + a_1x_2 + a_2x_2 + a_3x_2^2 + a_4x_2x_3 + a_4x_3^2 + \ldots \quad (6.26)$$

The order of pascal polynomial is the maximum of the degree of the polynomial. We use the order one of the Pascal polynomials as

$$W(x_2, x_3) = 1 + a_1x_2 + a_2x_2 \quad (6.27)$$

So that the warping field can be written as follows.

$$\begin{aligned} w_{10} &= a_1 + a_2x_2 + a_3x_3 \\ w_{20} &= a_4 + a_5x_2 + a_6x_3 \\ w_{30} &= a_7 + a_8x_2 + a_9x_3 \end{aligned} \quad (6.28)$$

Substituting the above equation into the strain energy, the strain energy of an isotropic beam with rectangular cross-section $\Omega = \{(x_2, x_3) \mid -b/2 \le x_2 \le b/2, -h/2 \le x_3 \le h/2\}$ is obtained by integrating the strain energy over the region Ω. Where *b* and *h* are the width height of the beam, respectively. The relation after integration will be as follows.

$$
\begin{aligned}
2U_0 = \int_{L_e} \Big(& \frac{Eh}{(2\nu^2+\nu-1)k_2^3} \Big(a_9{}^2 \nu b k_2{}^3 - a_6 a_8 b k_2{}^3 + a_5{}^2 \nu b k_2{}^3 + a_6{}^2 \nu b k_2{}^3 + a_8{}^2 \nu b k_2{}^3 \\
& + a_2{}^2 \nu b k_2{}^3 + a_3{}^2 \nu b k_2{}^3 - 2\bar{\kappa}_2 \bar{\gamma}_{11} b k_2{}^2 - \bar{\kappa}_2{}^2 \nu b k_2 - \bar{\kappa}_1{}^2 \nu b k_2 - \ln\left(\frac{1}{2}k_2 b + 1\right) \bar{\gamma}_{11}{}^2 k_2{}^2 \\
& + \ln\left(-\frac{1}{2}k_2 b + 1\right) \bar{\gamma}_{11}{}^2 k_2{}^2 + \ln\left(\frac{1}{2}k_2 b + 1\right) \bar{\kappa}_2{}^2 \nu + \ln\left(\frac{1}{2}k_2 b + 1\right) \bar{\kappa}_1{}^2 \nu \\
& - \ln\left(-\frac{1}{2}k_2 b + 1\right) \bar{\kappa}_2{}^2 \nu - \ln\left(-\frac{1}{2}k_2 b + 1\right) \bar{\kappa}_1{}^2 \nu - 2a_5 \bar{\gamma}_{11} \nu b k_2{}^3 - 2a_5 a_9 \nu b k_2{}^3 \\
& - 2a_9 \bar{\gamma}_{11} \nu b k_2{}^3 + 2a_6 a_8 \nu b k_2{}^3 + 2\bar{\kappa}_2 \bar{\gamma}_{11} \nu b k_2{}^2 - 0.08 \ln\left(-\frac{1}{2}k_2 b + 1\right) \bar{\kappa}_1{}^2 \nu h^2 k_2{}^2 \\
& - 0.08 \bar{\kappa}_3{}^2 \ln\left(-\frac{1}{2}k_2 b + 1\right) \nu h^2 k_2{}^2 + 0.08 \bar{\kappa}_3{}^2 \ln\left(\frac{1}{2}k_2 b + 1\right) \nu h^2 k_2{}^2 \\
& + 0.08 \ln\left(\frac{1}{2}k_2 b + 1\right) \bar{\kappa}_1{}^2 \nu h^2 k_2{}^2 + 2.\ln\left(-\frac{1}{2}k_2 b + 1\right) \bar{\kappa}_2 \bar{\gamma}_{11} \nu k_2 \\
& - 2\ln\left(\frac{1}{2}k_2 b + 1\right) \bar{\kappa}_2 \bar{\gamma}_{11} \nu k_2 + \bar{\kappa}_2{}^2 b k_2 + \frac{1}{2}\bar{\kappa}_1{}^2 b k_2 - a_5{}^2 b k_2{}^3 - \frac{1}{2}a_6{}^2 b k_2{}^3 \\
& - \frac{1}{2}a_8{}^2 b k_2{}^3 - a_9{}^2 b k_2{}^3 - \frac{1}{2}a_2{}^2 b k_2{}^3 - \frac{1}{2}a_3{}^2 b k_2{}^3 - \ln\left(-\frac{1}{2}k_2 b + 1\right) \bar{\gamma}_{11}{}^2 \nu k_2{}^2 \\
& - 2.\ln\left(-\frac{1}{2}k_2 b + 1\right) \bar{\kappa}_2 \bar{\gamma}_{11} k_2 + 2\ln\left(\frac{1}{2}k_2 b + 1\right) \bar{\kappa}_2 \bar{\gamma}_{11} k_2 + \ln\left(\frac{1}{2}k_2 b + 1\right) \bar{\gamma}_{11}{}^2 \nu k_2{}^2 \\
& - 0.04 \ln\left(\frac{1}{2}k_2 b + 1\right) \bar{\kappa}_1{}^2 h^2 k_2{}^2 + 0.04 \ln\left(-\frac{1}{2}k_2 b + 1\right) \bar{\kappa}_1{}^2 h^2 k_2{}^2 + 0.08 \bar{\kappa}_3{}^2 \ln\left(-\frac{1}{2}k_2 b + 1\right) h^2 k_2{}^2 \\
& - 0.08 \bar{\kappa}_3{}^2 \ln\left(\frac{1}{2}k_2 b + 1\right) h^2 k_2{}^2 - \ln\left(\frac{1}{2}k_2 b + 1\right) \bar{\kappa}_2{}^2 \\
& - \frac{1}{2}\ln\left(\frac{1}{2}k_2 b + 1\right) \bar{\kappa}_1{}^2 + \ln\left(-\frac{1}{2}k 2b + 1.\right) \bar{\kappa}_2{}^2 + \frac{1}{2}\ln\left(-\frac{1}{2}k_2 b + 1\right) \bar{\kappa}_1{}^2 \Big)
\end{aligned}
\tag{6.29}
$$

The procedure of dimensional reduction method using Pascal polynomials is to minimize the obtained strain energy using the Euler-Lagrange equation as follows.

$$
\frac{\partial U_0}{\partial a_i} = 0,\ a_i = 1..9 \tag{6.30}
$$

The obtained coefficients a_i can be substituted in the strain energy Eq. (6.30). Collecting the coefficients of $\bar{\gamma}_{11}{}^2$ leads to extensional stiffness ($\bar{S}_{11}$), coefficients of $\bar{\kappa}_1$ results in torsional stiffness ($\bar{S}_{22}$), coefficients of $\bar{\kappa}_2$ and $\bar{\kappa}_3$ lead to bending stiffness $\bar{S}_{33}$ and $\bar{S}_{44}$, respectively. The coefficients of $\bar{\gamma}_{11}$ and $\bar{\kappa}_2$ leads to extension-bending stiffness of the curved beam.

$$\bar{S}_{11}=\frac{Eh}{\left(2\nu^2+\nu-1\right)k_2}\left(2\nu^2bk_2-\ln\left(-\frac{1}{2}k_2b+1\right)\nu+\ln\left(\frac{1}{2}k_2b+1\right)\nu+\ln\left(-\frac{1}{2}k_2b+1\right)-\ln\left(\frac{1}{2}k_2b+1\right)\right) \quad (6.31)$$

$$\bar{S}_{22}=\frac{E}{\left(2\nu^2+\nu-1\right)}\left(\frac{1}{2}\frac{\ln\left(-\frac{k_2b}{2}+1\right)h}{{k_2}^3}-\frac{0.041\ln\left(\frac{k_2b}{2}+1\right)h^3}{k_2}-\frac{1}{2}\frac{\ln\left(\frac{k_2b}{2}+1\right)h}{{k_2}^3}+\frac{1}{2}\frac{hb}{{k_2}^2}+\frac{0.041\ln\left(-\frac{k_2b}{2}+1\right)h^3}{k_2}\right) \quad (6.32)$$

$$\bar{S}_{33}=\frac{E}{\left(2\nu^2+\nu-1\right)}\left(\frac{\ln\left(-\frac{k_2b}{2}+1\right)h}{{k_2}^3}-\frac{\ln\left(\frac{k_2b}{2}+1\right)h}{{k_2}^3}+\frac{hb}{{k_2}^2}-\frac{\ln\left(-\frac{k_2b}{2}+1\right)\nu h}{{k_2}^3}-\frac{\nu hb}{{k_2}^2}+\frac{\ln\left(\frac{k_2b}{2}+1\right)\nu h}{{k_2}^3}\right) \quad (6.33)$$

$$\bar{S}_{44}=\frac{E}{\left(2\nu^2+\nu-1\right)k_2}\left(-0.083\ln\left(\frac{k_2b}{2}+1\right)h^3+0.083\ln\left(-\frac{k_2b}{2}+1.\right)h^3+0.083\ln\left(\frac{k_2b}{2}+1\right)\nu h^3-0.083\ln\left(-\frac{k_2b}{2}+1\right)\nu h^3\right) \quad (6.34)$$

$$\bar{S}_{13}=\frac{2E}{\left(2\nu^2+\nu-1\right)}\left(-\frac{\ln\left(\frac{1}{2}k_2b+1\right)\nu h}{{k_2}^2}+\frac{\ln\left(-\frac{1}{2}k_2b+1\right)\nu h}{{k_2}^2}+\frac{\nu hb}{k_2}+\frac{\ln\left(\frac{1}{2}k_2b+1.\right)h}{{k_2}^2}-\frac{hb}{k_2}-\frac{\ln\left(-\frac{1}{2}k_2b+1\right)h}{{k_2}^2}\right) \quad (6.35)$$

The 1D strain energy of the beam is

$$2U^e=\int_{L_e}\left\{\bar{\boldsymbol{\varepsilon}}^T[\bar{S}]\bar{\boldsymbol{\varepsilon}}\right\}dx_1 \quad (6.36)$$

Using Eq. (6.31-6.35), and (6.36), and $\bar{\boldsymbol{\varepsilon}}=\begin{bmatrix}\bar{\gamma}_{11} & \bar{\kappa}_1 & \bar{\kappa}_2 & \bar{\kappa}_3\end{bmatrix}^T$, the expanded 2D strain energy of the beam is

$$\begin{aligned}2U_0=\frac{1}{2\nu^2+\nu-1}\int_{L_e}\Bigg(&\left(\begin{array}{l}\frac{1}{k_2}\bar{\gamma}_{11}\left(2\nu^2bk_2-\ln\left(-\frac{1}{2}k_2b+1\right)\nu+\ln\left(\frac{1}{2}k_2b+1\right)\nu+\ln\left(-\frac{1}{2}k_2b+1\right)-\ln\left(\frac{1}{2}k_2b+1\right)\right)Eh\\+\bar{\kappa}_2\left(-\frac{2}{{k_2}^2}E\ln\left(\frac{k_2b}{2}+1\right)\nu h+\frac{2}{{k_2}^2}E\ln\left(-\frac{k_2b}{2}+1\right)\nu h+\frac{2E\nu hb}{k_2}+\frac{2}{{k_2}^2}E\ln\left(\frac{k_2b}{2}+1\right)h-\frac{2}{k_2}Ehb-\frac{2}{{k_2}^2}E\ln\left(-\frac{k_2b}{2}+1\right)h\right)\end{array}\right)\bar{\gamma}_{11}\\&+\bar{\kappa}_1^2\left(\frac{1}{2{k_2}^3}E\ln\left(-\frac{k_2b}{2}+1\right)h-\frac{1}{k_2}0.041E\ln\left(\frac{k_2b}{2}+1\right)h^3-\frac{1}{2{k_2}^3}E\ln\left(\frac{k_2b}{2}+1\right)h+\frac{1}{2{k_2}^2}Ehb+\frac{1}{k_2}0.041E\ln\left(-\frac{k_2b}{2}+1\right)h^3\right)\\&+\bar{\kappa}_1^2\left(-\frac{1}{{k_2}^3}E\ln\left(-\frac{k_2b}{2}+1\right)\nu h-\frac{1}{{k_2}^2}E\nu hb+\frac{1}{k_2}0.083E\ln\left(\frac{k_2b}{2}+1\right)\nu h^3+\frac{1}{{k_2}^3}E\ln\left(\frac{k_2b}{2}+1\right)\nu h-\frac{1}{k_2}0.083E\ln\left(-\frac{k_2b}{2}+1\right)\nu h^3\right)\\&+\bar{\gamma}_{11}\left(-\frac{2}{{k_2}^2}E\ln\left(\frac{k_2b}{2}+1\right)\nu h+\frac{2}{{k_2}^2}E\ln\left(-\frac{k_2b}{2}+1\right)\nu h+\frac{2}{k_2}E\nu hb+\frac{2}{{k_2}^2}E\ln\left(\frac{k_2b}{2}+1\right)h-\frac{2}{k_2}Ehb-\frac{2}{{k_2}^2}E\ln\left(-\frac{k_2b}{2}+1\right)h\right)\bar{\kappa}_2\\&+\bar{\kappa}_2^2\left(\frac{1}{{k_2}^3}E\ln\left(-\frac{k_2b}{2}+1\right)h-\frac{1}{{k_2}^3}E\ln\left(\frac{k_2b}{2}+1\right)h+\frac{1}{{k_2}^2}Ehb-\frac{1}{{k_2}^3}E\ln\left(-\frac{k_2b}{2}+1\right)\nu h-\frac{1}{{k_2}^2}E\nu hb+\frac{1}{{k_2}^3}E\ln\left(\frac{k_2b}{2}+1\right)\nu h\right)\\&+\bar{\kappa}_3^2\left(-\frac{0.083}{k_2}E\ln\left(\frac{k_2b}{2}+1\right)h^3+\frac{0.083}{k_2}E\ln\left(-\frac{k_2b}{2}+1\right)h^3+\frac{0.083}{k_2}E\ln\left(\frac{k_2b}{2}+1\right)\nu h^3-\frac{0.083}{k_2}E\ln\left(-\frac{k_2b}{2}+1\right)\nu h^3\right)\Bigg)dx_1\end{aligned} \quad (6.37)$$

For the case of a straight beam, the stiffness constants of Eqs. (6.31- 6.35) can be changed by setting the limit of k_2 to be zero, as follows.

$$\begin{aligned}\lim_{k_2\to0}\bar{S}_{11}=\lim_{k_2\to0}\frac{Eh}{\left(2\nu^2+\nu-1\right)k_2}&\left(2\nu^2bk_2-\ln\left(-\frac{1}{2}k_2b+1\right)\nu+\ln\left(\frac{1}{2}k_2b+1\right)\nu+\ln\left(-\frac{1}{2}k_2b+1\right)\right.\\&\left.-\ln\left(\frac{1}{2}k_2b+1\right)\right)=Ehb\end{aligned} \quad (6.38)$$

$$\lim_{k_2\to 0}\bar{S}_{22}=\lim_{k_2\to 0}\frac{1}{\left(2\nu^2+\nu-1\right)}\left(\frac{1}{2}\frac{E\ln\left(-\frac{k_2 b}{2}+1.\right)h}{k_2{}^3}-\frac{0.041E\ln\left(\frac{k_2 b}{2}+1.\right)h^3}{k_2}-\frac{1}{2}\frac{E\ln\left(\frac{k_2 b}{2}+1\right)h}{k_2{}^3}\right.$$
$$\left.+\frac{1}{2}\frac{Ehb}{k_2{}^2}+\frac{0.041E\ln\left(-\frac{k_2 b}{2}+1\right)h^3}{k_2}\right)=\frac{3.125\times 10^9 E(hb^3+h^3 b)}{7.5\times 10^{10}(1+\nu)} \tag{6.39}$$

$$\lim_{k_2\to 0}\bar{S}_{33}=\lim_{k_2\to 0}\frac{E}{\left(2\nu^2+\nu-1\right)}\left(\frac{\ln\left(-\frac{k_2 b}{2}+1\right)h}{k_2{}^3}-\frac{\ln\left(\frac{k_2 b}{2}+1\right)h}{k_2{}^3}+\frac{Ehb}{k_2{}^2}-\frac{\ln\left(-\frac{k_2 b}{2}+1\right)\nu h}{k_2{}^3}\right.$$
$$\left.-\frac{\nu hb}{k_2{}^2}+\frac{\ln\left(\frac{k_2 b}{2}+1\right)\nu h}{k_2{}^3}\right)=\frac{E(hb^3\nu-hb^3)}{12(2\nu^2+\nu-1)} \tag{6.40}$$

$$\lim_{k_2\to 0}\bar{S}_{13}=\lim_{k_2\to 0}\frac{2E}{\left(2\nu^2+\nu-1\right)}\left(-\frac{\ln\left(\frac{1}{2}k_2 b+1\right)\nu h}{k_2{}^2}+\frac{\ln\left(-\frac{1}{2}k_2 b+1\right)\nu h}{k_2{}^2}+\frac{\nu hb}{k_2}+\frac{\ln\left(\frac{1}{2}k_2 b+1.\right)h}{k_2{}^2}-\frac{hb}{k_2}-\frac{\ln\left(-\frac{1}{2}k_2 b+1\right)h}{k_2{}^2}\right)=0 \tag{6.41}$$

Comparison of the Eqs. (6.31-6.35) and (6.38-6.41) shows that the initial curvature has effect on the cross-sectional stiffness constants. The values of $\bar{S}_{13}$ becomes zero for the case of straight beam while this value for the case of curved beam is non-zero.

For the studied rectangular section with isotropic material, the change of $\bar{S}_{11}$, $\bar{S}_{22}$, $\bar{S}_{33}$, $\bar{S}_{44}$, and $\bar{S}_{13}$ based on classical beam model versus the initial curvature are shown in Fig. (6.39). Different orders of polynomial are applied for this study. For the order (*m*=1), the Eqs. (6.31-6.35) are used. The orders (*m*=2, 4, and 5) are also used to obtain more accurate results. By increasing the initial curvature the values of $\bar{S}_{11}$, $\bar{S}_{22}$, $\bar{S}_{33}$, and $\bar{S}_{44}$ do not change significantly for the isotropic rectangular section. While, the magnitudes of $\bar{S}_{13}$ increase considerably.

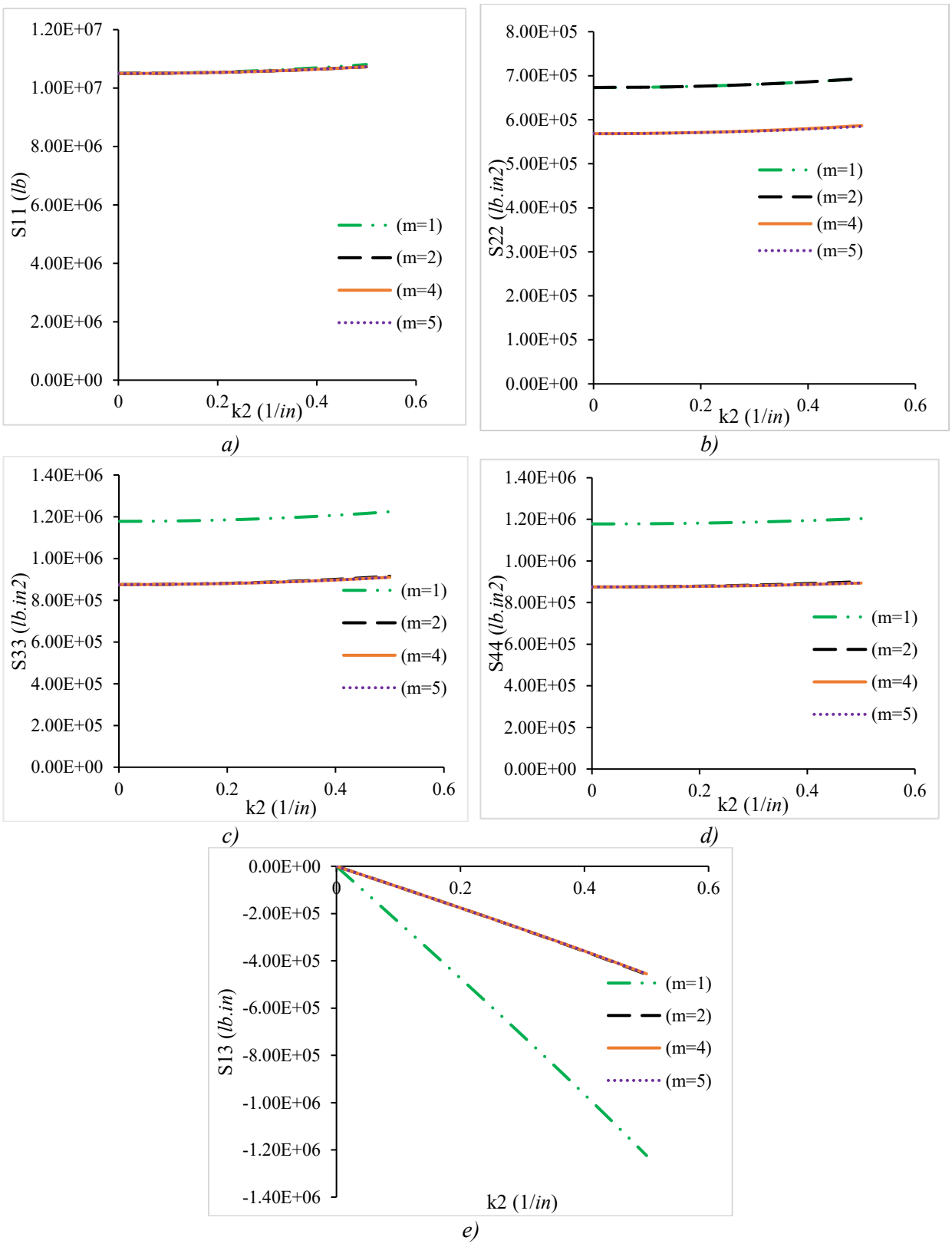

Fig. (6.39). The variation of stiffness constants of the rectangular isotropic cross-section versus initial curvature, (b=1 *in*, h=1 *in*, $E = 10.5\times10^{6}$ *psi*, v=0.3).

6.5.2 Effect of initial curvature on the stiffness constants of initially curved tubes

We selected isotropic and orthotropic tubes to study the effect of curvature on their mechanical behavior such as cross-sectional stiffness constants and displacement. All the isotropic and orthotropic tubes have outer diameter of D_o=118 *mm* and inner diameter of D_i=98 *mm*. The isotropic tubes have E=69.7 Gpa and v=0.3. The orthotropic tubes have material properties of E_1=138 GPa, E_3= E_2=10.5 GPa, v_{12}=v_{13}=0.3 and v_{23}=0.33, G_{12}=G_{13}=G_{23}=5.53 GPa. The tubes have the lay-up of [-α_5/α_5]. Each layer has the thickness of t= 1 *mm*. The variation of S_{11} for different initial curvatures of isotropic and orthotropic tubes with various fiber angles α are shown in Table (6.14). It can be observed that by increasing the initial curvature, the values of S_{11} have fluctuations. This fluctuation will have effect on the distribution of strains as well as changes the 1D global behavior of the tube. But these fluctuations should be considered with the other stiffness constants to have a correct judgement to understand the behavior of the tube. This augmentation in the S_{11} is more prominent for lower fiber angles. By increasing the fiber angle, the effect of initial curvature on the S_{11} decreases. A good agreement between the present polynomial based method and VABS is observed. It should be pointed out that the order (m=7) of pascal polynomials has been applied to calculate the stiffness constants.

Table (6.14). Variation of S_{11} (N) of Timoshenko beam model for different initial curvatures k_2 (1/m) of isotropic and orthotropic tubes [-α_5/α_5] with various fiber angles (α).

Fiber angle (α)	(Straight) (Present)	(k_2=0.5) (Present)	(k_2=0.5) (VABS)	(k_2=1) (Present)	(k_2=1.5) (Present)	(k_2=1.5) (VABS)
Isotropic	2.36×10^8	2.37×10^8	2.35×10^8	2.44×10^8	2.21×10^8	2.24×10^8
0	4.68×10^8	4.68×10^8	4.68×10^8	4.72×10^8	4.77×10^8	4.70×10^8
15	3.82×10^8	3.59×10^8	3.34×10^8	3.94×10^8	3.87×10^8	3.85×10^8
45	6.63×10^7	6.62×10^7	6.63×10^7	7.05×10^7	6.69×10^7	7.53×10^7
50	5.32×10^7	5.30×10^7	5.32×10^7	5.54×10^7	5.43×10^7	5.85×10^7
60	4.09×10^7	4.10×10^7	4.09×10^7	4.16×10^7	4.15×10^7	4.28×10^7
90	3.57×10^7	3.58×10^7	3.57×10^7	3.59×10^7	3.51×10^7	3.59×10^7

The influence of change of initial curvature on the variation of S_{55} of isotropic and orthotropic tubes is shown in Table (6.15). It can be seen that for the case of isotropic tube, as the initial curvature increases, the values S_{55} do not change significantly. While, for the case of orthotropic

tubes, the initial curvature has more effect on the change of S_{55}, specifically in the lower fiber angles of angle-ply tubes.

Table (6.15). Variation of S_{55} ($N.m^2$) of Timoshenko beam model for different initial curvatures k_2 ($1/m$) of isotropic and orthotropic tubes [$-\alpha_5/\alpha_5$] with various fiber angles (α).

Fiber angle (α)	(Straight) (Present)	(k_2=0.5) (Present)	(k_2=0.5) (VABS)	(k_2=1) (Present)	(k_2=1.5) (Present)	(k_2=1.5) (VABS)
Isotropic	3.47×10^5	3.48×10^5	3.42×10^5	3.53×10^5	3.58×10^5	3.04×10^5
0	6.88×10^5	6.89×10^5	6.88×10^5	6.90×10^5	6.90×10^5	6.93×10^5
15	5.61×10^5	5.00×10^5	4.70×10^5	5.60×10^5	6.05×10^5	5.63×10^5
45	9.78×10^4	9.68×10^4	9.67×10^4	1.03×10^5	9.02×10^4	8.81×10^4
50	7.84×10^4	7.83×10^4	7.78×10^4	8.48×10^4	8.39×10^4	7.32×10^4
60	6.02×10^4	6.01×10^4	5.99×10^4	6.01×10^4	6.20×10^4	5.80×10^4
90	5.25×10^4	5.26×10^4	5.24×10^4	5.27×10^4	5.29×10^4	5.20×10^4

The effect of fiber angle of tubes [$-\alpha_5/\alpha_5$] on the $\bar{S}_{13}$ of the classical stiffness matrix of (up to second order) for various levels of initial curvature is demonstrated in Fig. (6.40) . It is seen that the maximum of values of $\bar{S}_{13}$ happens at fiber angle of $\alpha=15^\circ$ for different levels of initial curvature. Moreover, the values of $\bar{S}_{13}$ do not change significantly as the fiber angle is more than $\alpha=50^\circ$. Also, as the initial curvature increases, the values of S_{13} increase. It is noted that for the case of beams with initial curvature k_2=0 $1/m$ (straight), S_{13} is zero. The variation of extension-bending stiffness (S_{15}) of tubes based on Timoshenko-Like beam model for different levels of initial curvature and various fiber angles is shown in Fig. (6.41). Comparing the obtained extension-bending stiffness of Fig. (6.40) and Fig. (6.41), one can find that the magnitudes of S_{15} are higher than those of $\bar{S}_{13}$.

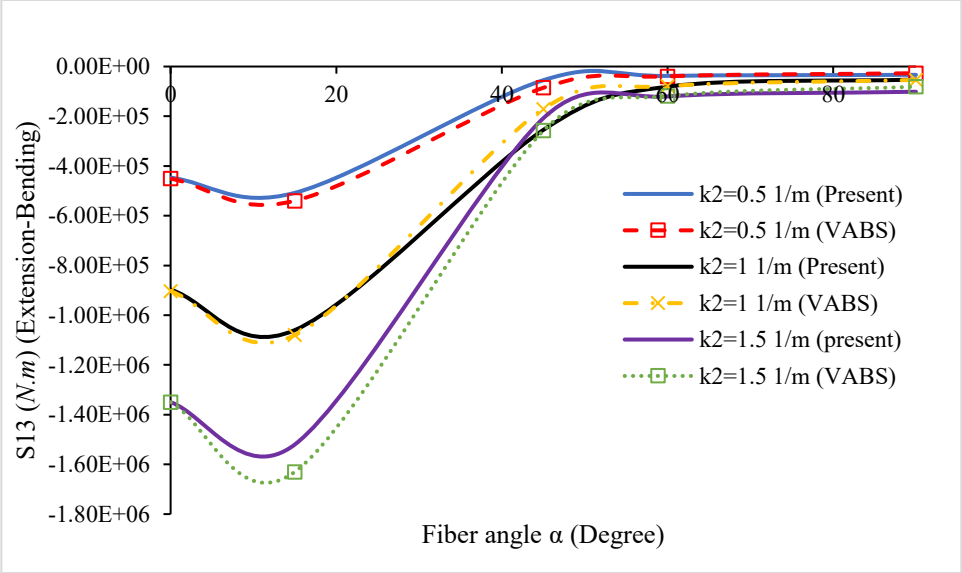

Fig. (6.40). The variation of S_{13} of cross-sectional stiffness matrix (up to second order) for different levels of initial curvature k_2 of composite tubes $[-\alpha_5/\alpha_5]$.

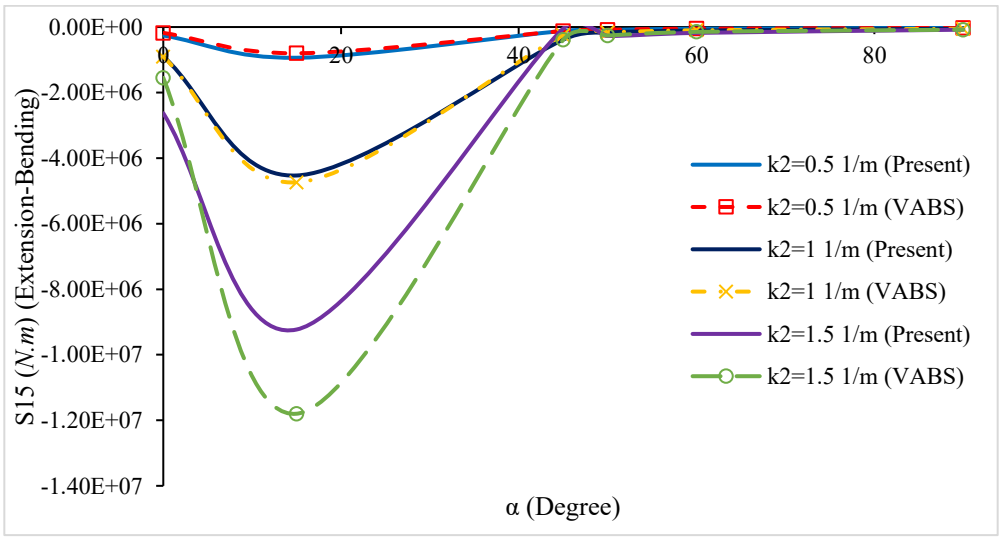

Fig. (6.41). The variation of S_{15} of cross-sectional stiffness matrix (Timoshenko) for different levels of initial curvature k_2 of composite tubes $[-\alpha_5/\alpha_5]$.

6.6 Stress analysis of initially curved tube under four-point bending loadings

The experimental tests in this thesis have been conducted by a teamwork at Concordia Center for Composites (CONCOM), under the umbrella of the NSERC Industrial Chair on Automated Composites Manufacturing held by Professor Suong V. Hoa, in collaboration with Bell Flight Ltd.

The general configuration of the tubes has been guided by people at Bell Flight (Pierre Beulieu and Simon Bernier). The design and fabrication of the test set up was done by Dr. Ashraf Ahmed Fathy. Dr. Daniel Rosca developed the manufacturing procedure and fabricated the tubes using the Automated Fiber Placement machine at Concordia. Dr. Daniel Rosca and Ashraf Fathy carried out the test of the tubes.

6.6.1 Four-point bending experimental test of curved tube

An initially curved tube is fabricated using Automated Fiber Placement (AFP) machine. The tube consists of 7 layers of a 5-harness carbon epoxy satin woven which is used as a mandrel and 36 layers of Carbon/PEEK lay-up using AFP. The fabrication process is shown in Fig. (6.42).

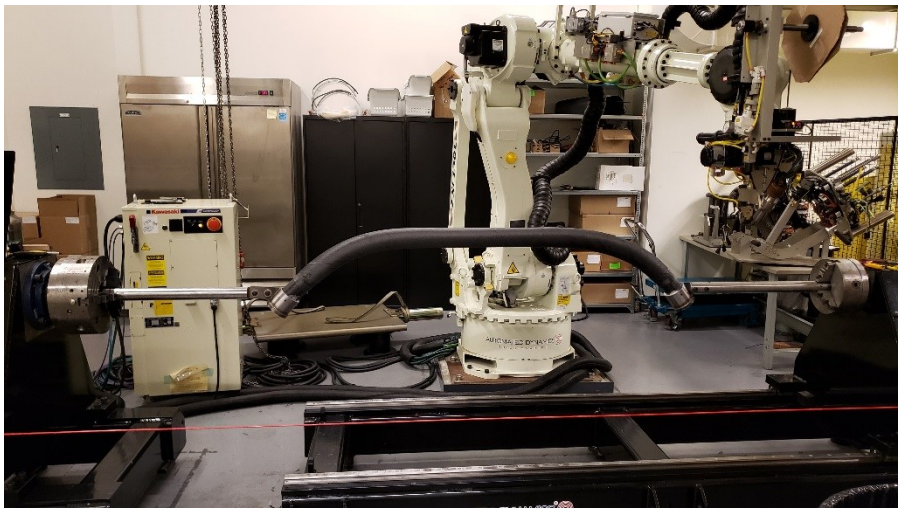

Fig. (6.42) Fabricating the curved tube using AFP.

The tube has the stacking sequence of $[(5Harness\ \text{satin})_7 / 90_4 / (\pm 30)_4 / 90_4 / (\pm 35)_4 / 90_4 / (\pm 45)_4]$, inner and outer radiuses of r_{in}=36.33 *mm* and r_{out}=42.32 *mm*. The thickness of each layer of 5 harness satin woven is 0.285 *mm* and the thickness of each layer of Carbon/PEKK is 0.111 *mm*. Fig. (6.43) shows the lay-up of the tube.

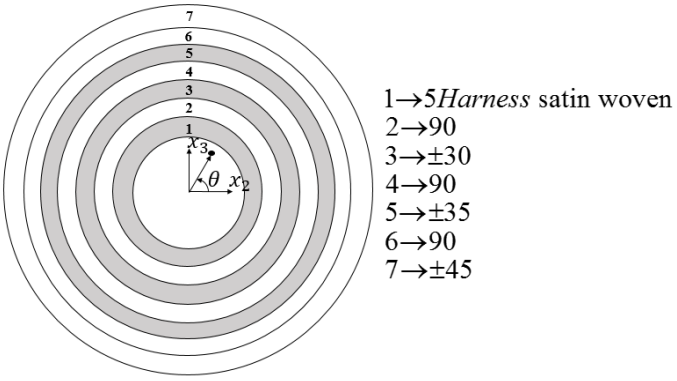

Fig. (6.43). Lay-up sequence of the tube

$[(5Harness\ \text{satin})_7 / 90_4 / (\pm 30)_4 / 90_4 / (\pm 35)_4 / 90_4 / (\pm 45)_4]$.

The material properties of the 5-harness satin woven are $E_1 = E_2 = 54$ GPa, $E_3 = 9.964$ GPa, $G_{12} = 4$ GPa, $G_{13} = G_{23} = 2.5$ GPa and poisson ratio of $v_{12} = 0.05$, $v_{13} = 0.254$ and $v_{23} = 0.289$ [78]. The material properties of Carbon/PEKK are $E_1 = 138$ GPa, $E_2 = E_3 = 10.2$ GPa, $G_{12} = G_{13} = G_{23} = 5.7$ GPa and $v_{12} = v_{13} = 0.31$ and $v_{23} = 0.33$.

A test setup for bending test of the tube which simulates the bending of cross-tube for landing gear of helicopter is fabricated and shown in Fig. (6.44).

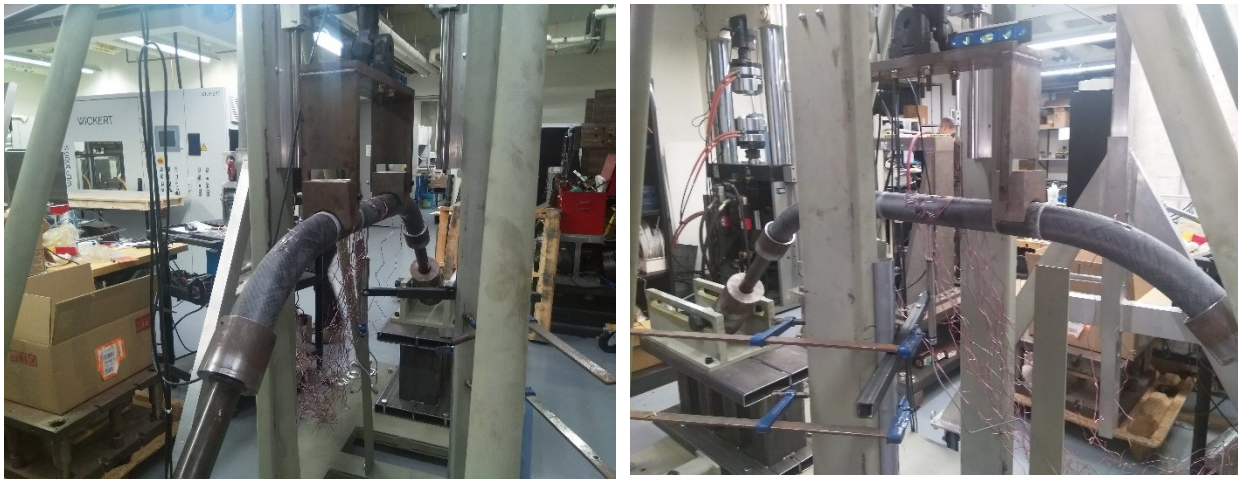

Fig. (6.44) Bending test setup of curved tube.

The locations of the tube which are under loading are boosted by using glass fibers to prevent local failure and stress concentration. The supports at the two ends of the tube can rotate and slide. The

test setup and tube dimensions are illustrated in Fig. (6.45). The tube is attached to the two steel arms where the arms can slide in the *z* direction.

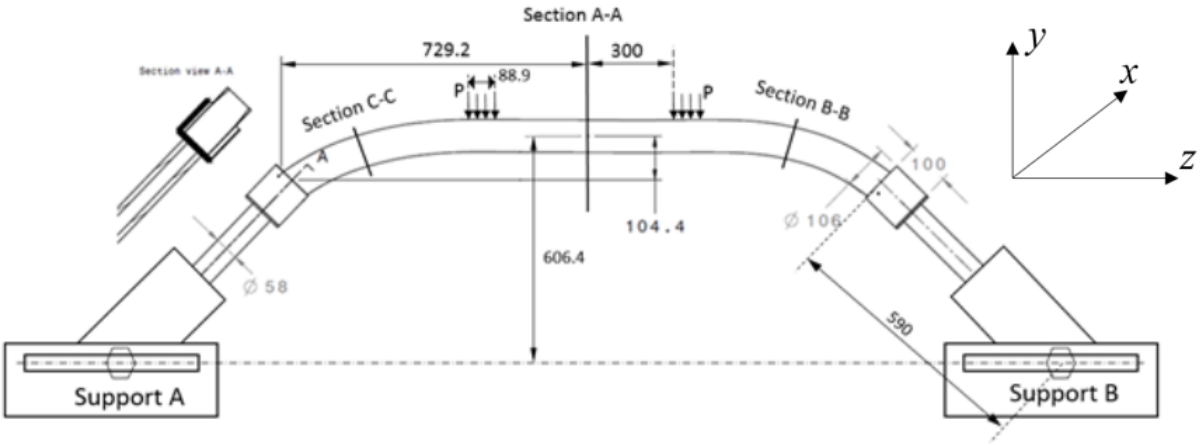

Fig. (6.45). Composite tube and the test setup dimension, (dimensions are in millimeter).

Six rosettes at section A-A and two longitudinal strain gages at top and bottom surfaces of section B-B and section C-C are installed to capture all the strains. The circumferential position of each strain gage according to the coordinate of the Fig. (6.45), are reported in the Table (6.16). The circumferential locations of longitudinal strain gages at sections B-B and C-C are shown in Table (6.17).

Table (6.16) Circumferential position of each rosette at section A-A.

Rosette number	Circumferential angle (θ)
1	90°
2	45°
3	0°
4	270°
5	180°
6	135°

Table (6.17) Circumferential position of each strain gage at sections B-B and C-C.

Strain gage number	Circumferential angle (θ)
1 (Section B-B)	90°
2 (Section B-B)	270°
3 (Section C-C)	90°
4 (Section C-C)	270°

Three spots of the tube are considered for measuring the strains. The first spot is at the center of the tube which is section A-A located at the straight region (mid-length) of the tube and second spot is the section B-B located at the curved region of the tube. The third spot is located at section C-C.

VABS modeling

The VABS modeling of the tube under four-point bending loadings has been reported in Appendix A.

ANSYS 3D modeling

In this section, we provided the explanation concerning with the modeling procedure of the curved tubular beam including steel arms as well as the composite part. The tube has three parts, the steel part has the inner and outer radiuses similar to the composite part mentioned in section 6.6.1. The Steel parts have the material properties E=210 GPa and v=0.3. The dimensions of the curved part is measured and imported to ANSYS workbench. All the three parts are then imported to ANSYS in which the two Steel arms are joined to the composite part by bonding contact method in ANSYS. So, the arms are clamped to the composite part. Fig. (6.46) shows the designed tube and the arms which is based on the measurements in CATIA.

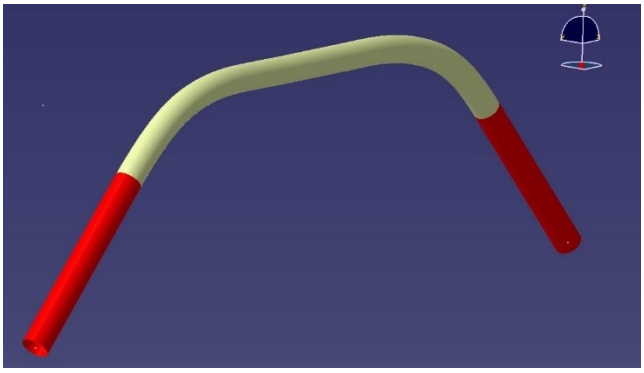

Fig. (6.46). The configuration of measured and designed tube in CATIA.

The stack-up sequence of the curved part is $[(5Harness\ \text{satin})_7 / 90_4 / (\pm 30)_4 / 90_4 / (\pm 35)_4 / 90_4 / (\pm 45)_4]$ where two fabrics are defined as 5-Harness satin and Carbon/PEKK. The rosettes which are coordinate systems used to set the reference direction of oriented selection sets are defined to be edgewise. They follow an edge parallel to the reference axis of the whole the tube. Fig. (6.47) shows the fiber direction of 90° layers in the tube as an example.

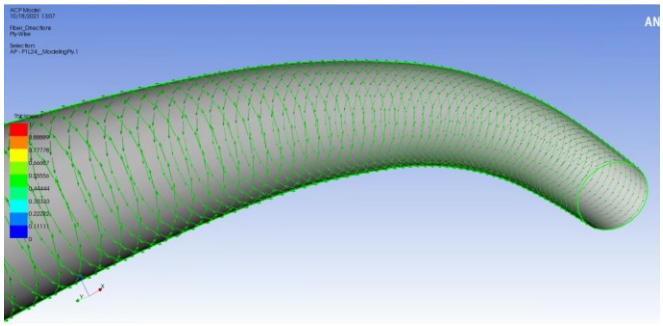

Fig. (6.47). Direction of 90° fibers throughout the tube.

The schematic of the modelled tube in ANSYS workbench is demonstrated in Fig. (6.48). The boundary conditions at two end rings (C and D; two ends of the Steel arms) of the beam are defined in which along the z direction the displacement is free ($u_z \neq 0$), along the y and x directions the displacements are restricted ($u_x = u_y \neq 0$). The rotations about z and y directions are restricted ($Rot_z = Rot_y = 0$) and rotation about x direction is free ($Rot_x \neq 0$). The loadings are applied at nodes (nodal force at points A and B) with the amount of -1500 N along the y coordinate where the applied loading is divided by nodes, (Fig. (6.48)). It is noted that the center point of the loading is similar to the experiment, while the loading surface area is less than the experiment due to surface imperfections of the tube in the experiment. A single node at the middle of the tube is

selected and restricted along z axis to avoid rigid body motion of the beam. The element SOLID 186 has been used for the composite part. This element is a higher order 3D with 20 node solid element that exhibits quadratic displacement behavior. The element is defined by 20 nodes having three degrees of freedom at each node. The element SOLID 187 has been used for Steel arms. This element is a higher order 3D with 10 nodes. This element is suitable for modeling of irregular meshes (such as those produced form CAD systems), [88]. The total number of elements of the tube is 231020. Due to the hardware limitation, it was not possible to increase the number of elements.

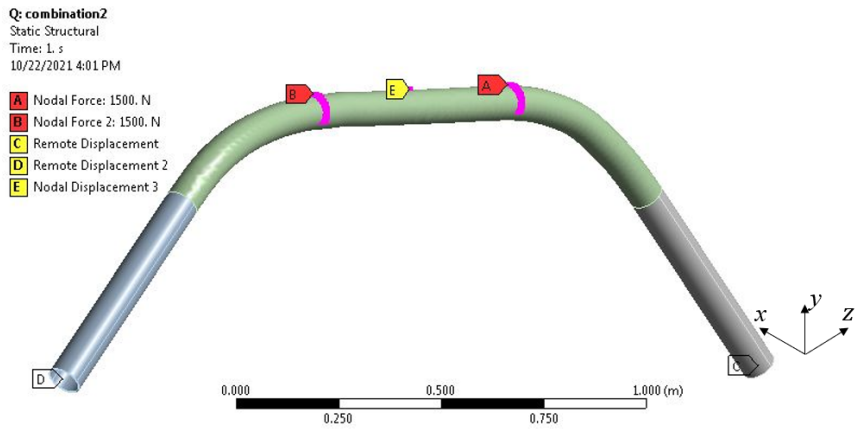

Fig. (6.48). The modeled tube in ANSYS, loadings and boundary conditions.

Section A-A

The obtained Timoshenko-like 6×6 cross-sectional stiffness constants of section A-A which is the straight region of the tube is shown in Table (6.18).

Table (6.18). Timoshenko-Like stiffness constants of straight region (k_2=0) of the tube.

Method	S_{11} (N)	S_{14} (N.m)	S_{22} (N)	S_{33} (N)	S_{44} (N.m^2)	S_{25} (N.m)	S_{36} (N.m)	S_{55} (N.m^2)	S_{66} (N.m^2)
VABS 3.9	7.045e7	4.131e4	1.173e7	1.160e7	4.104e4	-1.962e4	-2.188e4	5.429e4	5.405e4
Present	7.176e7	6.850e4	1.269e7	1.271e7	4.427e4	-3.287e4	-3.288e4	5.495e4	5.495e4

The value of S_{55} indicates the flexural stiffness of the tube about axis x_2. This value has substantial effect on the longitudinal strain of the straight part of the tube. The load-longitudinal and load-circumferential strain diagrams of the section A-A at different circumferential positions of section A-A are obtained as follows.

- Strains at rosette 1 where $\theta = 90^\circ$ and outer surface of the tube are shown in Fig. (6.49).

- Strains at rosette 2 where $\theta = 45^{\circ}$ and outer surface of the tube are shown in Fig. (6.50).
- Strains at rosette 4 where $\theta = 270^{\circ}$ and outer surface of the tube are shown in Fig. (6.51).
- Strains at rosette 6 where $\theta = 135^{\circ}$ and outer surface of the tube are shown in Fig. (6.52).

It can be observed that there is a good agreement between the VABS and experimental strains at section A-A.

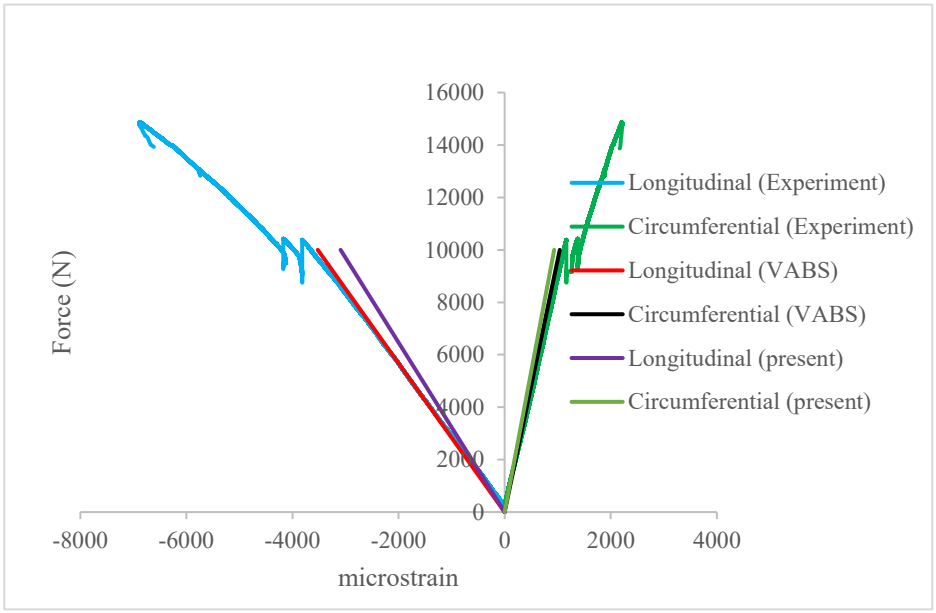

Fig. (6.49). Load-strain at section A-A and $\theta = 90^{\circ}$ (rosette 1) of the tube, F=2P.

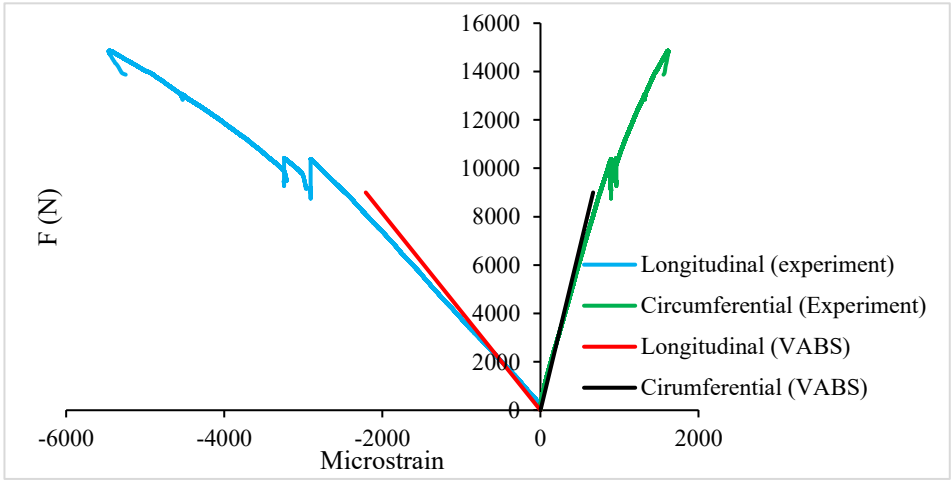

Fig. (6.50). Load-strain at section A-A and $\theta = 45^{\circ}$ (rosette 2) of the tube, F=2P.

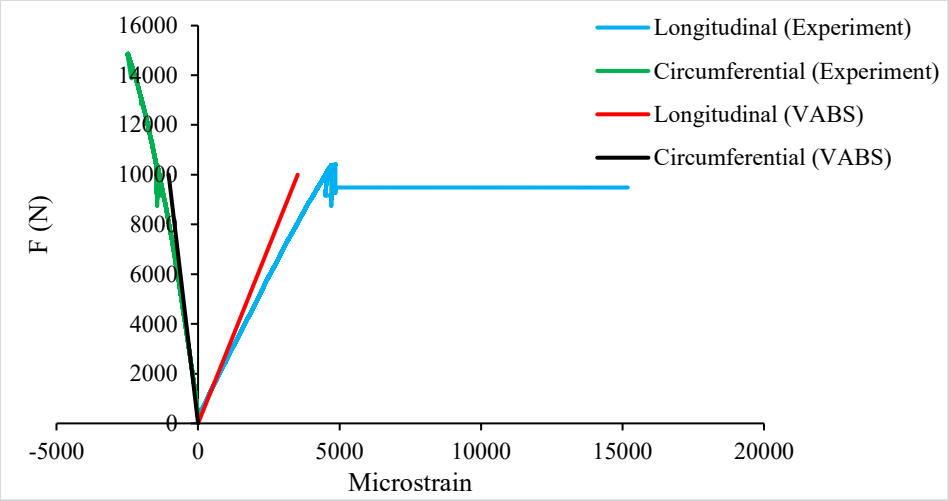

Fig. (6.51). Load-strain at section A-A and $\theta = 270^{\circ}$ (rosette 4) of the tube, F=2P.

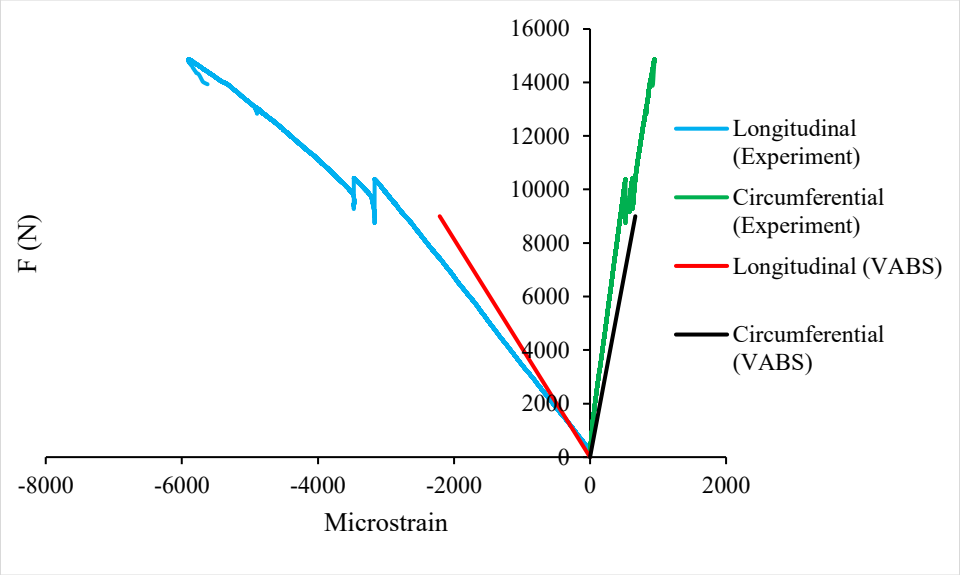

Fig. (6.52). Load-strain at section A-A and $\theta = 135^{\circ}$ (rosette 6) of the tube, F=2P.

The distribution of longitudinal strain and circumferential strain of the tube at section A-A under load 3000 *N* are demonstrated in Fig. (6.53). It can be seen that at top surface of the tube, there is a compression and at the bottom of the tube there is tension.

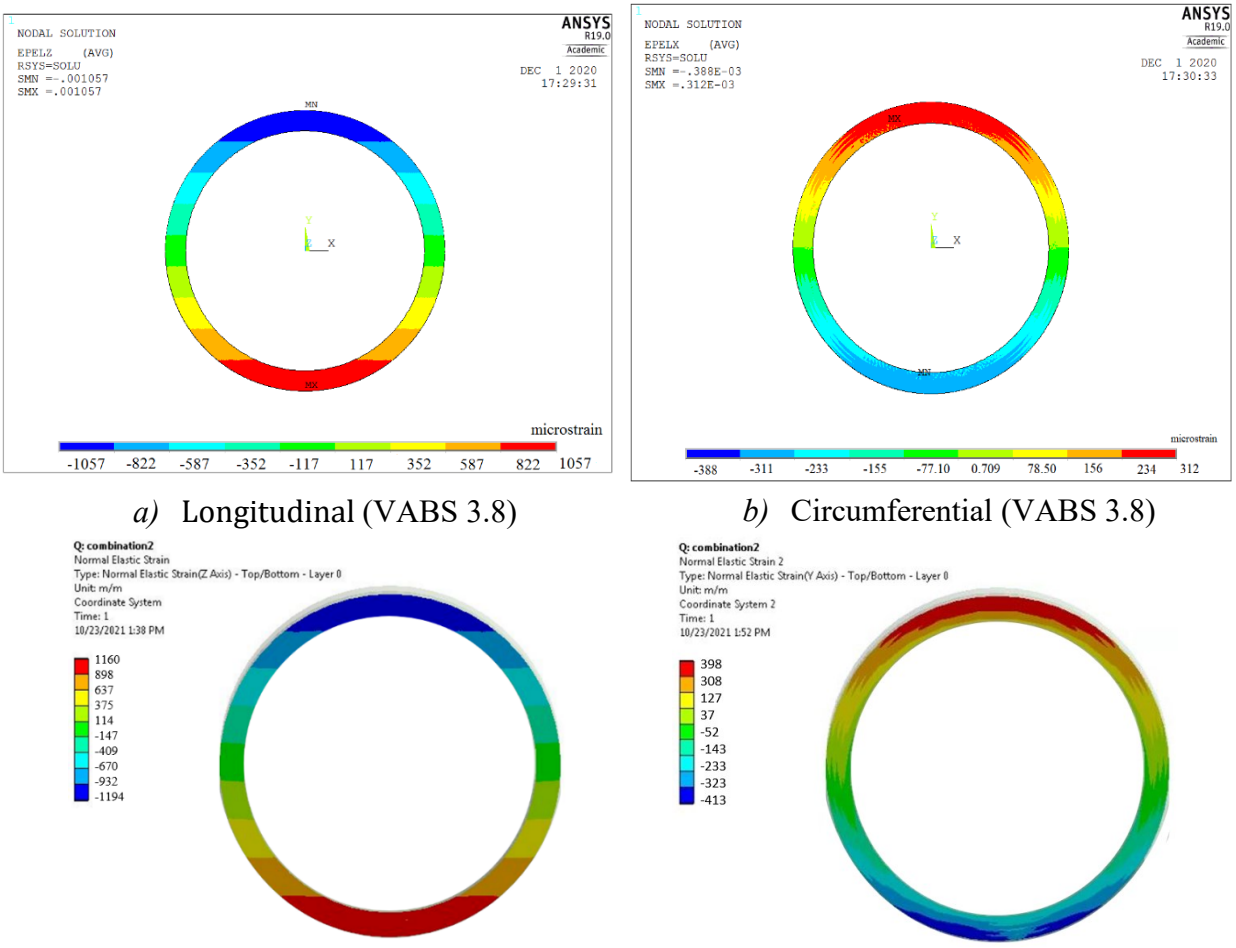

a) Longitudinal (VABS 3.8) *b)* Circumferential (VABS 3.8)

c) Longitudinal (ANSYS 3D) d) Circumferential (ANSYS 3D)

Fig. (6.53). Distribution of longitudinal strain and circumferential strain at section A-A under load 3000 N, F=2P.

Section B-B

At the section B-B, since the tube is curved and there exist the shear loading, the loading condition is more complicated. At the section B-B, the tube has k_2=1.61 1/*m* curvature. Due to the initial curvature, the additional stiffness constants will be added to the stiffness matrix, (see Table (6.19)). Moreover, the flexural stiffness constant (S_{55}) of the curved tube decreases compared to straight part. In spite of the fact that the values of S_{11} and S_{55} decrease compared to straight part, it does not have meaning that the curved part has less stiffness with respect to the straight part. The value of S_{15} increases. Moreover, it is observed that the FE stiffness matrix of curved tube will be more affected which is due to the change of geometry of the tube. These are the main effects of initial curvature on the strain and displacement behavior of a beam. Fig. (6.54) shows the force-strain at

strain gages 1 and 2 located at top and bottom surfaces of the tube. The longitudinal strain at top surface of the theoretical method agrees well with the experiment. However, there is a difference at the bottom surface between the experiment and theoretical strain after the load 3000 N.

Table (6.19). The non-zero Timoshenko-Like cross-sectional stiffness constants of the curved part with k_2=1.61 1/m, (Section B-B).

Method	S_{11} ***(N)***	S_{14} ***(N.m)***	S_{15} ***(N.m)***	S_{22} ***(N)***	S_{24} ***(N.m)***	S_{25} ***(N.m)***	S_{33} ***(N.m)***	S_{36} ***(N.m)***	S_{44} ***(N.m^2)***	S_{55} ***(N.m^2)***	S_{66} ***(N.m^2)***
VABS 3.9	5.501e7	-1.05e6	-6.05e4	1.038e7	1.898e4	4.320e5	1.036e7	4.168e5	4.155e4	3.859e4	3.737e4
Present	5.842e7	-7.700e5	-6.147e4	1.057e7	1.049e5	4.367e5	1.05e7	4.367e5	3.732e4	3.763e4	3.720e4

The distribution of longitudinal and circumferential strains are shown in Fig. (6.55). Comparison of distribution of strains of curved and straight regions show that the initial curvature affects the distribution of strains along both directions in terms of distribution pattern.

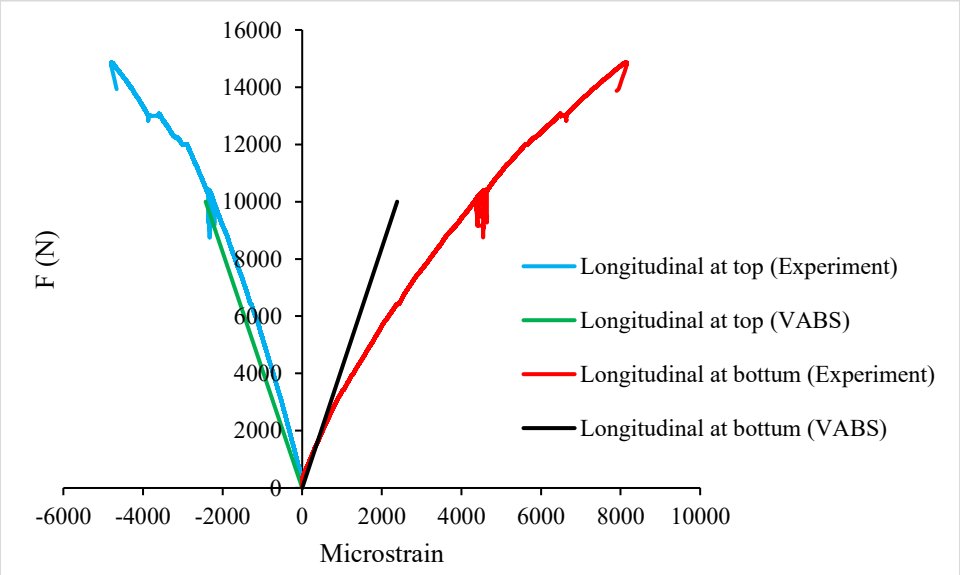

Fig. (6.54). Force-strain at section B-B and $\theta = 90^\circ$ and 270° (strain gages 1 and 2) of the tube, F=2P.

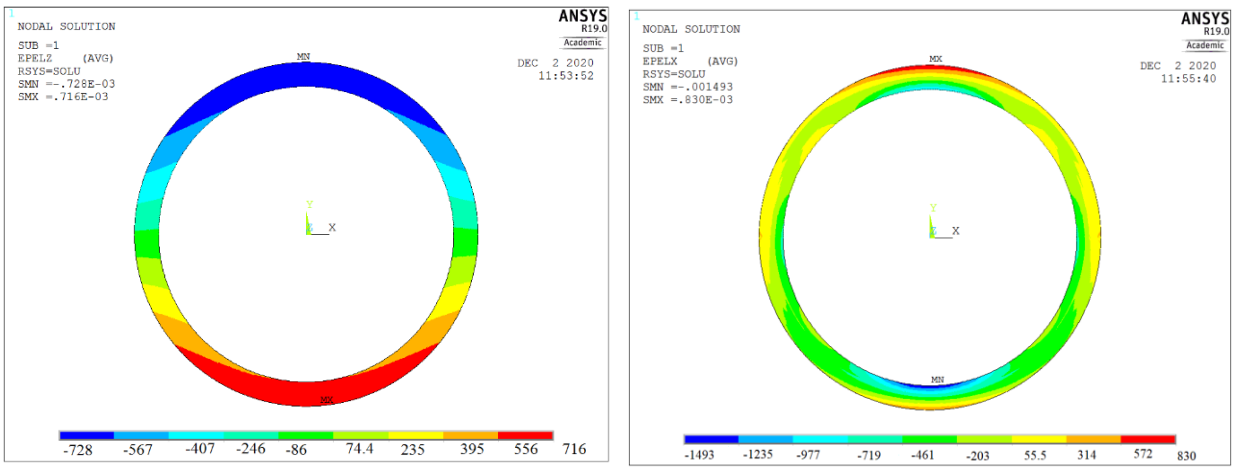

a) *b*)

Fig. (6.55). Distribution of *a*) Longitudinal, and *b*) Circumferential strains at section B-B under load F=3000 N, F=2P.

Section C-C

At the section C-C, the tube has k_2=2.06 1/*m* curvature. The curvature of this section is more than section B-B. The 1D FE stiffness matrix of section C-C will be stiffer with respect to section B-B which is due to change in geometry. The obtained cross-sectional stiffness constants of this section are tabulated in Table (6.20).

Table (6.20). The non-zero Timoshenko-Like cross-sectional stiffness constants of the curved part (Section C-C).

Method	S_{11} ***(N)***	S_{14} ***(N.m)***	S_{15} ***(N.m)***	S_{22} ***(N)***	S_{24} ***(N.m)***	S_{25} ***(N.m)***	S_{33} ***(N.m)***	S_{36} ***(N.m)***	S_{44} ***($N.m^2$)***	S_{55} ***($N.m^2$)***	S_{66} ***($N.m^2$)***
VABS 3.8	6.019e7	-1.178e6	-7.707e4	9.956e6	3.930e4	4.286e5	1.003e7	4.116e5	4.170e4	3.847e4	3.570e4
Present	7.509e7	-9.042e5	-6.214e4	1.281e7	3.996e4	4.342e5	1.281e7	4.342e5	3.966e4	3.783e4	3.720e4

The force-longitudinal strain at top and bottom surfaces of the tube at section C-C are shown in Fig. (6.56). It can be seen that there is a good agreement between VABS and experiment longitudinal strain at top surface ($\theta = 90^{\circ}$). However, there is a difference between the theoretical and experimental strain after the load of 4000 *N* at the bottom surface.

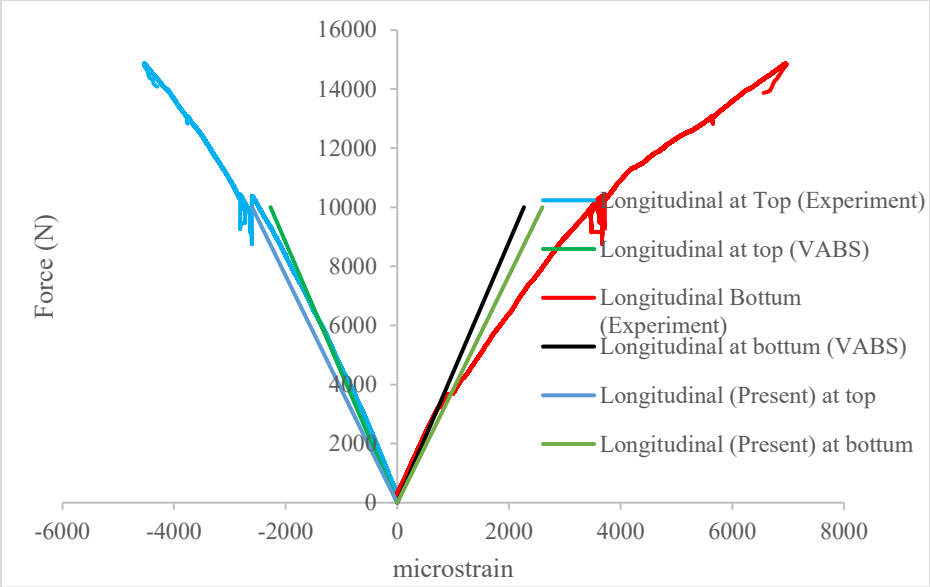

Fig. (6.56). Load-strain at section C-C and $\theta = 90^{\circ}$ and 270° (strain gages 3 and 4) of the tube, F=2P.

The distribution of longitudinal strain at section C-C under load 3000 N is shown in Fig. (6.57).

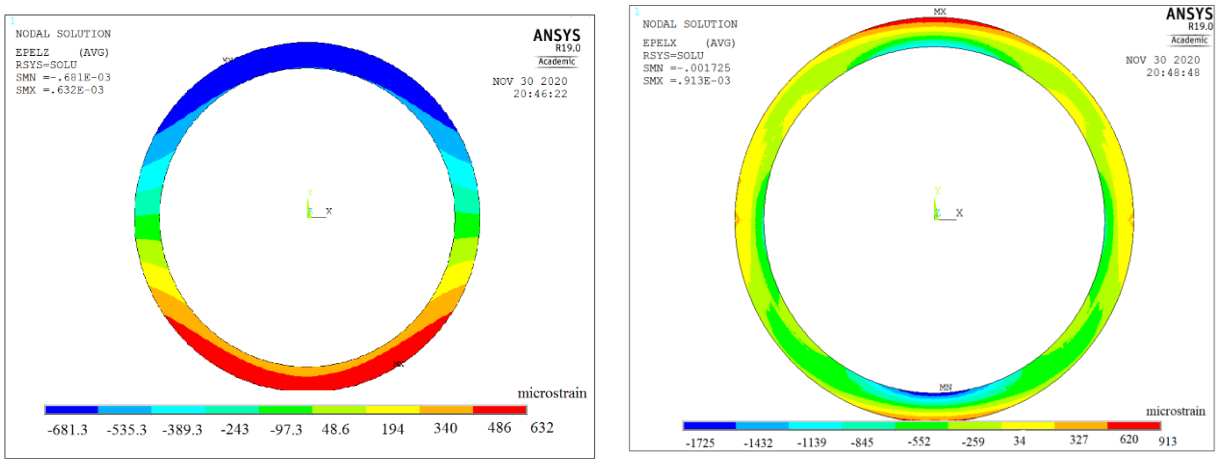

a) *b*)

Fig. (6.57). Distribution of *a*) Longitudinal, and *b*) circumferential strains at section C-C under load F=3000 N, F=2P.

Transverse Displacement calculation by ANSYS 3D

The transverse displacement (along *y*) distribution of the tube under total loading F=3000 N using ANSYS 3D is demonstrated in Fig. (6.58). The maximum magnitude of transverse displacement of the tube is 19.59 *mm*.

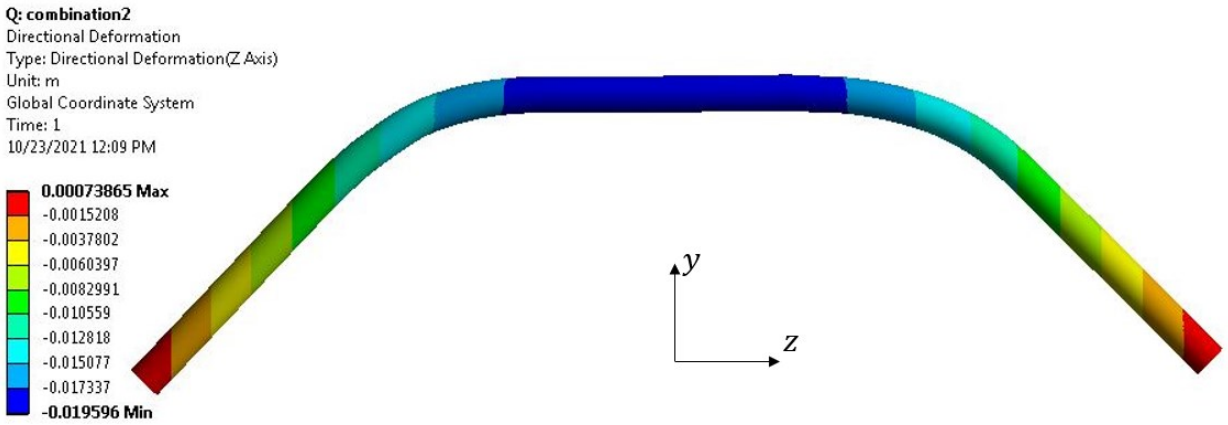

Fig. (6.58). Transverse displacement distribution (in *m*) along *y* of the tube using ANSYS 3D.

Transverse displacement using VABS+ANSYS 1D

To model a curved beam which consists of combinations of curved and straight parts, we use the obtained cross-sectional stiffness matrices calculated by VABS. The beam consists of a straight composite part with cross-sectional stiffness matrix (S_1), two curved composite parts with cross-sectional stiffness matrices (S_2 and S_3), and two Steel arms with cross-sectional stiffness matrix (S_4), as shown in Fig. (6.59). These matrices are imported to assemble the complete beam in ANSYS-APDL. The element type beam 189 is employed in ANSYS-APDL. For each straight and curved part, different mesh attribute with its specific section type is defined. The total number of elements is 200 for the whole tube. The boundary conditions are defined that the displacement at two ends of the beam structure along *z* direction is free ($u_z \neq 0$), and the displacements along *y* and *x* directions are restricted ($u_x = u_y = 0$). The rotations about *y* and *z* are restricted ($\theta_y = \theta_z = 0$) and about *x* is free ($\theta_x \neq 0$). The loads *P* are applied at the center of crossheads. The transverse displacement distribution of the tube under total loading F=3000 N along *y* is shown in Fig. (6.60). A good agreement between the ANSYS 3D and VABS+ANSYS 1D for transverse displacement is observed. It should be pointed out that for each straight and curved part, a specific cross-sectional stiffness matrix with its initial curvature (k_2) is used. The joint at straight and curved parts might have relatively little effect on the overall accuracy except in the vicinity of the discontinuity. A sufficiently large number of elements should be used to make sure that the results are converged. The maximum magnitude of transverse displacement at the middle of the beam is 19.71 *mm* which agrees with what obtained by ANSYS 3D.

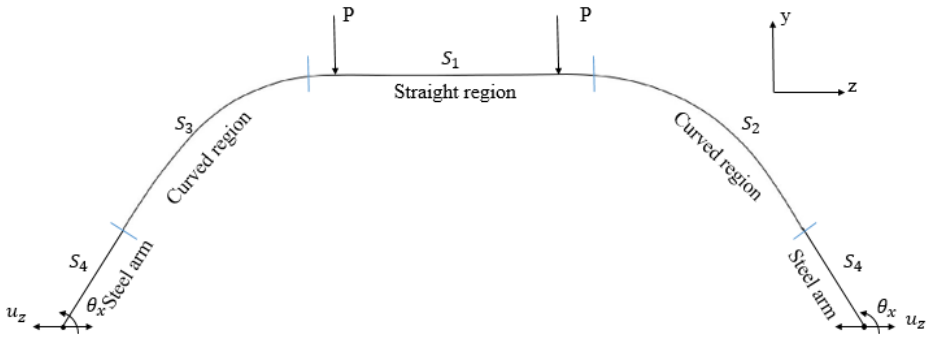

Fig. (6.59). 1D sketch of the tube with straight and curved parts under four-point bending loading.

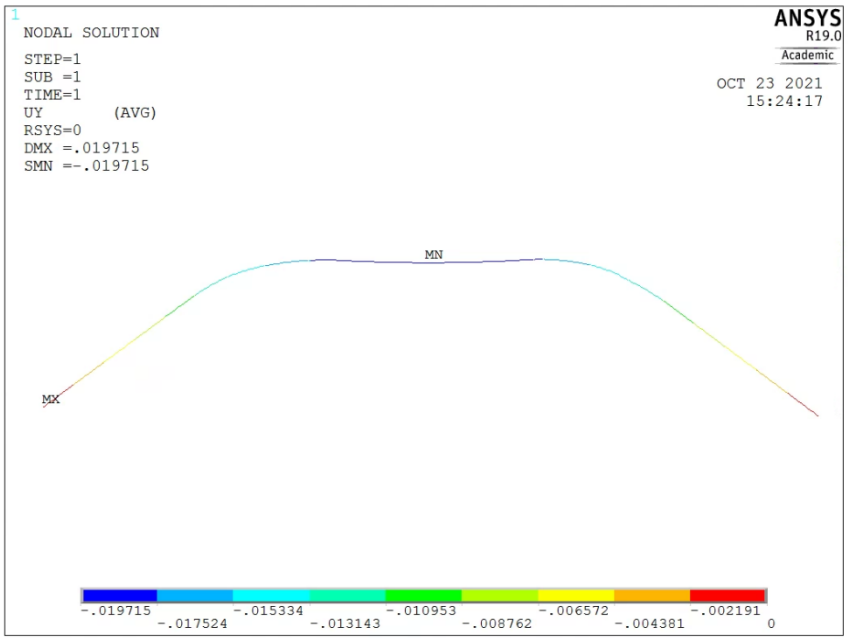

Fig. (6.60). Transverse displacement of the tube along *y* direction using VABS+ANSYS-APDL.

The obtained transverse displacement distribution of this tube using the presented 1D FE solution using Classical beam model up to 2nd order stiffness matrix is shown in Fig. (6.61). A percentage difference of 24% is observed between the VABS+ANSYS 1D and the present solution. This difference can be due to the effect of shear which has not been considered in the present solution.

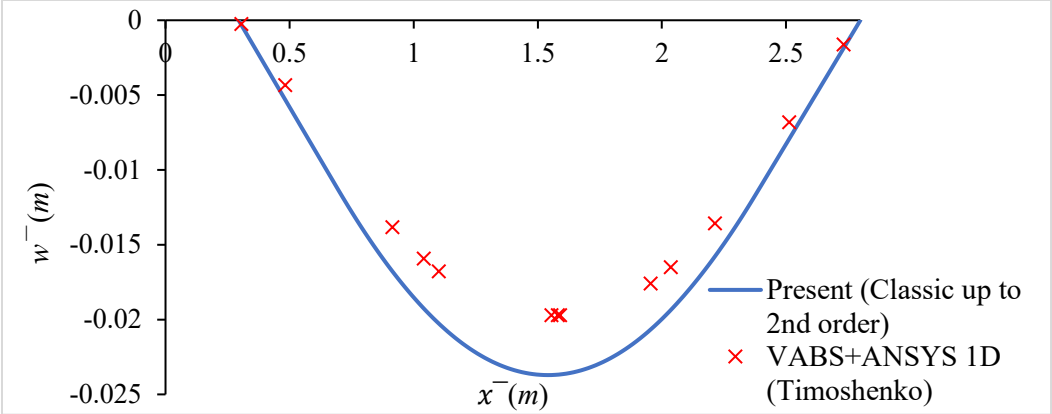

Fig. (6.61). Transverse displacement of the tube along *y* direction using VABS+ANSYS-APDL.

6.7 Conclusion remarks

The analytical meshless Pascal polynomial method for cross-sectional analysis of initially curved composite beams with rectangular and tubular sections presented in chapter (3) is examined. Using the VAM, the Pascal polynomials in the Cartesian coordinates are introduced to the warping field in the Cartesian coordinates for rectangular cross-section and they are applied to the polar coordinates system for tubular section with considering the layer angle in the circumference. The presented method is examined by comparing the obtained strains and cross-sectional stiffness constants with the literature, ANSYS 3D and VABS 3.8. The present method is computationally more efficient compared to the ANSYS 3D for determining the mechanical behavior of composite curved tubes under complex loading condition since there is no need to generate mesh of the 3D body. The parametric study is performed, and the following conclusions can be drawn for curved tubes.

- As a simple example, the explicit formulations for the strain energy of the curved isotropic beam with rectangular cross-section are provided to understand the utilization of **Pascal polynomial method in conjunction with the VAM**. Then, the cross-sectional stiffness constants of curved rectangular isotropic section have been obtained.
- The presented meshless cross-sectional analysis for composite tubes **saves** computational time compared **to ANSYS 3D**. (from hours to minutes)
- It is observed that the change of initial curvature does not have effect on the extensional stiffness (S_{11}), shearing stiffness (S_{22}, S_{33}), torsional stiffness (S_{44}) and bending stiffness (S_{55}, and S_{66}) of the curved isotropic beam. While, as the initial curvature increases, the magnitudes

of extension-bending (S_{15} (Timoshenko-Like) or $\bar{S}_{13}$ (Classic up to 2nd order)) stiffness increase.

- It is seen that increasing the initial curvature, increases the S_{11} and S_{55} and then they decrease for higher values of initial curvature of [-α/ α] tubes.
- For composite tubes with complex lay-up, the change of curvature affects more the S_{11} and S_{55} of the tube.
- It can be concluded that two factors affect the global behavior of composite tubes under bending loading as the initial curvature increases, one is the cross-sectional stiffness constants and the other is the change of geometry of the beam which affects the FE global stiffness matrix.
- The obtained extensional-bending (S_{15}) and shear-torsion (S_{24}) stiffness have substantial effect on the strain distributions of the curved composite tubes under bending loading.
- A good agreement between the present meshless method and VABS 3.8 has been observed for strains and cross-sectional stiffness constants for different values of initial curvature.
- The obtained bending stiffness of the $[\alpha]_{10}$ of the Timoshenko beam model and Classical beam model (up to 2nd order of the strain energy) are different. However, for the curved tubes with the fiber angles (*i.e.* $[0_5/45_5]$), the obtained Timoshenko bending stiffness is similar to Classical beam model (up to 2nd order of the strain energy).
- As the fiber angle increases for tubes with [-α/α], the value of the transverse deflection increases dramatically for the curved tubes. Moreover, increasing the initial curvature, decreases the transverse deflection of the beam noticeably.
- One can model a composite curved tube with straight elements where the cross-sectional stiffness matrix can be curved (with $k_2 \neq 0$) or (with $k_2=0$). The number of elements should be large enough to have convergence.
- By meshing a tube with sufficiently large number of elements, it is possible to model a composite tube which is a combination of straight and curved parts using VABS method with a very good agreement compared to ANSYS 3D.

7 Chapter 7: Contributions and conclusions

7.1 Contributions

In this dissertation, first, a 3D elasticity solution of Lekhnitskii for anisotropic cylindrical bodies under pure bending moment has been used for stress analysis of straight composite tubes under four-point bending loadings. The first ply failure analysis using Tsai-Wu and maximum stress criteria of composite tubes has been done. Then, a new methodology for investigating the mechanical behavior of composite straight and initially curved tubular beams has been presented. The presented methodology for analysis of straight and initially curved composite tubes allows an engineer to take advantage of composite materials when designing composite beams in which the modeling procedure is simple-input, easy to use and computational time is much less than regular 3D FEA.

A **meshless** dimensional reduction of a **composite tubular** beam structure is developed for 3D orthotropic initially curved and straight composite tube. The method takes advantage of small parameters associated with the tube geometry. The dimensional reduction has been done using variational asymptotic method and a 3D beam problem is split into a 2D cross-sectional analysis and a 1D beam analysis along the length. The **Pascal polynomials** in **polar coordinates** have been used to perform cross-sectional discretization. Therefore, one does not need to model and mesh the tubular composite beam cross-section. As such, the optimization procedure to find the best lay-up sequence and dimensional geometry of a composite tube will be straightforward. Moreover, the stress analysis of a composite tube will be carried out easily.

The contributions of these new developments can be summarized as follows:

- Development of a **meshless** dimensional reduction method for stress analysis of straight composite tubes under complex loading in which Pascal polynomials in polar coordinates are used for warping field. Unlike the 3D regular FEM which uses 3D elements for generating mesh and VABS which uses the 2D FEM for cross-sectional discretization, the present work eliminates generating CAD modeling and mesh of composite tube. Therefore, the optimization and parametric study is more straightforward. The computational time reduces considerably compared to ANSYS 3D. As the radius of curvature increases, the number of elements to predict the behavior of the curved composite tube need to be increased. This leads to more computational time. The analysis of tube $[90_{40}/60_{60}/\text{-}60_{60}]$ in section 6.2.4 spends about two

hours while the analysis of this tube using the Pascal polynomial dimensional reduction method takes 30 minutes.

- The obtained 6×6 cross-sectional stiffness matrix based on Timoshenko-Like beam model is incorporated to a developed 1D FE for determining the displacements of straight composite tubes under complex loadings. The obtained 4×4 is incorporated into a developed 1D FE for initially curved beams to determine transverse deflection of curved tubes under complex loading condition.
- A **meshless dimensional reduction method** to perform the cross-sectional analysis of elliptical composite tubes has been developed to obtain the 6×6 as well as 4×4 cross-sectional stiffness matrix of elliptical composite tube. The strain distribution within the section of elliptical tube has been obtained. Also, the 1D FE analysis of elliptical tubes has been done to obtain the transverse deflection of tube under complex loadings.
- A **meshless dimensional reduction method** for determining cross-sectional stiffness matrices (Classical and Timoshenko-Like) as well as strains distribution of cross-section of initially curved composite tubes has been developed.
    - The global behavior and strain distribution of initially curved composite tubes under tip loading has been done.
    - The parametric study has been performed to provide insight into mechanical behavior of straight and curved composite tubes including cross-sectional analysis and determining strain and deflections under four-point bending loadings.
    - The presented method of solution can be used for analysis of tubes under axial force, torque, shear loading and bending moment.
    - To determine the transverse deflection of an initially curved tube one can use elements with curved and straight cross-sectional stiffness matrices.

7.2 Recommendation for future works

The methodology presented in this dissertation fulfills the objectives of this thesis work. Potential works can be listed as

- The order of Pascal polynomial affects substantially the accuracy of the strain distribution. Increasing the polynomial order increases the accuracy of the determined strains.

- Investigating failure of composite tubes using meshless polynomial based method is feasible.
- Performing vibration analysis of straight and initially curved composite tubes and also transient analysis.
- An analysis for helicopter landing gears under impact loading conditions can be conducted.
- An optimization technique can be developed to propose proper lay-up sequences based on cross-sectional and structural analyses.
- Developing an initially curved element for finite element analysis of curved tubes can predict more accurate the global behavior of composite tubes.

List of publications

Journal papers

- **Khadem Moshir S**., Suong V. Hoa, Farjad Shadmehri, Stress analysis of elliptical composite tubular beams using a meshless dimensional reduction method, Composite Structures Journal, 2021, DOI: 10.1016/j.compstruct.2021.114323
- **Khadem Moshir S**., Suong V. Hoa, Farjad Shadmehri, Structural analysis of composite tubes using a meshless analytical dimensional reduction method, International Journal for Numerical Methods in Engineering, 2021, DOI: 10.10002/nme.6660
- **Khadem Moshir S**., Suong V. Hoa, Farjad Shadmehri, Daniel Rosca, Ashraf Ahmed, Mechanical behavior of thick composite tubes under four-point bending, Composite Structures Journal, 2020, DOI: 10.1016/j.compstruct.2020.112097
- **Khadem Moshir S**., Suong V. Hoa, Farjad Shadmehri, Stress analysis of initially curved composite beams with tubular and rectangular sections using an asymptotic meshless method (in progress)

Conference papers

- **Khadem Moshir S**., Hoa S.V., Shadmehri, F., Stress analysis of thick-walled composite tube under bending moment, CANCOM, Kelowna, Canada, 2019.

8 Appendix A

VABS modeling of initially curve tube under four-point bending loadings

In this section, we provided the procedure of modeling of the curved tube in VABS 3.8 and performing 1D FEM in ANSYS. The VABS modeling of composite beams has been provided in VABS user manual, [94].

Defining the material properties

Defining the material properties in the VABS using ANSYS-APDL interface. The material properties are then imported in the VABS input file control.

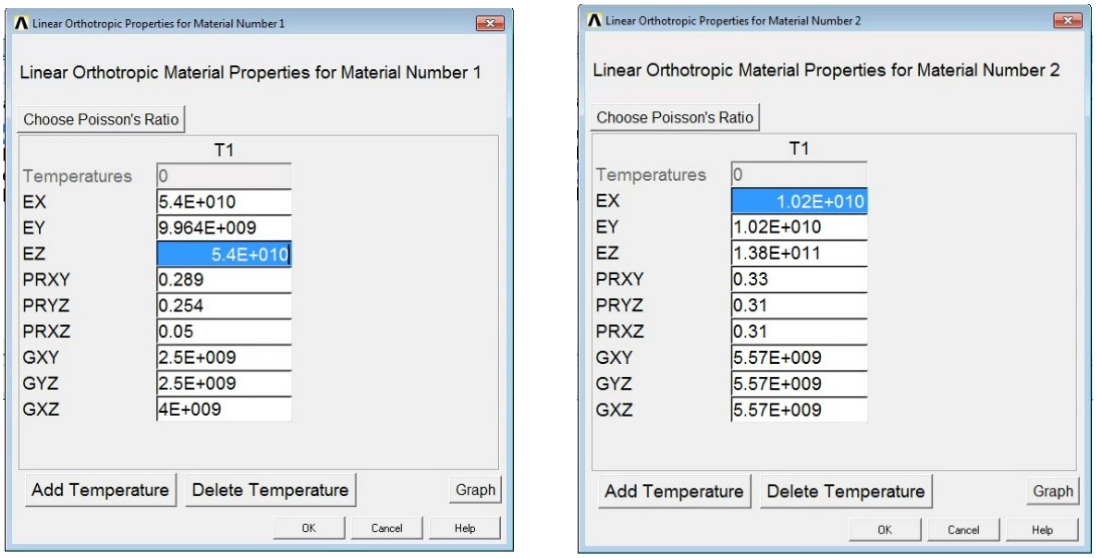

a) 5-harness satin woven b) Carbon/PEKK

Fig. (A 1). Defined material properties in VABS.

Defining the lay-up sequence and layers thickness

The material properties and layer thickness are defined in the user layout types as follows:

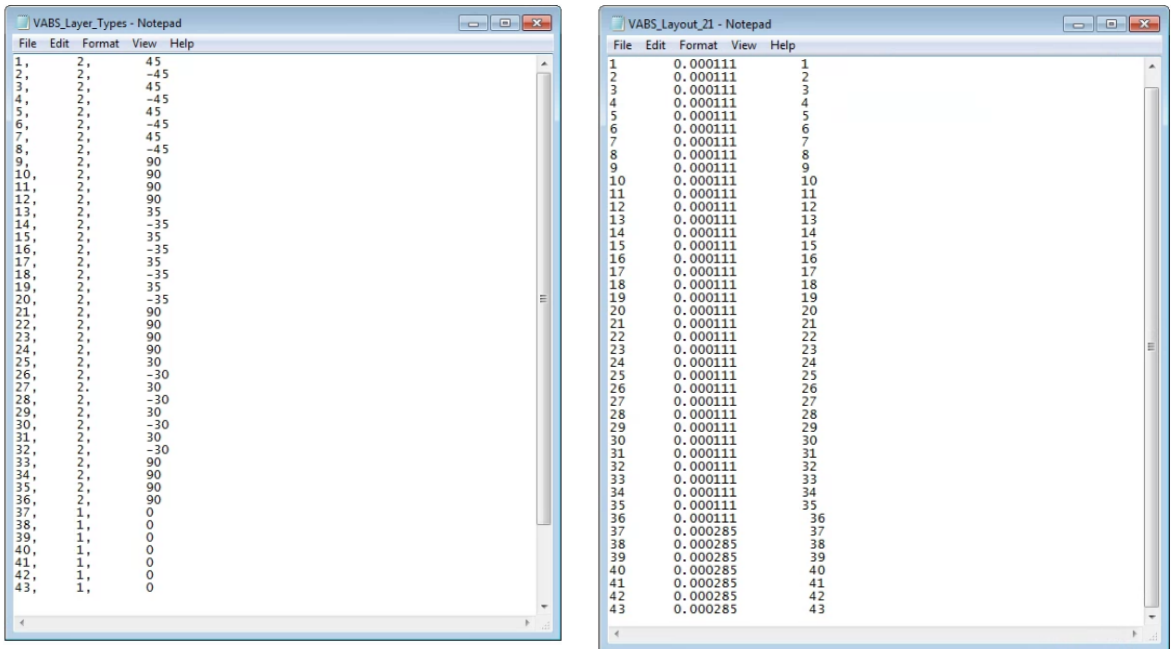

a) *b*)

Fig. (A 2). *a*) The defined lay-up sequence in VABS, *b*) The defined layer thickness in VABS.

Input the basic settings in VABS

At this step one needs to input the beam model and total number of layers. For straight tubes, the $k_1=k_2=k_3=0$. For initially curved tubes we set $k_1=k_3=0$ and $k_2=1.61$ $1/m$ (section B-B) and $k_2=2.06$ $1/m$ (section C-C). We selected the Timoshenko beam model.

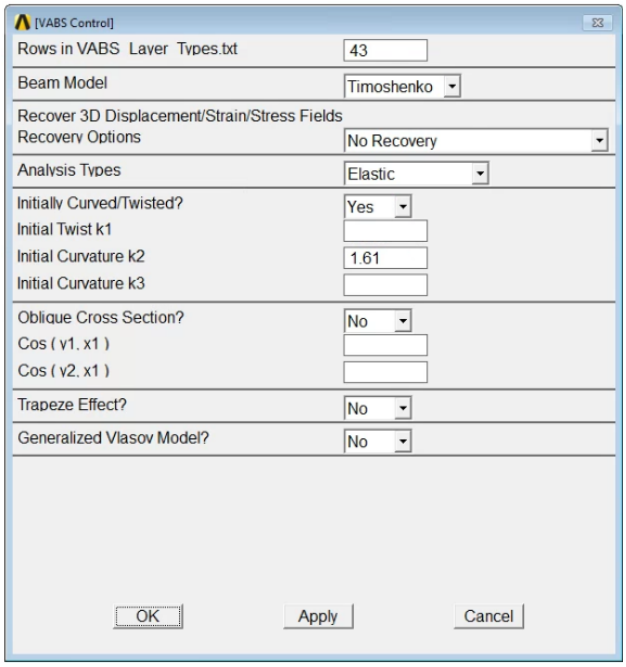

Fig. (A 3). VABS user input control.

Defining the mold lines of the cross-section

The mold lines of the tubular cross-section are created in the preprocessor of the ANSYS. The following APDL ANSYS code is created for the cross-section of the tube.

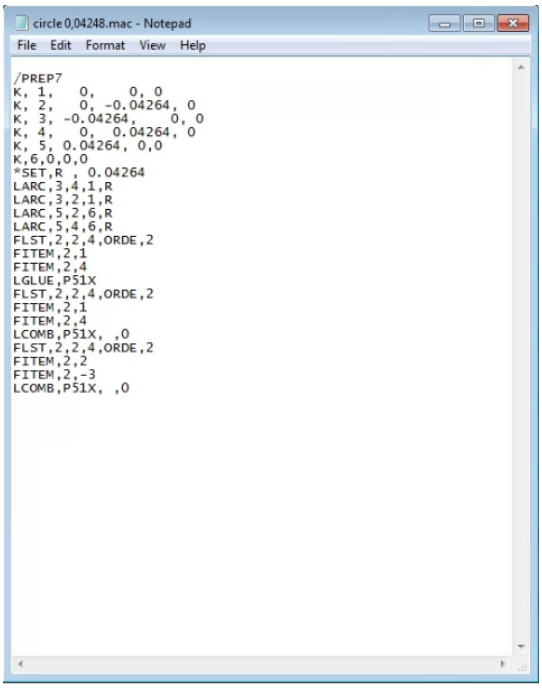

Fig. (A 4). The created mold line code of ANSYS APDL.

The obtained cross-section mold line in the ANSYS APDL is shown in the following Figure. The figure consists of two mold lines as L1 and L2.

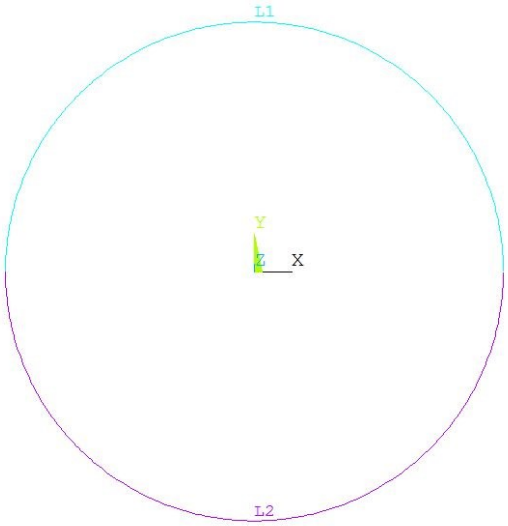

Fig. 6. The generated mold lines of the tubular section.

Defining the lamination direction

In the next step we input the number of laminas, file name of the VABS lay-out as well as define the lamination direction vector. For the mold line L1, we select -Y which determines the direction of the lamination from the mold line to downward. For the mold line L2 we select +Y as the direction of the laminating to the upward or positive direction. The projection direction on X axis is selected as default. The Fig. 7a shows the segment overview through the segment layout procedure. Fig. 7b shows the generated area by selecting and gluing all areas.

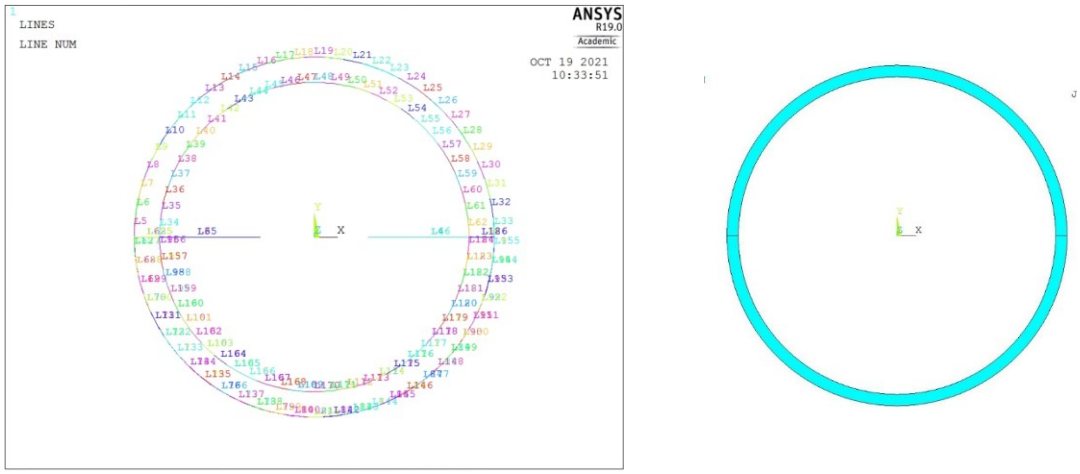

Fig. (A 5). a) Segment overview in VABS, *b)* generated area of the section

Assign laminating

In this step, we assign the laminates that were defined before on each mold line. The figure below shows the laminate on the mold line for the mold lines L_1 and L_2.

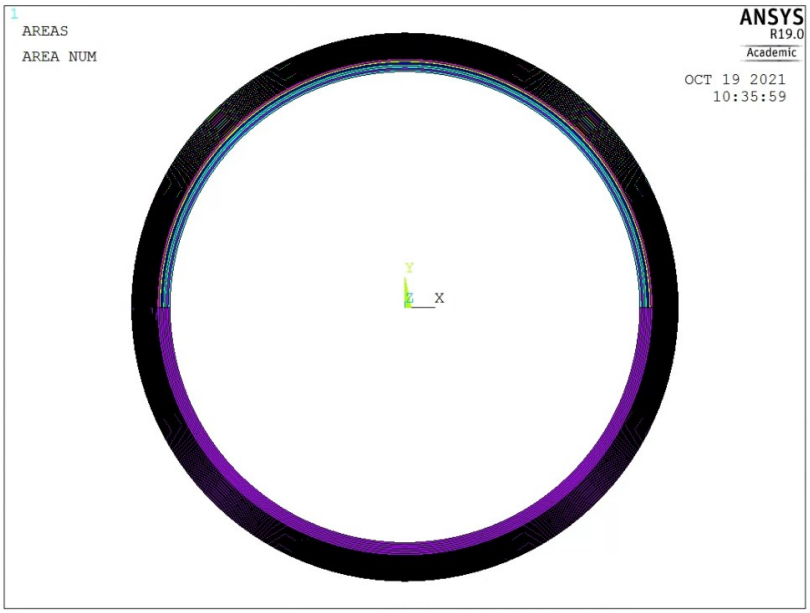

Fig. (A 6). The created laminates on the mold lines in VABS.

Selecting the element type and quick mesh in VABS

The element 8-node quadrilateral has been selected for both the segment mold lines L_1 and L_2 with the smart size level of the mesh.

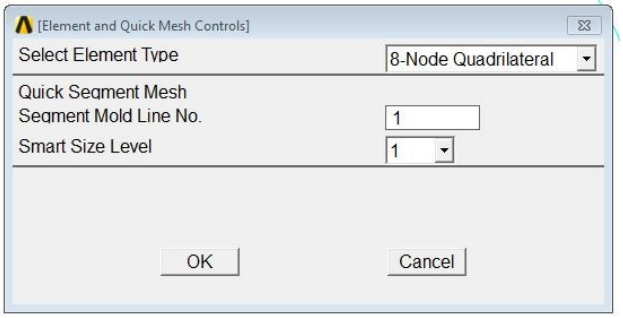

Fig. (A 7). Selecting the element type and quick mesh

The generated mesh for the mold lines L_1 and L_2 are as follows.

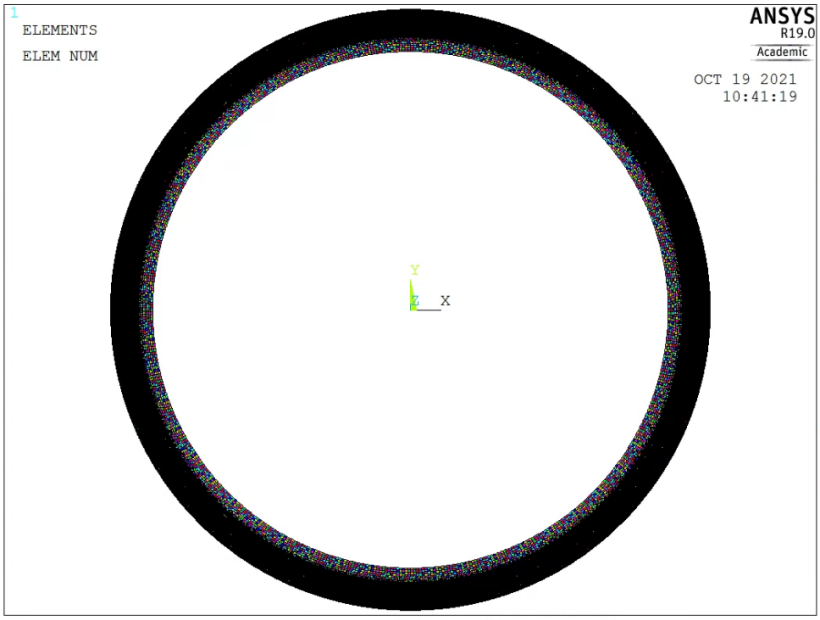

Fig. (A 8). The generated mesh through the element type and quick mesh of VABS.

Extracting the cross-sectional stiffness matrix

The cross-sectional stiffness matrix for tube at section B-B is reported in Table (6.19).

Recovery Analysis

According to the recovery analysis presented in [94], we carried out the recovery analysis of the tube under bending moment M_2=-906 N.m. and shear loading F_3=-1409 N. $\bar{u}, \bar{v},$ and $\bar{w}$ are the displacements obtained through 1D analysis. C_{ij} are the direction cosines. In order to obtain the 3D strains, it is not necessary input $\bar{u}, \bar{v},$ and $\bar{w}$ and direction cosines. F_1 is the sectional axial force, F_2 and F_3 are the sectional transverse shear forces along x_2 and x_3. M_1 is the sectional torque, M_2 is the sectional bending moment about x_2 and M_3 is the sectional bending moment about x_3. $f_1, f_2,$ f_3 are distributed forces (including both applied forces and inertial forces) per unit span along x_1, x_2 and x_3, respectively. m_1, m_2, m_3 are distributed moment (including both applied and inertial moments) per unit span along x_1, x_2 and x_3. Prime is the derivative with respect to x_1. For the recovery, VABS requires the following data.

$$
\begin{array}{cccccc}
u_1 & u_2 & u_3 & & & \\
C_{11} & C_{12} & C_{13} & & & \\
C_{21} & C_{22} & C_{23} & & & \\
C_{31} & C_{32} & C_{33} & & & \\
F_1 & M_1 & M_2 & M_3 & & \\
F_2 & F_3 & & & & \\
f_1 & f_2 & f_3 & m_1 & m_2 & m_3 \\
f_1' & f_2' & f_3' & m_1' & m_2' & m_3' \\
f_1'' & f_2'' & f_3'' & m_1'' & m_2'' & m_3''
\end{array}
$$

Fig. (A 9). Required data for recovery analysis of a beam in VABS.

The moment M_2=-906 N.m and the shear force F_3=-1556 N input in VABSInputFile.

9 References

[1] Derisi B. Development of thermoplastic composite tubes for large deformation, Ph.D thesis: Concordia University, 2008.

[2] Moshir SK, Hoa SV, Shadmehri F, Rosca D, Ahmed A. Mechanical behavior of thick composite tubes under four-point bending. Composite structures. 2020;242:112097.

[3] https://www.bellflight.com/products/bell-412.

[4] Derisi B, Hoa SV, Xu D, Hojjati M, Fews R. Mechanical Behavior of Carbon/PEKK Thermoplastic Composite Tube Under Bending Load. Journal of Thermoplastic Composite Materials. 2010;24:29-49.

[5] Lekhnitskii S, Fern P, Brandstatter JJ, Dill E. Theory of elasticity of an anisotropic elastic body. Physics Today. 1964;17:84.

[6] Davies GC, Bruce DM. A stress analysis model for composite coaxial cylinders. Journal of Materials Science. 1997;32:5425-37.

[7] Hu G, Bai J, Demianouchko E, Bompard P. Mechanical behaviour of±55° filament-wound glass-fibre/epoxy-resin tubes—III. Macromechanical model of the macroscopic behaviour of tubular structures with damage and failure envelope prediction. Composites science and technology. 1998;58:19-29.

[8] Bai J, Hu G, Bompard P. Mechanical behaviour of±55° filament-wound glass-fibre/epoxy-resin tubes: II. Micromechanical model of damage initiation and the competition between different mechanisms. Composites science and technology. 1997;57:155-64.

[9] Bouhafs M, Sereir Z, Chateauneuf A. Probabilistic analysis of the mechanical response of thick composite pipes under internal pressure. International Journal of Pressure Vessels and Piping. 2012;95:7-15.

[10] Aksoy Ş, Kurşun A, Çetin E, Haboğlu MR. Stress Analysis of Laminated Cylinders Subject to the Thermomechanical Loads. World Academy of Science, Engineering and Technology, International Journal of Mechanical, Aerospace, Industrial, Mechatronic and Manufacturing Engineering. 2014;8:244-9.

[11] Yuan F. Exact solutions for laminated composite cylindrical shells in cylindrical bending. Journal of Reinforced Plastics and Composites. 1992;11:340-71.

[12] Jolicoeur C, Cardou A. Analytical solution for bending of coaxial orthotropic cylinders. Journal of Engineering Mechanics. 1994;120:2556-74.

[13] Tarn J-Q, Wang Y-M. Laminated composite tubes under extension, torsion, bending, shearing and pressuring: a state space approach. International Journal of Solids and Structures. 2001;38:9053-75.

[14] Xia M, Takayanagi H, Kemmochi K. Bending behavior of filament-wound fiber-reinforced sandwich pipes. Composite Structures. 2002;56:201-10.

[15] Zhang C, Hoa SV. A limit-based approach to the stress analysis of cylindrically orthotropic composite cylinders (0/90) subjected to pure bending. Composite Structures. 2012;94:2610-9.

[16] Zhang C, Hoa SV, Liu P. A method to analyze the pure bending of tubes of cylindrically anisotropic layers with arbitrary angles including 0 or 90. Composite structures. 2014;109:57-67.
[17] Ahmad MG, Hoa S. Flexural stiffness of thick walled composite tubes. Composite Structures. 2016;149:125-33.
[18] Sun X, Tan V, Chen Y, Tan L, Jaiman R, Tay T. Stress analysis of multi-layered hollow anisotropic composite cylindrical structures using the homogenization method. Acta Mechanica. 2014;225:1649-72.
[19] Menshykova M, Guz IA. Stress analysis of layered thick-walled composite pipes subjected to bending loading. International Journal of Mechanical Sciences. 2014;88:289-99.
[20] Blom A, Stickler P, Rassaian M, Gürdal Z. Bending Test of a Variable-Stiffness Fiber Reinforced Composite Cylinder. 51st AIAA/ASME/ASCE/AHS/ASC Structures, Structural Dynamics, and Materials Conference 18th AIAA/ASME/AHS Adaptive Structures Conference 12th2010. p. 2600.
[21] Sarvestani HY, Hoa SV, Hojjati M. Three-dimensional stress analysis of orthotropic curved tubes-part 1: single-layer solution. European Journal of Mechanics-A/Solids. 2016;60:327-38.
[22] Yazdani Sarvestani H. High-order Simple-input Methods for Thick Laminated Composite Straight and Curved Tubes, Ph.D thesis: Concordia University, 2016.
[23] Yazdani Sarvestani H, Hojjati M. Effects of lay-up sequence in thick composite tubes for helicopter landing gears. Proceedings of the Institution of Mechanical Engineers, Part G: Journal of Aerospace Engineering. 2017;231:2098-110.
[24] Fuchs HP, Hyer MW. Bending response of thin-walled laminated composite cylinders. Composite Structures. 1992;22:87-107.
[25] Wang C, Reddy JN, Lee K. Shear deformable beams and plates: Relationships with classical solutions: Elsevier, 2000.
[26] Tatting BF, Gürdal Z, Vasiliev VV. The brazier effect for finite length composite cylinders under bending. International Journal of Solids and Structures. 1997;34:1419-40.
[27] Sanders Jr JL. Nonlinear theories for thin shells. Quarterly of Applied Mathematics. 1963;21:21-36.
[28] Di S, Rothert H. A solution of laminated cylindrical shells using an unconstrained third-order theory. Composite structures. 1995;32:667-80.
[29] Kollár L, Springer GS. Stress analysis of anisotropic laminated cylinders and cylindrical segments. International Journal of Solids and Structures. 1992;29:1499-517.
[30] Love AEH. A treatise on the mathematical theory of elasticity: Cambridge university press, 2013.
[31] Chan WS, Demirhan KC. A Simple Closed-Form Solution of Bending Stiffness for Laminated Composite Tubes. Journal of Reinforced Plastics and Composites. 2000;19:278-91.
[32] Saggar P. Experimental study of laminated composite tubes under bending. 2007.

[33] Kim SJ, Shin JW, Kim H-G, Kim T-U, Kim S. The modified Brazier approach to predict the collapse load of a stiffened circular composite spar under bending load. Aerospace Science and Technology. 2016;55:474-81.
[34] Nayfeh AH, Pai PF. Linear and nonlinear structural mechanics: John Wiley & Sons, 2008.
[35] Librescu L, Song O. Behavior of thin-walled beams made of advanced composite materials and incorporating non-classical effects. Applied Mechanics Reviews. 1991;44:S174-S80.
[36] Rehfield LW, Atilgan AR, Hodges DH. Nonclassical Behavior of Thin-Walled Composite Beams with Closed Cross Sections. Journal of the American Helicopter Society. 1990;35:42-50.
[37] Kim C, White SR. Thick-walled composite beam theory including 3-D elastic effects and torsional warping. International Journal of Solids and Structures. 1997;34:4237-59.
[38] Shadmehri F, Derisi B, Hoa S. On bending stiffness of composite tubes. Composite structures. 2011;93:2173-9.
[39] Silvestre N. Non-classical effects in FRP composite tubes. Composites Part B: Engineering. 2009;40:681-97.
[40] Hodges DH. Nonlinear composite beam theory: American Institute of Aeronautics and Astronautics, 2006.
[41] Yu W, Volovoi VV, Hodges DH, Hong X. Validation of the Variational Asymptotic Beam Sectional Analysis. AIAA journal. 2002;40:2105-12.
[42] Danielson DA, Hodges DH. Nonlinear Beam Kinematics by Decomposition of the Rotation Tensor. Journal of Applied Mechanics. 1987;54:258-62.
[43] Berdichevskii V. Variational-asymptotic method of constructing a theory of shells: PMM vol. 43, no. 4, 1979, pp. 664–687. Journal of Applied Mathematics and Mechanics. 1979;43:711-36.
[44] Ho J, Yu W, Hodges D. Energy Transformation to Generalized Timoshenko Form by the Variational Asymptotic Beam Sectional Analysis. 51st AIAA/ASME/ASCE/AHS/ASC Structures, Structural Dynamics, and Materials Conference.
[45] Hodges DH, Atilgan AR, Cesnik CE, Fulton MV. On a simplified strain energy function for geometrically nonlinear behaviour of anisotropic beams. Composites Engineering. 1992;2:513-26.
[46] Cesnik CE, Hodges DH, Sutyrin VG. Cross-sectional analysis of composite beams including large initial twist and curvature effects. AIAA journal. 1996;34:1913-20.
[47] Cesnik CE, Hodges DH. VABS: a new concept for composite rotor blade cross-sectional modeling. Journal of the American Helicopter Society. 1997;42:27-38.
[48] Yu W, Hodges DH, Volovoi V, Cesnik CE. On Timoshenko-like modeling of initially curved and twisted composite beams. International Journal of Solids and Structures. 2002;39:5101-21.

[49] Yu W, Hodges DH, Ho JC. Variational asymptotic beam sectional analysis – An updated version. International Journal of Engineering Science. 2012;59:40-64.
[50] Ghafari E, Rezaeepazhand J. Isogeometric analysis of composite beams with arbitrary cross-section using dimensional reduction method. Computer Methods in Applied Mechanics and Engineering. 2017;318:594-618.
[51] Rajagopal A. Variational Asymptotic Based Shear Correction Factor for Isotropic Circular Tubes. AIAA journal. 2018:1-7.
[52] Harursampath D, Hodges DH. Asymptotic analysis of the non-linear behavior of long anisotropic tubes. International journal of non-linear mechanics. 1999;34:1003-18.
[53] Jiang F, Yu W. Nonlinear Variational Asymptotic Sectional Analysis of Hyperelastic Beams. AIAA journal. 2016;54:679-90.
[54] Jiang F, Yu W. Damage analysis by physically nonlinear composite beam theory. Composite structures. 2017;182:652-65.
[55] Popescu B, Hodges DH. On asymptotically correct Timoshenko-like anisotropic beam theory. International Journal of Solids and Structures. 2000;37:535-58.
[56] Zupan D, Saje M. The linearized three-dimensional beam theory of naturally curved and twisted beams: The strain vectors formulation. Computer Methods in Applied Mechanics and Engineering. 2006;195:4557-78.
[57] Tabarrok B, Farshad M, Yi H. Finite element formulation of spatially curved and twisted rods. Computer Methods in Applied Mechanics and Engineering. 1988;70:275-99.
[58] Ecsedi I, Dluhi K. A linear model for the static and dynamic analysis of non-homogeneous curved beams. Applied Mathematical Modelling. 2005;29:1211-31.
[59] Hajianmaleki M, Qatu MS. Static and vibration analyses of thick, generally laminated deep curved beams with different boundary conditions. Composites Part B: Engineering. 2012;43:1767-75.
[60] Yu AM, Nie GH. Explicit solutions for shearing and radial stresses in curved beams. Mechanics Research Communications. 2005;32:323-31.
[61] Sheikh AH. New Concept to Include Shear Deformation in a Curved Beam Element. Journal of Structural Engineering. 2002;128:406-10.
[62] Dasgupta S, Sengupta D. Horizontally curved isoparametric beam element with or without elastic foundation including effect of shear deformation. Computers & Structures. 1988;29:967-73.
[63] Yazdani Sarvestani H, Hojjati M. Three-dimensional stress analysis of orthotropic curved tubes-part 2: Laminate solution. European Journal of Mechanics - A/Solids. 2016;60:339-58.
[64] Berdichevsky V, Armanios E, Badir A. Theory of anisotropic thin-walled closed-cross-section beams. Composites Engineering. 1992;2:411-32.

[65] Borri M, Merlini T. A large displacement formulation for anisotropic beam analysis. Meccanica. 1986;21:30-7.
[66] Giavotto V, Borri M, Mantegazza P, Ghiringhelli G, Carmaschi V, Maffioli GC, et al. Anisotropic beam theory and applications. Computers & Structures. 1983;16:403-13.
[67] Borri M, Ghiringhelli GL, Merlini T. Linear analysis of naturally curved and twisted anisotropic beams. Composites Engineering. 1992;2:433-56.
[68] Stemple AD, Lee SW. Finite-element model for composite beams with arbitrary cross-sectional warping. AIAA journal. 1988;26:1512-20.
[69] Meyers CA, Hyer MW. RESPONSE OF ELLIPTICAL COMPOSITE CYLINDERS TO INTERNAL PRESSURE LOADING. Mechanics of Composite Materials and Structures. 1997;4:317-43.
[70] Meyers CA. Response of Elliptical Composite Cylinders to Axial Compression Loading. Mechanics of Composite Materials and Structures. 1999;6:169-94.
[71] Lin C, Chan W. Stiffness evaluation of elliptical laminated composite tube under bending. 19th AIAA Applied Aerodynamics Conference2001. p. 1336.
[72] Akgun G, Algul I, Kurtaran H. Nonlinear Static Analysis of Laminated Composite Hollow Beams with Super-Elliptic Cross-Sections. International Journal of Materials and Metallurgical Engineering. 2017;11:1467-72.
[73] Chen D, Sun G, Jin X, Li Q. Quasi-static bending and transverse crushing behaviors for hat-shaped composite tubes made of CFRP, GFRP and their hybrid structures. Composite structures. 2020;239:111842.
[74] Szabó G, Váradi K, Felhős D. Bending analysis of a filament-wound composite tube. Modern Mechanical Engineering. 2018;8:66.
[75] Reddy JN. Mechanics of laminated composite plates and shells: theory and analysis: CRC press, 2004.
[76] Hyer MW. Stress analysis of fiber-reinforced composite materials: DEStech Publications, Inc, 2009.
[77] Na S. Control of dynamic response of thin-walled composite beams using structural tailoring and piezoelectric actuation: Virginia Tech, 1997.
[78] Gay D, Hoa SV. Composite Materials: Design and Applications, Second Edition: CRC Press, 2007.
[79] Moshir SK, Hoa SV, Shadmehri F. Structural analysis of composite tubes using a meshless analytical dimensional reduction method. International Journal for Numerical Methods in Engineering.n/a.
[80] Zhao J-M, Song X-X, Liu B. Standardized Compliance Matrices for General Anisotropic Materials and a Simple Measure of Anisotropy Degree Based on Shear-Extension Coupling Coefficient. International Journal of Applied Mechanics. 2016;8:1650076.
[81] Stoer J, Bulirsch R. Introduction to numerical analysis: Springer Science & Business Media, 2013.
[82] Wang HW, Zhou HW, Gui LL, Ji HW, Zhang XC. Analysis of effect of fiber orientation on Young's modulus for unidirectional fiber reinforced composites. Composites Part B: Engineering. 2014;56:733-9.

[83] Sheikh AH, Thomsen OT. An efficient beam element for the analysis of laminated composite beams of thin-walled open and closed cross sections. Composites science and technology. 2008;68:2273-81.
[84] Sheikh AH, Thomsen OT. An efficient beam element for the analysis of laminated composite beams of thin-walled open and closed cross sections. Composites science and technology. 2008;68:2273-81.
[85] Seli H, Awang M, Ismail AIM, Rachman E, Ahmad ZA. Evaluation of properties and FEM model of the friction welded mild steel-Al6061-alumina. Materials Research. 2013;16:453-67.
[86] Hartmann F, Jantzen R. Apollonius' ellipse and evolute revisited. Manuscript http://www42 homepage villanova edu/frederick hartmann/resume html. 2003.
[87] Irgens F. Continuum mechanics: Springer Science & Business Media, 2008.
[88] ANSYS. Element Reference www.ANSYS.stuba.sk.
[89] Kovvali RK, Hodges DH. Verification of the variational-asymptotic sectional analysis for initially curved and twisted beams. Journal of Aircraft. 2012;49:861-9.
[90] Timoshenko SP, Goodier JN. Theory of elasticity. 1951.
[91] Borri M, Ghiringhelli GL, Merlini T. Linear analysis of naturally curved and twisted anisotropic beams. Composites Engineering. 1992;2:433-56.
[92] TANG YQ, ZHOU ZH, CHAN SL. AN ACCURATE CURVED BEAM ELEMENT BASED ON TRIGONOMETRICAL MIXED POLYNOMIAL FUNCTION. International Journal of Structural Stability and Dynamics. 2013;13:1250084.
[93] DeWolf JT, Mazurek D, Beer FP, Johnston ER. Mechanics of Materials: McGraw-Hill Education, 2014.
[94] Yu W. VABS Manual for Users. 2013.